

**Microwave Technique for Monitoring Fluid Level
in the Horizontal Petroleum Carrying Pipeline**

BY

Yanal Shaher A. AlFaouri

A Dissertation Presented to the
DEANSHIP OF GRADUATE STUDIES

KING FAHD UNIVERSITY OF PETROLEUM & MINERALS

DHAHRAN, SAUDI ARABIA

In Partial Fulfillment of the
Requirements for the Degree of

DOCTOR OF PHILOSOPHY

In

ELECTRICAL ENGINEERING

April 2014

KING FAHD UNIVERSITY OF PETROLEUM & MINERALS

DHAHRAN- 31261, SAUDI ARABIA

DEANSHIP OF GRADUATE STUDIES

This thesis, written by Yanal Shaher AlFaouri under the direction his thesis advisor and approved by his thesis committee, has been presented and accepted by the Dean of Graduate Studies, in partial fulfillment of the requirements for the degree of **DOCTOR OF PHILOSOPHY IN ELECTRICAL ENGINEERING.**



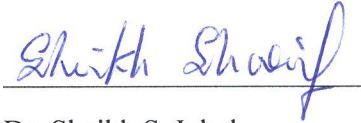
Dr. Ali A. Al-Shaikhi
Department Chairman



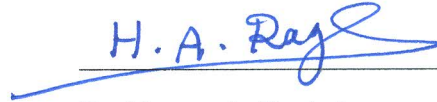
Dr. Salam A. Zummo
Dean of Graduate Studies

Date

13/5/14



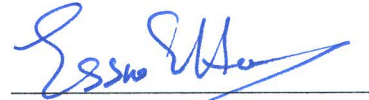
Dr. Sheikh S. Iqbal
(Advisor)



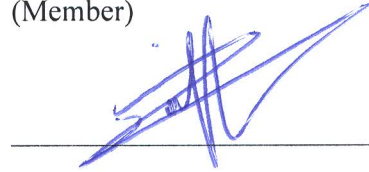
Dr. Hassan A. Ragheb
(Co-Advisor)



Dr. Raj Mittra
(Member)



Dr. Essam E.M. Hassan
(Member)



Dr. Mohammad S. Sharawi
(Member)

© Yanal S. Faouri

2014

Dedication

My Parents & Wife

Whose Prayers and Perseverance Led to this Achievement

ACKNOWLEDGMENTS

In the name of Allah, the Most Gracious and the Most Merciful

All praises and glory be to Allah (SWT) for blessing me with opportunities abound and showering upon me his mercy and guidance all through the life. I pray that He continues the same the rest of my life. Moreover, may his peace and blessings of Allah be upon Prophet Muhammad, a guidance and inspiration to our lives.

I would like to thank my supervisors, Dr. Sheikh Sharif Iqbal and Dr. Hassan A. Ragheb for their guidance and expertise throughout this thesis. There were always there when I needed them, and even with their tight schedule, they have always found time for me. I am extremely grateful to them for their prompt replies and their numerous proofreads. I am also very grateful to my thesis committee members, Dr. Essam Hassan, Dr. Mohammad S. Sharawi, Dr. Raj Mittra and Dr. Mohammad A. Alsunaidi, for their care, cooperation and constructive advice.

Special thanks to my colleagues and friends for their encouragements and various help that they provided throughout my graduate studies at KFUPM. I would like to give my special thanks to my parents, wife, brother and my sister for their support, patience and love. Without their encouragement, motivation and understanding it would have been impossible for me to complete this work.

TABLE OF CONTENTS

ACKNOWLEDGMENTS	V
TABLE OF CONTENTS	VI
LIST OF TABLES	IX
LIST OF FIGURES	XI
LIST OF ABBREVIATIONS	XV
ABSTRACT	XVII
ملخص الرسالة	XIX
1 CHAPTER 1 INTRODUCTION	1
1.1 Introduction	1
1.2 Thesis Motivation	3
1.3 Thesis Objectives	3
1.4 Thesis Overview	4
2 CHAPTER 2 LITERATURE REVIEW	7
2.1 Introduction	7
2.2 Dielectric Loaded Circular Waveguide	7
2.2.1 Concentric Loading	8
2.2.2 Eccentric Loading.....	9
2.3 Multiphase Sensors and Techniques	14
2.3.1 Flow Patterns.....	14
2.3.2 Multiphase Flow Sensors.....	16
2.3.3 Measurement Techniques	17
2.4 Antenna Basics	24
2.4.1 Basic Antenna Parameters.....	24
2.4.2 Microstrip Patch Antenna.....	31

3	CHAPTER 3 ELECTROMAGNETIC FIELDS INSIDE A DIELECTRIC LOADED CIRCULAR WAVEGUIDE.....	36
3.1	Introduction.....	37
3.2	Solution of Wave Equation in Cylindrical Coordinates.....	38
3.3	Geometry Description.....	42
3.4	Problem Formulation.....	44
3.5	Algorithm for Obtaining Cutoff Wavenumbers.....	56
3.6	Results and Discussion.....	58
3.6.1	Verification of the Code.....	59
3.6.2	Cutoff Wavenumbers of Two Dielectric Loaded Circular Waveguide.....	64
3.6.3	Modified Expression.....	66
3.6.4	Optimizing Simulated Model.....	67
3.6.5	Simulation of More Complex Models.....	76
3.7	Conclusion.....	85
4	CHAPTER 4 MICROWAVE MONITORING OF OIL CARRYING PIPELINE.....	86
4.1	Introduction.....	88
4.2	Design of Aperture Coupled Microstrip Patch Antenna.....	89
4.3	Excitation of Two-Phase Petroleum Carrying Pipeline.....	93
4.3.1	Aperture Fed Antenna Integrated with a 2-inch Pipeline.....	93
4.3.2	Eliminating Higher Order Modes.....	95
4.3.3	Optimizing Antenna Placement and Orientation within the Pipeline.....	97
4.3.4	Look-Up Table for Content-Ratio versus Resonant Frequency for Shielded Pipeline.....	103
4.3.5	Look-Up Table for Content-Ratio versus Power of the Reflected Signal for non-Shielded Pipeline.....	105
4.4	Excitation of Three-Phase Petroleum Carrying Pipeline.....	108
4.5	Conclusion.....	117
5	CHAPTER 5 FABRICATION PROCESS AND EXPERIMENTAL RESULTS.....	118
5.1	Introduction.....	119
5.2	Fabrication Process.....	119
5.2.1	Fabrication of the Aperture Coupled Microstrip Patch Antenna.....	119
5.2.2	Assembly of the Pipeline Measurement Setup.....	123

5.3	Experimental Setup	125
5.3.1	Antenna Scattering Parameter Measurements.....	125
5.3.2	Antenna Radiation Pattern Measurements.....	128
5.3.3	S_{11} Measurements Technique for the 3-Phase Contents of the Pipeline	129
5.4	Experimental Results and Comparison	134
5.4.1	Antenna Results.....	134
5.4.2	Antenna S_{11} Measurements for Two-Phase Contents of the Pipeline	139
5.4.3	Antenna S_{11} Measurements for Three-Phase Contents of the Pipeline	147
5.4.4	Measurements of S_{11} Response without Using Network Analyzer.....	151
5.5	Conclusion	154
6	CHAPTER 6 CONCLUSION AND FUTURE WORK	155
6.1	Conclusion	155
6.2	Future Work	156
6.2.1	Analytical Solution	156
6.2.2	Antenna Design	157
6.2.3	Circuit Design	157
	APPENDIX A	158
	Procedure Followed in Achieving the Optimum Design	158
A.1	Microstrip Path Antenna without a Superstrate Layer	158
A.2	Microstrip Patch Antenna with a Superstrate Layer	162
A.3	Excitation of Two-Phase Petroleum Carrying Pipeline	164
	REFERENCES	182
	VITAE	190

LIST OF TABLES

Table 2-1: Sensor Selection Criteria [2]	17
Table 2-2: Antenna Comparison	25
Table 3-1: Convergence of Numerical Results for the First Cutoff Wavenumber	57
Table 3-2: Cutoff Phase Constants of Eccentrically Loaded Circular Waveguide for Various Geometrical Parameters, $\epsilon_{r1}=3.6$, $\epsilon_{r2}=\epsilon_{r3}=1.0$, $c=0.1 \lambda$ and $d_2=0.1 \lambda$.	62
Table 3-3: Cutoff Phase Constants of Eccentrically Loaded Circular Waveguide for Various Geometrical Parameters, $\epsilon_{r1}=1.0$, $\epsilon_{r2}=\epsilon_{r3}=3.6$, $c=0.1 \lambda$ and $d_2=0.1 \lambda$.	63
Table 3-4: Cutoff Phase Constants of Two Cylinders Eccentrically Loaded Circular Waveguide for Various Geometrical Parameters, $\epsilon_{r1}=2.15$, $\epsilon_{r2}=2.15$, $\epsilon_{r3}=1.0$	65
Table 3-5: Maximum Mesh Tuning for HFSS	69
Table 3-6: Calculated and Simulated Cutoff Frequency for the First Five Modes	70
Table 3-7: Summary of the Complicated Simulation Models	80
Table 3-8: Comparison between Wavy Flow and Stratified Flow	81
Table 3-9: Stratified Flow Results for Different Oil-Air Portions	84
Table 4-1: Specifications of Aperture Coupled Microstrip Patch Antenna that is integrated with the 2-inch Pipeline Model	91
Table 4-2: Cutoff Frequencies of the First Three Modes for Different Materials	96
Table 4-3: Specifications of Aperture Coupled Microstrip Antenna that is integrated with the 2-inch Pipeline Model	97
Table 4-4: Response of the Antenna Integrated in the Shielded Pipeline for Different Air – Oil Proportions	104
Table 4-5: Response of the Antenna Integrated in the un-Shielded Pipeline for Different Air – Oil Proportions	107
Table 4-6: Reflection Coefficient of the un-Shielded Plexiglass Antenna at 30% of Oil Level	112
Table 4-7: Reflection Coefficient of the un-Shielded Plexiglass Antenna at 40% of Oil Level	112
Table 4-8: Reflection Coefficient of the un-Shielded Plexiglass Antenna at 50% of Oil Level	112
Table 4-9: Reflection Coefficient of the un-Shielded Plexiglass Antenna at 60% of Oil Level	113
Table 4-10: Reflection Coefficient of the un-Shielded Plexiglass Antenna at 70% of Oil Level	113
Table 4-11: Reflection Coefficient of the Shielded Plexiglass Antenna at 4% of Water Level	114
Table 4-12: Reflection Coefficient of the Shielded Plexiglass Antenna at 8% of Water Level	115
Table 4-13: Reflection Coefficient of the Shielded Plexiglass Antenna at 12% of Water Level	116

Table 5-1: Detected Voltages Responses for Different Materials	151
Table A-1: Microstrip Antenna Specifications without the Superstrate layer	159
Table A-2: Microstrip Antenna Specifications with the Superstrate layer	163
Table A-3: Center Frequency for the Three Medium under Investigation	167
Table A-4: Microstrip Antenna Specifications that Located inside a 2-inch Pipeline ...	175
Table A-5: 3.6 GHz Aperture Coupled Microstrip Antenna Specifications.....	177
Table A-6: Antenna Behavior for Different Oil Percentages	180

LIST OF FIGURES

Figure 2-1: (a) Partially Filled Waveguide; (b) Phase Constant for the Partially Filled Waveguide [11].....	9
Figure 2-2: Circular Waveguide Loaded with One Eccentric Conductor or Dielectric Cylinder.....	12
Figure 2-3: Cutoff Wavenumber versus Eccentricity for Odd Modes ($a=0.5\lambda$, $b=0.2\lambda$, $\epsilon_{r2}=1$) [12]	13
Figure 2-4: Two-Phase Flow Patterns in Horizontal Tubes [38].....	15
Figure 2-5: Schematic of the Device that Consider the Annular Case Flow [41]	18
Figure 2-6: Capacitance Wire-Mesh Sensor [42]	19
Figure 2-7: Laboratory Prototype Cavity Resonator Setup [43].....	20
Figure 2-8: (a) Cross Section, (b) Side View of the Measurement Unit. [44].....	20
Figure 2-9: Two Microstrip Patch Couplers Assembled as a Microstrip Sensor [45].....	21
Figure 2-10: Electrical Resistance Tomographic (ERT) Sensors Placed at the Periphery of the Test Pipeline and Embedded on the Acrylic Wall. [59]	23
Figure 2-11: Construction of Basic Rectangular Microstrip Patch Antenna	31
Figure 2-12: Microstrip Line Feed.....	32
Figure 2-13: Coaxial Probe Feed	33
Figure 2-14: Aperture Coupling.....	34
Figure 2-15: Proximity Coupling.....	34
Figure 3-1: Cross Section of a Petroleum Carrying Pipeline: (a) Two-Phase Flow Scenarios, (b) Approximated Model.....	37
Figure 3-2: Cylindrical Coordinate System	39
Figure 3-3: Geometry of the Problem.....	43
Figure 3-4: Triangle Used to Form the Addition Theorem of Bessel Function [71].....	49
Figure 3-5: Normalized Phase Constant for Different Dielectric Loading Cylinder Radii	60
Figure 3-6: Modification to our Geometry to be an Equivalent Representation to One Cylinder Loading	61
Figure 3-7: Schematic Diagram for a General Case	64
Figure 3-8: Mode Chart for Circular Waveguide Partially Filled with Concentric Oil Cylinder.....	67
Figure 3-9: Proper Excitation of the Structure.....	70
Figure 3-10: Simulated Model for One Cylinder Symmetrically Loaded to a Circular Waveguide	72
Figure 3-11: Mode Chart for a Circular Waveguide Filled with a Concentric Oil Cylinder	72
Figure 3-12: Simulated Model for One Oil Filled Cylinder Eccentrically Loaded to a Circular Waveguide	73

Figure 3-13: Mode Chart for a Circular Waveguide Filled with an Eccentric Oil Cylinder	73
Figure 3-14: Simulated Model for a Circular Waveguide Loaded with Two Dielectric Oil Cylinders	74
Figure 3-15: Mode Chart for a Circular Waveguide Loaded with Two Oil Cylinders.....	74
Figure 3-16: Analytically and Simulated Mode Chart for Odd Hybrid Modes	75
Figure 3-17: Analytically and Simulated Mode Chart for Even Hybrid Modes.....	75
Figure 3-18: Four Oil Cylinders Loading a Circular Waveguide (Case 1).....	78
Figure 3-19: Eight Oil Cylinders Loading a Circular Waveguide (Case 2)	78
Figure 3-20: Twelve Oil Cylinders Loading a Circular Waveguide with Mixed Radii (Case 3)	79
Figure 3-21: Overlapping of the Loaded Dielectric Cylinders (Case 4).....	79
Figure 3-22: Wavy Flow Case	80
Figure 3-23: Stratified Flow Case.....	81
Figure 4-1: Petroleum Carrying Pipeline with Multiphase Mixture and the Integrated Aperture Coupled Antenna	87
Figure 4-2: Aperture Coupled Microstrip Patch Antenna.....	91
Figure 4-3: Reflection Coefficient of the Aperture Coupled Antenna	92
Figure 4-4: Two Dimensional Radiation Pattern (a) Azimuth Cut ($\Phi=0^\circ$) (b) Azimuth Cut ($\Phi=90^\circ$) and	93
Figure 4-5: Pipeline Model Filled with Air with an Aperture Coupled Antenna Attached to it	94
Figure 4-6: Reflection Coefficient of the Shielded Pipeline with the Integrated Antenna	95
Figure 4-7: Placement of the Antenna with Respect to the Contents Level (a) Antenna on Top of the Pipeline (Parallel to the Level), (b) Antenna on the Side of the Pipeline (Perpendicular to the Level)	99
Figure 4-8: Reflection Coefficient for Different Antenna Placement within the Pipeline	99
Figure 4-9: Antenna Placed on the Top of the Pipeline with its Feed Rotated.....	101
Figure 4-10: Reflection Coefficient of the Antenna Placed on the Top of the Pipeline with its Feed Rotated.....	101
Figure 4-11: Modified Antenna Placed on the Side of a Pipeline with its Feed Rotated	102
Figure 4-12: Reflection Coefficient of the Modified Antenna Placed on the Side of a Pipeline with its Feed Rotated	102
Figure 4-13: 2-inch Pipeline Filled with Water – Oil	106
Figure 4-14: Reflection Coefficient of the 2-inch Pipeline for Different Water-Air Proportions.....	106
Figure 4-15: Reflection Coefficient of the 2-inch Pipeline for Different Water-Oil Proportions.....	107
Figure 4-16: Pipeline Model with Two Integrated Antennas in Shielded and non-Shielded Regions	110

Figure 4-17: Reflection Coefficient of the 2-inch Pipeline for Different Oil Proportions at a 10% of Water	110
Figure 4-18: Reflection Coefficient of the 2-inch Pipeline for Different Water Proportions at 60% of Oil.....	111
Figure 4-19: A Case of 80% Oil and 12% Water	111
Figure 5-1: The LPKF ProtoMat® S62 [74].....	120
Figure 5-2: The Fabricated Sample, (a) Side View (b) Front View (c) Back View	121
Figure 5-3: The Antenna Fabricated on a Curved Plexiglass Sample, (a) Side View (b) Front View (c) Back View.....	123
Figure 5-4: Pipeline Filled with 3-Phase Mixture of Air, Oil and Water	124
Figure 5-5: Shielded Plexiglass Pipeline with Integrated Aperture Coupled Antenna...	125
Figure 5-6: S_{11} Measurement of the Patch Antenna Using Vector Network Analyzer ..	126
Figure 5-7: Reflection Coefficient for Different Plexiglass Dielectric Constant	127
Figure 5-8: Aperture Coupled Microstrip Line Antenna Radiation Pattern Measurement	129
Figure 5-9: S_{11} Measurement of the Aperture Coupled Antenna within the Pipeline Using Network Analyzer.....	131
Figure 5-10: Microwave Circuitry for Detecting the Reflected Signal from the Pipeline	133
Figure 5-11: Microwave Circuitry with Arduino for Detecting, Analyzing and Displaying the Pipeline Contents	133
Figure 5-12: Antenna Resonant Frequency for Different Dielectric Constant of Plexiglass	135
Figure 5-13: Simulated and Measured S_{11} for the Aperture Coupled Patch Antenna	136
Figure 5-14: 3D Polar Plot of the Designed Antenna Directivity, (a) Simulation Using HFSS (b) Measured Using RFXpert.....	137
Figure 5-15: Simulated & Measured 2D Radiation Pattern at $\text{PHI}=90^\circ$	138
Figure 5-16: Simulated and Measured S_{11} for the Antenna Designed on a Curved Plexiglass	139
Figure 5-17: Measured S_{11} for a Pipeline Filled with Air, 10 % & 50 % of Crude Oil..	141
Figure 5-18: Simulated and Measured S_{11} for a Pipeline Filled with Air.....	142
Figure 5-19: Simulated and Measured S_{11} for a Pipeline Filled with 10 % of Crude Oil	142
Figure 5-20: Simulated and Measured S_{11} for a Pipeline Filled with 50 % of Crude Oil	143
Figure 5-21: Simulated Reflection Coefficient of the 2-inch Pipeline for Different Water-Air Proportions.....	145
Figure 5-22: Measured Reflection Coefficient of the 2-inch Pipeline for Different Water-Air Proportions.....	145

Figure 5-23: Simulated and Measured Reflection Coefficient of the 2-inch Pipeline filled with 8% of Water	146
Figure 5-24: Measured S_{11} for a Pipeline for Different Air-Oil Proportions at a 10% of Water	149
Figure 5-25: Simulated Reflection Coefficient of the 2-inch Pipeline for Different Air-Oil Proportions at a 10% of Water	149
Figure 5-26: Measured S_{11} for a Pipeline for Different Water Proportions at 60% of Oil	150
Figure 5-27: Reflection Coefficient of the 2-inch Pipeline for Different Water Proportions at 60% of Oil	150
Figure 5-28: Arduino Program	153
Figure 5-29: Computer Side Program, (a) Sub Model for Receiving the Material Decision from Arduino (b) Displaying the Pipeline Contents	153
Figure A-1: A Coaxially Fed 10 GHz Microstrip Patch Antenna	159
Figure A-2: Reflection Coefficient for the Patch without Superstrate Layer	160
Figure A-3: 2D Radiation Pattern (a) Azimuth Cut ($\phi=0^\circ$), (b) Azimuth Cut ($\phi=90^\circ$)	161
Figure A-4: Elevation Cut of a Radiation Pattern at ($\Theta=90^\circ$)	161
Figure A-5: Microstrip Antenna with Superstrate Fed with a Coaxial Input	162
Figure A-6: Reflection Coefficient for the Patch with Superstrate	163
Figure A-7: 2D Radiation Pattern (a) Azimuth Cut ($\phi=0^\circ$), (b) Azimuth Cut ($\phi=90^\circ$)	164
Figure A-8: Model of a Pipeline with the Designed Antenna on its Side	165
Figure A-9: The Reflection Coefficient of the Model	166
Figure A-10: Radiation Pattern (a) Azimuth Cut ($\phi=0^\circ$), (b) Azimuth Cut ($\phi=90^\circ$)	166
Figure A-11: Reflection Coefficient for Air, Oil and Water versus Frequency for a 4-inch Pipeline	167
Figure A-12: Microstrip Antenna Transceiver Attached to the Pipeline Model	168
Figure A-13: Reflection and Transmission Coefficients for the Pipeline Transceiver	169
Figure A-14: Pipeline with Multiple Receivers	170
Figure A-15: Reflection Coefficient for Air Filled Pipeline	171
Figure A-16: Transmission Coefficient for Air Filled Pipeline	171
Figure A-17: Shape of the Radiation from the Transmitter	172
Figure A-18: Reflection Coefficient for Oil Filled Pipeline	173
Figure A-19: Transmission Coefficient for an Oil Filled Pipeline	173
Figure A-20: MPA Located on the Inner Perimeter of a 2-inch Pipeline Sample	174
Figure A-21: Reflection Coefficient for Air, Oil and Water versus Frequency for a 2-inch Pipeline	175
Figure A-22: 3.6 GHz Aperture Antenna on a Curve Plexiglass Section	177

Figure A-23: Reflection Coefficient of the Aperture Antenna on a Curve Plexiglass Section	178
Figure A-24: 3.6 GHz Patch Antenna Attached to a 2-inch Pipeline Sample	179
Figure A-25: Reflection Coefficient for Different Oil-Air Proportions	180

LIST OF ABBREVIATIONS

ADC	:	Analog to Digital Convertor
BVM	:	Boundary Value Method
CIR	:	Circulator
CRLH	:	Composite Right/Left-Handed
DC	:	Directional Coupler
ENA	:	Expands Network Analysis
ERT	:	Electrical Resistance Tomographic
EM	:	Electromagnetic
FD-TD	:	Finite Difference-Time Domain
FEM	:	Finite Element Method
HFSS	:	High Frequency Structure Simulator
LMD	:	LPKF Mill Drill for LPKF BoardMaster
LSBRM	:	Least-Square Boundary Residual Method
NMR	:	Nuclear Magnetic Resonance
PC	:	Personal Computer
PCB	:	Printed Circuit Board

PML	:	Perfect Match Layer
RF	:	Radio Frequency
SMA	:	Sub-Miniature version A
TE	:	Transverse Electric
TEM	:	Transverse Electro-Magnetic
TM	:	Transverse Magnetic
USB	:	Universal Serial Bus
VCO	:	Voltage Control Oscillator
VNA	:	Vector Network Analyzer

ABSTRACT

Full Name : [Yanal Shaher A. AlFaouri]
Thesis Title : [Microwave Technique for Monitoring Fluid Level in the Horizontal Petroleum Carrying Pipeline]
Major Field : [Electrical Engineering]
Date of Degree : [April 2014]

Crude-oil production process from a horizontal or near horizontal well often extracts a multiphase mixture of oil, water and gas. Accurate measurement of the ratio of multi-phase contents within the pipeline is important for successful logging and monitoring the oil supply. Although several electrical techniques exist in the literature to determine the phase ratio, a few of them use microwave sensors. The aim of this research work is to design the front-end of a simple microwave sensor to determine the contents of multiphase liquids flowing through a petroleum-carrying pipeline.

Electromagnetic (EM) scattering within the pipeline is governed by the geometrical and electrical properties of the pipeline. Since a pipeline resembles a cylindrical structure, a thorough analysis is essential on the modal behaviour of the cylindrical waveguide filled with multi-phase fluid. Calculated solutions for single phase and simple two-phase cases are used to verify the model used by a full wave Finite Element Method (FEM) based simulator (HFSS). Simulated reflection responses (S_{11}) of the pipeline model with two integrated antennas are used to monitor the oil and water level. The antenna places in the shielded region of the Plexiglass pipeline are used to monitor the resonant frequency changes with changing oil level of the pipeline. The antenna integrated in the non-shielded

region of the pipeline is used to monitor the changes of the reflected power ($|S_{11}|$) due to changing water level of the pipeline. The observed responses are tabulated to generate a look-up table that can be used with experimental measurements of S_{11} to determine the contents of the steady-state three-phase pipeline.

Measurement setups are fabricated to experimentally verify the simulated look-up tables. Minor discrepancies between simulated and measured S_{11} curves are due to human errors during the in house fabrication and assembly process. Measurement setup without using the network analyser is also investigated. Basic measurements are performed using microwave components (VCO, circulator, directional coupler, detector, and voltmeter) demonstrated the proof of concept. An Arduino microcontroller is also integrated with this setup, which can store the look-up tables and display the contents level of the three-phase pipeline on a laptop.

The major drawback of the this two antenna reflection measurement setup is low resolution and measurement limit of maximum 30% of water contents of the steady state pipeline.

ملخص الرسالة

الاسم الكامل: ينال شاهر عبد الفتاح الفاعوري

عنوان الرسالة: طريقة كهرومغناطيسية في مدى المايكرويف لقياس مستوى المواد في أنابيب النفط

التخصص: الهندسة الكهربائية

تاريخ الدرجة العلمية: نيسان 2014

عملية الإنتاج من النفط الخام من بئر أفقي أو قريب من الأفقي في كثير من الأحيان يتم استخراج خليط من مكونات متعددة من النفط والماء والغاز. ومن المهم الحصول على قياسات دقيقة لنسبة كل مادة من المحتويات الموجودة في خط الأنابيب لنجاح تسجيل ورصد إمدادات النفط. على الرغم من أن العديد من التقنيات الكهربائية موجودة في عدد من الأوراق البحثية المنشورة لتحديد نسب هذه المكونات، إلا أن عدد قليل منهم يستخدم أجهزة استشعار المايكرويف. لذلك فإن الهدف من هذا العمل البحثي هو تصميم الواجهة الأمامية من جهاز استشعار مايكرويف مبسط لتحديد محتويات السوائل المتعددة التي تتدفق من خلال خطوط الأنابيب التي تحمل البترول.

وتخضع الأمواج الكهرومغناطيسية (EM) المنبعثة داخل خط الأنابيب إلى الخصائص الهندسية والكهربائية لخط الأنابيب. وبما أن خط الأنابيب مشابه لهيكل أسطواني الشكل، لذلك فإن من الضروري إجراء تحليلًا شاملاً على هذا الهيكل الأسطواني المملوء بسائل متعدد المكونات. وتستخدم الحلول المحسوبة للنموذج الأسطواني المملوء بمادة واحدة أو مادتين للتحقق من النتائج التي سيتم الحصول عليها من قبل برنامج المحاكاة المستخدم. وتم استخدام الموجات الكهرومغناطيسية المنعكسة والتي تم الحصول عليها من برنامج المحاكاة لأنبوب النفط المثبت عليه هوائي من أجل قياس نسبة النفط والماء. الهوائي المثبت على جزء الأنبوب المحاط بطبقة موصلة، استخدم من أجل قياس الموجات المنعكسة والترددات لمستويات مختلفة من النفط. وكذلك الهوائي المثبت على الجزء العازل من الأنبوب استخدم لقياس مقدار الطاقة المنعكسة لمستويات مختلفة من الماء. وتم رصد النتائج التي حصل عليها من أجل تكوين جدول مرجعي والذي سيستخدم مع النتائج المقاسة عملية من أجل تحديد نسب المواد الثلاثة الساكنة داخل أنبوب النفط.

عدد من الخطوات العملية تم بنائها من أجل التحقق من صحة الجداول المرجعية التي تم تكوينها من خلال برنامج المحاكاة. وتم ملاحظة نسبة اختلاف بسيطة بين النتائج وذلك بسبب عدم الدقة البشرية في استخدام الأجهزة المتوفرة في المختبر أثناء عملية تجميع الهوائي مع الأنبوب. وتم التحقق من تجربة عملية لإيجاد النتائج بدون استخدام جهاز تحليل الإشارات. وهذه التجربة تم عملها باستخدام أدوات عدة مثل: (جهاز التردد المتحكم من قبل الجهد، مدور الإشارة، موجه الإشارة، وجهاز قياس الجهد) من أجل تأكيد صحة المبدأ. وأيضاً معالج من نوع Arduino تم استخدامه في هذه التجربة من أجل تخزين الجداول في ذاكرته والذي يقوم بتحليل النتائج وعرض مستوى المواد على جهاز الحاسوب.

ولكن هذا الهوائي المصنع لمراقبة المواد يعاني من قلة الدقة في تحديد نسب المياه الساكنة في الأنبوب والتي تزيد عن 30% من ارتفاع الأنبوب.

CHAPTER 1

INTRODUCTION

1.1 Introduction

Multiphase flow refers to the flow of two or more physically distinct or mixed materials in a container or a pipeline. It can be widely found in many engineering applications, such as, power generation, chemical engineering and crude oil extraction and processing. Oil production and supply involves multiphase flow of liquids composed of oil, water and gas [1]. Oil retrieval process often involves the injection of water and gas into the well to maintain the pressure and viscosity of the extracted liquids. This process requires constant monitoring using multiphase flow sensors, to optimize the efficiency of the oil production line.

The existing multiphase flow sensors can be classified into the following major groups: Mechanical (visual, float-type mechanisms, absolute pressure, differential pressure, thermal, weight measuring), Optical, X-ray or Gamma ray, Nuclear Magnetic resonance (NMR) and Electrical [2], [3]. Popular electrical sensors excite the two-phase fluid with a low frequency signal and measures the electrical parameters between electrodes. Commonly measured parameters are capacitance, resistance and inductance, which can determine the dielectric properties (permittivity and conductivity) of the mixture related to two phase contents oil and gas.

In industrial conditions, non-intrusive sensors are preferable because they are reliable, easier to maintain and less prone to erosion, corrosion or excessive pressure drop problems. Some examples of non-intrusive sensors used in multiphase measuring are: Absolute Pressure, Temperature, Differential Pressure, Conductance, Capacitance, Gamma, X-ray, Microwave, Ultrasound and infrared. [2]. There are various approaches based on microwave techniques to measure volume fraction and phase distributions in multiphase flow, such as: microwave tomography [4], [5], open cylindrical resonator based on two microstrip patch couplers [6], near field proximity measurements [7], Composite Right/Left-Handed (CRLH) Transmission Line resonator [8] and capacitive electromagnetic flow meter [9], [10].

In this research, the steady state three-phase contents within a petroleum-carrying pipeline are excited with two simple microwave sensors (antennas) located on the perimeter of the pipeline in a consecutive manner. The optimized antennas are located in the shielded and the non-shielded regions of the pipeline depending on the requirement of monitoring oil-air or water-oil levels of the mixture. The resonant frequency and power level of the reflected signal (S_{11}) are observed to detect the oil and water levels, respectively. Initial measurements are done using the network analyzer to check and verify the simulated look-up tables, which relates the S_{11} responses with the content level within the pipeline. Final measurements are done with a standalone system that eliminates the requirement of the expensive network analyzer. Finally, a sample measurement is done to proof that an Arduino microcontroller can be used to store the look-up tables with which the measured S_{11} responses can be compared to display the three phase content ratio of the pipeline.

1.2 Thesis Motivation

Different concepts and devices are available for measuring the phase fractions of the multi-phase flow within petroleum carrying pipeline. Some of these devices use microwave signals but they are either complex or expensive. Therefore, a simple microwave measurement technique is needed to reliably observe the ratio of steady state two-phase and three-phase contents within the petroleum-carrying pipeline.

1.3 Thesis Objectives

The objectives for this work can be summarized as follow:

- 1.** Analytically solve, understand and analyze the modal behavior of a cylindrical pipeline, loaded with single-phase or simple two-phase mixture of air, oil or water. This will help understand the Electromagnetic (EM) characteristics of the multiphase mixture within the pipeline, resembling the cylindrical waveguide.
- 2.** Using the analytical solutions, select proper meshing and excitation techniques available in the professional software (HFSS) to model the steady state multiphase pipeline with ideal excitation. Verify the model by comparing the simulated mode charts with analytical results of step 1.
- 3.** Use the validated software model to analyze the multi-phase petroleum-carrying pipeline, which is too complicated to solve analytically. Thoroughly investigate the modal behavior of the pipeline to understand how modes are affected by changing levels of the three-phase contents of the pipeline.

4. Design and optimize practical microwave excitation/measurement techniques of the pipeline using low profile printed antennas. Determine the techniques best suited for monitoring the levels of air, oil and water contents of the mixture. This is important, as due to different electrical properties of water and oil, same technique may not be suitable for monitoring both materials.
5. Use the optimized simulated model of the pipeline with two integrated antennas to generate the look-up tables, which links the oil and water levels with measured S_{11} responses.
6. Fabricate the pipeline segment with two integrated antennas to perform the two-phase and three-phase measurements for monitoring the oil and water levels. These measurements will help in corroborating the two look-up charts, prepared in step 5. Design and use an experimental setup (using microwave VCO, control components, microcontroller) that can monitor the multiphase contents without using the expensive network analyzer and provide the content level by comparing the measured S_{11} response with pre-generated look-up table.

1.4 Thesis Overview

This thesis is organized in six chapters as follows:

Chapter 2 of this thesis briefly describes the existing analytical methods available in the literature to calculate the cutoff wavenumbers of a partially loaded circular waveguide. In addition, this chapter also discusses the basic techniques and sensors

available in the literature for detecting the content level of a multi-phase mixture within a petroleum-carrying pipeline.

In Chapter 3, the analytical derivation is presented to find the cutoff wavenumbers in a circular waveguide loaded with two off-centric dielectric cylinders. This novel formulation and solution is used to determine the theoretical electrical parameters of a petroleum-carrying pipeline, ideally loaded with two cylindrical oil samples.

Chapter 4 discusses the design of the microwave monitoring setup in details and the steps followed to achieve the optimum design of the level sensors to correctly find the content levels of the pipeline. Initially, the relative permittivity (ϵ_r) of the available Plexiglass material is determined by curve fitting techniques, where the experimental S_{11} response is fitted with simulated (HFSS) reflection responses for different predicted ϵ_r values. Then, the effect of the curved Plexiglass substrate on the resonance condition of the antenna is investigated to optimize the design. Finally, the pipeline with integrated antennas is designed and optimized. Correct monitoring technique is finalized to monitor the two-phase mixtures (oil-air and water-oil) within the pipeline. Simulation results for the pipeline filled with different combinations of two-phase (Air-Oil, Oil-Water) and three phase (Air-Oil-Water) cases are plotted and analyzed. Look-up tables that relates the changes in resonant frequency with changing level of oil and changes in reflected power with changing level of water are tabulated.

In the 1st part of Chapter 5, the relative permittivity of the available Plexiglass material is found by fabricating and testing the designed patch antenna using available Plexiglass substrate. Curve fitting technique is used for this purpose. Similar antenna on a

curved Plexiglass substrate is also fabricated and tested to predict the antenna behavior within the pipeline. Finally, the optimized design of the measurement setup required the fabrication of 3 GHz and 3.3 GHz aperture coupled patch antennas and assembling them within the shielded (with conductive cover around the outer surface of the pipeline) and non-shielded part of the pipeline to monitor air, oil and water level changes, respectively. This chapter also presents the look-up table formulated to relate the S_{11} response of the measurement setup with the level of its multi-phase contents. Random entries in the look-up table are validated with experimental results. The last part of chapter 5 discusses a self-sufficient measurement setup made of an S-band microwave components and Arduino microcontroller. Sample test results of this setup are presented to encourage future studies in this topic. Finally, chapter 6 describes the conclusions drawn from this research work and recommendations on future work to be carried on this subject.

CHAPTER 2

LITERATURE REVIEW

2.1 Introduction

This chapter will focus on the methods and the techniques that are available in the literature to determine the content ratio of a circular petroleum-carrying pipeline. The literature review chapter is split into two parts. The first part covers the methods and approximations that are used to come up with a basic analytical solution of the targeted structure. The second part covers some of the popular techniques used to measure the two- and the three-phase contents of the petroleum carrying pipeline.

2.2 Dielectric Loaded Circular Waveguide

In order to analyze the dielectric properties of the multiphase contents of a petroleum-carrying pipeline, the pipeline is modeled as a circular waveguide. The equations governing the waveguide are then used to calculate the modal behavior of a dielectric loaded circular waveguide. In the literature, models exist for perfectly conducting waveguides loaded with dielectric rods in a concentric or off-centric manner (eccentric).

2.2.1 Concentric Loading

In the case of a concentric loading, equations governing the modal behavior exist in the literature [11] and most of the published papers dealing with eccentric loading verified their solution process with concentric solutions first [12]. Figure 2-1(a) shows a circular waveguide (filled with ϵ_2 and μ_2) is concentrically loaded with a dielectric rod (with ϵ_1 and μ_1). The related phase constant, normalized to the material of the outer cylinder, is plotted in Figure 2-1(b). The radius of the outer cylinder is $b=0.4\lambda_2$ and it is filled with air ($\epsilon_{r2}=1$, $\mu_2= \mu_0$), while the inner cylinder is filled with a material having a dielectric constant of ($\epsilon_{r1}=10$, $\mu_1= \mu_0$) and radius varying from $a=0.01b$ to $a=b$. Note that Figure 2-1(b) has the following limitations:

- Every point in this curve corresponds to different geometry (different a or b).
- The curve corresponds to a certain frequency.
- The curve combined both real ($kz < k_2$) and complex ($kz > k_2$) values of the Bessel functions.

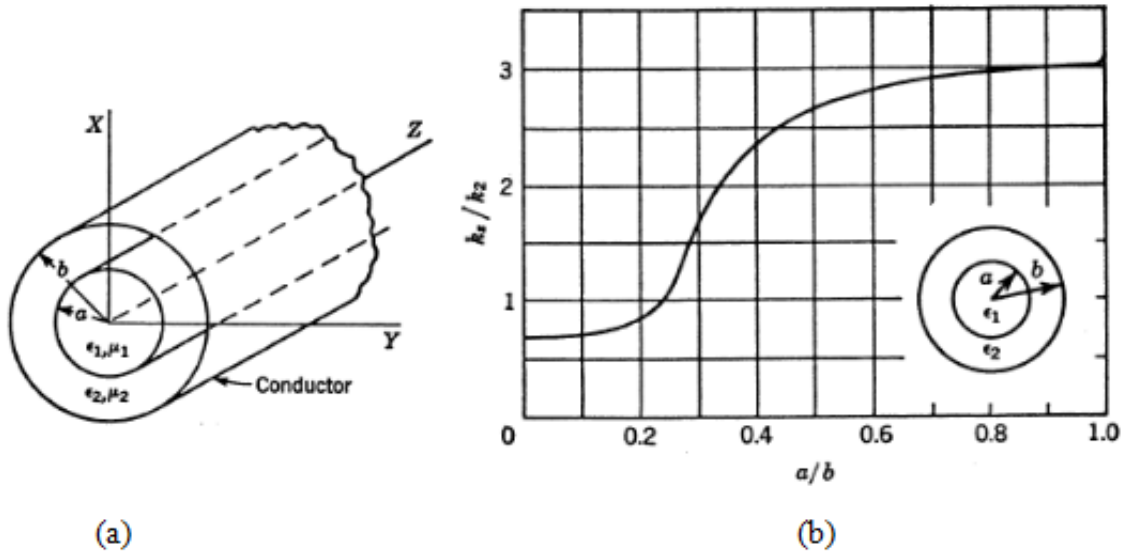


Figure 2-1: (a) Partially Filled Waveguide; (b) Phase Constant for the Partially Filled Waveguide [11]

2.2.2 Eccentric Loading

The calculation of the cutoff frequencies and propagation constants of a cylindrical waveguide, eccentrically (off-centrally) loaded with a dielectric cylinder, has been the subject of many investigations. Some of the popular methods to find the cutoff frequencies are as follows:

(I) Simple point-matching method [13], is popular in loaded waveguide with two conductors, where one conductor encloses the other. In reference [14] Davies et al. has investigated the legitimacy of this method as a modeling tool. Another example of this technique has been reported in [15].

(II) Least-squares boundary residual method (LSBRM) [16], where Yeo has described the application of LSBRM to the analysis of a circular waveguide loaded with an off-centric dielectric rod. Because this technique represents a particular case of least-

squares minimization, it is mathematically more rigorous than the point matching method. In addition, the LSBRM has already been successfully utilized to model a variety of other complicated structures, such as planar transmission lines and symmetrical waveguide junctions.

(III) The third technique available in the literature is called the null-field method [17]. In reference [18], the null-field method has been used to compute the cutoff frequencies of the asymmetrically loaded cylindrical waveguide for both the transverse electric and transverse magnetic modes. This technique is important for hybrid microwave-integrated-circuit designers, interested in accurately modeling the dielectric resonator enclosed within a metallic box.

(IV) Vector Finite Element Approach. In reference [19], this method has been applied to study the cutoff frequencies of higher-order modes and dispersion characteristics of a uniform waveguide with circular outer conductor and eccentric inner conductor supported by dielectric slab between the conductors. In this method the structure is divided into triangular elements, with each one represented by three edge elements. The electric field in a single triangular element is expressed as a superposition of three edge elements with three vector basis functions overlapping each triangular cell. The value of the basis function is constant along one edge while it is simultaneously zero along the other two edges.

(V) Surface Integral Formulation. This method has been used in [20] to obtain the cutoff wavenumbers for an arbitrary waveguide, but this method leads to the existence of spurious modes. A modification to this technique to get rid of these modes has been

reported in [21]. They use this method to obtain the cutoff wavenumbers for TE and TM modes for a coaxial waveguide with the outer conductor having circular cross section and the inner conductor having a rectangular cross section. The advantage of this technique is that it can be applied to any cross section because it depends on the method of moments to find the electric field and because of this, the formulation becomes a little complicated and needs more processor time to find the modes. Several comments on the formulation followed in this paper [21] has been pointed out in [22].

(VI) Finite Difference in Time Domain (FD-TD) which has been used in [23] to find the cutoff frequencies for the coaxial waveguide with circular and rectangular cross sections for the inner and outer conductors. This method is better than the Finite Difference (FD) method since it has a second order accuracy in time and space derivation, also; it did not need any special treatment on the structure boundaries.

(VII) Boundary Value Method (BVM). An example of this method is used in reference [12], where Ragheb applied it to a circular waveguide loaded with eccentric dielectric cylinder as shown in Figure 2-2. The behavior of the cutoff wavenumbers versus eccentricity from the center of the circular waveguide has been plotted in Figure 2-3, where this figure shows how the normalized cutoff wavenumber will act due to an increase in the eccentricity of the loaded cylinder from the center of the outer cylinder. The field components of circular waveguide modes have angular variations and split into odd and even modes when the central conductor begins to shift axis from concentric to off-centric configuration. However, only even modes in the off-centric guide correspond to the coaxial modes with no angular variations.

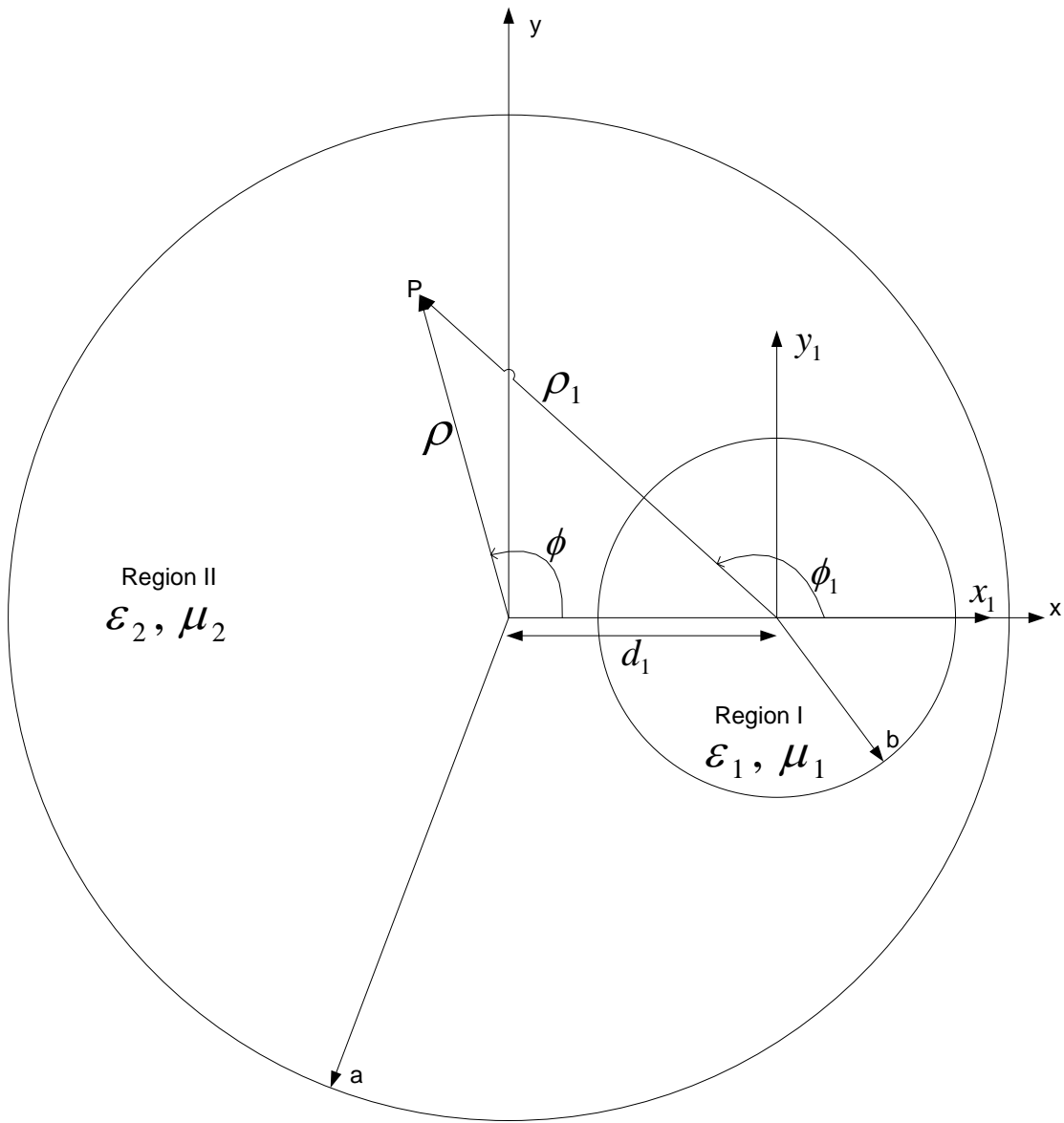


Figure 2-2: Circular Waveguide Loaded with One Eccentric Conductor or Dielectric Cylinder

The modal characteristics of the eccentric structure, shown in Figure 2-2 above, has also been solved using Boundary value method in references [24], [25], [26], [27], [28]. Using separation of variables in [29], Conformal Mapping in [30], [31], [32] and Finite Difference in [33]. Electromagnetic properties of this structure using point matching and conformal mapping methods are also available in literatures [34], [35], [36].

For the behavior of the propagation constant in the region below cutoff frequency, an exact solution based on the characteristic equation has been worked out in [37] for the case of a coaxial waveguide. It was demonstrated that two types of hybrid electromagnetic fields could propagate in the structure: (1) the even hybrid field which has even TE and odd TM fields and (2) the odd hybrid field that has odd TE and even TM fields.

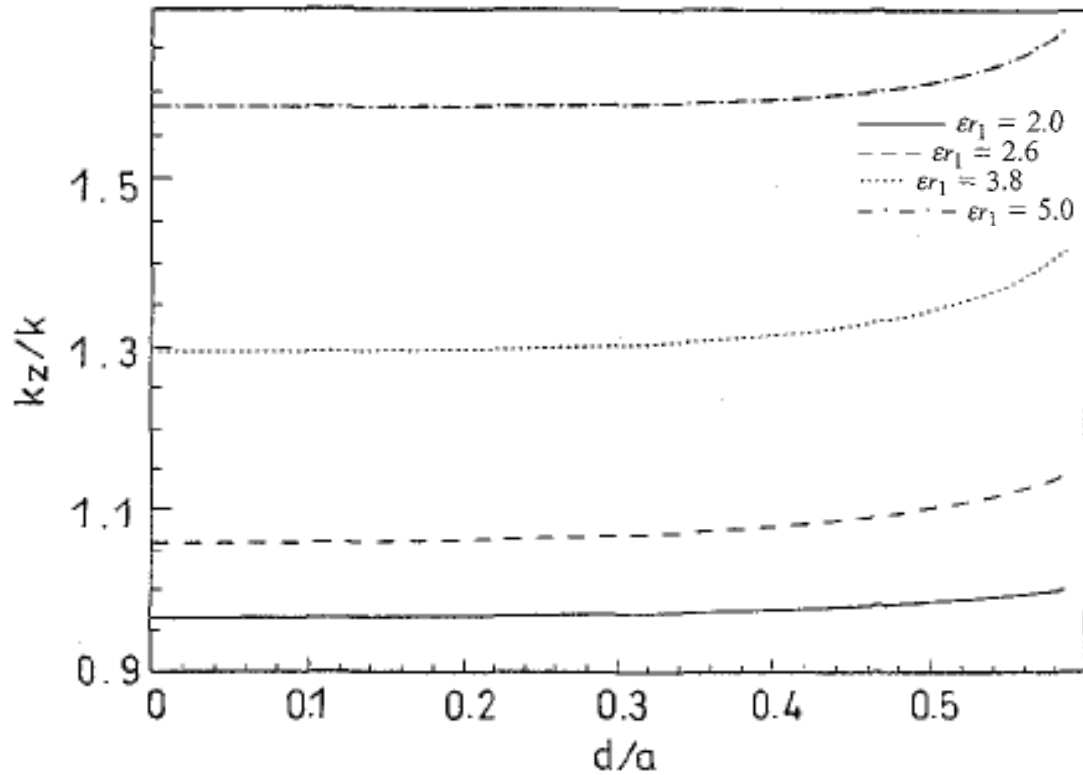


Figure 2-3: Cutoff Wavenumber versus Eccentricity for Odd Modes ($a=0.5\lambda$, $b=0.2\lambda$, $\epsilon_r=1$) [12]

2.3 Multiphase Sensors and Techniques

There are many research papers on multiphase flow and it is very important for industrial applications, especially for petroleum producing companies. Particularly the ratio of the multiphase contents within the pipeline allowed the determination of the water-cut, which is important to monitor and optimize the oil flow. In addition, modelling the nonlinear interaction between the multi-phase contents of the pipeline is also important in analyzing the oil flow.

2.3.1 Flow Patterns

The flow pattern of the two-phase contents within the pipeline mainly depends on the pipeline orientation, such as vertical or horizontal. Figure 2-4 shows the two-phase flow patterns in a horizontal pipeline. Two types of flow are presented, which are the one considered in this research, wavy flow, where the fluid level is not constant due to the flow movement and the stratified flow, which has a steady state level and a comparison between them will be presented in the next chapter.

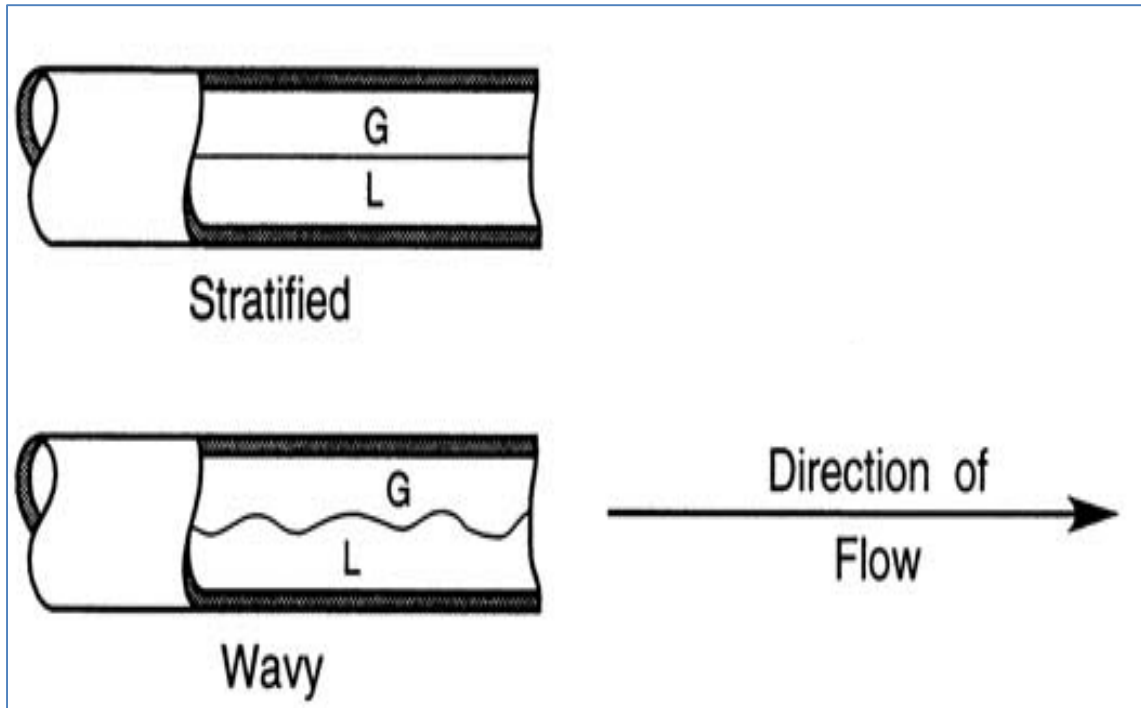


Figure 2-4: Two-Phase Flow Patterns in Horizontal Tubes [38]

The flow pattern within the pipeline are mostly determined by visual observations, e.g. by the use of a high-speed camera, but this is only possible for flows in transparent tubes. In recent years, analytical techniques have been made available that uses various instruments to determine the flow pattern for non-transparent pipes. Pressure transducers or void fraction sensors (either electrical impedance or radiation based techniques) together with mathematical and statistical models are commonly used to analyze the signal fluctuation characteristics to determine the flow pattern [39]. In [40] a more comprehensive and fundamental treatment of the two-phase flow transitions and a unified model for predicting flow-pattern transitions for the whole range of pipeline inclinations is presented.

2.3.2 Multiphase Flow Sensors

Some examples of non-intrusive sensors used in multiphase measuring are: Absolute Pressure, Differential Pressure, Conductance, Capacitance (Impedance), Gamma, X-ray, Microwave, Ultrasound and Infrared or Optical. [2]

In order to select a sensor for an application, the suitability of the sensor should be tested according to the following criteria [2]:

- (1) Known behavior in oil/water/gas flows
- (2) Frequency (or dynamic response)
- (3) Complexity of sensor output processing
- (4) Commercial availability
- (5) Cost
- (6) Non-intrusive design
- (7) Reproducibility
- (8) Ruggedness/complexity

The non-intrusive sensors mentioned above are tested according to these criteria and they are ranked as A (represent the best) B or C sensors, as summarized in Table 2-1. In spite of the microwave sensors is not the best, it is selected here because oil companies although it has all types of sensors but they are still interested into the microwave range to know their capabilities and to find a way to enhance their measurements.

Table 2-1: Sensor Selection Criteria [2]

Sensor	Criteria							
	1	2	3	4	5	6	7	8
Absolute pressure	A	A	A	A	A	A	A	A
Differential pressure	A	A	A	A	A	A	A	A
Conductance	A	A	A	B	B	A	A	A
Impedance	A	A	A	B	B	A	A	A
Gamma	A	B	A	A	B	A	A	B
X-ray	A	B	B	B	C	A	A	B
Microwave	B	B	B	B	B	A	B	B
Ultrasonic	B	B	B	B	B	A	B	B
IR/Optical	B	C	C	B	B	A	B	B

2.3.3 Measurement Techniques

In the literature, a variety of techniques exist to monitor the multiphase flow in the pipeline. In [41], they apply the method based on dielectric spectroscopy to investigate two kinds of flow in the pipeline: the homogeneous flow of oil and water and the annular flow oil, water and gas. In this process, two different probes are inserted within the pipeline: one at high frequency (around 40 GHz) to determine the composition of the liquid phase, i.e. the oil-liquid ratio and the water-liquid ratio; a second one at low frequency (10–800 MHz) to calculate the gas ratio or gas hold-up. The reason for the two frequency bands are based on the signal penetration, which is inversely proportional to the frequency, as shown

in Figure 2-5. However, this intrusive design needs to insert probes within the pipeline, which requires drilling and that will cause leaking or cleaning related problems.

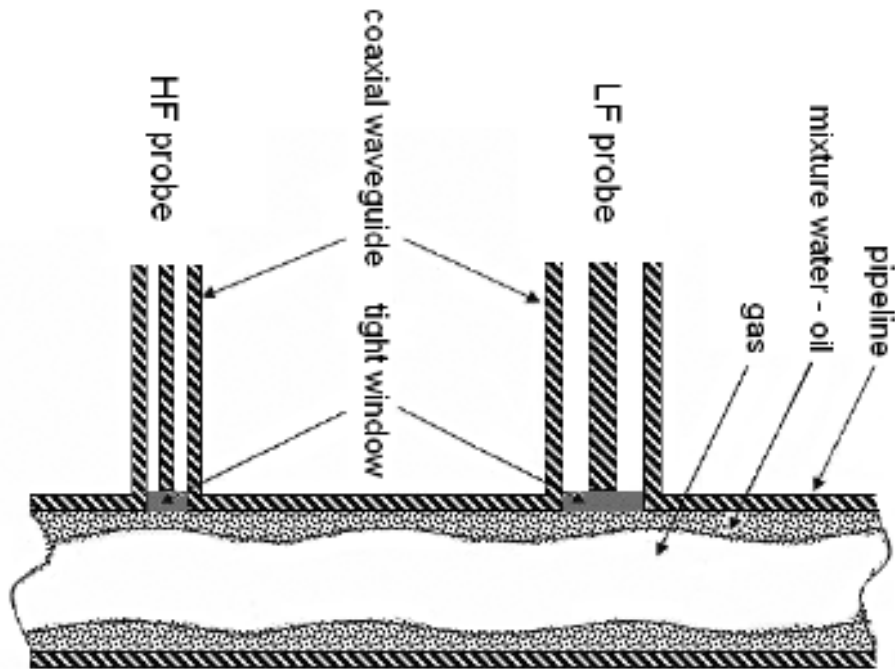


Figure 2-5: Schematic of the Device that Consider the Annular Case Flow [41]

In reference [42], the authors introduce a capacitance wire-mesh sensor to measure the permittivity of the mixture, as shown in Figure 2-6. This sensor consists of two plates placed at a certain distance from each other and connected to two probes. Each plate is made of 16 wires, mounted in a rectangular acrylic frame that itself is part of a rectangular flow channel. The sensor can be used to measure transient phase fraction distributions in a flow cross-section. The drawback of this intrusive sensor was low mechanical rigidity and less protection of the probes from sandy component or solid particles of the fluid.

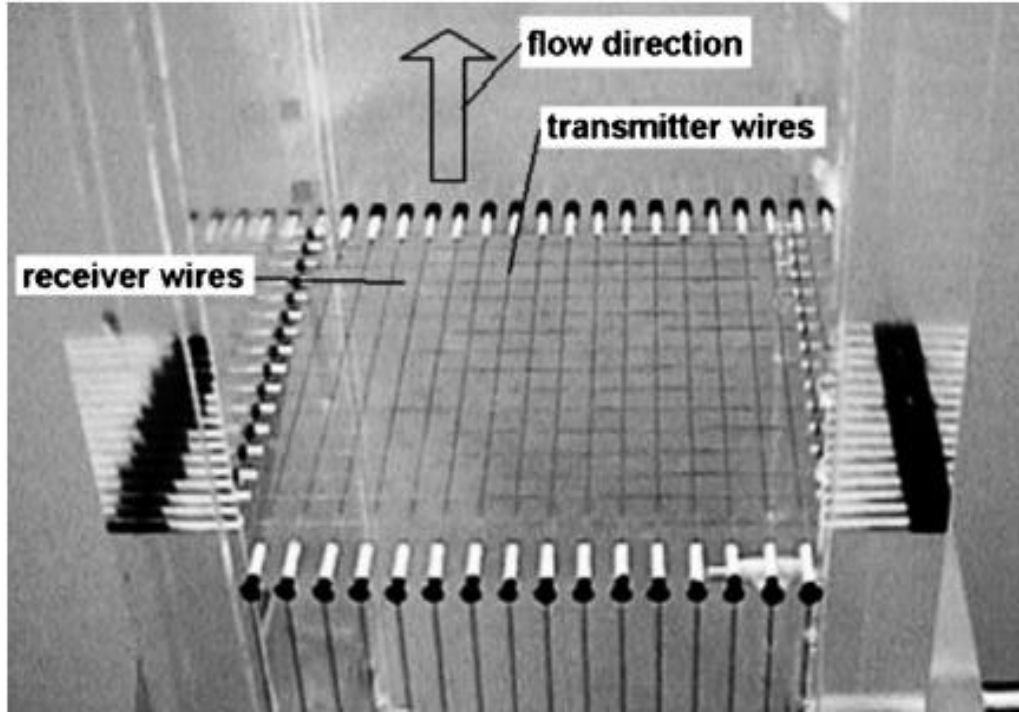


Figure 2-6: Capacitance Wire-Mesh Sensor [42]

In [43] a non-intrusive electromagnetic cavity sensor shown in Figure 2-7 is developed for detecting the content of an oil pipeline by transmitting a 10 mW signal in the range of 100 – 350 MHz. This sensor technique is based upon measuring the dielectric constant of the combined oil, gas and water phases. The drawbacks of this design are the antenna dimension is big, low resolution, and this is because the range of the frequency is in the MHz.

In reference [44] the microwave sensor consisted of two coaxial probes, separated by a certain distance, as shown in Figure 2-8. This sensor is used to determine the water holdup of the hydrocarbon mixture for a near horizontal oil-carrying pipeline. It is noticed from the figure that this design is intrusive and there is possibility for leakage due to high pressure within the pipeline.

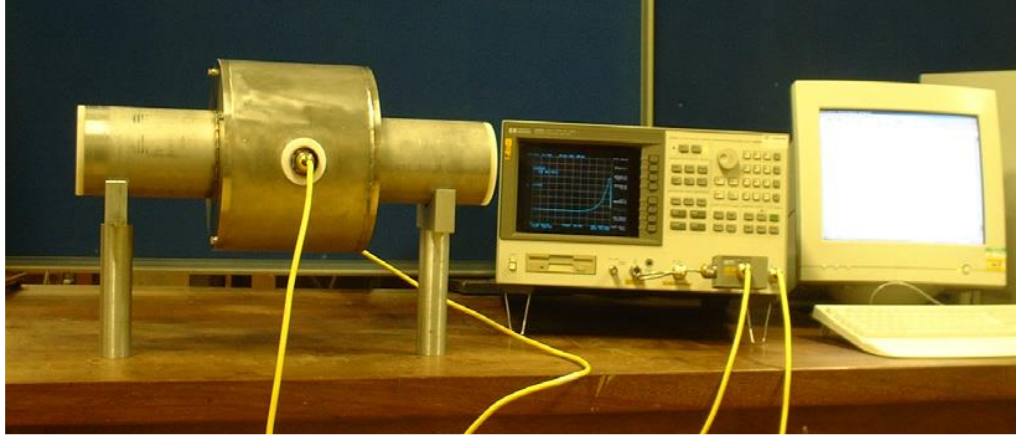


Figure 2-7: Laboratory Prototype Cavity Resonator Setup [43]

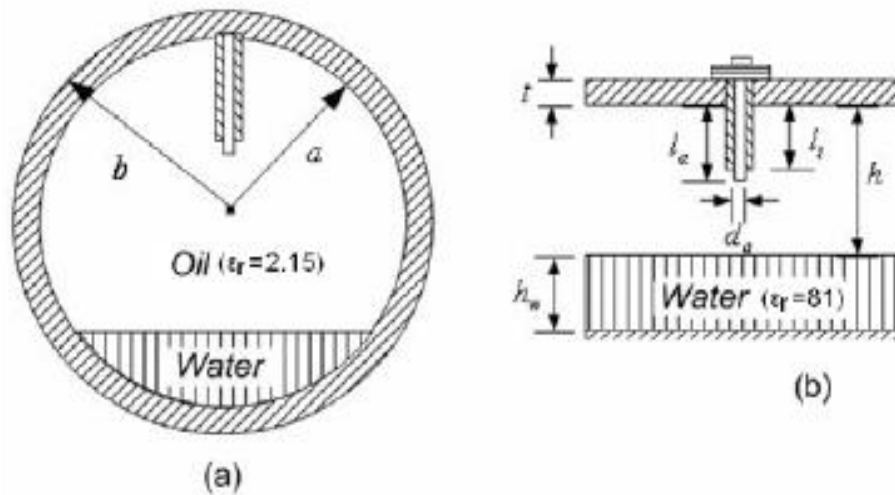


Figure 2-8: (a) Cross Section, (b) Side View of the Measurement Unit. [44]

Another intrusive technique was described in [45], [46], [47] and [48] are based on two microstrip couplers connected in a Composite Right Left Handed (CRLH) manner. An example of such a sensor is shown in Figure 2-9, which is related to [45]. The figure shows a schematic of the dominant mode excited within the cylindrical waveguide using the coaxially feed microstrip patch and a parasitic patch. Two sets of the patches are connected using microwave couplers to measure reflection and transmission parameters in order to determine the content ratio.

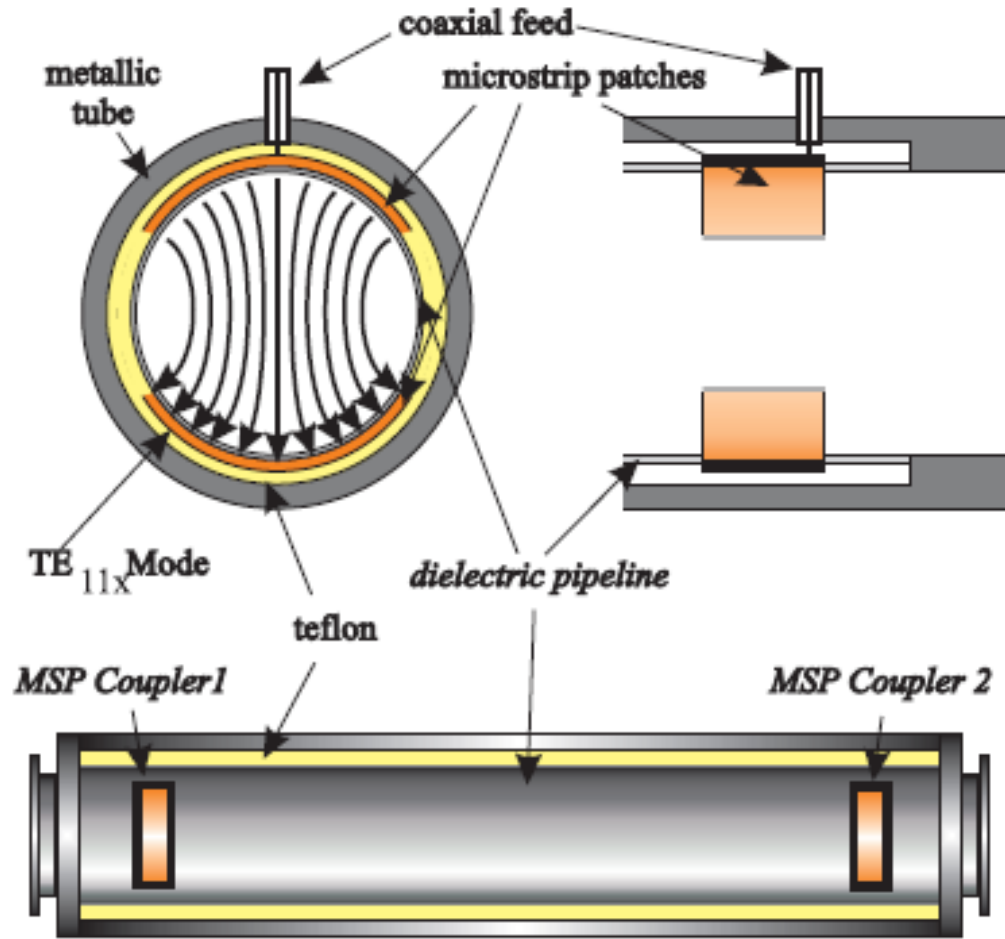


Figure 2-9: Two Microstrip Patch Couplers Assembled as a Microstrip Sensor [45]

In [49] an impedance technique is presented by placing electrodes at the perimeter of a pipeline and measuring the impedance across the electrodes, there are many different possibilities to arrange a system of electrodes for void fraction measurement purposes. Two cases have been considered electrical conductivity and capacitance probes; depending on the type of instrumentation used and liquid material to be investigated.

Commonly used radioactive sources of gamma radiation include isotopes of americium, cesium or cobalt. Radiation is generally detected by using a scintillator coupled

to a photo detector. The scintillator absorbs radiation and emits visible light by fluorescence [50].

Another technique for multiphase measurements is multiphase flow imaging tomographic and commonly called process tomography or industrial process tomography, finds many applications in the imaging and measurement of industrial processes. A tomographic image is a two-dimensional representation of a slice through an object. The use of various tomographic methods is widespread in diagnostic medicine [51] and several imaging modalities originally developed for medical imaging are now being adapted to industrial process imaging. The use of tomographic imaging for the investigation of multiphase flows has been reported in a few exhaustive review papers [52], [53], [54], [55] and books [56], [57], [58].

An application of one of the tomography types called Electric Resistance Tomography (ERT) has been done in [59]. Figure 2-10 shows the experimental setup for the ERT were it carried out in an acrylic test pipe in the horizontal direction with 38 mm in diameter. The phase continuity and appearance of phase inversion were investigated using conductivity (wire and ring) probes and an Electrical Resistance Tomographic (ERT) system. In this technique the phase has been monitored to determine the flow and especially the process of phase inversion or continuity affected by interfacial tension of the materials by adding a small concentration of glycerol to water.

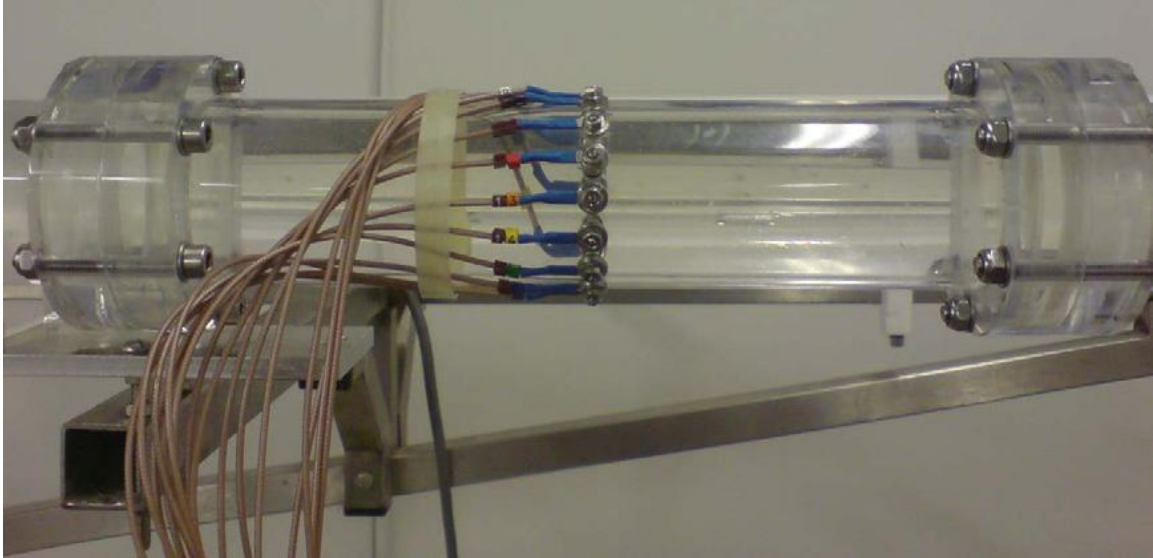


Figure 2-10: Electrical Resistance Tomographic (ERT) Sensors Placed at the Periphery of the Test Pipeline and Embedded on the Acrylic Wall. [59]

In spite of the huge contribution in the field of petroleum measurement, only 0.2% of current oil wells are instrumented with multiphase flow meters as estimated in [60]. Thus, there still exists the need for new researches and innovations for this field of study.

In this work, the designed sensor is not intrusive, which mean nothing will be inserted in the direction of flow like [41], [42] and [44] because it will be attached and wrapped around the inner perimeter of the pipeline. This will protect our sensor from damaging caused by high pressure, solid particles within the flow or even through the cleaning process of the pipeline, no hole in the pipeline wall required like [45], [46], [47] and [48]. In addition, it did not required complex processing of the output data compared to [59].

2.4 Antenna Basics

In this research work, a planar antenna will be designed and used to monitor the contents ratio of the pipeline. According to the IEEE Standard Definitions, the antenna or aerial is defined as “a means of radiating or receiving radio waves” [61]. In other words, antennas act as an interface for electromagnetic energy, propagating between free space and guided medium. Amongst the various types of antennas that include wire antennas, aperture antennas, reflector antennas, lens antennas etc., microstrip patches are one of the most versatile, conformal and easy to fabricate antennas.

Good antenna design is a critical factor in obtaining useful response from microwave sensors and wireless devices. This is especially true in low power and compact designs, where antenna space is less than optimal. To obtain the desired performance, the designed antenna needs to be optimized to provide required matching, gain/loss, and radiation pattern.

2.4.1 Basic Antenna Parameters

Some of the basic antenna characteristics that a designer should be familiar before starting the design process are briefly described below:

Antenna gain relates the intensity of an antenna in a given direction to the intensity that would be produced by a hypothetical ideal antenna that radiates equally in all directions (isotropically) and has no losses.

Antenna Directivity is defined by direction to the radiation intensity averaged over all directions.

Antenna Bandwidth is defined as the range of frequencies within which the performance of the antenna, with respect to some characteristics, conforms to a specified standard [61].

Antenna Radiation Patterns An antenna radiation pattern is a 3-D plot of its radiation far from the source. Antenna radiation patterns usually take two forms, the elevation pattern and the azimuth pattern. The elevation pattern is a graph of the energy radiated from the antenna looking at it from the side (E-Plane). The azimuth pattern is a graph of the energy radiated from the antenna as if you were looking at it from directly above the antenna (H-Plane).

To select correct antenna for our application, the basic characteristics of different types of antennas are tabulated in Table 2-2.

Table 2-2: Antenna Comparison

	Radiation Pattern	Power Gain	Directivity	Polarization
Dipole	Broadside	Low	Low	Linear
Multi Element Dipole	Broadside	Low/Medium	Low	Linear
Flat Panel Antenna	Broadside	Medium	Medium/High	Linear/Circular
Parabolic Dish Antenna	Broadside	High	High	Linear/Circular
Yagi Antenna	Endfire	Medium/High	Medium/High	Linear
Slotted Antenna	Broadside	Low/Medium	Low/Medium	Linear
Microstrip Antenna	Endfire	Medium	Medium	Linear

Maximum intensity (Max U)

The radiation intensity (U) is the power radiated from an antenna per unit solid angle. Professional simulator, HFSS, can calculate the maximum intensity of the radiation in watts per steradian using,

$$U(\theta, \phi) = \frac{|E|^2}{\eta_0} r^2 \quad (2.1)$$

Where

- $U(\theta, \phi)$ is the radiation intensity in watts per steradian.
- $|E|$ is the magnitude of the E-field.
- η_0 is the intrinsic impedance of free space and it is equal to 376.7 ohms.
- r is the distance from the antenna, in meters.

Peak Directivity

Directivity is defined as the ratio of an antenna's radiation intensity in a given direction to the radiation intensity averaged over all directions. Peak directivity, in turn, is the maximum directivity over all the user-specified directions of the far-field infinite sphere.

Directivity is a dimensionless quantity represented by

$$Directivity = 4\pi \frac{U}{P_{rad}} \quad (2.2)$$

Where

- U is the radiation intensity in watts per steradian in the direction specified.
- P_{rad} is the radiated power in watts.
- For a lossless antenna, the directivity will be equal to the gain. However, if the antenna has inherent losses, the directivity is related to the gain by the radiation efficiency of the antenna.

Peak Gain

Gain is four pi times the ratio of an antenna's radiation intensity in a given direction to the total power accepted by the antenna. Peak gain, in turn, is the maximum gain over all the user-specified directions of the far-field infinite sphere.

The following equation is used to calculate gain in HFSS:

$$Gain = 4\pi \frac{U}{P_{acc}} \quad (2.3)$$

Where

- P_{acc} is the accepted power in watts entering the antenna.

Gain can be confused with directivity, since they are equivalent for lossless antennas. Gain is related to directivity by the radiation efficiency of the antenna. If the radiation efficiency is 100%, they are equal. The realized gain however, is four pi times the ratio of an antenna's radiation intensity in a given direction to the total power incident

upon the antenna port(s). Peak realized gain, in turn, is the maximum realized gain over all the user-specified directions of the far-field infinite sphere.

Radiated Power

Radiated power is the amount of time-averaged power (in watts) exiting a radiating antenna structure through a radiation boundary.

For a general radiating structure in HFSS, radiated power is computed as

$$P_{rad} = Re\left\{\int_s E \times H^* \cdot ds\right\} \quad (2.4)$$

- Re is the real part of a complex number.
- s represents the radiation boundary surfaces.
- E is the radiated electric field.
- H^* is the conjugate of \mathbf{H} .
- ds is the local radiation-boundary unit normal directed out of the 3D model.

The accuracy of the computed radiated power depends on the accuracy of E and H on the absorbing boundary. In some cases it is possible that the computed radiated power may deviate slightly from the actual radiated power. To increase the accuracy of the radiated power, seed the mesh on the absorbing boundary. As a check, you can use the S-parameters — if ports have been defined — to calculate the radiated power.

Accepted Power

The accepted power is the amount of time-averaged power (in watts) entering a radiating antenna structure through one or more ports. For antennas with a single port, accepted power is a measure of the incident power reduced by the mismatch loss at the port plane.

For a general radiating structure in HFSS, accepted power is computed as

$$P_{acc} = Re\left\{\int_A E \times H^* \cdot ds\right\} \quad (2.5)$$

Where

- A is the union of all port boundaries in the model.

For the simple case of an antenna with one lossless port containing a single propagating mode, the above expression reduces to

$$P_{acc} = |a|^2(1 - |s_{11}|^2) \quad (2.6)$$

Where

- a is the complex modal excitation specified.
- s_{11} is the single-entry generalized scattering matrix (without renormalization) computed by HFSS.

Incident Power

Incident power is the total amount of time-averaged power (in watts) incident upon all port boundaries of an antenna structure. Incident power is set at your discretion in the **Edit Sources** window.

For the simple case of an antenna with one lossless port containing a single propagating mode, the incident power P_{incident} is given by propagating mode, the incident power P_{incident} is given by

$$P_{\text{incident}} = |a|^2 \quad (2.7)$$

Where

- a is the complex modal-project excitation specified in the **Edit Sources** window.

Radiation Efficiency

The radiation efficiency is the ratio of the radiated power to the accepted power given by

$$e = \frac{P_{\text{rad}}}{P_{\text{acc}}} \quad (2.8)$$

2.4.2 Microstrip Patch Antenna

This type of antenna is described in this subsection because it is used as a microwave sensor in chapter 4. The microstrip antenna, in its simplest form consists of a dielectric substrate sandwiched between two conducting surfaces: the antenna plane and the ground plane. The simplified microstrip patch antenna is shown in Figure 2-11.

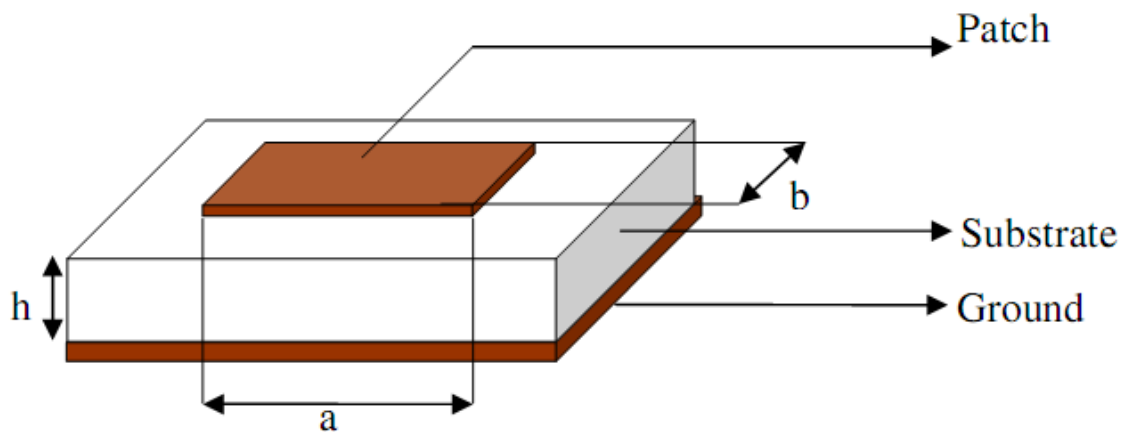


Figure 2-11: Construction of Basic Rectangular Microstrip Patch Antenna

Microstrip patch antennas radiate primarily because of the fringing fields between the patch edge and the ground plane. Since the propagating EM fields lay, both in the substrate and in free space, a quasi-TEM mode is generated. The length and width of the patch are given by (a) and (b) respectively. The substrate thickness is given by h.

Feeding Techniques

A number of feeding mechanisms have been developed for microstrip antennas [61]. Most often, the feed mechanism determines the complexity of the microstrip antenna design. Popular feed techniques can be classified into two major categories as follows.

1. Directly connected to the patch: A direct electrical connection is used to feed the radiating patch element. Like, microstrip line, coaxial probe.

Microstrip Line Feed is one of the most commonly used feed technique; a conducting strip is connected directly to the edge of the microstrip patch. Inset feed is one in which the microstrip line feed is inset into the patch [62] to provide the right impedance match between the patch and the feed line; refer Figure 2-12. The advantage of this technique is that both the feed and the patch lie on the surface of the substrate and therefore is planar in construction. This technique is efficient on thin substrates; thick substrates should be avoided as they could result in spurious feed radiation and cross polarization effects.

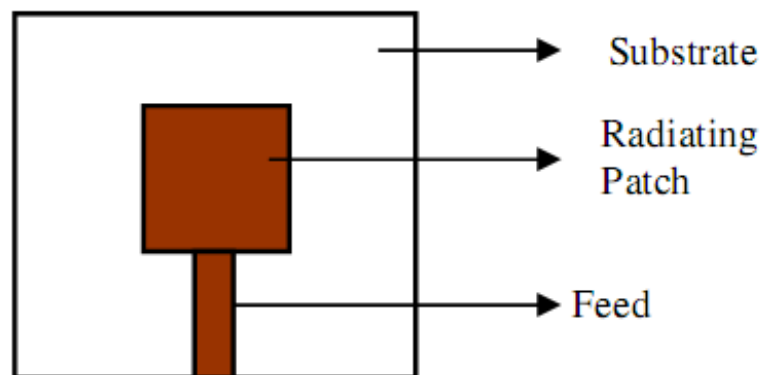


Figure 2-12: Microstrip Line Feed

The Coaxial feed or probe feed has the inner conductor connected of the coaxial cable to the patch through a hole in the substrate and the outer shield grounded by connecting to the microstrip ground plane; see Figure 2-13. Though it is easy to place the feed at any location on the patch, the disadvantage with this technique is it provides narrow impedance bandwidth and is difficult to model [63].

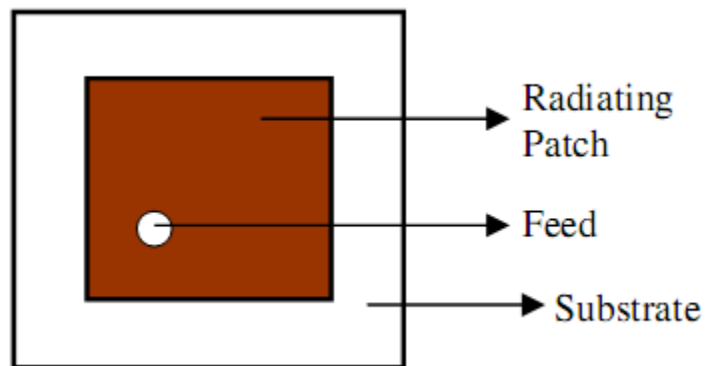


Figure 2-13: Coaxial Probe Feed

2. Coupled to the patch: Electromagnetic field coupling is used to feed the patch. Like, aperture coupling and proximity.

In Aperture Coupled Feed, the feed line is separated from the patch by the ground plane. Electromagnetic coupling is used to transfer power from the feed line to the patch through a small aperture in the ground plane. To avoid cross-polarization the coupling aperture is centered under the patch as shown in Figure 2-14. It is a multi-layered design, the efficiency of aperture coupling is lower compared to other techniques, but it is easy to model [64]. The drawback of this configuration in addition to the less in efficiency, a perfect alignment between layers and production cost.

Feed substrate guides the EM wave from the input point (SMA connector) to the coupling aperture. Thus, thinner substrate with higher dielectric constant is selected to effectively perform this operation with minimum feed-line radiation. Where, the width of the feed line is selected to match the characteristic impedance of the system.

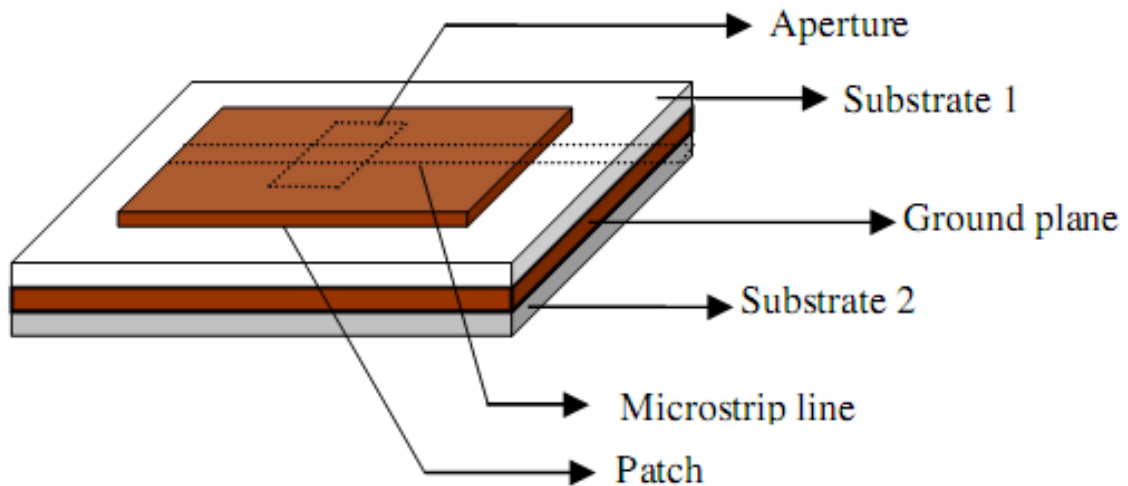


Figure 2-14: Aperture Coupling

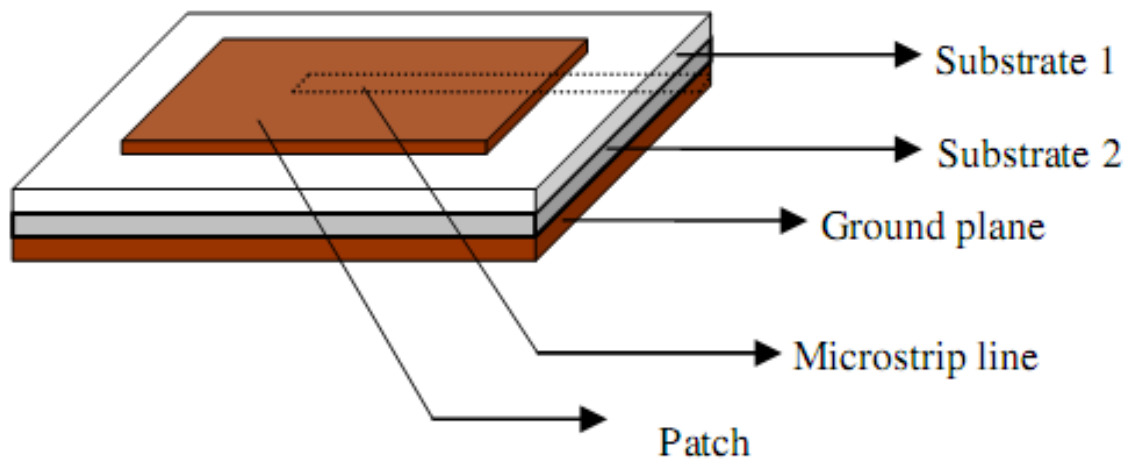


Figure 2-15: Proximity Coupling

Proximity coupling feeding technique, has a feed line sandwiched between two different substrates, see Figure 2-15. The microstrip antenna is on the top dielectric and the ground plane is on the bottom dielectric slab. The feed line is placed between the two dielectric slabs. The coupling is primarily capacitive in nature [64]. This feed mechanism provides greater than 13% fractional bandwidth [61] [64]. The fabrication complexity however is greater than any of the previous designs.

Along with a number of advantages [65] microstrip antennas also suffer from some disadvantages [62] [63] like narrow bandwidth, low efficiency, low Gain, spurious radiation and surface wave excitation. While spurious radiation and surface waves can be eliminated by using the right feed mechanisms and substrate thickness [62], the issues of major concern are poor bandwidth and low radiation efficiency. Microstrip antennas inherently suffer from ohmic losses and dielectric losses making it a high Q device [62]. In order to achieve greater bandwidth and gain we must increase substrate thickness but this could result in surface waves [63].

CHAPTER 3

ELECTROMAGNETIC FIELDS INSIDE A DIELECTRIC

LOADED CIRCULAR WAVEGUIDE

In this chapter, the cutoff wavenumbers are calculated for a cylindrical waveguide uniformly loaded with two dielectric cylinders. The analytical formulations based on the boundary value method are carried out for fields within the waveguide and the dielectric cylinders to find the corresponding guided-wave modes. This method is selected here because it is accurate and its dependency on the numerical approximation is the lowest compared to the other methods mentioned in the previous chapter. In addition, this method was used in [12] for finding the cutoff frequency for a circular waveguide loaded with one eccentric dielectric cylinder and it has been used to extend their work. The addition theorem of the Bessel function is used to transform the fields from one coordinate to other in order to apply the boundary conditions and to facilitate field matching using the orthogonally property of the Bessel functions. The present problem can be extended to model a circular waveguide loaded with multiple dielectric (oil) cylinders and to validate the excitation of related software (HFSS) model, suitable for finding the content ratio within three phase petroleum carrying pipeline.

3.1 Introduction

In Order to derive analytical expressions for the two-phase combinations shown in Figure 3-1(a), the models can be approximated to the one shows in Figure 3-1(b) and later in this chapter, it will be shown that this is a very good approximation. The analytical solution of the modal behavior of a simple dielectric (oil or water) loaded cylindrical pipelines are then used to validate the excitation and meshing of the software model of the same geometry. These software (HFSS) models are later used to find content ratio of more complicated mixture.

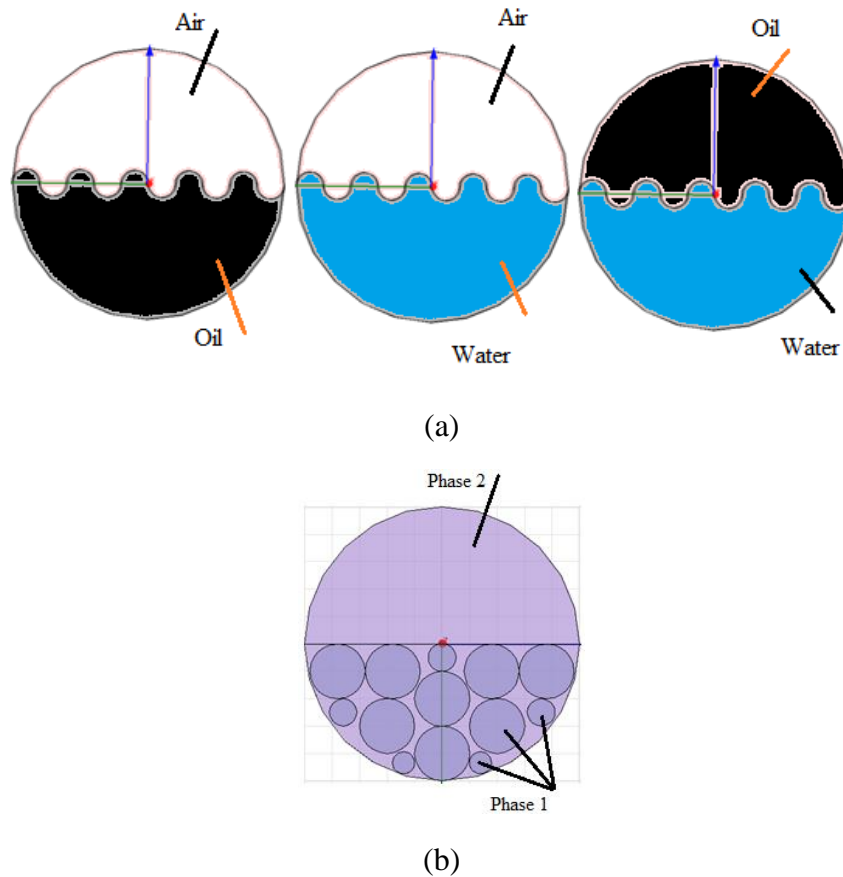


Figure 3-1: Cross Section of a Petroleum Carrying Pipeline: (a) Two-Phase Flow Scenarios, (b) Approximated Model

3.2 Solution of Wave Equation in Cylindrical Coordinates

Before the analysis for the targeted geometry starts, it will be better to know the behavior of the fields in general. The solution to this equation has been derived in many books [66], [67]. Here the solution is derived to relate it to our problem.

The general wave equation or the Helmholtz equation is given as

$$\nabla^2 \mathbf{X} + k^2 \mathbf{X} = 0 \quad (3.1)$$

$$\begin{aligned} \nabla^2 \mathbf{X} &= \frac{1}{\rho} \frac{\partial}{\partial \rho} \left(\rho \frac{\partial \mathbf{X}}{\partial \rho} \right) + \frac{1}{\rho^2} \frac{\partial^2 \mathbf{X}}{\partial \phi^2} + \frac{\partial^2 \mathbf{X}}{\partial z^2} \\ &= \frac{\partial^2 \mathbf{X}}{\partial \rho^2} + \frac{1}{\rho} \frac{\partial \mathbf{X}}{\partial \rho} + \frac{1}{\rho^2} \frac{\partial^2 \mathbf{X}}{\partial \phi^2} + \frac{\partial^2 \mathbf{X}}{\partial z^2} \end{aligned} \quad (3.2)$$

$$k = \omega \sqrt{\mu \varepsilon} \quad (3.3)$$

Where, (ρ, ϕ, z) are the cylindrical coordinates as illustrated in Figure 3-2, $\nabla^2 \mathbf{X}$ is the Laplacian operator of a scalar quantity (\mathbf{X}) and (k) is the propagation constant. Substituting Equation 3.2 into 3.1, we obtain the wave equation in cylindrical coordinates

$$\frac{\partial^2 \mathbf{X}}{\partial \rho^2} + \frac{1}{\rho} \frac{\partial \mathbf{X}}{\partial \rho} + \frac{1}{\rho^2} \frac{\partial^2 \mathbf{X}}{\partial \phi^2} + \frac{\partial^2 \mathbf{X}}{\partial z^2} + k^2 \mathbf{X} = 0 \quad (3.4)$$

In order to obtain a solution to Equation 3.4; the separation of variables method can be utilized as follow

$$\mathbf{X} = \mathbf{P}(\rho)\Phi(\phi)\mathbf{Z}(z) \quad (3.5)$$

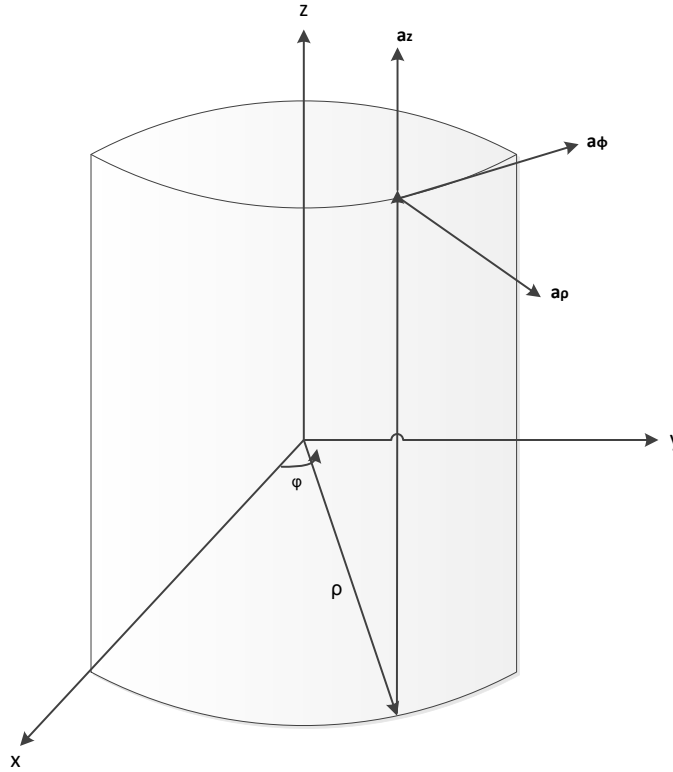


Figure 3-2: Cylindrical Coordinate System

Substitute 3.5 in 3.4 yields,

$$\Phi Z \frac{\partial^2 P}{\partial \rho^2} + \Phi Z \frac{1}{\rho} \frac{\partial P}{\partial \rho} + P Z \frac{1}{\rho^2} \frac{\partial^2 \Phi}{\partial \phi^2} + P \Phi \frac{\partial^2 Z}{\partial z^2} + k^2 P \Phi Z = 0 \quad (3.6)$$

Dividing both sides of Equation 3.6 by ΦZ and thus changing the partial derivatives to ordinary derivatives to have

$$\frac{1}{P} \frac{\partial^2 P}{\partial \rho^2} + \frac{1}{\rho P} \frac{\partial P}{\partial \rho} + \frac{1}{\Phi} \frac{1}{\rho^2} \frac{\partial^2 \Phi}{\partial \phi^2} + \frac{1}{Z} \frac{\partial^2 Z}{\partial z^2} = -k^2 \quad (3.7)$$

Since $k^2 = k_x^2 + k_y^2 + k_z^2$ in Cartesian coordinate, so by following the same procedure in cylindrical coordinate and starting by the last term since it is function in one variable only; one can assume

$$\frac{1}{Z} \frac{\partial^2 Z}{\partial z^2} = -k_z^2 \Rightarrow \frac{\partial^2 Z}{\partial z^2} = -Zk_z^2 \quad (3.8)$$

After substituting 3.8 in 3.7 and multiply both sides by ρ^2 , it can be written as

$$\frac{\rho^2}{P} \frac{\partial^2 P}{\partial \rho^2} + \frac{\rho}{P} \frac{\partial P}{\partial \rho} + \frac{1}{\Phi} \frac{\partial^2 \Phi}{\partial \phi^2} + (k^2 - k_z^2)\rho^2 = 0 \quad (3.9)$$

Now, the phi term is function in one variable so it can be equated to a constant i.e.

$-n^2$

$$\frac{1}{\Phi} \frac{\partial^2 \Phi}{\partial z^2} = -n^2 \Rightarrow \frac{\partial^2 \Phi}{\partial z^2} = -\Phi n^2 \quad (3.10)$$

Assume

$$k^2 - k_z^2 = k_\rho^2 \quad (3.11)$$

Replacing $k^2 - k_z^2$ in 3.9 by its equivalent in 3.11 and multiplying by P then

Equation 3.9 can be written as

$$\rho^2 \frac{\partial^2 P}{\partial \rho^2} + \rho \frac{\partial P}{\partial \rho} + ((k_\rho \rho)^2 - n^2)P = 0 \quad (3.12)$$

The separated equations given in 3.8, 3.10 and 3.12 have a known solution. The solution to 3.8 can be one of the following solutions

$$Z_1(z) = A_1 e^{-jk_z z} + B_1 e^{+jk_z z} \quad (3.13-a)$$

Or

$$Z_2(z) = C_1 \cos(k_z z) + D_1 \sin(k_z z) \quad (3.13-b)$$

Solution to 3.10 can have the similar representation as follows

$$\Phi_1(z) = A_2 e^{-jn\phi} + B_2 e^{+jn\phi} \quad (3.14-a)$$

Or

$$\Phi_2(z) = C_2 \cos(n\phi) + D_2 \sin(n\phi) \quad (3.14-b)$$

For Equation 3.12, the solution will be in the form of Bessel functions

$$P_1(z) = A_3 J_n(k_\rho \rho) + B_3 Y_n(k_\rho \rho) \quad (3.15-a)$$

Or

$$P_2(z) = C_3 H_n^{(1)}(k_\rho \rho) + D_3 H_n^{(2)}(k_\rho \rho) \quad (3.15-b)$$

The total solution will be the multiplication of the three separate solutions as Equation 3.5 implies. In our case, the solution will be the exponentially in z since the wave is travelling in the positive z direction and periodically in phi and for the radial direction, it will be the Bessel function solution since the outer cylinder will be conducting which

means that it is not radiating outside the outer cylinder. So the final solution will be of the following form,

$$X(\rho, \phi, z) = A_1 (A_3 J_n(k_\rho \rho) + B_3 Y_n(k_\rho \rho)) (C_2 \cos(n\phi) + D_2 \sin(n\phi)) e^{-jk_z z} \quad (3.16)$$

3.3 Geometry Description

The geometry of the problem is shown in Figure 3-3, which represents a cross section in the x-y plane of a circular waveguide partly filled with two eccentric dielectric cylinders. The outer circle represents a cross section of a perfectly conducting cylinder of radius (a), while the interior circles of radius (b) and (c) are representing the cross section of two dielectric cylinders. Three regions of interest are defined in this problem. Region (I) is inside the first dielectric cylinder which has a local coordinates as (x_1, y_1, z) , region (II) is inside the second dielectric cylinder which has a local coordinates as (x_2, y_2, z) . The permittivity and the permeability of the dielectric cylinder of region (I) are ϵ_1 and μ_1 and for the dielectric cylinder in region (II) are ϵ_2 and μ_2 while for the dielectric cylinder in region (III) are ϵ_3 and μ_3 respectively. In addition to the global coordinate system (x, y, z) at the center of the conducting circular cylinder, another coordinate system (x_1, y_1, z) at the center of the dielectric cylinder at region (I) and a third coordinate system (x_2, y_2, z) at the center of the dielectric cylinder at region (II) are defined.

The triangle shown in Figure 3-3 used to illustrate the addition theorem of the Bessel functions. This theorem means in transfer the electromagnetic fields that are represented in a certain coordinate to be represented into another coordinate system. Since the fields here are represented in Bessel functions; so this method will be of help.

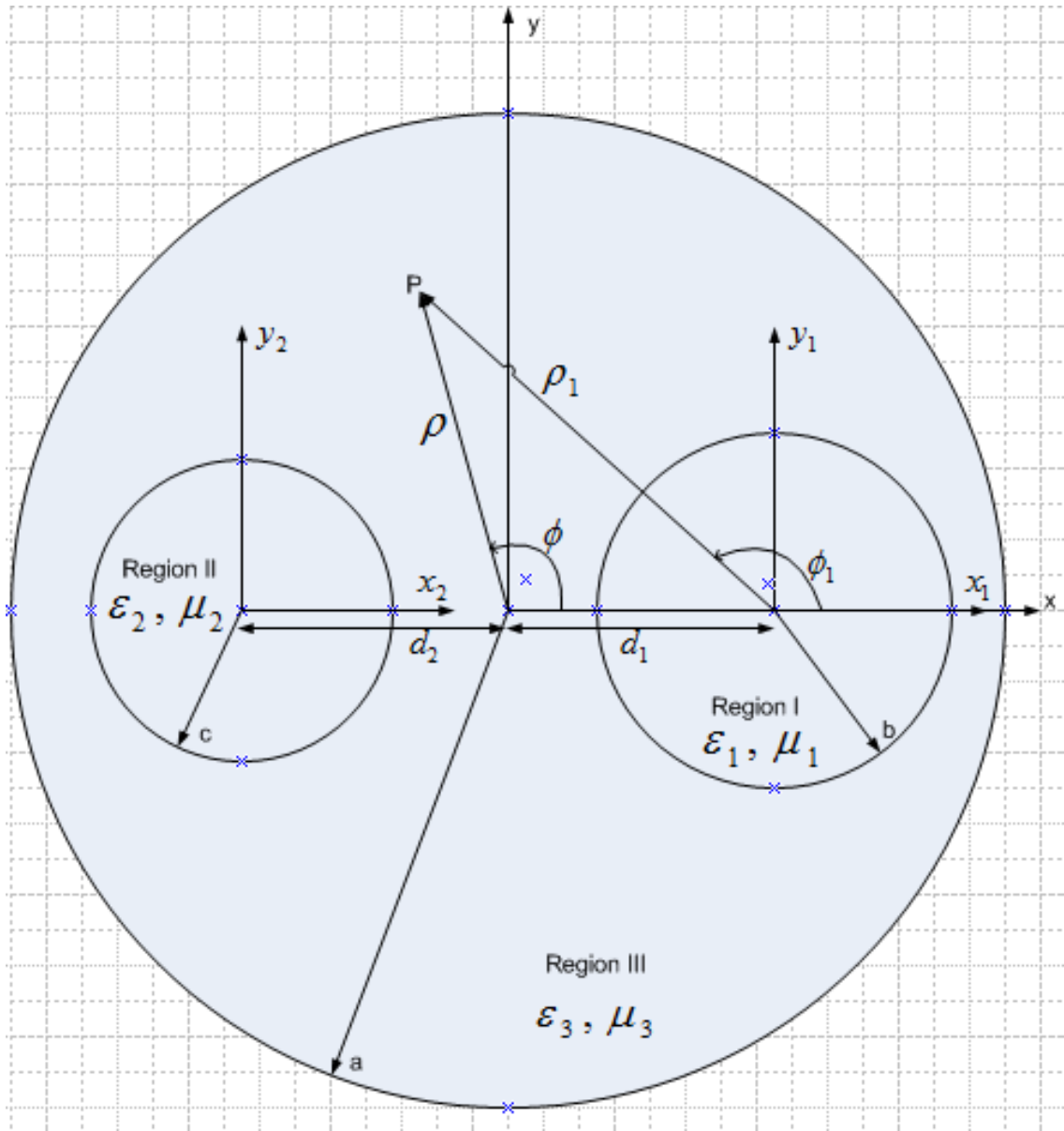


Figure 3-3: Geometry of the Problem

3.4 Problem Formulation

In order to analyze this problem it is preferred to use the cylindrical coordinates system (ρ, ϕ, z) in the three coordinates defined before.

The electric and magnetic fields components in region (I) in terms of the local coordinates (ρ_1) are:

$$E_z^{(I)} = \frac{k_{\rho_1}^2}{j\omega\epsilon_1} \sum_{n=0}^{\infty} A_n J_n(k_{\rho_1}\rho_1) \begin{Bmatrix} \cos n\phi_1 \\ \sin n\phi_1 \end{Bmatrix} e^{-jk_z z} \Rightarrow \begin{Bmatrix} \text{Even TM} \\ \text{Odd TM} \end{Bmatrix} \quad (3.17)$$

$$H_z^{(I)} = \frac{k_{\rho_1}^2}{j\omega\mu_1} \sum_{n=0}^{\infty} B_n J_n(k_{\rho_1}\rho_1) \begin{Bmatrix} \sin n\phi_1 \\ \cos n\phi_1 \end{Bmatrix} e^{-jk_z z} \Rightarrow \begin{Bmatrix} \text{Odd TE} \\ \text{Even TE} \end{Bmatrix} \quad (3.18)$$

The Fields in region (II) in terms of the local coordinates (ρ_1) are:

$$E_z^{(II)} = \frac{k_{\rho_2}^2}{j\omega\epsilon_2} \sum_{n=0}^{\infty} [C_n^{(1)} J_n(k_{\rho_2}\rho_1) + C_n^{(2)} Y_n(k_{\rho_2}\rho_1)] \begin{Bmatrix} \cos n\phi_1 \\ \sin n\phi_1 \end{Bmatrix} e^{-jk_z z} \Rightarrow \begin{Bmatrix} \text{Even TM} \\ \text{Odd TM} \end{Bmatrix} \quad (3.19)$$

$$H_z^{(II)} = \frac{k_{\rho_2}^2}{j\omega\mu_2} \sum_{n=0}^{\infty} [D_n^{(1)} J_n(k_{\rho_2}\rho_1) + D_n^{(2)} Y_n(k_{\rho_2}\rho_1)] \begin{Bmatrix} \sin n\phi_1 \\ \cos n\phi_1 \end{Bmatrix} e^{-jk_z z} \Rightarrow \begin{Bmatrix} \text{Odd TE} \\ \text{Even TE} \end{Bmatrix} \quad (3.20)$$

The Fields in region (III) in terms of the local coordinates (ρ_1) are:

$$E_z^{(III)} = \frac{k_{\rho_3}^2}{j\omega\epsilon_3} \sum_{n=0}^{\infty} [F_n^{(1)} J_n(k_{\rho_3}\rho_1) + F_n^{(2)} Y_n(k_{\rho_3}\rho_1)] \begin{Bmatrix} \cos n\phi_1 \\ \sin n\phi_1 \end{Bmatrix} e^{-jk_z z} \Rightarrow \begin{Bmatrix} \text{Even TM} \\ \text{Odd TM} \end{Bmatrix} \quad (3.21)$$

$$H_z^{(III)} = \frac{k_{\rho_3}^2}{j\omega\mu_3} \sum_{n=0}^{\infty} [G_n^{(1)} J_n(k_{\rho_3}\rho_1) + G_n^{(2)} Y_n(k_{\rho_3}\rho_1)] \begin{Bmatrix} \sin n\phi_1 \\ \cos n\phi_1 \end{Bmatrix} e^{-jk_z z} \Rightarrow \begin{Bmatrix} \text{Odd TE} \\ \text{Even TE} \end{Bmatrix} \quad (3.22)$$

Where

$$k_{\rho 1}^2 = k_1^2 - k_z^2, \quad k_{\rho 2}^2 = k_2^2 - k_z^2, \quad k_{\rho 3}^2 = k_3^2 - k_z^2 \quad (3.23)$$

$$k_1 = \omega\sqrt{\varepsilon_1\mu_1}, \quad k_2 = \omega\sqrt{\varepsilon_2\mu_2}, \quad k_3 = \omega\sqrt{\varepsilon_3\mu_3} \quad (3.24)$$

While $J_n(x)$ and $Y_n(x)$ are Bessel functions of the first and second kind respectively with argument x and order n . For odd fields the zero order coefficients are equal to zero.

The other field components in each region can be obtained by applying the Maxwell's equations. The boundary conditions that are applied in this case require the z and ϕ components of electric and magnetic fields (E_z, H_z, E_ϕ, H_ϕ) since these are the fields that are tangential to the cylinders considered. So the fields in region (I) can be derived as follows:

$$E_\phi^{(I)} = \frac{-jk_z}{\rho_1 k_{\rho 1}^2} \frac{\partial E_z^{(I)}}{\partial \phi_1} + \frac{j\omega\mu_1}{k_{\rho 1}^2} \frac{\partial H_z^{(I)}}{\partial \rho_1} \quad (3.25)$$

$$E_\phi^{(I)} = \frac{-nk_z}{\omega\varepsilon_1\rho_1} \sum_{n=0}^{\infty} A_n J_n(k_{\rho 1}\rho_1) \begin{Bmatrix} -\sin n\phi_1 \\ \cos n\phi_1 \end{Bmatrix} e^{-jk_z z} + k_{\rho 1} \sum_{n=0}^{\infty} B_n J'_n(k_{\rho 1}\rho_1) \begin{Bmatrix} \sin n\phi_1 \\ \cos n\phi_1 \end{Bmatrix} e^{-jk_z z} \quad (3.26)$$

$$H_\phi^{(I)} = \frac{-j\omega\varepsilon_1}{k_{\rho 1}^2} \frac{\partial E_z^{(I)}}{\partial \rho_1} - \frac{jk_z}{\rho_1 k_{\rho 1}^2} \frac{\partial H_z^{(I)}}{\partial \phi_1} \quad (3.27)$$

$$H_\phi^{(I)} = -k_{\rho 1} \sum_{n=0}^{\infty} A_n J'_n(k_{\rho 1}\rho_1) \begin{Bmatrix} \cos n\phi_1 \\ \sin n\phi_1 \end{Bmatrix} e^{-jk_z z} - \frac{nk_z}{\omega\mu_1\rho_1} \sum_{n=0}^{\infty} B_n J_n(k_{\rho 1}\rho_1) \begin{Bmatrix} \cos n\phi_1 \\ -\sin n\phi_1 \end{Bmatrix} e^{-jk_z z} \quad (3.28)$$

Using Maxwell's equations, the fields in region (III) can be derived as follows:

$$E_{\phi}^{(III)} = \left\{ \begin{array}{l} \frac{-nk_z}{\omega\epsilon_3\rho_1} \sum_{n=0}^{\infty} [F_n^{(1)} J_n(k_{\rho_3}\rho_1) + F_n^{(2)} Y_n(k_{\rho_3}\rho_1)] \left\{ \begin{array}{l} -\sin n\phi_1 \\ \cos n\phi_1 \end{array} \right\} + \\ k_{\rho_3} \sum_{n=0}^{\infty} [G_n^{(1)} J'_n(k_{\rho_3}\rho_1) + G_n^{(2)} Y'_n(k_{\rho_3}\rho_1)] \left\{ \begin{array}{l} \sin n\phi_1 \\ \cos n\phi_1 \end{array} \right\} \end{array} \right\} e^{-jk_z z} \quad (3.29)$$

$$H_{\phi}^{(III)} = \left\{ \begin{array}{l} -k_{\rho_3} \sum_{n=0}^{\infty} [F_n^{(1)} J'_n(k_{\rho_3}\rho_1) + F_n^{(2)} Y'_n(k_{\rho_3}\rho_1)] \left\{ \begin{array}{l} \cos n\phi_1 \\ \sin n\phi_1 \end{array} \right\} + \\ \frac{-nk_z}{\omega\mu_3\rho_1} \sum_{n=0}^{\infty} [G_n^{(1)} J_n(k_{\rho_3}\rho_1) + G_n^{(2)} Y_n(k_{\rho_3}\rho_1)] \left\{ \begin{array}{l} \cos n\phi_1 \\ -\sin n\phi_1 \end{array} \right\} \end{array} \right\} e^{-jk_z z} \quad (3.30)$$

The unknown coefficients in the above equations A_n , B_n , $C_n^{(1)}$, $C_n^{(2)}$, $D_n^{(1)}$, $D_n^{(2)}$, $F_n^{(1)}$, $F_n^{(2)}$, $G_n^{(1)}$ and $G_n^{(2)}$ can be obtained by applying the boundary conditions of continuous E_z , H_z , E_{ϕ} , H_{ϕ} on $\rho_1=b$ and $\rho_2=c$ and vanishing E_z , E_{ϕ} at $\rho=a$ surfaces.

Applying the boundary condition of continuous electric field E_z at $\rho_1=b$ leads to

$$\frac{k_{\rho_1}^2}{\epsilon_1} A_n J_n(k_{\rho_1}b) = \frac{k_{\rho_3}^2}{\epsilon_3} [F_n^{(1)} J_n(k_{\rho_3}b) + F_n^{(2)} Y_n(k_{\rho_3}b)] \quad (3.31)$$

$$A_n = \frac{k_{\rho_3}^2}{k_{\rho_1}^2} \frac{\epsilon_1}{\epsilon_3} \frac{1}{J_n(k_{\rho_1}b)} [F_n^{(1)} J_n(k_{\rho_3}b) + F_n^{(2)} Y_n(k_{\rho_3}b)] \quad (3.32)$$

While the continuous magnetic field H_z at $\rho_1=b$ leads to

$$\frac{k_{\rho_1}^2}{\mu_1} B_n J_n(k_{\rho_1}b) = \frac{k_{\rho_3}^2}{\mu_3} [G_n^{(1)} J_n(k_{\rho_3}b) + G_n^{(2)} Y_n(k_{\rho_3}b)] \quad (3.33)$$

$$B_n = \frac{k_{\rho_3}^2}{k_{\rho_1}^2} \frac{\mu_1}{\mu_3} \frac{1}{J_n(k_{\rho_1}b)} \left[G_n^{(1)} J_n(k_{\rho_3}b) + G_n^{(2)} Y_n(k_{\rho_3}b) \right] \quad (3.34)$$

Applying the boundary condition of continuous electric field E_ϕ at $\rho_1=b$ leads to

$$\begin{aligned} & \pm \frac{nk_z}{\omega \varepsilon_1 b} A_n J_n(k_{\rho_1}b) + k_{\rho_1} B_n J_n'(k_{\rho_1}b) = \\ & \pm \frac{nk_z}{\omega \varepsilon_3 b} \left[F_n^{(1)} J_n(k_{\rho_3}b) + F_n^{(2)} Y_n(k_{\rho_3}b) \right] + k_{\rho_3} \left[G_n^{(1)} J_n'(k_{\rho_3}b) + G_n^{(2)} Y_n'(k_{\rho_3}b) \right] \end{aligned} \quad (3.35)$$

Applying the boundary condition of continuous magnetic field H_ϕ at $\rho_1=b$ leads to

$$\begin{aligned} & k_{\rho_1} A_n J_n'(k_{\rho_1}b) \pm \frac{nk_z}{\omega \mu_1 b} B_n J_n(k_{\rho_1}b) = \\ & k_{\rho_3} \left[F_n^{(1)} J_n'(k_{\rho_3}b) + F_n^{(2)} Y_n'(k_{\rho_3}b) \right] \pm \frac{nk_z}{\omega \mu_3 b} \left[G_n^{(1)} J_n(k_{\rho_3}b) + G_n^{(2)} Y_n(k_{\rho_3}b) \right] \end{aligned} \quad (3.36)$$

Substitute (3.32) and (3.34) into (3.35) yields

$$\begin{aligned} \pm \frac{nk_z}{\omega \varepsilon_3 b} \left(\frac{k_{\rho_3}^2}{k_{\rho_1}^2} - 1 \right) \left[F_n^{(1)} J_n(k_{\rho_3}b) + F_n^{(2)} Y_n(k_{\rho_3}b) \right] &= k_{\rho_3} \left(J_n'(k_{\rho_3}b) - \frac{k_{\rho_3}}{k_{\rho_1}} \frac{\mu_1}{\mu_3} \frac{J_n'(k_{\rho_1}b)}{J_n(k_{\rho_1}b)} J_n(k_{\rho_3}b) \right) G_n^{(1)} \\ &+ k_{\rho_3} \left(Y_n'(k_{\rho_3}b) - \frac{k_{\rho_3}}{k_{\rho_1}} \frac{\mu_1}{\mu_3} \frac{J_n'(k_{\rho_1}b)}{J_n(k_{\rho_1}b)} Y_n(k_{\rho_3}b) \right) G_n^{(2)} \end{aligned} \quad (3.37)$$

Substitute (3.32) and (3.34) into (3.36) yields

$$\begin{aligned} \pm \frac{nk_z}{\omega \mu_3 b} \left(\frac{k_{\rho_3}^2}{k_{\rho_1}^2} - 1 \right) \left[G_n^{(1)} J_n(k_{\rho_3}b) + G_n^{(2)} Y_n(k_{\rho_3}b) \right] &= k_{\rho_3} \left(J_n'(k_{\rho_3}b) - \frac{k_{\rho_3}}{k_{\rho_1}} \frac{\varepsilon_1}{\varepsilon_3} \frac{J_n'(k_{\rho_1}b)}{J_n(k_{\rho_1}b)} J_n(k_{\rho_3}b) \right) F_n^{(1)} \\ &+ k_{\rho_3} \left(Y_n'(k_{\rho_3}b) - \frac{k_{\rho_3}}{k_{\rho_1}} \frac{\varepsilon_1}{\varepsilon_3} \frac{J_n'(k_{\rho_1}b)}{J_n(k_{\rho_1}b)} Y_n(k_{\rho_3}b) \right) F_n^{(2)} \end{aligned} \quad (3.38)$$

Equations (3.37) and (3.38) can be written as

$$U_\mu G_n^{(1)} + V_\mu G_n^{(2)} = nZ_3 [F_n^{(1)} J_n(\eta_3) + F_n^{(2)} Y_n(\eta_3)] \begin{pmatrix} W \\ W' \end{pmatrix} \Rightarrow \begin{pmatrix} n = 1, 2, \dots (\text{Odd HE}) \\ n = 0, 1, \dots (\text{Even HE}) \end{pmatrix} \quad (3.39)$$

$$U_\varepsilon F_n^{(1)} + V_\varepsilon F_n^{(2)} = \frac{n}{Z_3} [G_n^{(1)} J_n(\eta_3) + G_n^{(2)} Y_n(\eta_3)] \begin{pmatrix} W \\ W' \end{pmatrix} \Rightarrow \begin{pmatrix} n = 0, 1, \dots (\text{Odd HE}) \\ n = 1, 2, \dots (\text{Even HE}) \end{pmatrix} \quad (3.40)$$

Where;

$$\begin{pmatrix} W \\ W' \end{pmatrix} = \begin{pmatrix} + \\ - \end{pmatrix} \frac{k_z J_n(\eta_1)}{\eta_3 k_3} \left(\frac{k_{\rho 3}^2}{k_{\rho 1}^2} - 1 \right) \Rightarrow \begin{pmatrix} \text{Odd HE} \\ \text{Even HE} \end{pmatrix} \quad (3.41)$$

$$U_\mu = J_n(\eta_1) J_n'(\eta_3) - \frac{k_{\rho 3}}{k_{\rho 1}} \frac{\mu_1}{\mu_3} J_n'(\eta_1) J_n(\eta_3) \quad (3.42)$$

$$V_\mu = J_n(\eta_1) Y_n'(\eta_3) - \frac{k_{\rho 3}}{k_{\rho 1}} \frac{\mu_1}{\mu_3} J_n'(\eta_1) Y_n(\eta_3) \quad (3.43)$$

$$U_\varepsilon = J_n(\eta_1) J_n'(\eta_3) - \frac{k_{\rho 3}}{k_{\rho 1}} \frac{\varepsilon_1}{\varepsilon_3} J_n'(\eta_1) J_n(\eta_3) \quad (3.44)$$

$$V_\varepsilon = J_n(\eta_1) Y_n'(\eta_3) - \frac{k_{\rho 3}}{k_{\rho 1}} \frac{\varepsilon_1}{\varepsilon_3} J_n'(\eta_1) Y_n(\eta_3) \quad (3.45)$$

$$Z_3 = \sqrt{\frac{\mu_3}{\varepsilon_3}}, k_3 = \omega \sqrt{\mu_3 \varepsilon_3}, \eta_1 = k_{\rho 1} b, \eta_3 = k_{\rho 3} b \quad (3.46)$$

Now, to apply the boundary condition of continuous E_z , H_z , E_ϕ and H_ϕ at $\rho_2=c$, the fields in region-II and region-III should be expressed first in terms of the ρ_2 local coordinate system by using the addition theorem of Bessel functions illustrated by the triangle shown

in Figure 3-4. This theorem has been used a lot in the literature for its usefulness. [68], [69], [70]

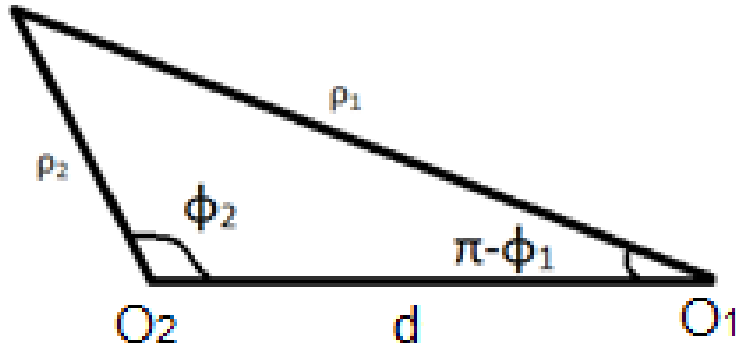


Figure 3-4: Triangle Used to Form the Addition Theorem of Bessel Function [71]

$$B_n(k_\rho \rho_1) \begin{pmatrix} \cos n\phi_1 \\ \sin n\phi_1 \end{pmatrix} = \sum_{m=-\infty}^{\infty} B_m(k_\rho d) J_{m-n}(k_\rho \rho_2) \begin{pmatrix} \cos m\phi_2 \\ \sin m\phi_2 \end{pmatrix}, \quad \text{if } d > \rho_2 \quad (3.47\text{-a})$$

$$B_n(k_\rho \rho_1) \begin{pmatrix} \cos n\phi_1 \\ \sin n\phi_1 \end{pmatrix} = \sum_{m=-\infty}^{\infty} B_m(k_\rho \rho_2) J_{m-n}(k_\rho d) \begin{pmatrix} \cos m\phi_2 \\ \sin m\phi_2 \end{pmatrix}, \quad \text{if } d < \rho_2 \quad (3.47\text{-b})$$

Equations (3.47-a) and (3.47-b) can be written as follows:

$$B_n(k_\rho \rho_1) \begin{pmatrix} \cos n\phi_1 \\ \sin n\phi_1 \end{pmatrix} = \sum_{m=0}^{\infty} \frac{\varepsilon_m}{2} B_m(k_\rho d) \begin{pmatrix} [J_{m-n}(k_\rho \rho_2) + (-1)^n J_{m+n}(k_\rho \rho_2)] \cos m\phi_2 \\ [J_{m-n}(k_\rho \rho_2) - (-1)^n J_{m+n}(k_\rho \rho_2)] \sin m\phi_2 \end{pmatrix} \quad (3.48-a)$$

$$B_n(k_\rho \rho_1) \begin{pmatrix} \cos n\phi_1 \\ \sin n\phi_1 \end{pmatrix} = \sum_{m=0}^{\infty} \frac{\varepsilon_m}{2} B_m(k_\rho \rho_2) \begin{pmatrix} [J_{m-n}(k_\rho d) + (-1)^n J_{m+n}(k_\rho d)] \cos m\phi_2 \\ [J_{m-n}(k_\rho d) - (-1)^n J_{m+n}(k_\rho d)] \sin m\phi_2 \end{pmatrix} \quad (3.48-b)$$

Where $B_n(x)$ could be $J_n(x)$ or $Y_n(x)$ and (d) is the distance between the centers of the two coordinates.

Applying equation (3.48-a) on Equations (3.19 and 3.20) gives:

$$E_z^{(II)} = \frac{k_{\rho 2}^2}{j\omega\varepsilon_2} \sum_{n=0}^{\infty} \sum_{m=0}^{\infty} \frac{\varepsilon_m}{2} [C_n^{(1)} J_m(k_{\rho 2}(d_1 + d_2)) + C_n^{(2)} Y_m(k_{\rho 2}(d_1 + d_2))] \begin{pmatrix} P_{m,n} \\ Q_{m,n} \end{pmatrix} \begin{Bmatrix} \cos m\phi_2 \\ \sin m\phi_2 \end{Bmatrix} e^{-jk_z z} \quad (3.49)$$

$$H_z^{(II)} = \frac{k_{\rho 2}^2}{j\omega\mu_2} \sum_{n=0}^{\infty} \sum_{m=0}^{\infty} \frac{\varepsilon_m}{2} [D_n^{(1)} J_m(k_{\rho 2}(d_1 + d_2)) + D_n^{(2)} Y_m(k_{\rho 2}(d_1 + d_2))] \begin{pmatrix} Q_{m,n} \\ P_{m,n} \end{pmatrix} \begin{Bmatrix} \sin m\phi_2 \\ \cos m\phi_2 \end{Bmatrix} e^{-jk_z z} \quad (3.50)$$

Where the previous two equations represent the continuous z-component of electric and magnetic fields in region (II) in terms of (ρ_2) coordinates. Using Maxwell's equations, the ϕ -components of continuous electric and magnetic fields in region (II) can be derived as follows:

$$E_{\phi}^{(II)} = \left\{ \begin{aligned} & \frac{-mk_z}{\omega \varepsilon_2 \rho_2} \sum_{n=0}^{\infty} \sum_{m=0}^{\infty} \frac{\varepsilon_m}{2} \left[C_n^{(1)} J_m(k_{\rho_2}(d_1 + d_2)) + C_n^{(2)} Y_m(k_{\rho_2}(d_1 + d_2)) \right] \begin{pmatrix} P_{m,n} \\ Q_{m,n} \end{pmatrix} \begin{Bmatrix} -\sin m\phi_2 \\ \cos m\phi_2 \end{Bmatrix} \\ & + k_{\rho_2} \sum_{n=0}^{\infty} \sum_{m=0}^{\infty} \frac{\varepsilon_m}{2} \left[D_n^{(1)} J_m(k_{\rho_2}(d_1 + d_2)) + D_n^{(2)} Y_m(k_{\rho_2}(d_1 + d_2)) \right] \begin{pmatrix} Q'_{m,n} \\ P'_{m,n} \end{pmatrix} \begin{Bmatrix} \sin m\phi_2 \\ \cos m\phi_2 \end{Bmatrix} \end{aligned} \right\} e^{-jk_z z} \quad (3.51)$$

$$H_{\phi}^{(II)} = \left\{ \begin{aligned} & -k_{\rho_2} \sum_{n=0}^{\infty} \sum_{m=0}^{\infty} \frac{\varepsilon_m}{2} \left[C_n^{(1)} J_m(k_{\rho_2}(d_1 + d_2)) + C_n^{(2)} Y_m(k_{\rho_2}(d_1 + d_2)) \right] \begin{pmatrix} P'_{m,n} \\ Q_{m,n} \end{pmatrix} \begin{Bmatrix} \cos m\phi_2 \\ \sin m\phi_2 \end{Bmatrix} \\ & + \frac{-mk_z}{\omega \mu_2 \rho_2} \sum_{n=0}^{\infty} \sum_{m=0}^{\infty} \frac{\varepsilon_m}{2} \left[D_n^{(1)} J_m(k_{\rho_2}(d_1 + d_2)) + D_n^{(2)} Y_m(k_{\rho_2}(d_1 + d_2)) \right] \begin{pmatrix} Q_{m,n} \\ P_{m,n} \end{pmatrix} \begin{Bmatrix} \cos m\phi_2 \\ -\sin m\phi_2 \end{Bmatrix} \end{aligned} \right\} e^{-jk_z z} \quad (3.52)$$

Where

$$P_{m,n} = J_{m-n}(k_{\rho_2} \rho_2) + (-1)^n J_{m+n}(k_{\rho_2} \rho_2) \quad (3.53)$$

$$P'_{m,n} = J'_{m-n}(k_{\rho_2} \rho_2) + (-1)^n J'_{m+n}(k_{\rho_2} \rho_2) \quad (3.54)$$

$$Q_{m,n} = J_{m-n}(k_{\rho_2} \rho_2) - (-1)^n J_{m+n}(k_{\rho_2} \rho_2) \quad (3.55)$$

$$Q'_{m,n} = J'_{m-n}(k_{\rho_2} \rho_2) - (-1)^n J'_{m+n}(k_{\rho_2} \rho_2) \quad (3.56)$$

Applying equation (3.48-a) on Equations (3.21 and 3.22) gives:

$$E_z^{(III)} = \frac{k_{\rho_3}^2}{j\omega \varepsilon_3} \sum_{n=0}^{\infty} \sum_{m=0}^{\infty} \frac{\varepsilon_m}{2} \left[F_n^{(1)} J_m(k_{\rho_3}(d_1 + d_2)) + F_n^{(2)} Y_m(k_{\rho_3}(d_1 + d_2)) \right] \begin{pmatrix} S_{m,n} \\ T_{m,n} \end{pmatrix} \begin{Bmatrix} \cos m\phi_2 \\ \sin m\phi_2 \end{Bmatrix} e^{-jk_z z} \quad (3.57)$$

$$H_z^{(III)} = \frac{k_{\rho_3}^2}{j\omega \mu_3} \sum_{n=0}^{\infty} \sum_{m=0}^{\infty} \frac{\varepsilon_m}{2} \left[G_n^{(1)} J_m(k_{\rho_3}(d_1 + d_2)) + G_n^{(2)} Y_m(k_{\rho_3}(d_1 + d_2)) \right] \begin{pmatrix} T_{m,n} \\ S_{m,n} \end{pmatrix} \begin{Bmatrix} \sin m\phi_2 \\ \cos m\phi_2 \end{Bmatrix} e^{-jk_z z} \quad (3.58)$$

$$E_{\phi}^{(III)} = \left\{ \begin{aligned} & \frac{-mk_z}{\omega \epsilon_3 \rho_2} \sum_{n=0}^{\infty} \sum_{m=0}^{\infty} \frac{\epsilon_m}{2} \left[F_n^{(1)} J_m(k_{\rho_3}(d_1 + d_2)) + \begin{pmatrix} S_{m,n} \\ T_{m,n} \end{pmatrix} \begin{Bmatrix} -\sin m\phi_2 \\ \cos m\phi_2 \end{Bmatrix} \right] \\ & + k_{\rho_3} \sum_{n=0}^{\infty} \sum_{m=0}^{\infty} \frac{\epsilon_m}{2} \left[G_n^{(1)} J_m(k_{\rho_3}(d_1 + d_2)) + \begin{pmatrix} T'_{m,n} \\ S'_{m,n} \end{pmatrix} \begin{Bmatrix} \sin m\phi_2 \\ \cos m\phi_2 \end{Bmatrix} \right] \end{aligned} \right\} e^{-jk_z z} \quad (3.59)$$

$$H_{\phi}^{(III)} = \left\{ \begin{aligned} & -k_{\rho_3} \sum_{n=0}^{\infty} \sum_{m=0}^{\infty} \frac{\epsilon_m}{2} \left[F_n^{(1)} J_m(k_{\rho_3}(d_1 + d_2)) + \begin{pmatrix} S'_{m,n} \\ T'_{m,n} \end{pmatrix} \begin{Bmatrix} \cos m\phi_2 \\ \sin m\phi_2 \end{Bmatrix} \right] \\ & + \frac{-mk_z}{\omega \mu_3 \rho_2} \sum_{n=0}^{\infty} \sum_{m=0}^{\infty} \frac{\epsilon_m}{2} \left[G_n^{(1)} J_m(k_{\rho_3}(d_1 + d_2)) + \begin{pmatrix} T_{m,n} \\ S_{m,n} \end{pmatrix} \begin{Bmatrix} \cos m\phi_2 \\ -\sin m\phi_2 \end{Bmatrix} \right] \end{aligned} \right\} e^{-jk_z z} \quad (3.60)$$

Where

$$S_{m,n} = J_{m-n}(k_{\rho_3} \rho_2) + (-1)^n J_{m+n}(k_{\rho_3} \rho_2) \quad (3.61)$$

$$S'_{m,n} = J'_{m-n}(k_{\rho_3} \rho_2) + (-1)^n J'_{m+n}(k_{\rho_3} \rho_2) \quad (3.62)$$

$$T_{m,n} = J_{m-n}(k_{\rho_3} \rho_2) - (-1)^n J_{m+n}(k_{\rho_3} \rho_2) \quad (3.63)$$

$$T'_{m,n} = J'_{m-n}(k_{\rho_3} \rho_2) - (-1)^n J'_{m+n}(k_{\rho_3} \rho_2) \quad (3.64)$$

In the above equations ϵ_m is 1 for $m=0$ and 2 otherwise.

Applying the boundary condition of continuous electric field E_z at $\rho_2=c$ leads to

$$\begin{aligned} & \frac{k_{\rho_2}^2}{\epsilon_2} \sum_{n=0}^{\infty} [C_n^{(1)} J_m(k_{\rho_2}(d_1 + d_2)) + C_n^{(2)} Y_m(k_{\rho_2}(d_1 + d_2))] \begin{pmatrix} P_{m,n} \\ Q_{m,n} \end{pmatrix} = \\ & \frac{k_{\rho_3}^2}{\epsilon_3} \sum_{n=0}^{\infty} [F_n^{(1)} J_m(k_{\rho_3}(d_1 + d_2)) + F_n^{(2)} Y_m(k_{\rho_3}(d_1 + d_2))] \begin{pmatrix} S_{m,n} \\ T_{m,n} \end{pmatrix} \end{aligned} \quad (3.65)$$

Applying the boundary condition of continuous magnetic field H_z at $\rho_2=c$ leads to

$$\begin{aligned} & \frac{k_{\rho_2}^2}{\mu_2} \sum_{n=0}^{\infty} [D_n^{(1)} J_m(k_{\rho_2}(d_1 + d_2)) + D_n^{(2)} Y_m(k_{\rho_2}(d_1 + d_2))] \begin{pmatrix} Q_{m,n} \\ P_{m,n} \end{pmatrix} = \\ & \frac{k_{\rho_3}^2}{\mu_3} \sum_{n=0}^{\infty} [G_n^{(1)} J_m(k_{\rho_3}(d_1 + d_2)) + G_n^{(2)} Y_m(k_{\rho_3}(d_1 + d_2))] \begin{pmatrix} T_{m,n} \\ S_{m,n} \end{pmatrix} \end{aligned} \quad (3.66)$$

Applying the boundary condition of continuous electric field E_ϕ at $\rho_2=c$ leads to

$$\begin{aligned} & \pm \frac{mk_z}{\omega \epsilon_2 c} \sum_{n=0}^{\infty} [C_n^{(1)} J_m(k_{\rho_2}(d_1 + d_2)) + C_n^{(2)} Y_m(k_{\rho_2}(d_1 + d_2))] \begin{pmatrix} P_{m,n} \\ Q_{m,n} \end{pmatrix} + \\ & k_{\rho_2} \sum_{n=0}^{\infty} [D_n^{(1)} J_m(k_{\rho_2}(d_1 + d_2)) + D_n^{(2)} Y_m(k_{\rho_2}(d_1 + d_2))] \begin{pmatrix} Q'_{m,n} \\ P'_{m,n} \end{pmatrix} = \\ & \pm \frac{mk_z}{\omega \epsilon_3 c} \sum_{n=0}^{\infty} [F_n^{(1)} J_m(k_{\rho_3}(d_1 + d_2)) + F_n^{(2)} Y_m(k_{\rho_3}(d_1 + d_2))] \begin{pmatrix} S_{m,n} \\ T_{m,n} \end{pmatrix} + \\ & k_{\rho_3} \sum_{n=0}^{\infty} [G_n^{(1)} J_m(k_{\rho_3}(d_1 + d_2)) + G_n^{(2)} Y_m(k_{\rho_3}(d_1 + d_2))] \begin{pmatrix} T'_{m,n} \\ S'_{m,n} \end{pmatrix} \end{aligned} \quad (3.67)$$

Applying the boundary condition of continuous magnetic field H_ϕ at $\rho_2=c$ leads to

$$\begin{aligned} & k_{\rho_2} \sum_{n=0}^{\infty} [C_n^{(1)} J_m(k_{\rho_2}(d_1 + d_2)) + C_n^{(2)} Y_m(k_{\rho_2}(d_1 + d_2))] \begin{pmatrix} P'_{m,n} \\ Q'_{m,n} \end{pmatrix} \pm \\ & \frac{mk_z}{\omega \mu_2 c} \sum_{n=0}^{\infty} [D_n^{(1)} J_m(k_{\rho_2}(d_1 + d_2)) + D_n^{(2)} Y_m(k_{\rho_2}(d_1 + d_2))] \begin{pmatrix} Q_{m,n} \\ P_{m,n} \end{pmatrix} = \\ & k_{\rho_3} \sum_{n=0}^{\infty} [F_n^{(1)} J_m(k_{\rho_3}(d_1 + d_2)) + F_n^{(2)} Y_m(k_{\rho_3}(d_1 + d_2))] \begin{pmatrix} S'_{m,n} \\ T'_{m,n} \end{pmatrix} \pm \\ & \frac{mk_z}{\omega \mu_3 c} \sum_{n=0}^{\infty} [G_n^{(1)} J_m(k_{\rho_3}(d_1 + d_2)) + G_n^{(2)} Y_m(k_{\rho_3}(d_1 + d_2))] \begin{pmatrix} T_{m,n} \\ S_{m,n} \end{pmatrix} \end{aligned} \quad (3.68)$$

In order to enforce the boundary condition of vanishing electric field at $\rho=a$, the fields in region-III must be expressed in terms of global coordinates using the addition theorem of Bessel functions given by

$$B_n(k_\rho \rho_1) \begin{Bmatrix} \cos n\phi_1 \\ \sin n\phi_1 \end{Bmatrix} = \sum_{m=-\infty}^{\infty} B_{n+m}(k_\rho \rho) J_m(k_\rho d) \begin{Bmatrix} \cos(m+n)\phi \\ \sin(m+n)\phi \end{Bmatrix} \quad (3.69)$$

Equation (3.69) can be written as follows

$$B_n(k_\rho \rho_1) \begin{Bmatrix} \cos n\phi_1 \\ \sin n\phi_1 \end{Bmatrix} = \sum_{m=0}^{\infty} \frac{\varepsilon_m}{2} B_m(k_\rho \rho) \begin{Bmatrix} [J_{m-n}(k_\rho d) + (-1)^n J_{m+n}(k_\rho d)] \cos(m)\phi \\ [J_{m-n}(k_\rho d) - (-1)^n J_{m+n}(k_\rho d)] \sin(m)\phi \end{Bmatrix} \quad (3.70)$$

Applying equation (3.70) on equations (3.21 and 3.29) gives:

$$E_z^{(III)} = \frac{k_{\rho 3}^2}{j\omega\varepsilon_3} \sum_{n=0}^{\infty} \sum_{m=0}^{\infty} \frac{\varepsilon_m}{2} [F_n^{(1)} J_m(k_{\rho 3} \rho) + F_n^{(2)} Y_m(k_{\rho 3} \rho)] \begin{Bmatrix} R_{m,n} \cos m\phi \\ R'_{m,n} \sin m\phi \end{Bmatrix} e^{-jk_z z} \quad (3.71)$$

$$E_\phi^{(III)} = \left\{ \begin{array}{l} \frac{-nk_z}{\omega\varepsilon_3 \rho} \sum_{n=0}^{\infty} \sum_{m=0}^{\infty} \frac{\varepsilon_m}{2} [F_n^{(1)} J_m(k_{\rho 3} \rho) + F_n^{(2)} Y_m(k_{\rho 3} \rho)] \begin{Bmatrix} -R_{m,n} \sin m\phi \\ R'_{m,n} \cos m\phi \end{Bmatrix} \\ + k_{\rho 3} \sum_{n=0}^{\infty} \sum_{m=0}^{\infty} \frac{\varepsilon_m}{2} [G_n^{(1)} J'_m(k_{\rho 3} \rho) + G_n^{(2)} Y'_m(k_{\rho 3} \rho)] \begin{Bmatrix} R'_{m,n} \sin m\phi \\ R_{m,n} \cos m\phi \end{Bmatrix} \end{array} \right\} e^{-jk_z z} \quad (3.72)$$

$$R_{m,n} = J_{m-n}(k_{\rho 3} d_1) + (-1)^n J_{m+n}(k_{\rho 3} d_1) \quad (3.73)$$

$$R'_{m,n} = J_{m-n}(k_{\rho 3} d_1) - (-1)^n J_{m+n}(k_{\rho 3} d_1) \quad (3.74)$$

Now, applying the boundary condition of vanishing E_z and E_ϕ components at $\rho=a$,

gives

$$E_z^{(III)} = \sum_{n=0}^{\infty} \frac{\varepsilon_m}{2} [F_n^{(1)} J_m(k_{\rho 3} a) + F_n^{(2)} Y_m(k_{\rho 3} a)] \begin{Bmatrix} R_{m,n} \\ R'_{m,n} \end{Bmatrix} = 0 \quad (3.75)$$

$$E_\phi^{(III)} = \frac{-nk_z}{\omega \varepsilon_3 a} \sum_{n=0}^{\infty} \frac{\varepsilon_m}{2} [F_n^{(1)} J_m(k_{\rho 3} a) + F_n^{(2)} Y_m(k_{\rho 3} a)] \begin{Bmatrix} -R_{m,n} \\ R'_{m,n} \end{Bmatrix} + k_{\rho 3} \sum_{n=0}^{\infty} \frac{\varepsilon_m}{2} [G_n^{(1)} J'_m(k_{\rho 3} a) + G_n^{(2)} Y'_m(k_{\rho 3} a)] \begin{Bmatrix} R'_{m,n} \\ R_{m,n} \end{Bmatrix} = 0 \quad (3.76)$$

Equation (3.76) can be written as follow

$$E_\phi^{(III)} = \sum_{n=0}^{\infty} \frac{\varepsilon_m}{2} [G_n^{(1)} J'_m(k_{\rho 3} a) + G_n^{(2)} Y'_m(k_{\rho 3} a)] \begin{Bmatrix} R'_{m,n} \\ R_{m,n} \end{Bmatrix} = 0 \quad (3.77)$$

Equations (3.39, 3.40, 3.65, 3.66, 3.67, 3.68, 3.75 and 3.77) have non-trivial solution if the determinant of the coefficients $C_n^{(1)}$, $C_n^{(2)}$, $D_n^{(1)}$, $D_n^{(2)}$, $F_n^{(1)}$, $F_n^{(2)}$, $G_n^{(1)}$ and $G_n^{(2)}$ vanishes. The solution of the resulting determinant will give the value of k_z corresponding to the 1st, 2nd ... and nth cutoff Wavenumbers. Once the value of k_z is obtained for the ith cutoff Wavenumbers, the unknown coefficients can be obtained and the field distribution inside the waveguide is then defined completely.

3.5 Algorithm for Obtaining Cutoff Wavenumbers

In order to solve for the fields inside the structure under consideration; it is needed to find the cutoff wavenumber.

The previous equations generated by applying the boundary conditions can be sorted and written in the following way

$$AX = B \quad (3.78)$$

Where A is the matrix of size $8N \times 8N$ that contain the fields coefficients. Since the geometry under consideration that is described by the previous equations, contain an infinite summation. It is observed that this summation can be limited to a few terms, which is enough to replace the infinite summation and at the same time insure the convergence.

Table 3-1 describe the number of terms needed to reach the convergence of the first cutoff wavenumber value for both cases odd hybrid mode and even hybrid mode for a geometrical characteristics of ($a=0.6 \lambda$, $b=0.2 \lambda$, $c=0.1 \lambda$, $d_1=0.3 \lambda$, $d_2=0.1 \lambda$, $\epsilon_{r1}=3.6$, $\epsilon_{r2}=1.0$, $\epsilon_{r3}=1.0$). From the table it is obvious that the convergence reached at the first nine terms for the even hybrid mode case and at the first ten terms of the odd hybrid mode case; so $N=10$ it is chosen for the simulation for both cases and this will make the size of matrix A 80×80 elements. X is a vector of size $8N \times 1$ which means eight set of unknowns and these unknowns are $C_n^{(1)}$, $C_n^{(2)}$, $D_n^{(1)}$, $D_n^{(2)}$, $F_n^{(1)}$, $F_n^{(2)}$, $G_n^{(1)}$ and $G_n^{(2)}$. For the value of B in the above equation, it is zero since the right side of all the boundary condition equations is zero.

Table 3-1: Convergence of Numerical Results for the First Cutoff Wavenumber

N	Kz Even	Running Time	Kz Odd	Running Time
1	0	2.979 s	0.02902	3.910 s
2	2.41140	5.772 s	4.11120	5.958 s
3	2.52927	9.816 s	3.97531	11.299 s
4	2.52217	15.638 s	3.99531	17.349 s
5	2.52233	21.718 s	3.99622	24.632 s
6	2.52224	29.839 s	3.99680	34.943 s
7	2.52226	36.789 s	3.99698	44.590 s
8	2.52227	45.719 s	3.99703	55.329 s
9	2.52228	55.501 s	3.99704	65.770 s
10	2.52228	65.178 s	3.99705	80.257 s
11	2.52228	74.504 s	3.99705	90.312 s

$$A = \begin{bmatrix} [a_{11}]_{N*N} & \cdot & \cdot & [a_{18}]_{N*N} \\ \cdot & \cdot & & \cdot \\ \cdot & & \cdot & \cdot \\ [a_{81}]_{N*N} & \cdot & \cdot & [a_{88}]_{N*N} \end{bmatrix}_{8N*8N} = 0 \quad (3.79)$$

Matrix A has only one unknown that is the cutoff wavenumber k_z and in order to find it and in the same time insuring a non-trivial solution; the determinant of matrix A should equal to zero. The procedure followed in finding the cutoff wavenumbers is as follow. First, an initial value is given for k_z i.e. $k_z=0$ and then evaluating the determinant of A then repeat the process by taking another value of k_z and notice that until $k_z=2\pi$; the

value of the determinant will be a real value and after that the determinant of A will be a complex value. To locate the cutoff wave number the vector that contains the values of the determinant corresponding to every value of k_z should be examined for any sign change. Once the sign change its location then another sub routine to exactly determined the value of the cutoff wavenumber to five decimal digits. Then go to the second sign change etc. If the value of the determinant is complex then the real part only is investigated; because the zero is determined by the sign change in the real part of the determinant and not the imaginary part, since the sign change in it will cross the imaginary axis and not the real one which means that the magnitude of the determinant at that point will not be zero.

After the value of the cutoff wavenumber is determined and matrix A is completely defined; then the system given in Equation 3.78 can be solved for the unknown X.

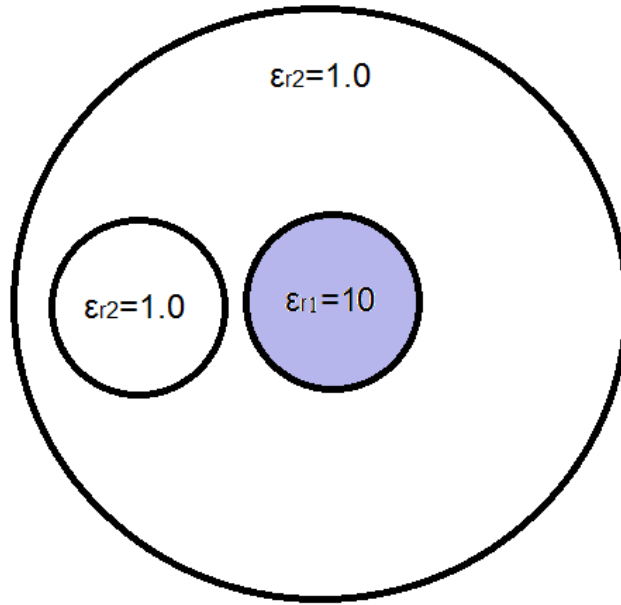
3.6 Results and Discussion

Five types of results are presented in this section. First, verification of the algorithm derived previously with the one concentric loading cylinder available in the literature, which is a relation between the cutoff wavenumber and the geometry at a certain frequency. Second, some examples of the cutoff wavenumbers for different geometrical parameters for the case of one eccentric dielectric cylinder loaded to a circular waveguide. Third, a general case in which the cutoff wavenumbers for a waveguide loaded with two dielectric cylinders are tabulated for different geometrical parameters. The fourth part introduced a modification to the expression involved in finding the cutoff wavenumber to be related to the operating frequency rather than the geometry. These solutions are used to validate the

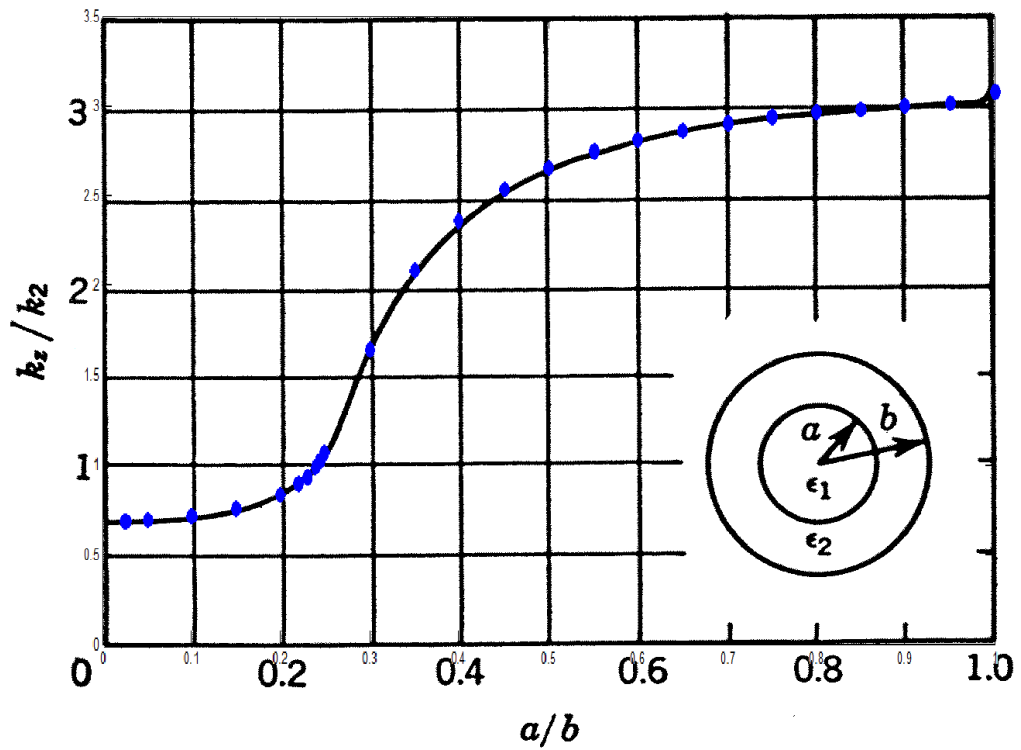
excitation of the software model of the related geometry. The last part present the simulation results from the validated software model for the cases that is either too difficult or cannot be solved analytically.

3.6.1 Verification of the Code

In order to check the accuracy of the analytical formulations for the dielectric (oil) loaded waveguide, the results are compared with two cases available in the literature. First the verification uses the findings of the concentrically loaded circular waveguide in [11]. In order to configure our geometry to match the concentric case, one of the dielectric cylinders has been positioned at the center of the circular waveguide while the other cylinder was filled with the same material of the waveguide, as sketched in Figure 3-5(a). The calculated phase constant (k_z) normalized to the propagation constant of the outer cylinder (k_2) is plotted with respect to the radius of the inner dielectric concentric cylinder for a fixed waveguide radius of $b=0.4 \lambda_2$ and $\epsilon_{r1}=10$, $\epsilon_{r2}=1$, as shown in Figure 3-5(b). The continuous line represent the literature while the dotted points generated from our code, which shows a perfect match in the results.



(a)



(b)

Figure 3-5: Normalized Phase Constant for Different Dielectric Loading Cylinder Radii

The second verification uses the results of reference [12] for a circular waveguide, eccentrically loaded with one dielectric cylinder. The value of k_z is calculated for different values of dielectric cylinder radii and different eccentricity. The geometry of our code has been modified according to what is shown in Figure 3-6, so by filling one of the cylinders with the material of the waveguide; it is considered as a one dielectric cylinder loading. Table 3-2 shows the cutoff phase constants of eccentrically loaded circular waveguide for various geometrical parameters, where (a, b and c) represent the radii of the circular waveguide and the two loaded cylinders respectively, (d_1 and d_2) represent the eccentricity of the two loaded cylinders from the origin of the global coordinates. The characteristics of the materials for this table are: $\epsilon_{r1}=3.6$, $\epsilon_{r2}=\epsilon_{r3}=1$ as described in A in Figure 3-6. Table 3-3 shows the cutoff phase constants of two eccentrically loaded circular waveguide for various geometrical parameters, $\epsilon_{r1}=1.0$, $\epsilon_{r2}=\epsilon_{r3}=3.6$ as representing by B in Figure 3-6. The cutoff wavenumbers in the bold format represents the new modes discovered for such a geometry, where it was not found for the code written for the one eccentric loaded cylinder and this is proofs the resolution of our code compared to the literature.

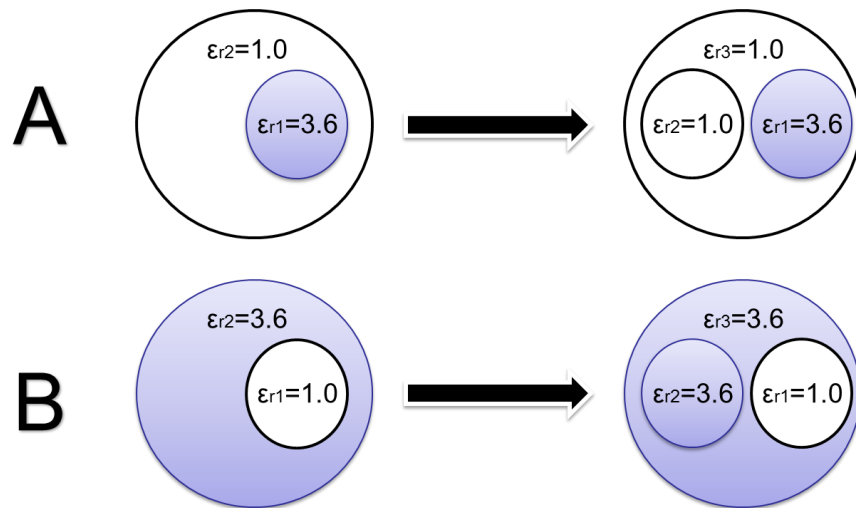


Figure 3-6: Modification to our Geometry to be an Equivalent Representation to One Cylinder Loading

Table 3-2: Cutoff Phase Constants of Eccentrically Loaded Circular Waveguide for Various Geometrical

Parameters, $\epsilon_{r1}=3.6$, $\epsilon_{r2}=\epsilon_{r3}=1.0$, $c=0.1 \lambda$ and $d_2=0.1 \lambda$

Parameters	K_z for Even Modes	Ragheb [12]	K_z for Odd Modes	Ragheb [12]
a=0.4 λ b=0.2 λ d1=0.1 λ	7.88283 7.65216	--- 7.65215	9.55673 7.85866 6.28244 5.67614	--- 7.85864 --- 5.67614
a=0.5 λ b=0.1 λ d1=0.1 λ	7.86626 5.53306 1.71487	--- 5.53306 1.71487	9.53589 6.28318 5.56400 4.86323 1.71695	--- --- 5.56400 4.86323 1.71695
a=0.5 λ b=0.25 λ d1=0.25 λ	8.73332 7.89547 6.51968 6.28318 5.02973 4.23373 2.91516	8.72719 --- --- --- 4.99398 4.20584 2.91066	9.74670 9.57228 6.32390 6.05857 4.39828 3.64735	9.72329 --- 6.32714 --- 4.34611 3.64868
a=0.4 λ b=0.3 λ d1=0.1 λ	9.71399 7.92129 6.75400 6.28318 6.02938 5.45116 3.83582	9.71125 --- --- --- 5.99272 5.43116 3.82775	10.20149 9.61720 7.53617 5.84622 3.79449	10.19060 --- 7.53065 5.78959 3.78590
a=0.6 λ b=0.2 λ d1=0.3 λ	7.88283 7.63256 4.72535 3.96839 2.52228	--- 7.63247 4.72539 3.96783 2.52241	8.05041 6.27944 5.81567 4.51392 3.99705	8.04762 --- 5.81567 4.51449 3.99511
a=0.6 λ b=0.5 λ d1=0.1 λ	11.07897 9.83641 9.72090 8.21116 8.09686 7.61821 6.91871 6.76650 6.28318 5.85652 3.89814 1.78024	11.07890 9.83541 9.71989 8.20779 --- 7.60648 --- --- --- --- --- ---	11.21953 10.18996 9.59565 8.31401 7.62994 7.24687 5.86445 5.78746 5.50953 3.90268 1.76785	11.21950 10.18980 9.67719 8.31385 7.62941 --- --- --- --- --- ---
a=0.6 λ b=0.3 λ d1=0.1 λ	9.84688 7.91121 7.51959 5.85324 5.30833 0.13050	9.84688 --- 7.51959 5.85324 5.30833 1.30543	9.85776 9.59120 6.99126 6.28309 5.85446 5.33106 0.36911	9.85776 --- 6.99126 --- 5.85446 5.33106 3.69184

Table 3-3: Cutoff Phase Constants of Eccentrically Loaded Circular Waveguide for Various Geometrical

Parameters, $\epsilon_{r1}=1.0$, $\epsilon_{r2}=\epsilon_{r3}=3.6$, $c=0.1 \lambda$ and $d_2=0.1 \lambda$

Parameters	K_z for even modes	Ragheb	K_z for odd modes	Ragheb
a=0.4 λ b=0.2 λ d1=0.1 λ	9.67465	9.67465		
	7.88562	---		
	7.71369	7.71369	8.76502	8.76502
	6.24732	6.28319	7.02305	7.02306
	5.56729	5.56729	6.24815	6.28319
	3.70285	3.70285	3.29720	3.29720
	1.10602	---	2.47475	---
a=0.5 λ b=0.1 λ d1=0.1 λ	11.06333	11.0633	11.06149	11.0615
	10.14808	10.1481	10.74860	10.7486
	9.08352	9.08352	10.1300	10.1299
	8.59944	8.59944	9.53590	---
	8.40708	8.40708	8.76263	8.76263
	7.86692	---	8.42120	8.42120
	5.91542	---	5.89887	---
	5.37234	---	5.37263	---
	4.42961	---	3.88760	---
			2.60970	---
a=0.5 λ b=0.25 λ d1=0.25 λ	10.83814	10.83881	10.90504	10.9050
	9.50857	9.50848	10.23675	10.2367
	8.79523	8.79521	9.57258	---
	7.90003	---	8.67393	8.67388
	7.34011	7.33952	7.56225	7.56224
	6.16453	---	6.34011	6.28319
	3.91598	---	6.00933	---
	2.49196	---	2.98744	---
		1.86793	---	
a=0.4 λ b=0.3 λ d1=0.1 λ	11.52435	---		
	8.20208	8.283 19	9.59922	---
	7.90976	---	8.21523	8.21523
	7.83077	7.83078	6.19387	6.28319
	6.29103	6.28319	4.06773	4.06773
4.72683	4.72682			
a=0.6 λ b=0.5 λ d1=0.1 λ	8.34424	8.34424	8.93669	8.93669
	7.94791	---	7.48205	7.48208
	6.64174	6.64174	6.30446	6.28319
	6.26141	6.28319	5.82425	5.82425
	5.16503	5.16503	4.88411	4.88411
	4.75667	4.75667	4.00887	---
a=0.6 λ b=0.3 λ d1=0.1 λ	10.69665	10.6967	10.86864	10.8686
	10.01160	10.0116	10.37987	10.3799
	9.29181	9.29181	9.72070	9.72070
	9.04351	9.04351	9.59180	---
	7.91809	---	8.98442	8.98442
	7.79675	7.79675	8.55893	8.55893
	7.51143	---	7.50705	---
	6.59679	---	6.76139	---
	4.82163	---	4.82139	---
	3.84946	---	3.81566	---
3.63660	---	3.58350	---	

3.6.2 Cutoff Wavenumbers of Two Dielectric Loaded Circular Waveguide

After the code had been verified, now the cutoff wavenumber for more general cases can be evaluated. Figure 3-7 shows an example of a circular waveguide (resembling a petroleum carrying pipeline) loaded with two dielectric cylinders with $\epsilon_r=2.15$ (similar to crude oil). The results of the cutoff wavenumber for this structure for different radii of the dielectric cylinders and the waveguide and for different eccentricity have been calculated and tabulated in Table 3-4, where the even and odd cutoff wavenumbers are calculated according to the previous algorithm. These tabulated cutoff wavenumbers represents the modes that can propagate in the structure shown in Figure 3-7 with the parameters given in the Table 3-4. The parameters given in the table it similar to ones described in Figure 3-3.

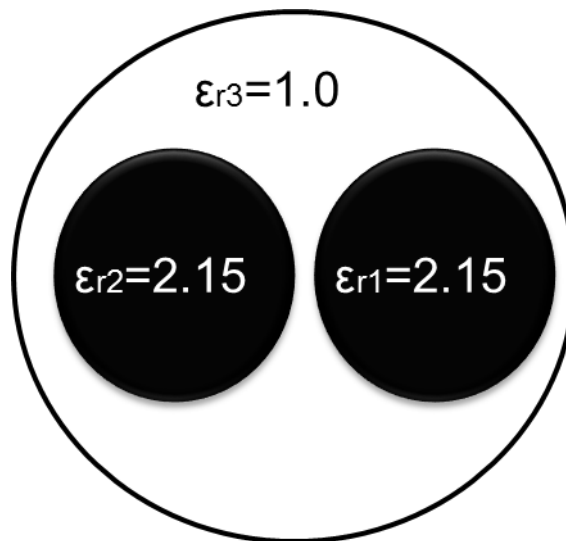


Figure 3-7: Schematic Diagram for a General Case

Table 3-4: Cutoff Phase Constants of Two Cylinders Eccentrically Loaded Circular Waveguide for Various Geometrical Parameters, $\epsilon_{r1}=2.15$, $\epsilon_{r2}=2.15$, $\epsilon_{r3}=1.0$

Parameters	K_z for Even Modes	K_z for Odd Modes
a=0.50 λ	---	7.88698
b=0.10 λ	---	6.28318
c=0.10 λ	7.34254	5.35209
d ₁ =0.10 λ	5.33528	4.44753
d ₂ =0.10 λ	1.62922	1.63212
a=0.50 λ	---	7.88698
b=0.10 λ	---	6.28318
c=0.10 λ	7.34254	5.34106
d ₁ =0.20 λ	5.27728	4.38069
d ₂ =0.20 λ	1.79629	1.83878
a=0.60 λ	---	6.28318
b=0.10 λ	7.34254	5.65617
c=0.10 λ	5.62455	5.00665
d ₁ =0.20 λ	3.76931	3.77480
d ₂ =0.20 λ	0.25929	1.59460
a=0.60 λ	6.30099	7.02976
b=0.25 λ	6.28318	6.26537
c=0.20 λ	4.43664	5.52063
d ₁ =0.30 λ	3.15239	4.34293
d ₂ =0.40 λ	2.08326	3.40394

3.6.3 Modified Expression

The Previously calculated cutoff wavenumbers are waveguide geometry dependent. Since petroleum-carrying pipelines have a few preset dimensions and the requirement are to observe the frequency dependency of the cutoff wavenumbers, the derived expressions is modified in this section. This allowed us to observe the cutoff charts for a fixed geometry with respect to a desired microwave frequency sweep.

In order to do this, the code should not be normalized with respect to frequency. An example of this is shown in Figure 3-8; this figure represents the mode chart for a circular waveguide concentrically loaded with an oil cylinder. The cutoff wavenumbers have been calculated at certain frequency values for the first few number of modes, which is noticed from the discrete plot.

The cutoff frequencies for any propagating mode can be easily found from the cutoff wavenumber of that mode using [66]

$$\frac{f_m}{f_c} = \sqrt{1 - \left(\frac{k_z}{k_{1,2,3}} \right)^2}, k_z < k_{1,2,3} \quad (3.80)$$

Where;

f_m is the cutoff frequency for a certain mode

f_c is the operating frequency

k_z is the cutoff wavenumber

k_1, k_2, k_3 is the propagation constant in region 1, 2 and 3 respectively.

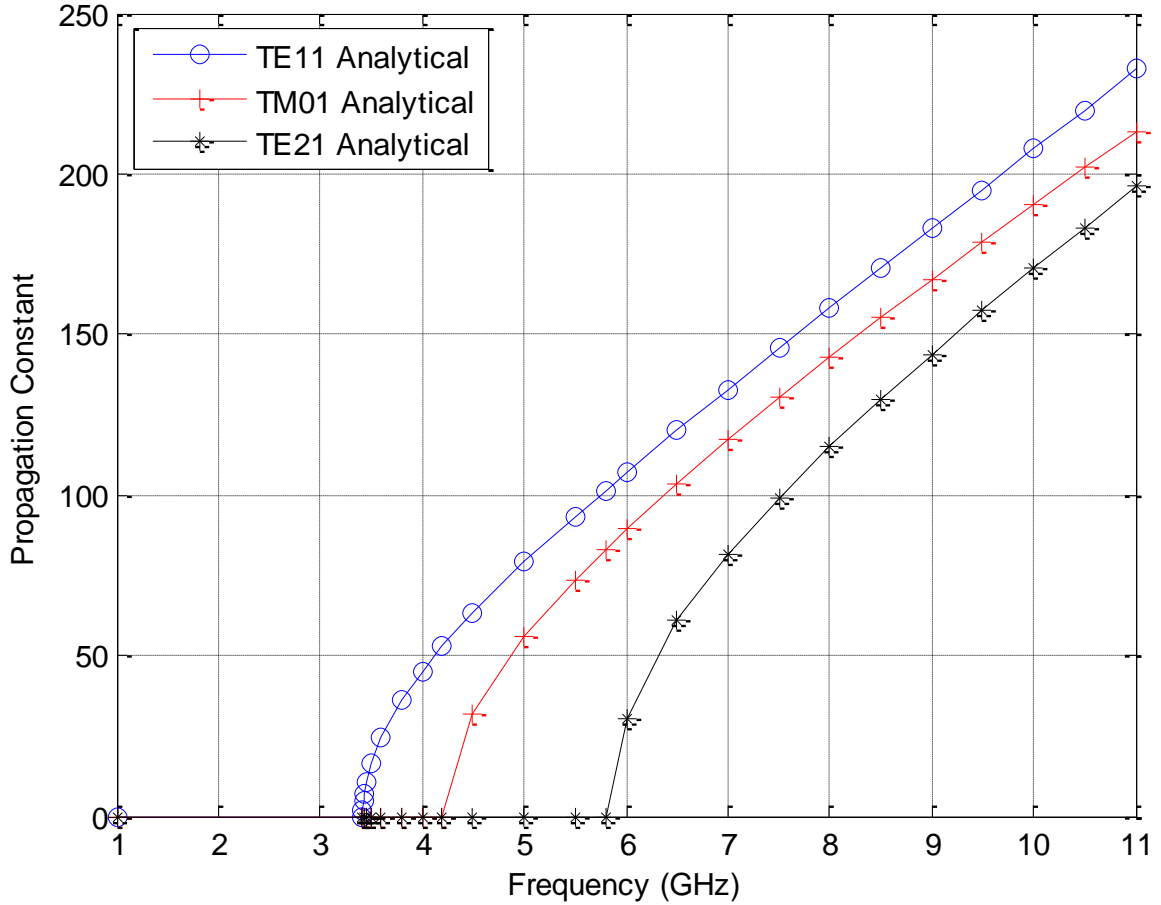


Figure 3-8: Mode Chart for Circular Waveguide Partially Filled with Concentric Oil Cylinder

3.6.4 Optimizing Simulated Model

To solve the waveguide with a more complicated air-dielectric mixtures; a commercial finite element method based simulation software called High Frequency Structure Simulator (HFSS) is used. However, proper excitation and modelling of the dielectric loaded waveguide is critical to get accurate results. So the analytically calculated cutoff wavenumbers of the two dielectric cylinder loaded circular waveguide is compared with the simulated cutoff wavenumbers of the same geometry to verify/tune the simulated

model. Once verified, the software model is used to observe the resonance behavior of more complicated mixtures within the petroleum-carrying pipeline.

3.6.4.1 Excitation Method

The validated excitation method for this structure is shown in Figure 3-9, where the cross section of the circular waveguide along with the cross sections of the two dielectric cylinders should all be selected and assigned as one port. By exciting the structure with this method, the cutoff wavenumbers and other properties will differ for any change in the eccentricity. In addition to excitation, proper meshing is also selected to match the simulated cutoff wavenumbers with the calculated values.

3.6.4.2 Solution Method

After the structure is properly excited, the solution type should be tuned to match the theoretical calculation. Since the HFSS is based on finite element method and this method is based on dividing the structure into a mesh grid, the smaller the mesh size the more exact you can get but of course more processing time. The mesh size was tuned according to its Maximum Normal Deviation and it is found that using a normal deviation of 7.5 degree will give an excellent approximation to the calculated value with percentage of error between 0.1 % - 0.28 % for the first three modes and with suitable processing time as detailed in Table 3-5. A comparison between calculated and simulated results are tabulated in Table 3-6 for the first five modes.

Table 3-5: Maximum Mesh Tuning for HFSS

Maximum Normal Deviation (Degree)	f_c (GHz) TE ₁₁	f_c (GHz) TM ₀₁	f_c (GHz) TE ₂₁
22.5	3.54	4.64	5.88
15	3.52	4.6	5.84
10	3.52	4.6	5.84
7.5	3.52	4.58	5.82
5	3.52	4.58	5.82
Calculated	3.516432975	4.593020672	5.832710354

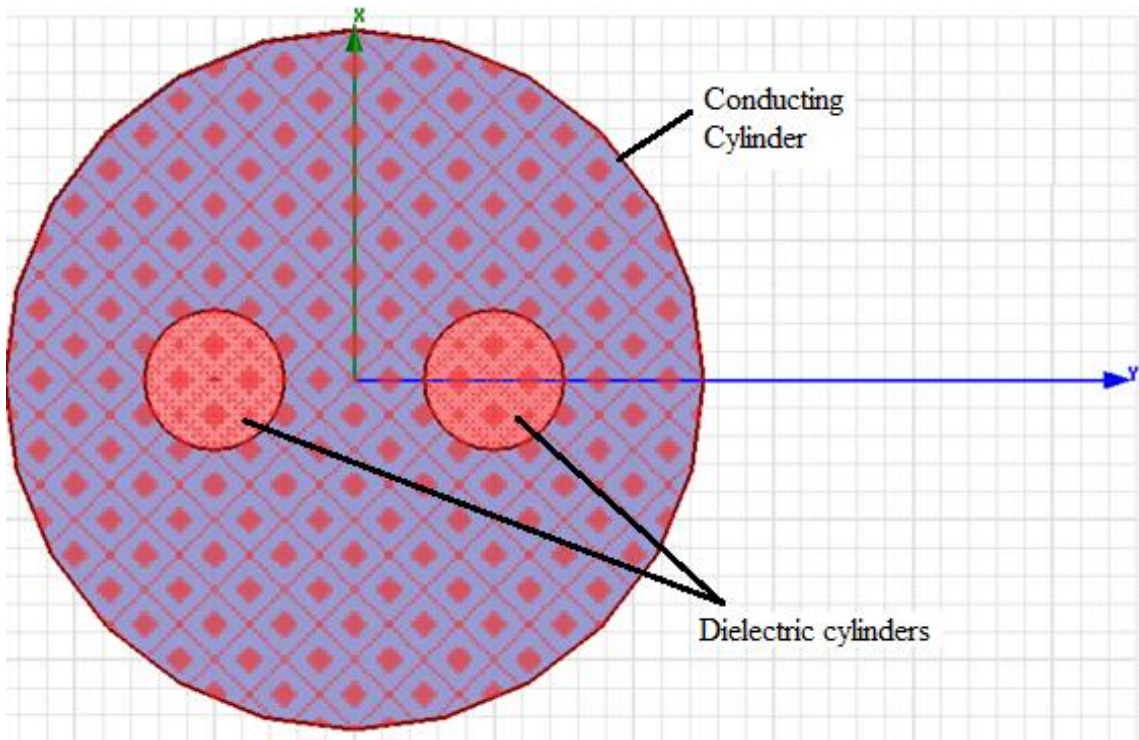


Figure 3-9: Proper Excitation of the Structure

Table 3-6: Calculated and Simulated Cutoff Frequency for the First Five Modes

Mode	Analytical f_c (GHz)	Simulation f_c (GHz)
TE ₁₁	1.7582	1.7675
TM ₀₁	2.2957	2.3525
TE ₂₁	2.9165	2.9375
TM ₁₁	3.6591	3.7175
TE ₀₁	3.6591	3.7175

At this point, as the analytical code has been validated by the results available in the literature and the software model in turn has been verified by the analytical results, the pipeline with complex mixtures can be simulated for the required frequency range. From now on, the cylindrical waveguide geometry is fixed to $a=25\text{mm}$, the reason for this specific radius because it is the radius of the pipeline sample used in the experimental process as will explain more in the next chapters.

The simulated model of the concentrically loaded waveguide is shown in Figure 3-10. Initially the air filled ($\epsilon_r=1$) waveguide radius is selected to be $a=25\text{mm}$. The radius of the concentric dielectric cylinder representing crude oil ($\epsilon_r=2.15$) is selected to be 5mm . The simulated cutoff frequencies are observed at the edges of the circular waveguide, where the port is defined and excited as described before. Figure 3-11 shows the mode chart of both analytical and simulated data for the first three modes TE_{11} , TM_{01} and TE_{21} . For one eccentric loaded cylinder model shown in Figure 3-12, the simulated and the analytically found cutoff wavenumbers are plotted in Figure 3-13. The simulated model for a circular waveguide loaded with two eccentric dielectric cylinders (crude oil) is shown in Figure 3-12 and its mode chart is plotted in Figure 3-13.

The mode chart shown in Figure 3-15 is validated with the cutoff wavenumbers generated from the analytical solution for the model shown in Figure 3-14. In order to have a clear view for the verifications, it splits into two plots; the odd hybrid modes are shown

in Figure 3-16 and for the even hybrid modes it is verified in Figure 3-17. From these figures, it is noticed that an excellent agreement between the results are achieved.

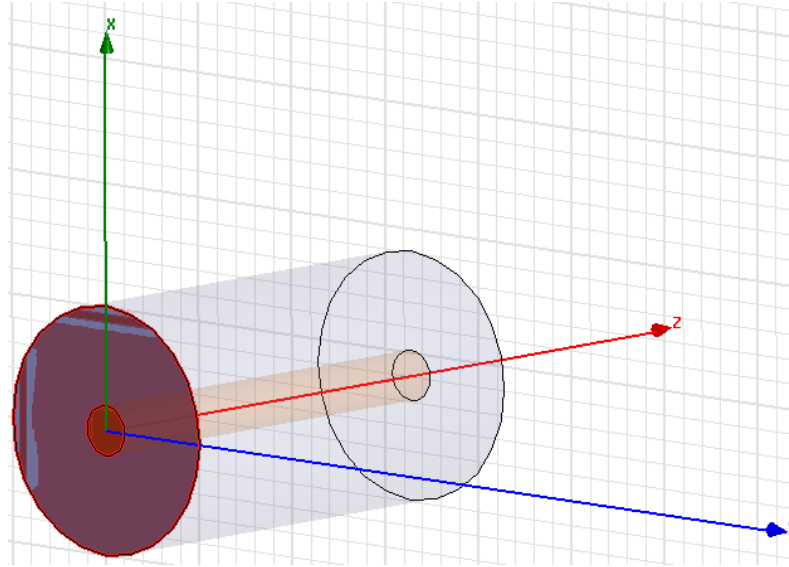


Figure 3-10: Simulated Model for One Cylinder Symmetrically Loaded to a Circular Waveguide

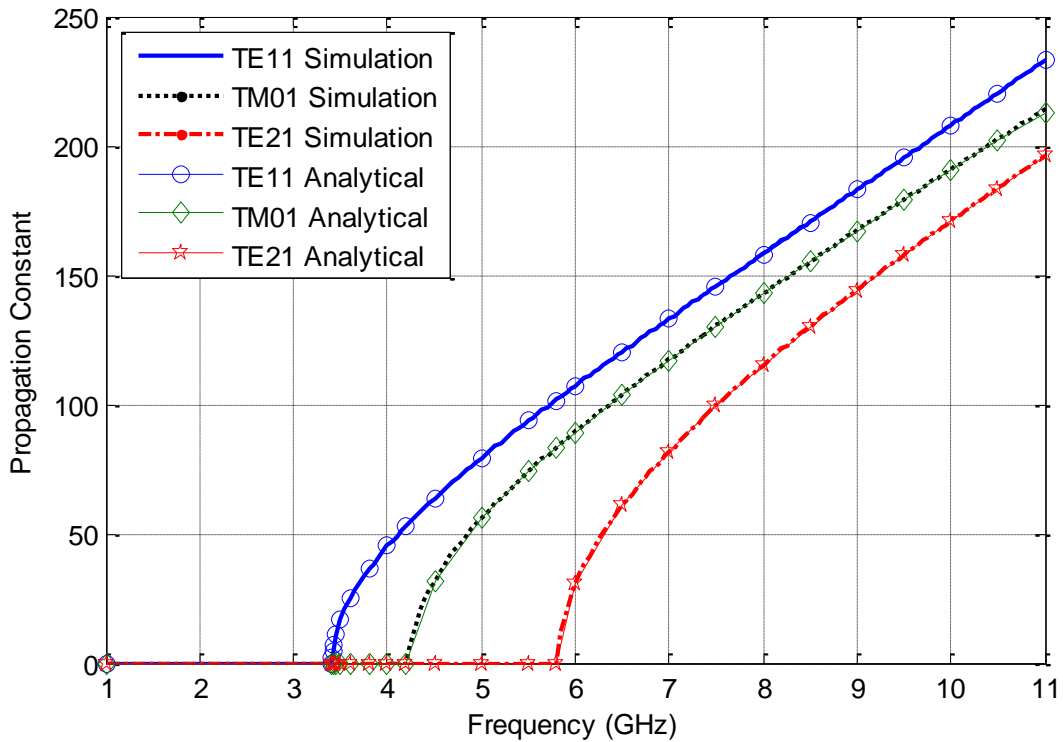


Figure 3-11: Mode Chart for a Circular Waveguide Filled with a Concentric Oil Cylinder

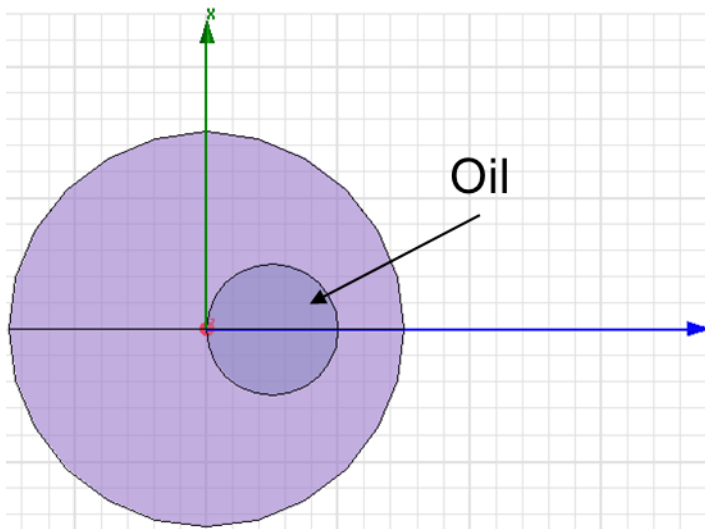


Figure 3-12: Simulated Model for One Oil Filled Cylinder Eccentrically Loaded to a Circular Waveguide

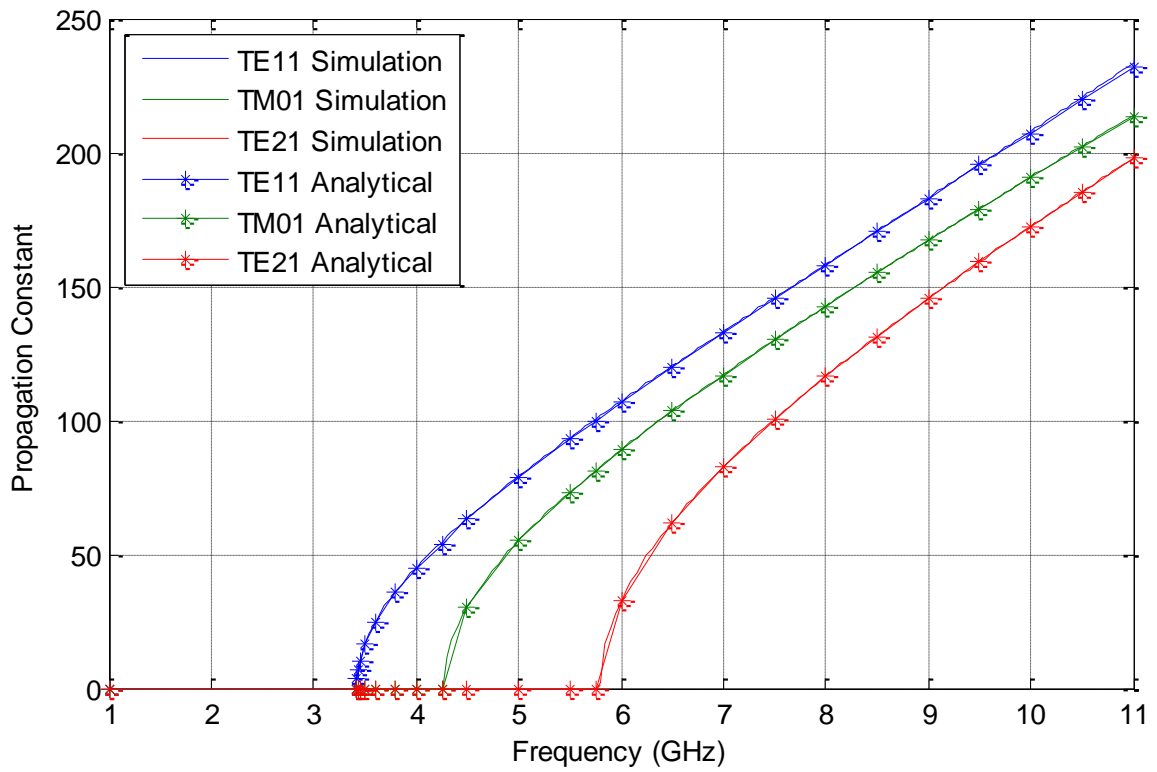


Figure 3-13: Mode Chart for a Circular Waveguide Filled with an Eccentric Oil Cylinder

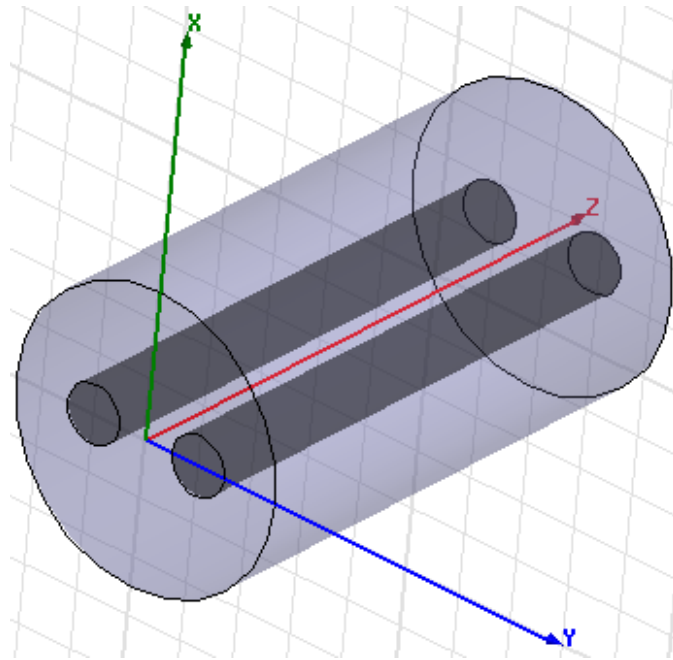


Figure 3-14: Simulated Model for a Circular Waveguide Loaded with Two Dielectric Oil Cylinders

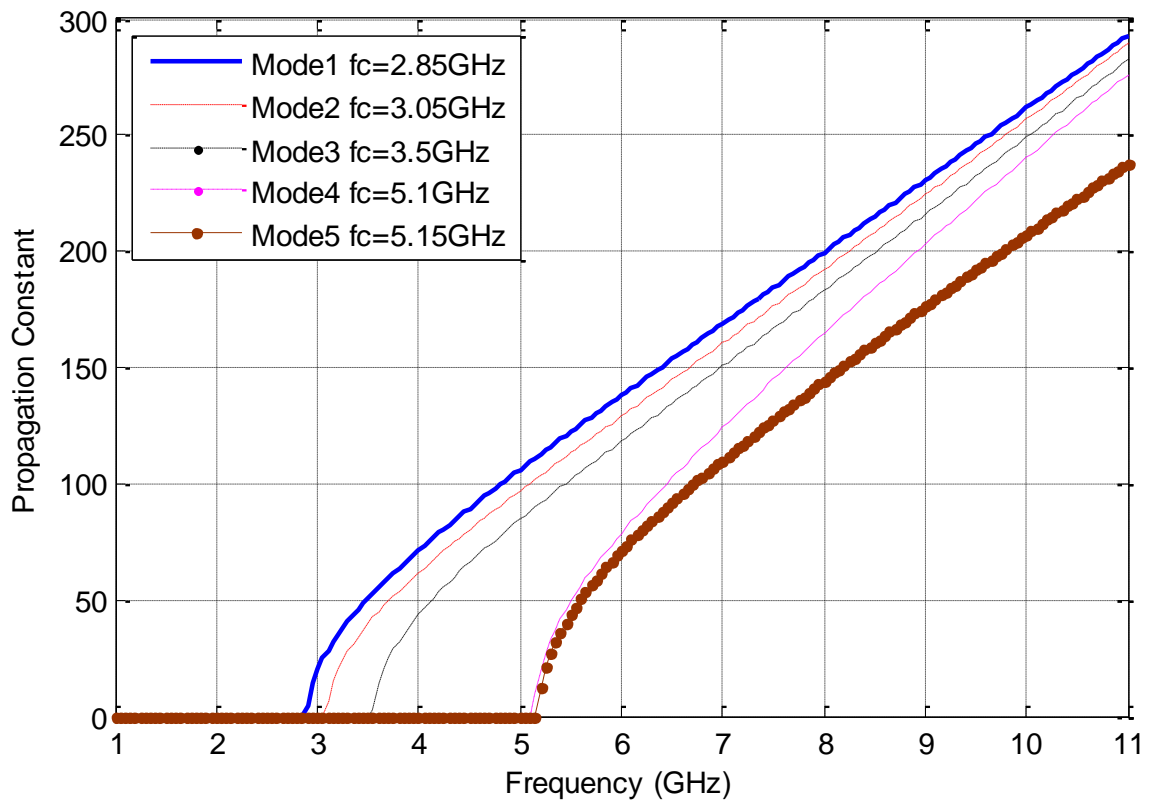


Figure 3-15: Mode Chart for a Circular Waveguide Loaded with Two Oil Cylinders

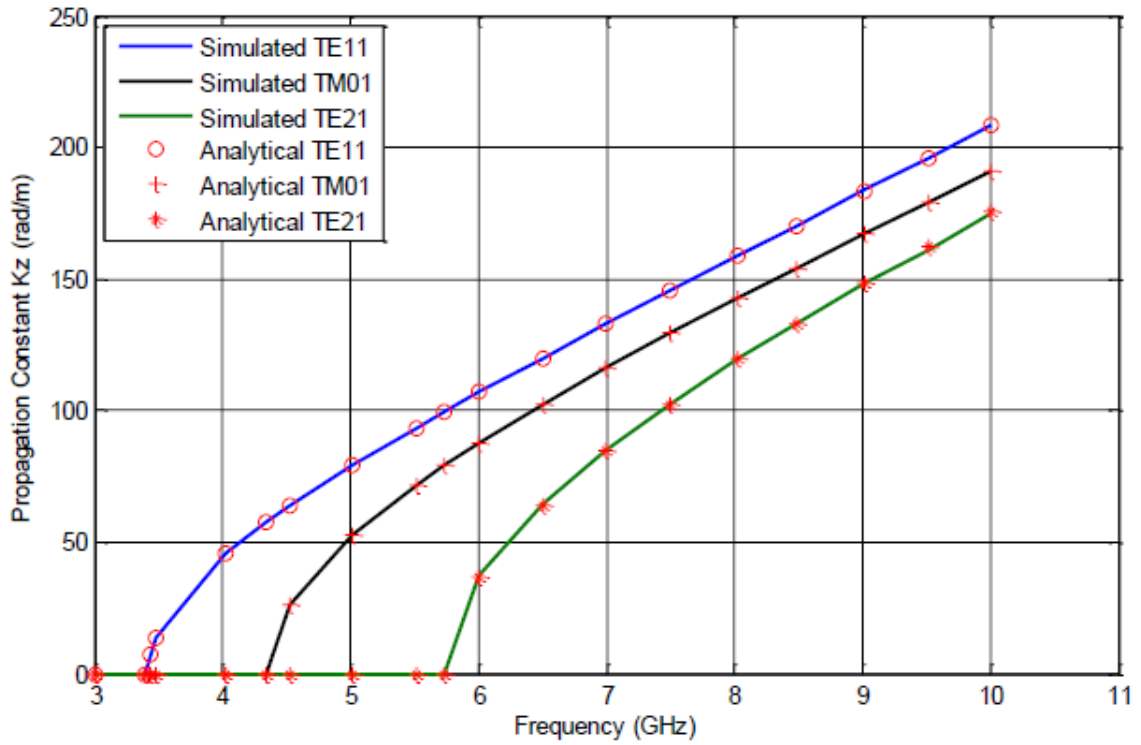


Figure 3-16: Analytically and Simulated Mode Chart for Odd Hybrid Modes

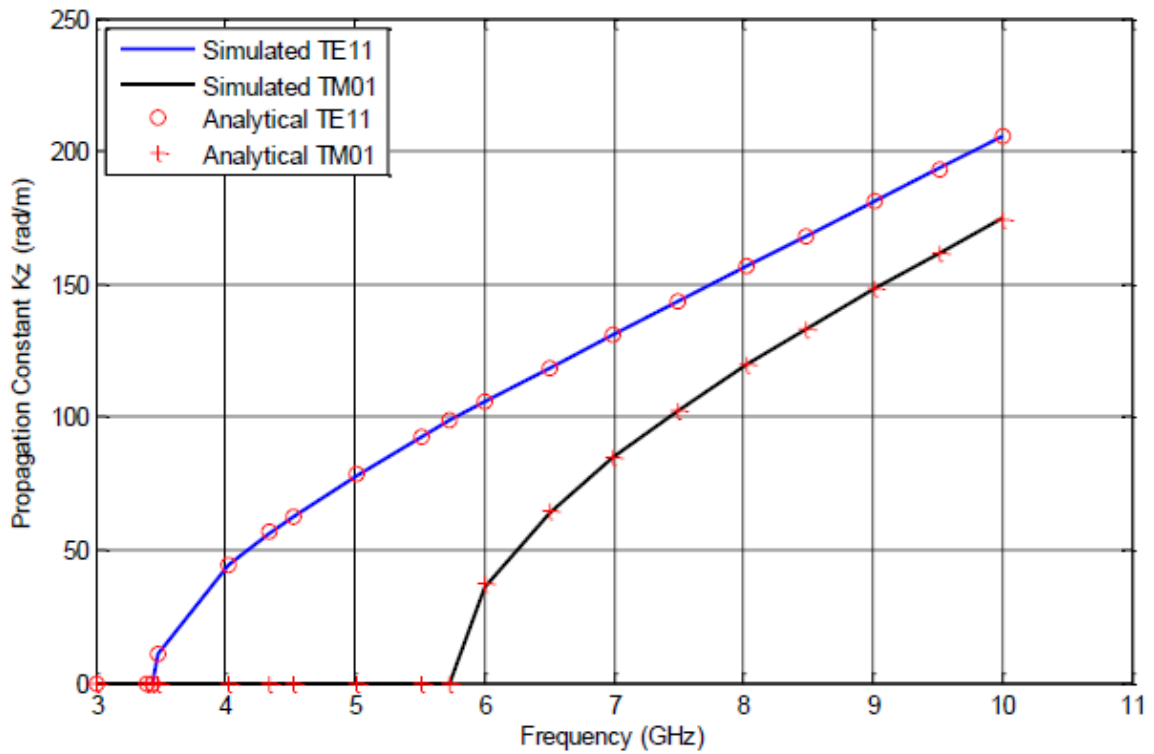


Figure 3-17: Analytically and Simulated Mode Chart for Even Hybrid Modes

3.6.5 Simulation of More Complex Models

As increasing the number of the cylinders loaded into the waveguide considerably increases the complexity of analysis, analytical formulation is extremely tedious. So the validated HFSS model is used in this section to obtain the cutoff frequencies of the waveguide (pipeline) arbitrarily loaded with multiple dielectric (oil) cylinders.

Conventional Circular waveguides normally supports TE or TM modes. The dominant/fundamental mode supported by this structure is the TE_{11} mode, which is double degenerate (in sines and cosines). Therefore, the first two modes on HFSS appear to be 90° rotated (mode 1 and mode 2 in Figure 3-15). The next mode is TM_{01} , which is non-degenerate and has a circular symmetry (mode 3 in Figure 3-15). Then, follow, TE_{21} , which is a double degenerate in sines and cosines (mode 4 and mode 5 in Figure 3-15). So the first five modes are processed in the simulated model to represent the first three modes in a conventional circular waveguide.

Once the circular waveguide is eccentrically loaded with another dielectric cylinder, the modes will change from pure TE/TM to hybrid modes. These hybrid modes can be divided into odd or even categories as explained earlier and it can be seen from the shift in the odd double degenerate modes TE_{11} and TE_{21} curves as shown in the mode chart for the two cylinder loaded case of Figure 3-15. This shift it is not noticeable for the concentric loaded case of Figure 3-11.

The mode chart for four different cases of circular waveguide loaded with multiple dielectric cylinders are plotted in Figure 3-18 to Figure 3-21. The cutoff wavenumbers and

dielectric constant at an operating frequency of 10 GHz are summarized in Table 3-7. The purpose is to investigate the cutoff wavenumbers with increased dielectric loading simulating a wavy flow of oil within the pipeline. The resulted cutoff chart is plotted in Figure 3-22. The cutoff frequency of a waveguide modes are inversely proportional to the dielectric constant as given by,

$$f_{c_{mn}}^{TE/TM} = \frac{X_{mn}}{2\pi a \sqrt{\mu\epsilon}} \quad (3.81)$$

Where, X_{mn} represents the n^{th} zero ($n=1, 2, 3, \dots$) of the Bessel function of the first kind of order m ($m=0, 1, 2, \dots$) in case of TE modes or its derivatives in case of TM modes, the relative permeability is usually one for the materials under consideration air, oil and water so Equation 3.81 can be written as

$$f_{c_{mn}}^{TE/TM} = \frac{X_{mn} * c}{2\pi a \sqrt{\epsilon_r}} \quad (3.82)$$

Where, c is the speed of the light in free space and it is equal to $3*10^8$ m/s

As the number of the loaded oil cylinders increased, the effective dielectric constant of the mixture also increased and this will reduce the cutoff frequency for all modes as shown in Figure 3-18 to Figure 3-23. Although the wavy flow of oil within the pipeline is more realistic, for simplicity of analysis a more simplified stratified flow of oil is considered. The resulted mode charts of air-oil mixture within a pipeline metal case is shown in Figure 3-23. Note that the tabulated results in Table 3-8 shows less than 0.3% difference in the simulated cutoff wavenumbers for wavy and stratified flow.

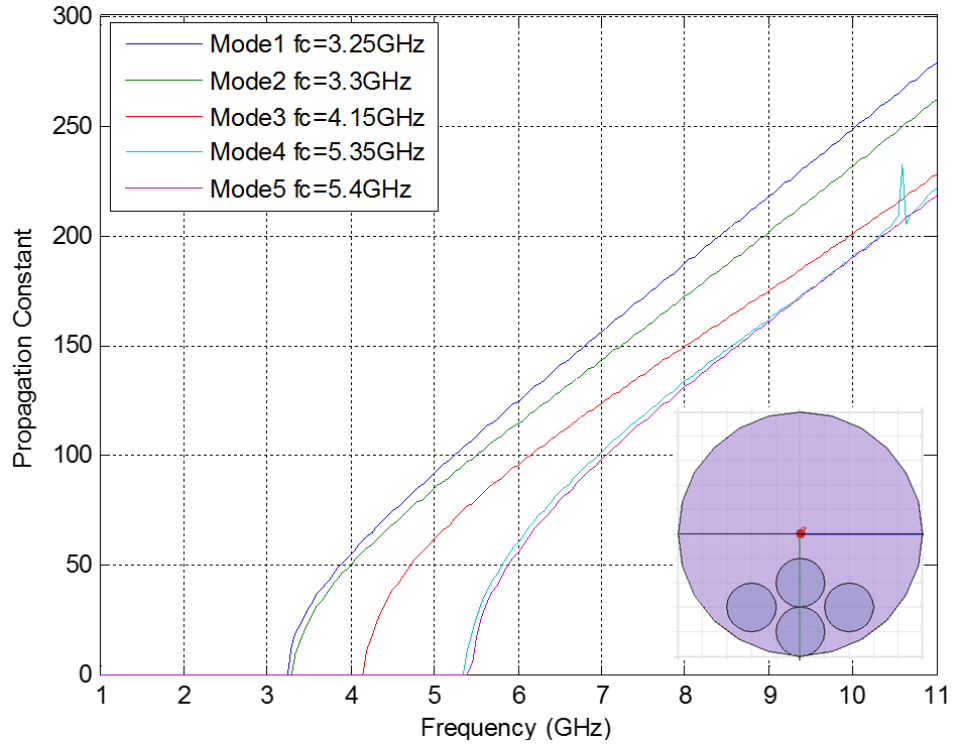


Figure 3-18: Four Oil Cylinders Loading a Circular Waveguide (Case 1)

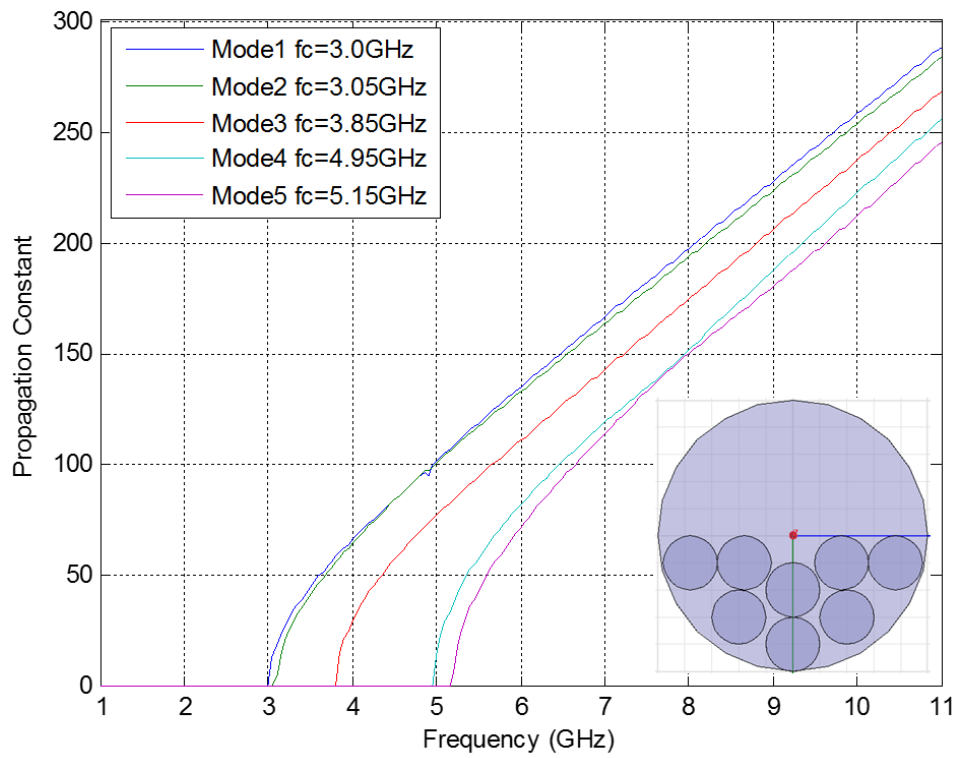


Figure 3-19: Eight Oil Cylinders Loading a Circular Waveguide (Case 2)

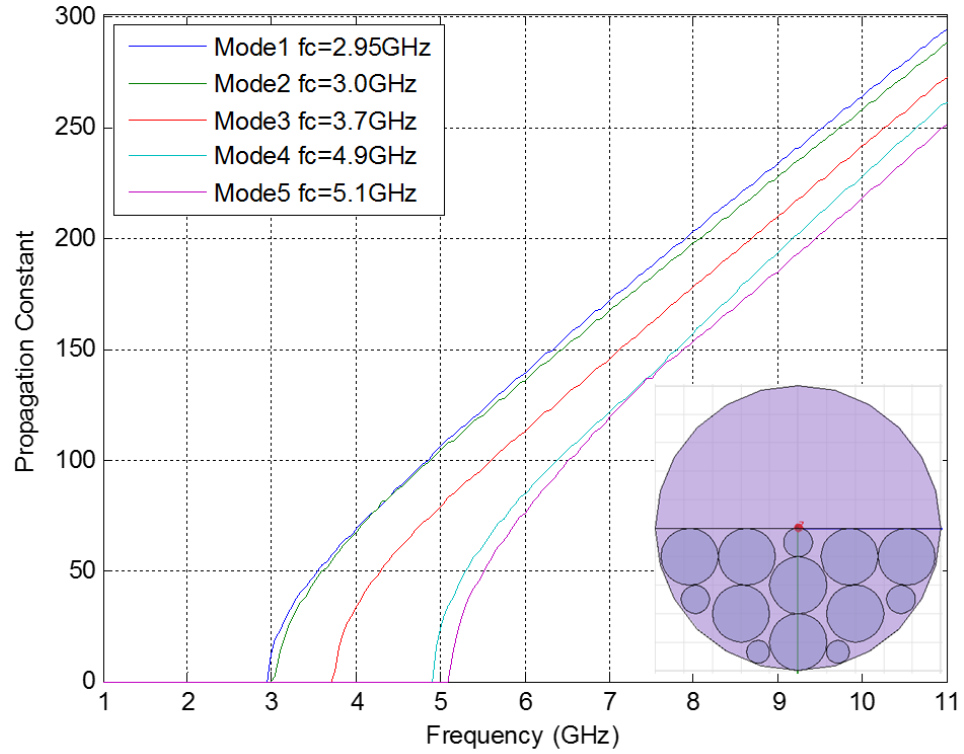


Figure 3-20: Twelve Oil Cylinders Loading a Circular Waveguide with Mixed Radii (Case 3)

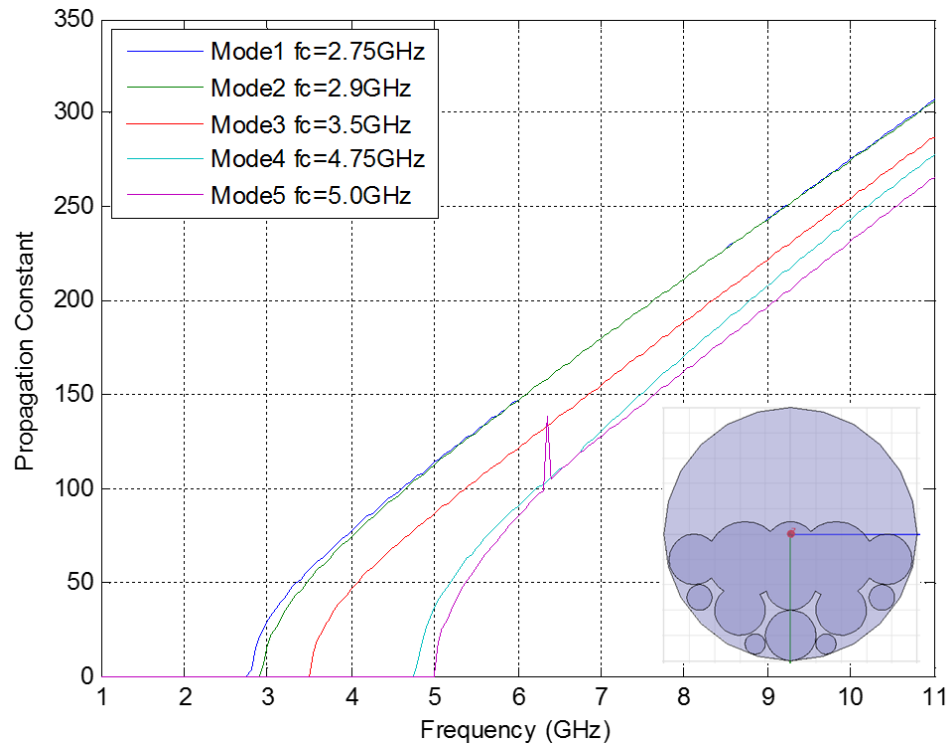


Figure 3-21: Overlapping of the Loaded Dielectric Cylinders (Case 4)

Table 3-7: Summary of the Complicated Simulation Models

Case #	Cutoff Wavenumber	Dielectric Constant
Case 1	248.1513	1.4019
Case 2	258.0564	1.5160
Case 3	263.9892	1.5866
Case 4	275.3913	1.7266

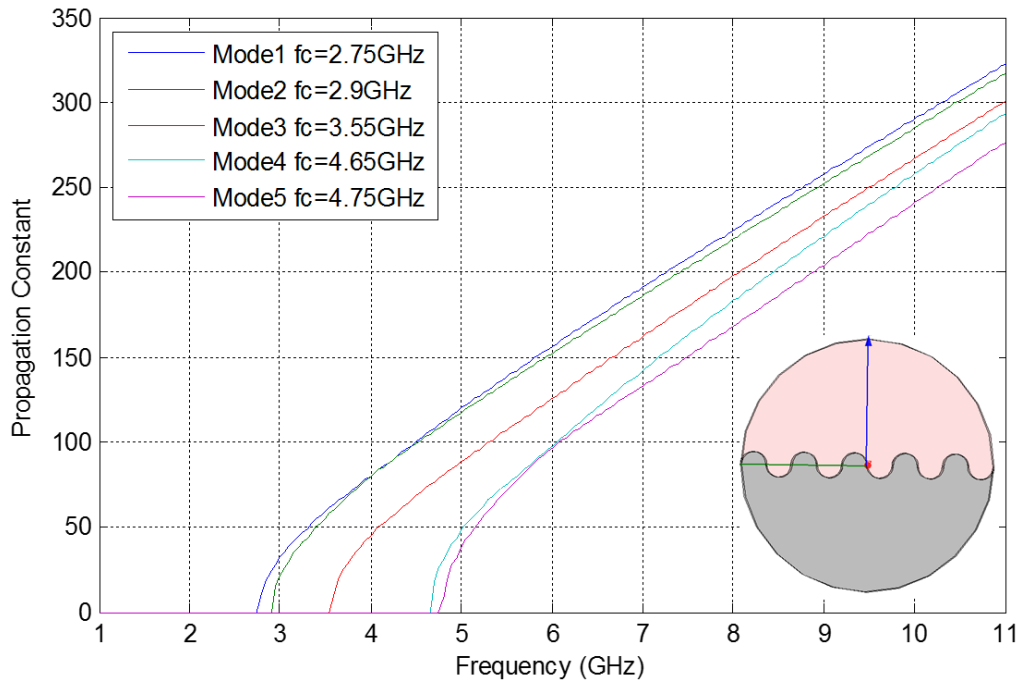


Figure 3-22: Wavy Flow Case

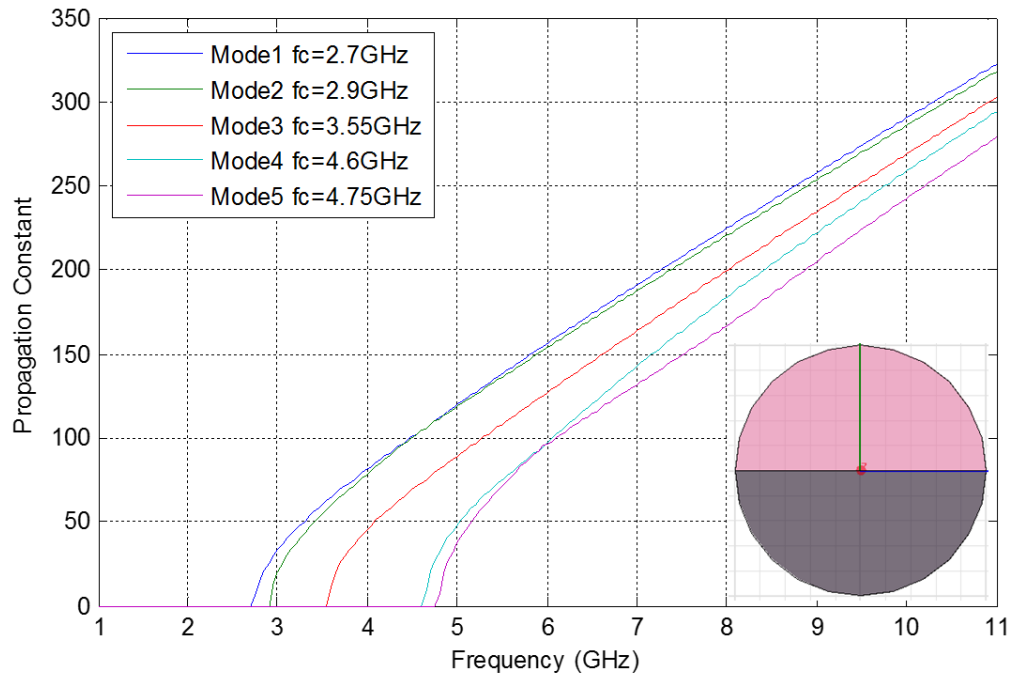


Figure 3-23: Stratified Flow Case

Table 3-8: Comparison between Wavy Flow and Stratified Flow

Case #	Cutoff Wavenumber	Effective Dielectric Constant
Wavy Flow	290.0821	1.9157
Stratified Flow	290.3813	1.9196
Error Percentage	0.07664 %	0.20316 %

When the center of the loaded dielectric cylinder starts to shift from the center of the circular waveguide, the conventional waveguide mode of TE and TM will become hybrid modes that combine both TE and TM, that mean all the electric and magnetic field components will exist in the direction of the propagation. In this case and with the eccentricity increased, it is became difficult to find a single mode of operation. However, the existence of the second mode does not cause any interference as the level of oil increases.

Although the mode chart shown in Figure 3-18 to Figure 3-21, has not to do anything in the determination of the mode charts for different oil portions and not to be analytically verified since it is too much complicated to be solved analytically. It there just to check the consistency of the HFSS results by monitoring the cutoff frequencies in addition the effective dielectric constant of the mixture, which are better than directly converts from tow dielectric loading cylinders to the stratified flow case.

Since the stratified flow and the wavy flow are very close to each other, the stratified flow is considered for different oil-air levels. These levels are tabulated in what is called a fill factor table and it is listed in Table 3-9. This table summarize the first five hybrid modes along with the propagation constant and the effective waveguide wavelength for the first mode at 10 GHz operating frequency for a completely air filled waveguide with 5% increment in oil level until the case of completely oil filled waveguide.

From Table 3-9, it is noticed that the first five modes are changing with this 5% resolution especially the first mode, which is changed from 2.4 GHz for complete oil filled waveguide to 3.5 GHz for complete air filled waveguide. So, in order to select a suitable

frequency to design the microwave sensor, which is the main purpose of this table, a frequency of 3.6 GHz is selected, which insure only the first two hybrid modes will propagate for the case of air filled waveguide. However, later in chapter 4, it is noticed that at this frequency with more oil fluid loaded to the waveguide, the third hybrid mode will interfere with the first mode of other oil-air filling. Therefore, an operating frequency of 3 GHz will be the suitable frequency of operation since the third mode, which starts at 3.1 GHz will be excluded.

Table 3-9: Stratified Flow Results for Different Oil-Air Portions

Percentage of Oil	Cutoff Frequencies (GHz)	Propagation Constant (rad/m) @ (f=10GHz)	λ_{eff} (mm) (f=10GHz)
100 %	2.395, 2.4, 3.1, 3.95, 3.95	298.3304	21.055
95 %	2.4, 2.415, 3.12, 3.96, 4.0	298.2580	21.066
90 %	2.4, 2.445, 3.12, 4, 4.08	297.9766	21.086
85 %	2.41, 2.485, 3.12, 4.04, 4.16	297.4648	21.122
80 %	2.425, 2.53, 3.16, 4.12, 4.2	296.7285	21.175
75 %	2.45, 2.58, 3.16, 4.2, 4.28	295.7668	21.244
70 %	2.48, 2.6, 3.2, 4.32, 4.36	294.8597	21.309
65 %	2.52, 2.68, 3.28, 4.4, 4.4	294.1253	21.362
60 %	2.56, 2.76, 3.32, 4.48, 4.52	293.1839	21.431
55 %	2.64, 2.8, 3.44, 4.52, 4.64	291.9676	21.520
50 %	2.72, 2.88, 3.56, 4.6, 4.76	290.3813	21.638
45 %	2.84, 2.96, 3.68, 4.72, 4.88	288.2912	21.795
40 %	2.92, 3.04, 3.84, 4.84, 4.92	285.4691	22.010
35 %	3.08, 3.12, 4.0, 5.0, 5.0	281.5684	22.315
30 %	3.2, 3.2, 4.2, 5.04, 5.16	275.9802	22.768
25 %	3.28, 3.32, 4.36, 5.16, 5.32	267.5935	23.480
20 %	3.36, 3.4, 4.48, 5.36, 5.48	254.5455	24.684
15 %	3.4, 3.44, 4.56, 5.56, 5.6	234.1554	26.833
10 %	3.44, 3.48, 4.56, 5.68, 5.72	209.5861	29.979
5 %	3.48, 3.48, 4.56, 5.76, 5.8	198.0457	31.726
0 %	3.5, 3.5, 4.56, 5.8, 5.8	196.2470	32.018

3.7 Conclusion

An analytical solution based on the boundary value method is formulated to calculate the cutoff phase constants of a circular waveguide (oil pipeline) loaded with two eccentric dielectric (oil) cylinders. Simulated mode charts from an equivalent HFSS software model is compared with the analytical results to optimize the HFSS model excitation and meshing. Both cases for odd and even hybrid field are investigated.

Verification of the analytical results with concentrically and eccentrically loaded dielectric cylinders are compared with literature to validate the analytical formulation. Higher number of modes are detected with our code compared to the cases reported in the literature which proof the sensitivity and the resolution of the code.

The optimized HFSS model is used to solve the cutoff characteristics of more complex mixtures of air-oil contents within the pipeline. This allowed monitoring the variance of the cutoff wavenumbers and dielectric constants with small change in the air-oil ratio within the pipeline. In addition, it is noted that wavy and stratified flow of oil within the pipeline shows similar electrical characteristics.

CHAPTER 4

MICROWAVE MONITORING OF OIL CARRYING

PIPELINE

A simple three-phase microwave monitoring system is designed in this chapter by integrating two aperture coupled patch antennas into a 2-inch Plexiglass pipeline. Two different measurement techniques are used for the two different antennas placed in shielded and non-shielded parts of the pipeline for monitoring oil-air and water-oil levels, respectively. The aperture coupled patch antennas are placed in the inner side of the pipeline Plexiglass wall with the ground plane placed in the outer side. So the patch antenna is based on a curved Plexiglass substrate with thickness $t=3$ mm and relative permittivity of 2.7. The microstrip feed line that excites the antenna is based on a Roger substrate with thickness $t=1.27$ mm and relative permittivity of 6. Figure 4-1 shows a 2-inch shielded pipeline with an integrated antenna. Note that for accurately modeling the setup, the correct values of the relative permittivity of Plexiglass needs to be determined. Experimental investigation together with simulated reflection responses of the antenna is used for this purpose. Once optimized, the reflection response of the setup (antenna integrated within the pipeline) is used to generate a look-up table, which links the S_{11} responses to the multi-phase content ratio of the petroleum-carrying pipeline.

The chapter starts with an introduction to the type of the antenna that will be used as the microwave monitoring setup and the description of the pipeline sample used to model the petroleum-carrying pipeline. After that, the design of the microstrip patch antenna is introduced. Then the optimization process of the simulated model and the generation of the look-up table from the optimized setup is presented. Note that different other techniques and setups were investigated during the research work, which led to the adopted technique, details are presented in Appendix A.

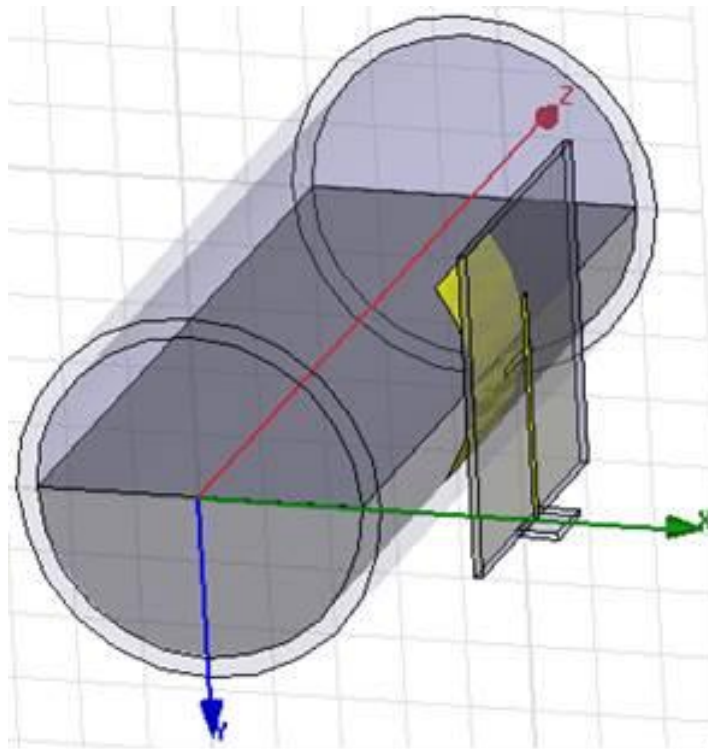


Figure 4-1: Petroleum Carrying Pipeline with Multiphase Mixture and the Integrated Aperture Coupled Antenna

4.1 Introduction

Microstrip patch antennas have the advantages of being conformal and easily installable despite of its inherent narrow impedance bandwidth. Detail characteristics and design process of this class of antenna is described in section 2.4.2 of chapter 2. In this chapter, aperture coupled microstrip antennas will be integrated to a 2-inch Plexiglass pipeline to monitor the level of its two and three phase contents. This simple non-intrusive technique uses only the reflection or S_{11} measurements from two antennas placed in the shielded and non-shielded part of the pipeline. Note that shielded pipeline means the outer wall of the pipeline is covered with conductive silver coating with appropriate patch excitation apertures on them. The 3 mm thick Plexiglass wall of the pipeline acted as the substrate of the patch. Since relative permittivity for the Plexiglass used ranges from (2.6 - 3.5) [72], a combination of experimental and simulated studies are used to find the accurate value. Since petroleum companies are predicting the use of Plexiglass pipelines in near future and they are more suitable for laboratory experiments due to their transparency, pipelines made of Plexiglass material is used in this study. Plexiglass pipelines also have the advantages of integrating the patch antennas on the outer or inner perimeter, which can be excited using coaxial or aperture coupled feeding mechanism. All of these cases are briefly investigated in this research work. The related simulation models and their results are presented in Appendix A. Note that these investigations allowed the design of the optimal setup for monitoring the multi-phase contents of the pipeline, by pointing out the problems associated with other dimensions and methods.

4.2 Design of Aperture Coupled Microstrip Patch Antenna

A patch antenna that will be integrated within the pipeline is initially selected to operate at 10 GHz. The reason behind this selection is the small size of the antenna, which may allow the deployment of multiple elements with the circumference of the pipeline. To better couple the energy from the radiating patch to the multi-phase mixture within the pipeline, the patch is placed in the inner side of the pipeline wall. Thus, the antenna has to be based on Plexiglass substrate and the correct value of the relative permittivity was required for the available Plexiglass material. This is achieved by designing a patch antenna and experimentally observing its reflection (S_{11}) response. Then, the HFSS simulator is used to obtain the S_{11} response for different values of relative permittivity (ϵ_r), until the simulated S_{11} response matches the experimental curve. The ϵ_r value of the simulated model that produced this match can be considered as the correct relative permittivity. This process resulted in an $\epsilon_r = 2.7$ for the available Plexiglass material, as demonstrate in chapter 5.

In an aperture coupled microstrip antenna, two substrates are separated by a ground plane, which has an aperture to couple energy from the feed line to the radiating patch. Typically, in an aperture-coupled antenna, the relative permittivity of the patch substrate is selected to be lower than the feed line substrate. In addition, the thickness (t) of the feed substrate is selected to be lower compared to antenna substrate. This is because the feed line substrate with high ϵ_r and low ' t ' supports the surface waves and better guide the inputted signal towards the aperture. On the other hand, the lower ϵ_r and higher ' t ' of the

antenna substrate maximizes radiated waves. The aperture coupled antenna designed in this chapter used Plexiglass with $t=3$ mm and $\epsilon_r=3.4$ as the antenna substrate and Rogers (TMM 6 (tm)) substrate with $t=1.27$ mm and $\epsilon_r=6$ as feed line substrate.

The reason for selecting the aperture coupling method for this operation is to avoid liquid leakage that may occur by exciting the patch using coaxial probe feeding. In addition, aperture coupled antennas exhibit low spurious radiation due to the existence of the ground plane between the feed and the patch. However, the disadvantage of this feeding mechanism is the requirement of thoroughly aligning the feed line, the aperture and the patch to achieve good radiation characteristics. This makes the fabrication or assembly of this class of antenna challenging. The aperture size and position is selected to optimize antenna performance, where matching is performed by controlling the width of feed line.

The initial design of the 10 GHz aperture coupled microstrip patch antenna is illustrated in Figure 4-2. Note that the antenna is based on flat Plexiglass substrate as this antenna is used to find the correct relative permittivity of the Plexiglass material (as described earlier). The dimensions of the patch, feed line, aperture and substrates are listed in Table 4-1. Professional software (HFSS) is used to simulate the designed antenna. To properly create a software model, the designed antenna is enclosed by an air box (not shown in Figure 4-2), which has a distance of $0.25*\lambda$ from the edges of the substrate to properly implement perfectly match Layer (PML) boundary. The slab shown in Figure 4-2 is for assigning the excitation to the antenna. The port should be 5 to 10 times as wide as the width of the trace and 5 times as high as the thickness of the dielectric. Further, one edge of the port should coincide with the ground plane [73].

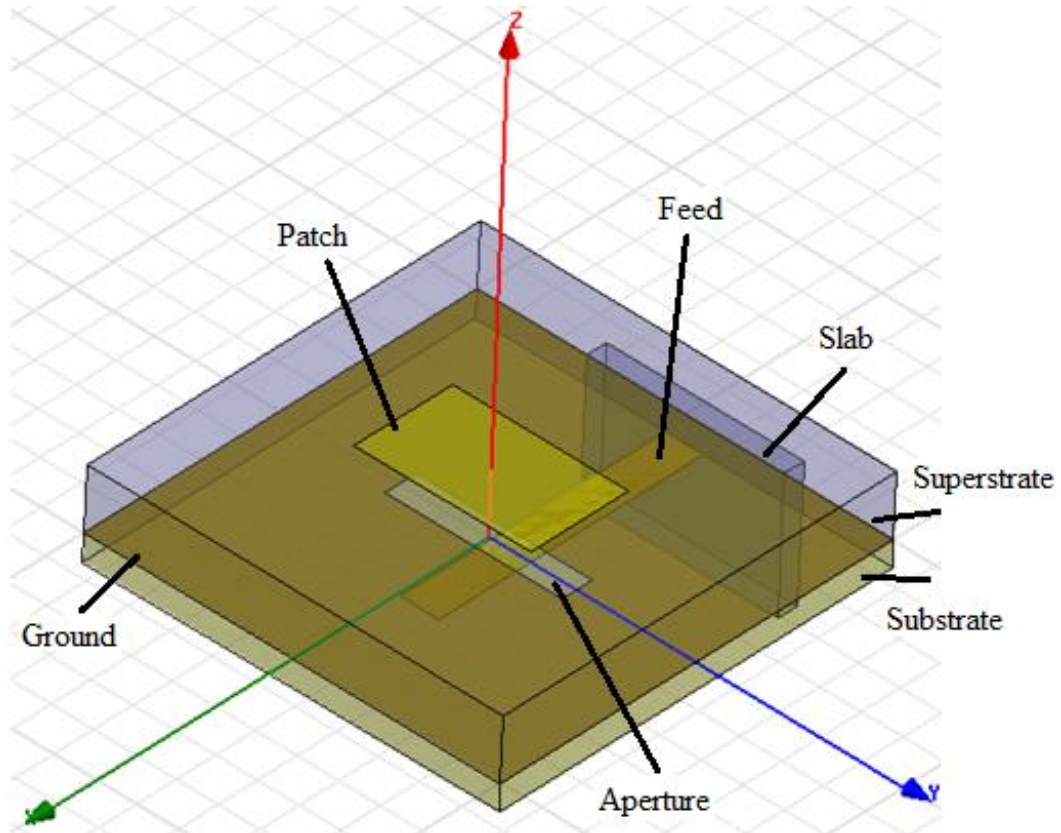


Figure 4-2: Aperture Coupled Microstrip Patch Antenna

Table 4-1: Specifications of Aperture Coupled Microstrip Patch Antenna that is integrated with the 2-inch Pipeline Model

Patch Width (mm)	8.5
Patch Length (mm)	5
Aperture Width (mm)	1.55
Aperture Length (mm)	8.5
Feed Width (mm)	1.9
Feed Length (mm)	13.46
Feed line Substrate Width (mm)	20
Feed line Substrate Length (mm)	20
Feed line Substrate Height (mm)	1.27
Antenna Substrate Height (mm)	3
Antenna Substrate Permittivity	6
Antenna Substrate Permittivity	3.4

The simulated reflection response (S_{11}) of the aperture-coupled antenna is shown in Figure 4-3. Note that the designed antenna is resonating at a center frequency of 9.9 GHz with a -10 dB impedance bandwidth of 19.2% and antenna gain of 6.45 dB. The 3D radiation pattern of the antenna is plotted in the inset of Figure 4-3. The 2D radiation pattern of the aperture-coupled antenna is shown in Figure 4-4. Note that Figure 4-4(a) plots the azimuthal cut at $\phi=0^\circ$ and Figure 4-4(b) plots the azimuthal cut at $\phi=90^\circ$.

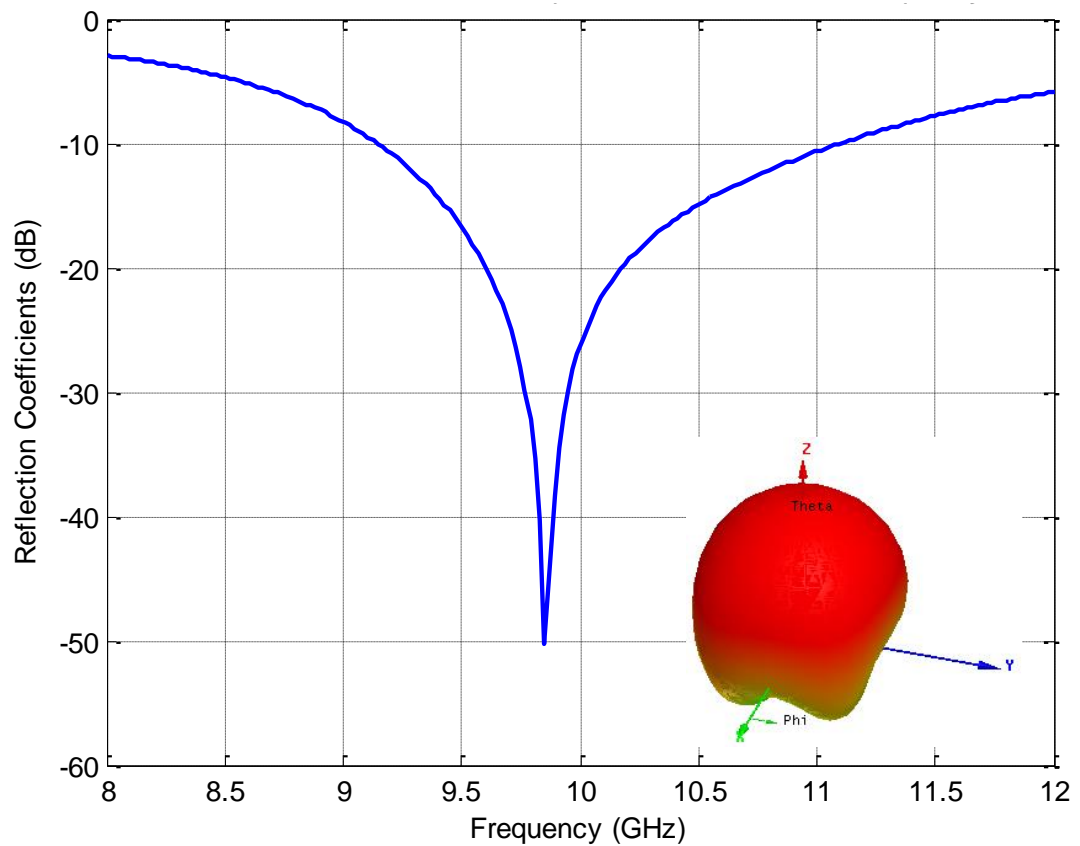


Figure 4-3: Reflection Coefficient of the Aperture Coupled Antenna

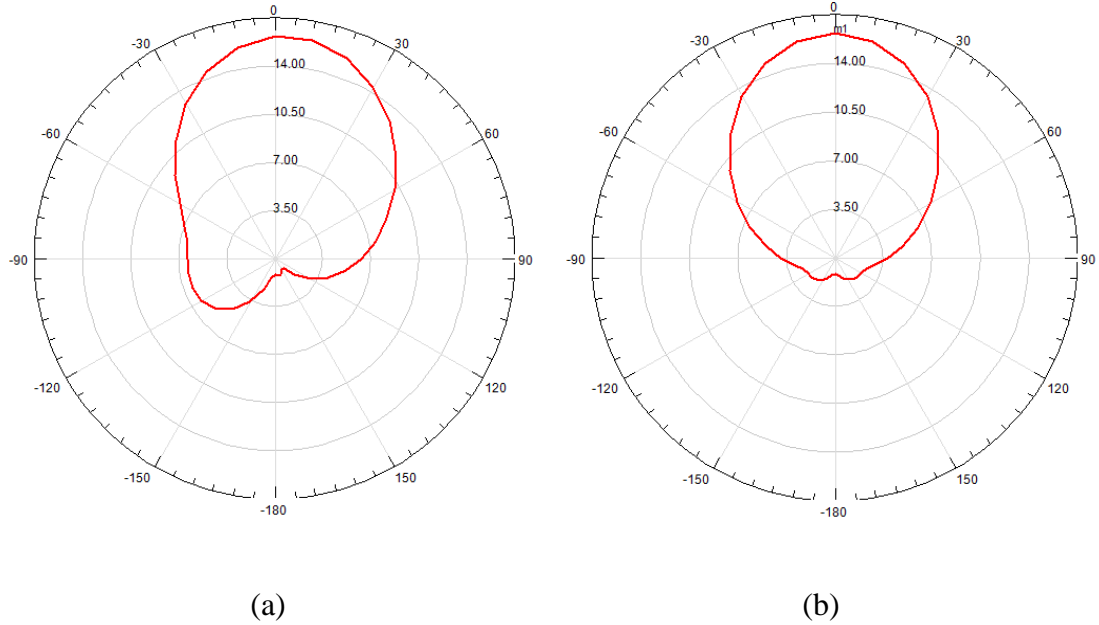


Figure 4-4: Two Dimensional Radiation Pattern (a) Azimuth Cut ($\Phi=0^\circ$) (b) Azimuth Cut ($\Phi=90^\circ$) and

4.3 Excitation of Two-Phase Petroleum Carrying Pipeline

4.3.1 Aperture Fed Antenna Integrated with a 2-inch Pipeline

The software model of the aperture fed patch antenna, integrated with a 2-inch petroleum-carrying pipeline is shown in Figure 4-5. To reduce the computational time, the pipeline is modeled as polyhedron with 15 semi-circle segments. This also allowed us to better integrate the antenna with the pipeline. Note that the substrate width has been changed to match the width of the pipeline segment. The outer boundary of the pipeline is modeled as perfect conductor or shielded, so that the mode-charts calculated for a circular waveguide (in chapter 3) can be used for analysis. The reflection response (S_{11}) for this

pipeline setup is shown in Figure 4-6. It is clear from the figure that there are many resonant modes. This is mostly due to the shielded outer conductor, as earlier demonstrated for a circular waveguide according to Equation 3.82.

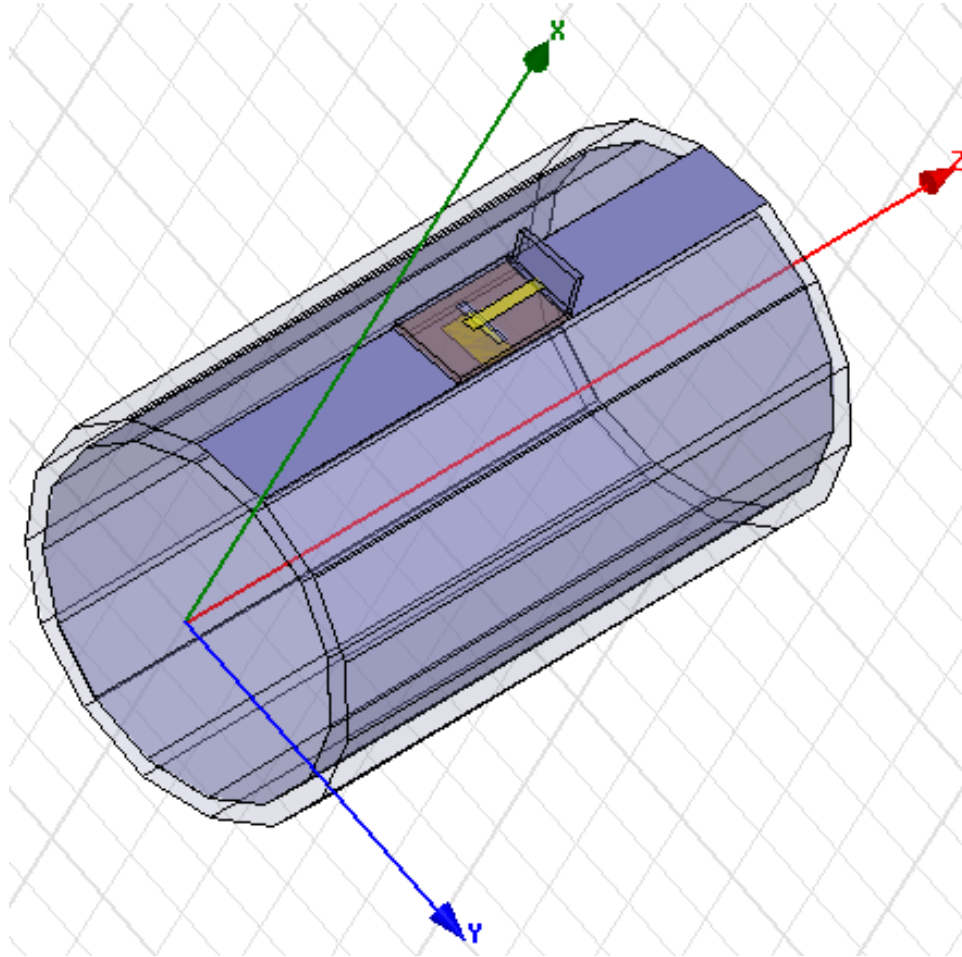


Figure 4-5: Pipeline Model Filled with Air with an Aperture Coupled Antenna Attached to it

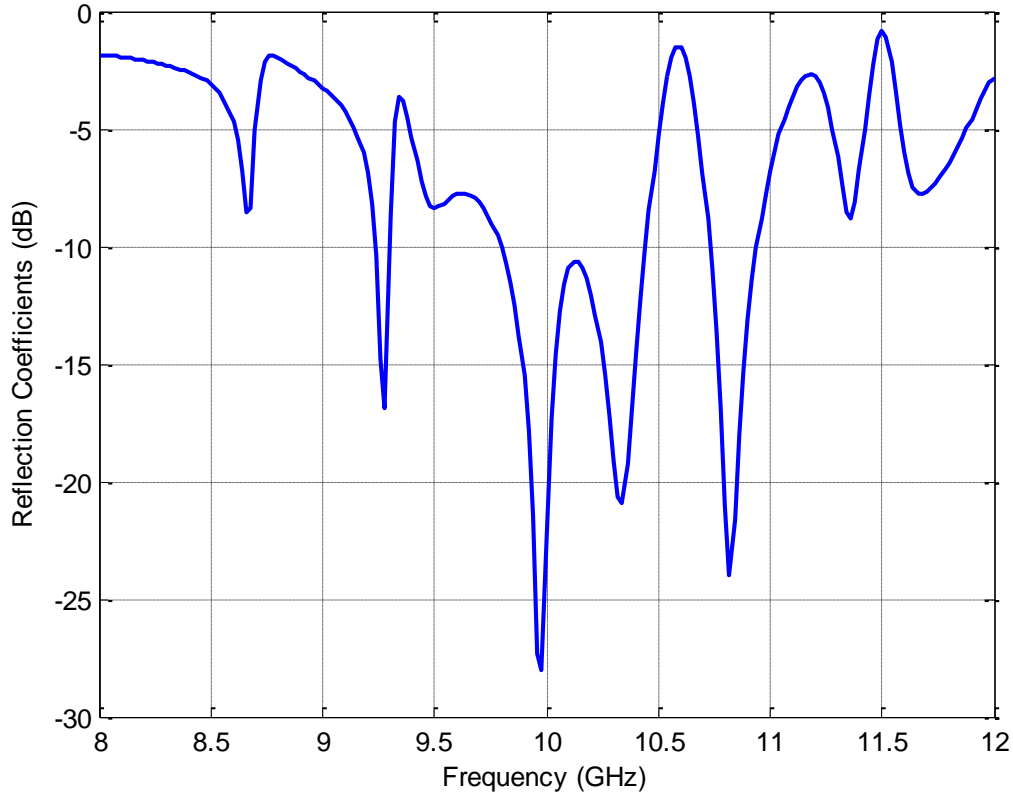


Figure 4-6: Reflection Coefficient of the Shielded Pipeline with the Integrated Antenna

4.3.2 Eliminating Higher Order Modes

In order to determine the level of the pipeline contents, the reflection coefficient should be reasonably distinct and preferably with predictable trends with respect to the changing contents of the pipeline. This can be achieved by reducing the number of modes excited within the pipeline, which require either reducing the operating frequency or the diameter of the pipeline. Since the pipeline diameter is already small (2-inch), reducing the operating frequency looked more feasible. However, this required modifying the design of the antenna to resonate at a lower frequency.

To select a proper frequency that insures single mode propagation within the pipeline, the cut-off numbers of the first three modes for the materials under investigation are calculated and tabulated in Table 4-2. It is clear from this table that two sets of antennas are needed to monitor oil-air and water-oil mixtures. For oil-air antenna, the resonant frequency of 3 GHz is selected, as it will optimally work for the central region with 50% oil and 50% air mixture within the shielded pipeline. For the water-oil antenna, instead of drastically redesigning the antenna, a similar antenna is used with a non-shielded pipeline. Since the absence of grounded silver coating reduces the surface waves within the Plexiglass, this also helps in limiting the excited modes for a water-oil filled pipeline.

Table 4-2: Cutoff Frequencies of the First Three Modes for Different Materials

Material	First Mode TE ₁₁	Second Mode TM ₀₁	Third Mode TE ₂₁
Air ($\epsilon_r = 1$)	3.516 GHz	4.592 GHz	5.8327 GHz
Oil ($\epsilon_r = 2.15$)	2.3981 GHz	3.1322 GHz	3.9778 GHz
Water ($\epsilon_r = 65$)	0.4361 GHz	0.56967 GHz	0.72345 GHz

The dimensions of the modified 3 GHz antenna are listed in Table 4-3 below:

Table 4-3: Specifications of Aperture Coupled Microstrip Antenna that is integrated with the 2-inch Pipeline Model

Patch Width (mm)	45
Patch Length (mm)	45
Aperture Width (mm)	1.55
Aperture Length (mm)	35
Feed Width (mm)	1.9
Feed Length (mm)	13.46
Feed line Substrate Width (mm)	20
Feed line Substrate Length (mm)	20
Feed line Substrate Height (mm)	1.27
Antenna Substrate Height (mm)	3
Antenna Substrate Permittivity	6
Antenna Substrate Permittivity	3.4

4.3.3 Optimizing Antenna Placement and Orientation within the Pipeline

In this subsection, a study on antenna location with respect to the content level and the antenna orientation is investigated.

4.3.3.1 Antenna Placement

Two possible locations for the antenna are displayed in Figure 4-7 considering the stratified flow case in a horizontal pipelines. The antenna in Figure 4-7(a) is placed on the top of the pipeline and is parallel to the boundary of the two-phase mixture. Whereas the antenna in Figure 4-7(b) is placed on the side of the pipeline and is perpendicular to the boundary of the mixture. The reflection coefficients (S_{11}) for these two cases are plotted in Figure 4-8, when the 2-inch pipeline is filled with a certain proportion of oil and water. It is noticed from the figure that both are resonating almost at the same frequency and the number of modes are the same. However, it is also clear from the figure that the antenna on the side of the pipeline is more sensitive to changing contents of the mixture compared to antenna placed on the top of the pipeline. So, the antenna positioned at the side of the pipeline is adopted for the optimum design.

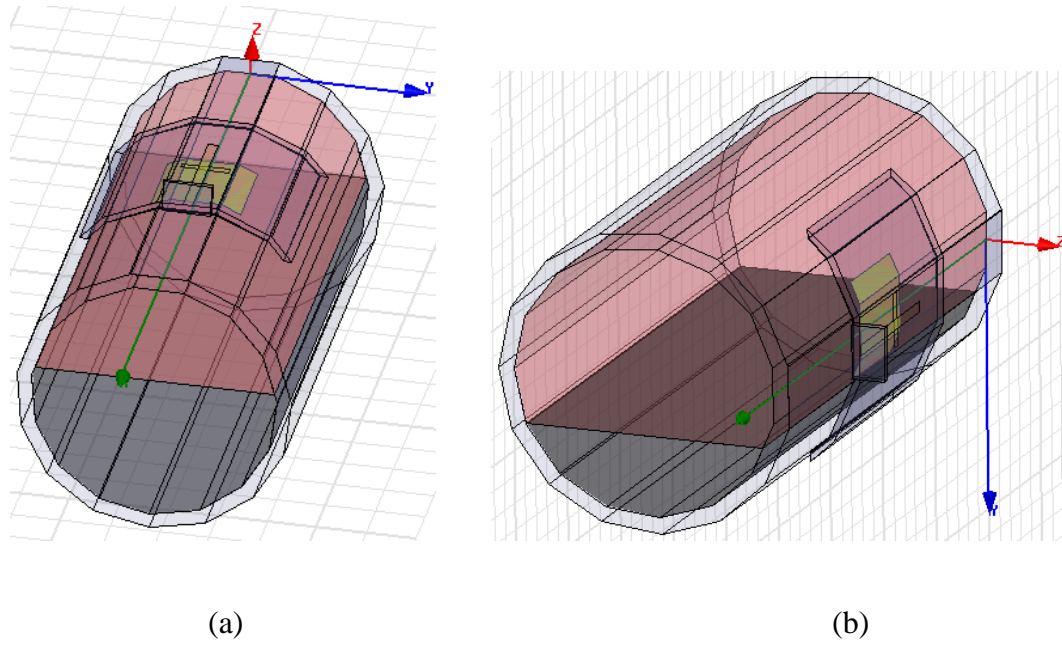


Figure 4-7: Placement of the Antenna with Respect to the Contents Level (a) Antenna on Top of the Pipeline (Parallel to the Level), (b) Antenna on the Side of the Pipeline (Perpendicular to the Level)

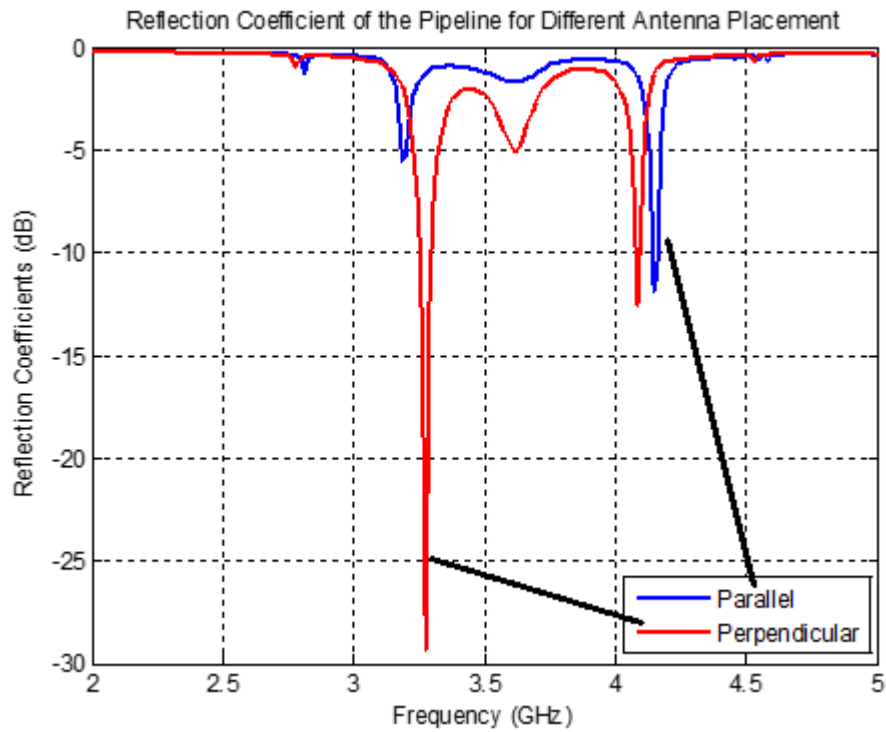


Figure 4-8: Reflection Coefficient for Different Antenna Placement within the Pipeline

4.3.3.2 Antenna Orientation

For a square patch antenna, the radiating edges are mainly determined by the orientation of the feeding mechanism. Thus, the orientation of the aperture and the feed line determines the radiating edges of the patch. As a first case, let us investigate the antenna with feed line directed in the axial direction of the pipeline, as shown in the simulation model of Figure 4-7(a) and Figure 4-7(b). Note that the major disadvantage of this type of feeding is the difficulty in soldering the coaxial connector at the end of the feed line during fabrication. However, L-type coaxial connector can be used with limited difficulty. As a second case, we can investigate the antenna with feed line directed in the transverse direction of the pipeline. Figure 4-9 and Figure 4-11 shows this type of feeding for antennas located on the top and side of the pipeline, respectively. Figure 4-9 shows the 2-inch pipeline model attached to it an aperture coupled antenna with transverse feeding mechanism. The related reflection response (S_{11}) is plotted in Figure 4-10 for different portions of oil-air mixture. The S_{11} curve of the antenna, shown in Figure 4-11, is plotted in Figure 4-12 for different level of oil-air mixture. It is clear from these figures (4-10 and 4-12) that as the level of oil changes 10% to 90% in steps of 10%, the resonant frequencies of Figure 4-12 changes more distinctive with an average frequency difference of 91 MHz due to every level change of oil within the mixture. Now although the power level of the reflected signals in Figure 4-10 are more compared to Figure 4-12, the different in resonant frequencies for the last few curves nearly overlapping to each other. So the feeding mechanism of Figure 4-11 is selected for the optimum design of the pipeline setup for monitoring the multi-phase contents.

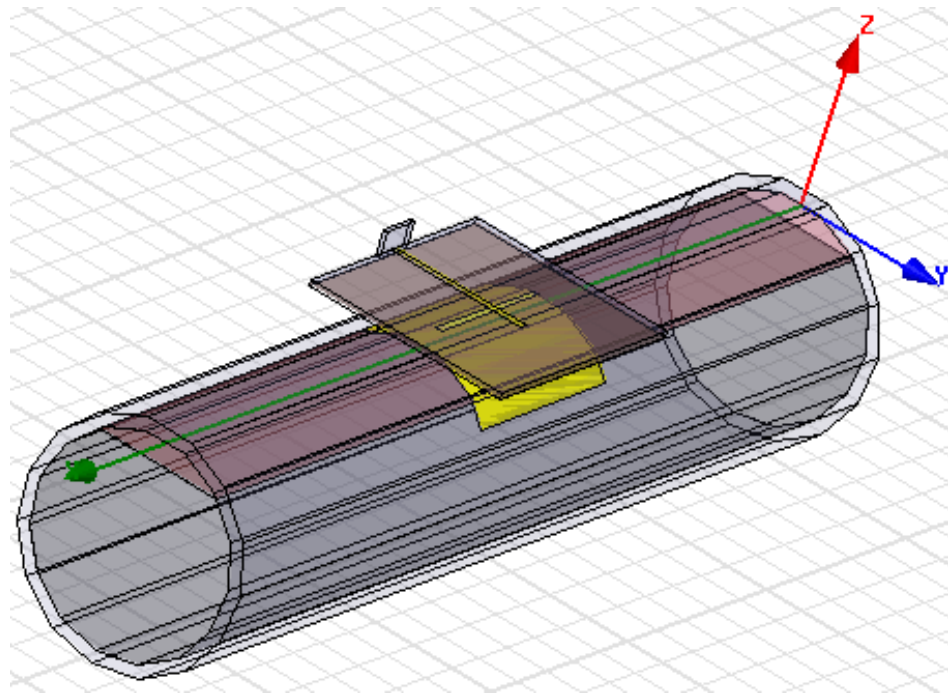


Figure 4-9: Antenna Placed on the Top of the Pipeline with its Feed Rotated

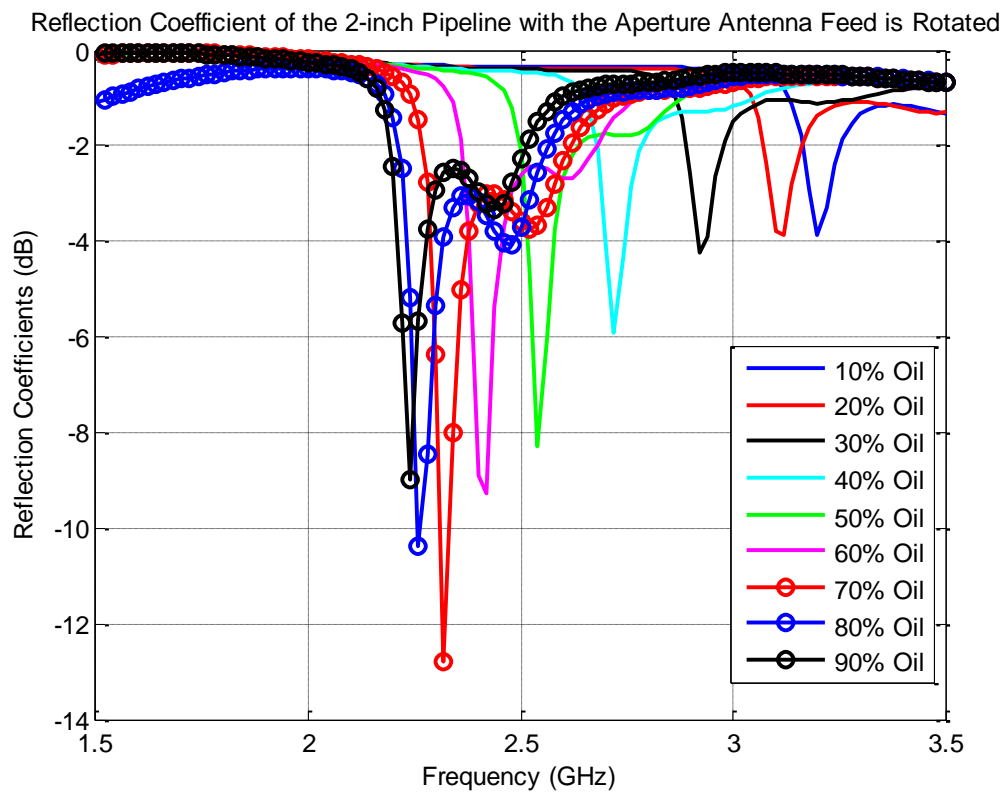


Figure 4-10: Reflection Coefficient of the Antenna Placed on the Top of the Pipeline with its Feed Rotated

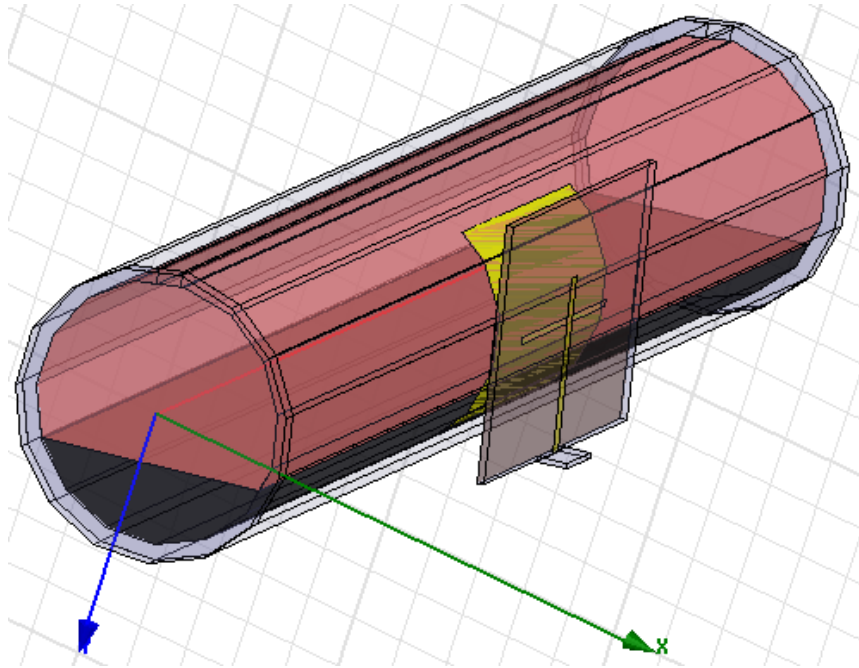


Figure 4-11: Modified Antenna Placed on the Side of a Pipeline with its Feed Rotated

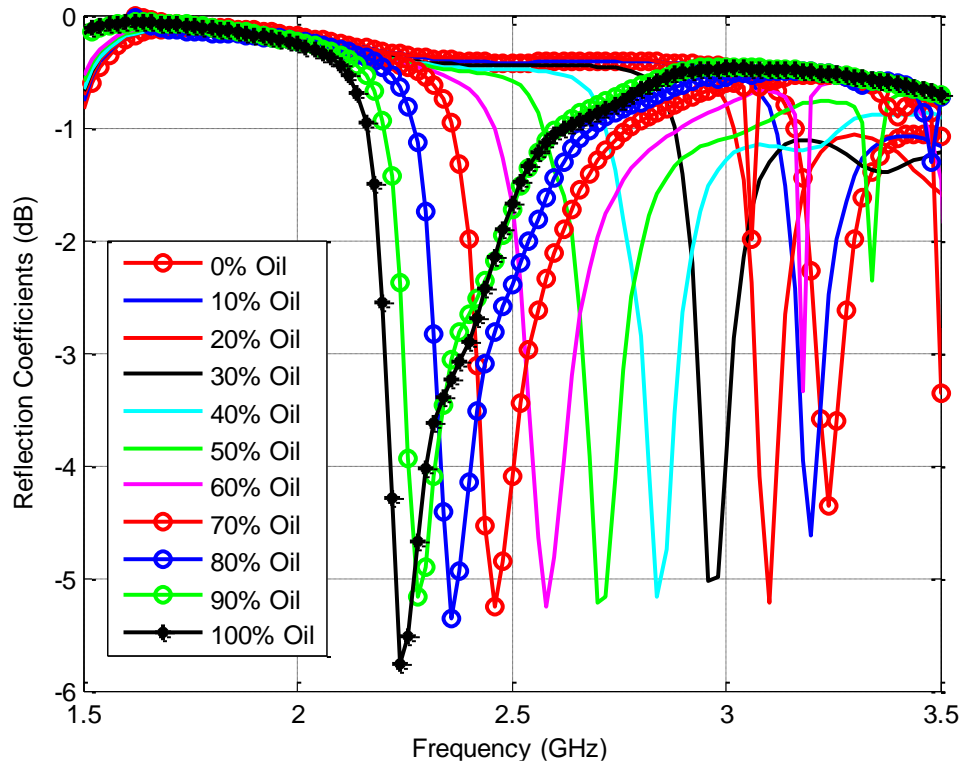


Figure 4-12: Reflection Coefficient of the Modified Antenna Placed on the Side of a Pipeline with its Feed

Rotated

4.3.4 Look-Up Table for Content-Ratio versus Resonant Frequency for Shielded Pipeline

Now since the optimum values of the patch dimension, position and orientation of the patch and the feeding mechanism are finalized, simulated results of the resonant behavior of a shielded pipeline can be recorded. Table 4-4 links the resonant behavior of the antenna with the contents ratio of the two-phase (oil-water) mixture within the 2-inch pipeline. These resonant frequencies have shown approximately same minimum value of $S_{11} \cong -5\text{dB}$. The average difference between the resonant frequencies is 91 MHz for an increment of 10% oil content of the 2-phase (oil-air) mixture. This table can be used as a look-up table to compare the experimentally measured resonant frequencies of a 2-inch pipeline to determine the content ratio of air-oil mixture.

Table 4-4: Response of the Antenna Integrated in the Shielded Pipeline for Different Air – Oil Proportions

Oil Percentage (%)	Resonant Frequency (GHz)	$ S_{11} $ (dB)	Angle of S_{11} (Degree)
100	2.24	-5.7558	-138.3609
90	2.28	-5.1655	-155.2883
80	2.38	-5.3609	-173.3193
70	2.46	-5.2491	148.7225
60	2.58	-5.2515	112.6414
50	2.7	-5.2150	71.8641
40	2.84	-5.1744	38.1486
30	2.96	-5.0321	16.3423
20	3.1	-5.2110	-21.1731
10	3.2	-4.6215	-39.0316
0	3.24	-4.3546	-50.3307

4.3.5 Look-Up Table for Content-Ratio versus Power of the Reflected Signal for non-Shielded Pipeline

In the previous setup, the pipeline with integrated antenna is optimized for detecting oil-air content ratio within a shielded pipeline. However, due to the different cut-off frequency of water filled pipeline, the antenna or the setup needs to be modified to successfully monitor the content ratio of water-oil mixture within the pipeline. Instead of drastically changing the dimension of the antenna, the selected modification to setup included minor modification of the antenna and removal of the silver shielding from the outer surface of the pipeline. This works as removal of the conductive layer reduces the unwanted surface wave modes and allow the reflected power to be controlled distinctively with changing ratio of water-oil mixture. Note that sea water in general has a very high relative permittivity of 81 and a conductivity of 4 S/m. The software model for the unshielded 2-inch pipeline filled with water-oil mixture is shown in Figure 4-13. Note that as per the design of the previous section, the same optimum position of the patch and feeding mechanism is used here. In this model, the pipeline is not covered with a perfect conductor sheet to avoid the higher order modes. In addition, a slightly modified 3.3 GHz antenna, which has an aperture area of 19*32 mm² is used. The reflection coefficient for different water-air proportions and water-oil proportions are plotted in Figure 4-14 and Figure 4-15 respectively, where the water level has been changed from 4% to 40% in steps of 4%. It is noticed that with increasing level of water within the water-oil mixture, the power of the reflected signal (S_{11}) distinctively reduces. This is due to higher relative permittivity and conductivity of sea water, which considerably reduces reflected power.

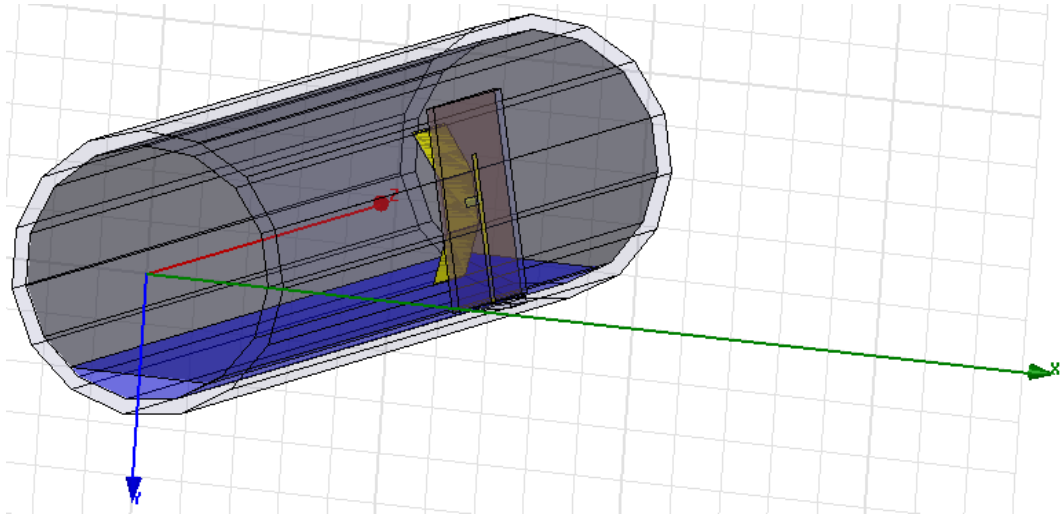


Figure 4-13: 2-inch Pipeline Filled with Water – Oil

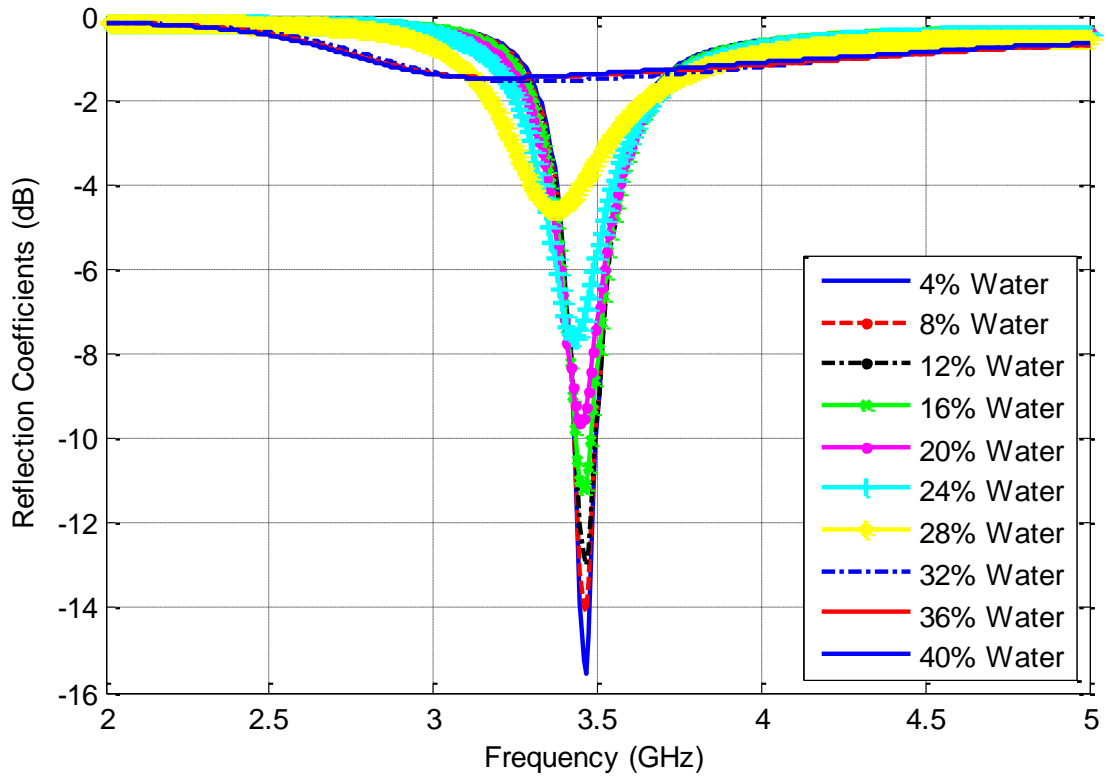


Figure 4-14: Reflection Coefficient of the 2-inch Pipeline for Different Water-Air Proportions

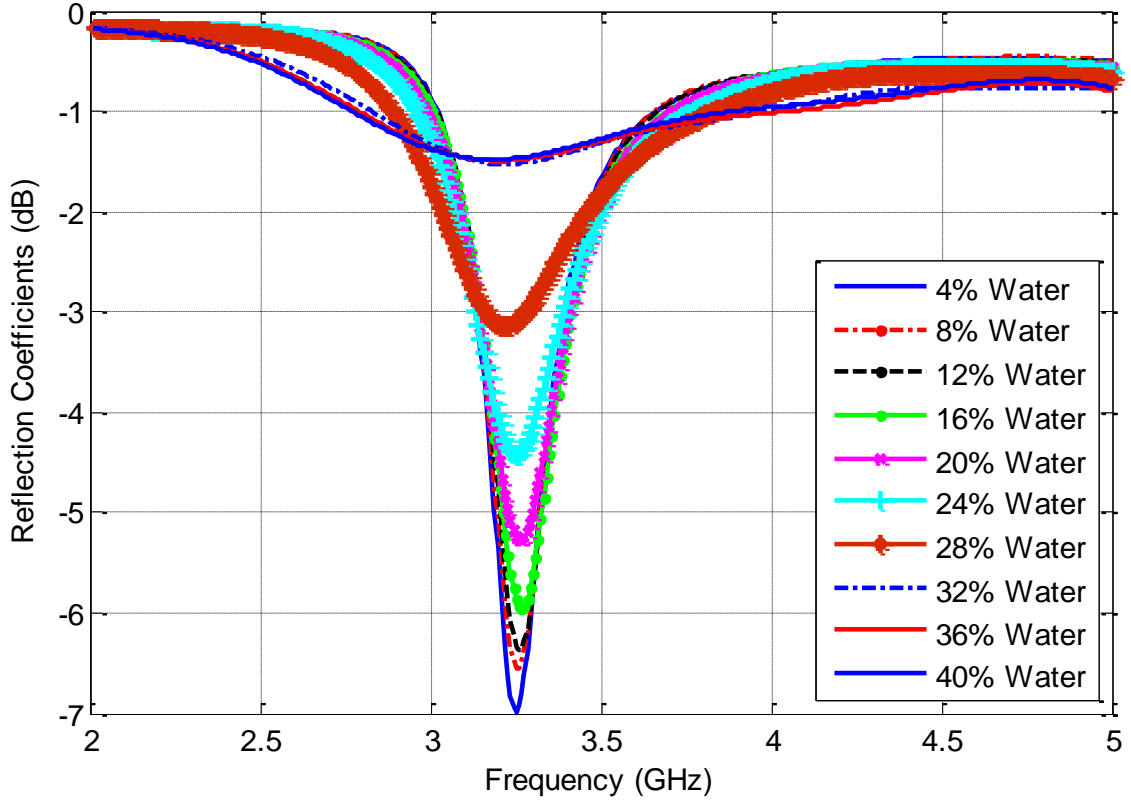


Figure 4-15: Reflection Coefficient of the 2-inch Pipeline for Different Water-Oil Proportions

Table 4-5: Response of the Antenna Integrated in the un-Shielded Pipeline for Different Air – Oil Proportions

Water Percentage (%)	$ S_{11} $ (dB)	Resonant Frequency (GHz)
4	-6.979	3.248
8	-6.543	3.256
12	-5.956	3.264
16	-5.276	3.264
20	-4.416	3.248
24	-3.137	3.224
28	-1.524	3.208
32	-1.492	3.208
40	-1.477	3.208

4.4 Excitation of Three-Phase Petroleum Carrying Pipeline

To measure the three phase contents within the 2-inch pipeline, a novel setup with two integrated antennas is proposed. The oil-air ratio monitoring needs a 3 GHz antenna integrated within the shielded part of the pipeline and the water-oil ratio monitoring needs a 3.3 GHz antenna integrated within the un-shielded region of the pipeline. The simulated model is shown in Figure 4-16. To study the reflection coefficient for different contents levels, two antennas are excited consecutively. Figure 4-17 plots the simulation results of a three-phase pipeline with 10% water and oil level is changed from 10% to 80%, where the remaining portion will be filled by air. Since the level of water is low, as the level of oil increased the shift in the resonant frequency became more obvious and distinctive. The simulation model of a second three-phase mixture is also investigated. When the 3 GHz antenna in the shielded part of the pipeline is excited, it detected the presence of 60% oil within the pipeline. Now the 3.3 GHz antenna of the non-shielded part of the pipeline is excited and the resulted S_{11} response is plotted in Figure 4-18 for a mixture with 60% oil and changing water level from 4% to 20% with steps of 4%. It is clear from this figure that measuring the power level of the reflected signal (S_{11}) will allow the determination of the water level from the look-up table, prepared in the previous section.

In this 3rd example, the look-up table is again used to find the level of the three-phase contents within the pipeline. As previously, the 3.3 GHz antenna in the non-shielded part of the pipeline is used to detect the water level and the 3-GHz antenna in the shielded part of the pipeline is used to detect the oil level. Thus, when the known three-phase mixture (80% oil, 12% water and 8% air) within the pipeline is excited with both the

antennas, it produced two distinct S_{11} curves. Figure 4-19 superimposes these responses. Note that the resonant frequency of left curve should provide information about the oil level and the lowest magnitude ($|S_{11}|$) of the right curve should help detect the water level of the pipeline. Since the reflection coefficient for the shielded antenna (left curve) is resonating at 2.33 GHz, it is within the range of the resonance frequencies from 2.33GHz to 2.42GHz and as per look-up table of Table 4-4 the related oil level within the pipeline is 80%. Now, measuring the level of the reflected power ($|S_{11}|$) of the right curve, it is clear that the value of -6.179 dB is within the range of the tabulated (Table 4-5) values of -6.2495 to -5.616 dB, which relates to water level of 12%. Thus, the measured values correctly predicted the oil and water level of the pipeline. The remaining area of the pipeline that is occupied by air can be calculated from these values.

In the design shown in Figure 4-16, the excitation of one antenna at the time or excitation both antennas together will not be of difference since the isolation between the antennas is less than -40 dB and this is due to the separation distance between the antennas, orientation and the location of the antennas are not on the same level. The antenna on the un-shielded part of the pipeline is at a lower level than the antenna on the shielded part in order to detect water level in a way that is more accurate.

Several look-up tables have been generated from the model shown in Figure 4-16. By fixing the oil level and varying the water levels from 4% to 20% as tabulated in Table 4-6 to Table 4-10 and also by fixing the water level and changing the oil levels from 10% to 90% as shown listed in Table 4-11 to Table 4-13.

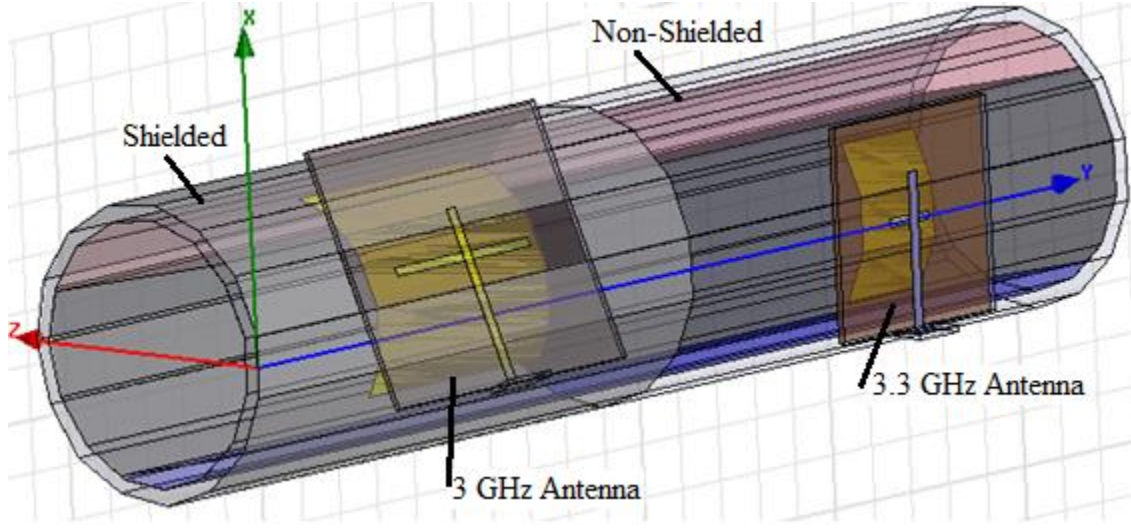


Figure 4-16: Pipeline Model with Two Integrated Antennas in Shielded and non-Shielded Regions

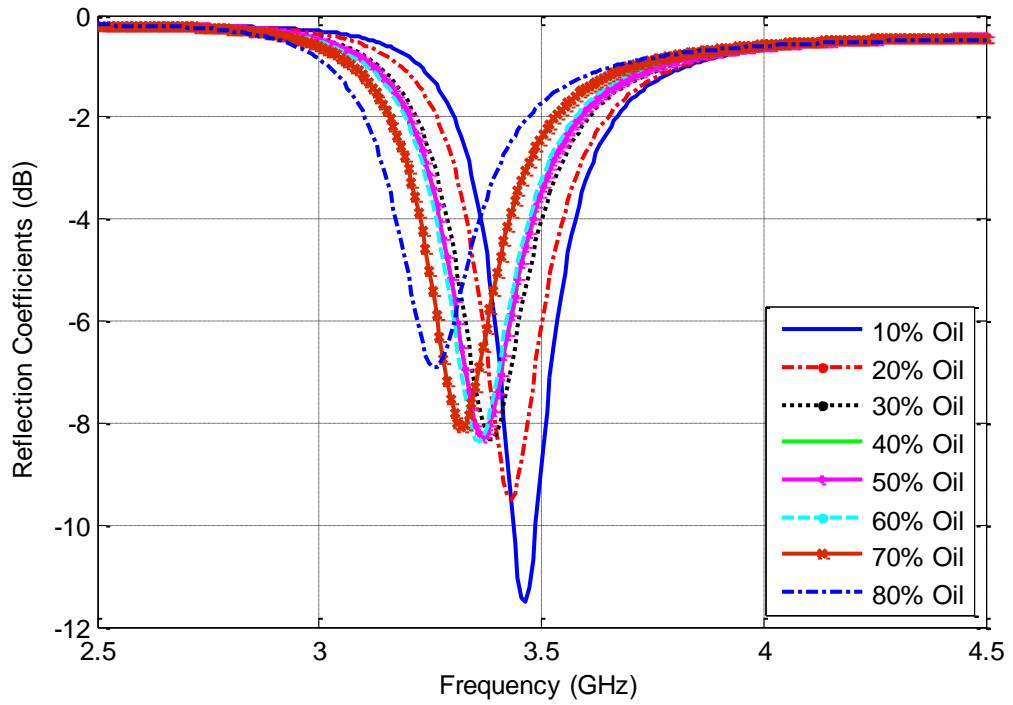


Figure 4-17: Reflection Coefficient of the 2-inch Pipeline for Different Oil Proportions at a 10% of Water

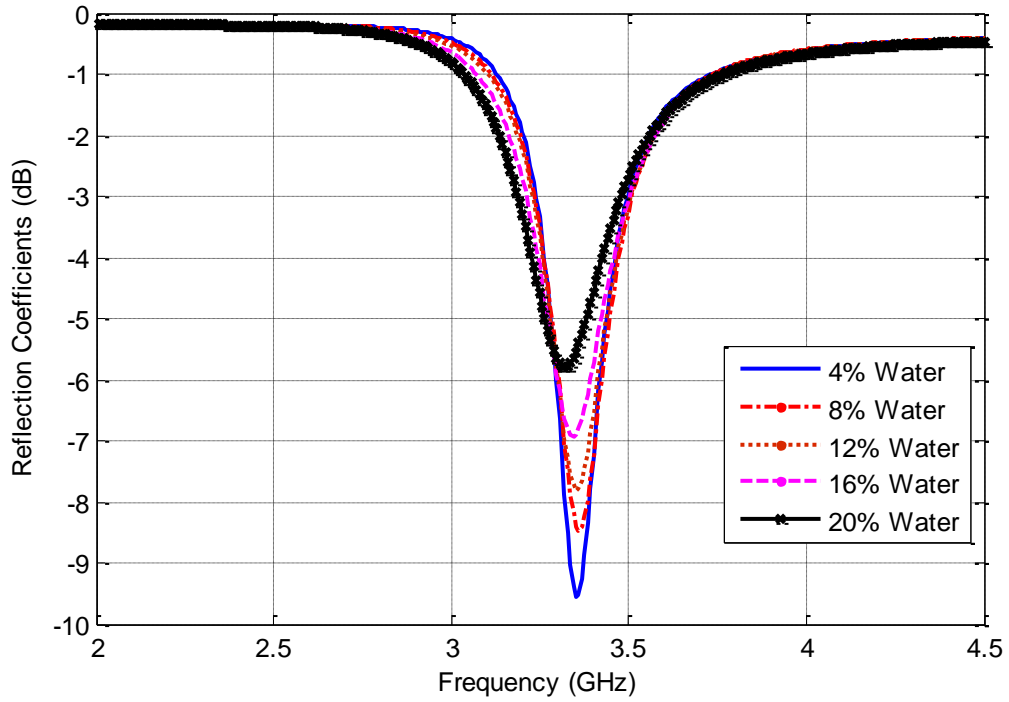


Figure 4-18: Reflection Coefficient of the 2-inch Pipeline for Different Water Proportions at 60% of Oil

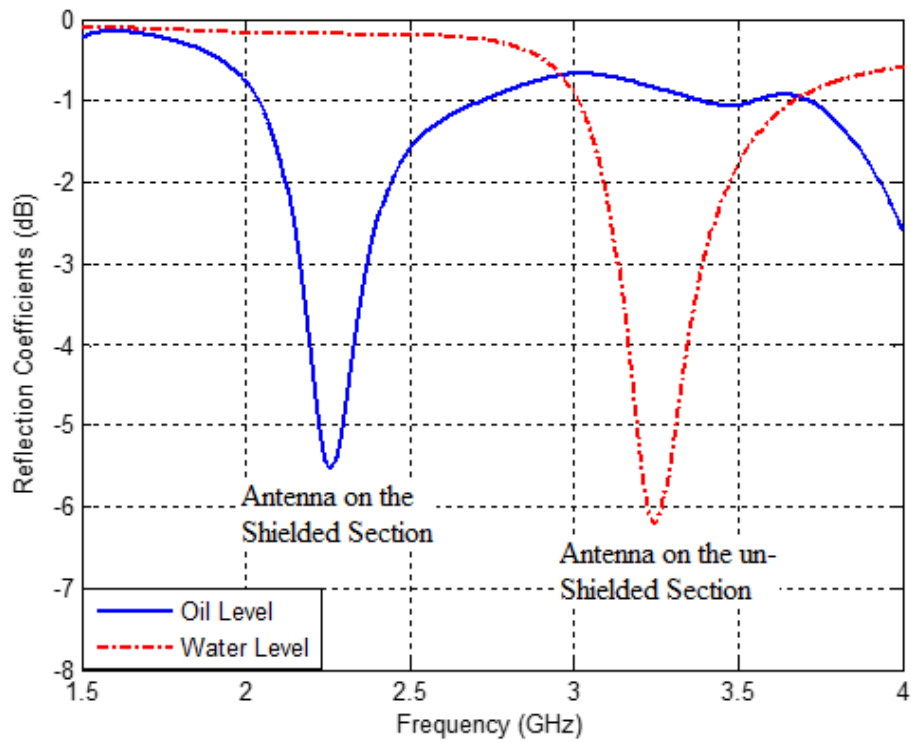


Figure 4-19: A Case of 80% Oil and 12% Water

Table 4-6: Reflection Coefficient of the un-Shielded Plexiglass Antenna at 30% of Oil Level

Water Percentage (%)	 S₁₁ (dB)	Resonant Frequency (GHz)
4	-10.4053	3.40
8	-8.7364	3.39
12	-7.9712	3.384
16	-6.8251	3.376
20	-5.8426	3.368

Table 4-7: Reflection Coefficient of the un-Shielded Plexiglass Antenna at 40% of Oil Level

Water Percentage (%)	 S₁₁ (dB)	Resonant Frequency (GHz)
4	-9.3477	3.368
8	-8.4009	3.368
12	-7.9065	3.368
16	-6.8288	3.376
20	-5.8877	3.368

Table 4-8: Reflection Coefficient of the un-Shielded Plexiglass Antenna at 50% of Oil Level

Water Percentage (%)	 S₁₁ (dB)	Resonant Frequency (GHz)
4	-9.3581	3.36
8	-8.4148	3.368
12	-7.8032	3.368
16	-6.7878	3.376
20	-5.8584	3.36

Table 4-9: Reflection Coefficient of the un-Shielded Plexiglass Antenna at 60% of Oil Level

Water Percentage (%)	 S₁₁ (dB)	Resonant Frequency (GHz)
4	-9.432	3.352
8	-8.4332	3.36
12	-7.8476	3.36
16	-6.9130	3.344
20	-5.8617	3.32

Table 4-10: Reflection Coefficient of the un-Shielded Plexiglass Antenna at 70% of Oil Level

Water Percentage (%)	 S₁₁ (dB)	Resonant Frequency (GHz)
4	-9.4475	3.336
8	-8.2775	3.328
12	-7.5945	3.312
16	-6.4377	3.296
20	-5.3860	3.272

From the reflection coefficient of the antenna located in the un-shielded part, if for example the detected reflected value is -8 dB, from the Table 4-6 through Table 4-10, this will represent a water level of 8%. Then to determine the oil level, the table of the 8% of water will be used, which is Table 4-12 and the oil level is determined by the value of the operating frequency that is provided from the reflection coefficient of the antenna located in the shielded part of the pipeline. The air level will be the remaining portions of the pipeline as it is assumed that the pipeline contain a three-phase contents.

Table 4-11: Reflection Coefficient of the Shielded Plexiglass Antenna at 4% of Water Level

Oil Percentage (%)	f_c (GHz)	S_{11} (dB)
10	3.12	-4.2469
20	3.02	-4.8092
30	2.88	-5.8998
40	2.74	-6.7890
50	2.62	-7.1990
60	2.50	-8.2756
70	2.38	-8.3331
80	2.30	-9.2567
90	2.24	-8.6286

Table 4-12: Reflection Coefficient of the Shielded Plexiglass Antenna at 8% of Water Level

Oil Percentage (%)	f_c (GHz)	 S₁₁ (dB)
10	3.04	-4.8571
20	2.90	-5.6785
30	2.78	-6.6462
40	2.64	-7.9778
50	2.52	-8.7206
60	2.40	-8.5696
70	2.32	-9.1447
80	2.24	-8.9877
90	2.20	-9.0248

Table 4-13: Reflection Coefficient of the Shielded Plexiglass Antenna at 12% of Water Level

Oil Percentage (%)	f_c (GHz)	S_{11} (dB)
10	2.88	-3.0018
20	2.74	-4.3088
30	2.60	-5.6677
40	2.50	-7.0498
50	2.40	-7.8536
60	2.30	-8.8356
70	2.22	-8.5738
80	2.16	-7.9667
90	---	---

4.5 Conclusion

Due to limiting higher order modes, the initially designed 10 GHz antenna is modified to resonate at 3 GHz and is integrated in the shielded part of the 2-inch pipeline for detecting the contents of oil-air mixture. However, for detecting the contents of water-oil mixture, the antenna is modified to resonate at 3.3 GHz and is integrated in the non-shielded part of the pipeline. Note that the change of resonant frequency is measured to find the changing level of oil within the pipeline, whereas the change in the power level of the reflected signal is measured to find the level of water contents within the pipeline. Look-up tables is prepared and presented for both measurements to enable the experimental detection of three-phase contents ratio within a 2-inch pipeline. Note that during the three-phase measurements, both antennas need to be excited in a consecutive manner. Note that this analysis assumes that the pipeline only filled with three-phase mixture. The main drawback of this technique is the level resolution that can be measured are quite large and a maximum of 30% water can be detected with an acceptable error as can be concluded from Figure 4-15.

CHAPTER 5

FABRICATION PROCESS and EXPERIMENTAL

RESULTS

In the previous chapter, professional software is used to simulate a petroleum-carrying pipeline with multi-phase contents. The simulated results are then tabulated in a look-up table, linking the S-parameter responses with content ratio of the multiphase mixture of air, oil and water. This chapter describes the fabrication and the experimental process, which will be used to verify the simulated results. First part of this chapter describes the fabrication of the aperture coupled patch antenna and the experimental verification of the exact relative permittivity of the FR4 substrate. This part also describes the integration process of antenna within the petroleum-carrying pipeline. The second part of the chapter describes the experimental setup and the steady state monitoring of two and three phase contents within the pipeline. This process involves the experimental validation of the simulated S_{11} responses (resonant frequency and power level), used in chapter 4 to create the look-up table.

5.1 Introduction

The accuracy of simulated results generated using professional software mainly depends on the competency of the user. Although the author has considerable experience in using HFSS software, the best way to verify the accuracy of the simulated response is to compare them with experimental results. However, reliable measurement results requires fabricated prototype to perfectly match the simulated model, which is often difficult to achieve during in-house assembly. In this research work, maximum caution is used during the fabrication of the antenna and its placement within the pipeline to minimize misalignments or fabrication errors. Antenna resonance and radiation properties are verified using proper tools before integrating them within the pipeline.

5.2 Fabrication Process

In this section, an overview of the patch antenna fabrication and its integration into the pipeline is presented.

5.2.1 Fabrication of the Aperture Coupled Microstrip Patch Antenna

The printed circuit board (PCB) plotter is used to fabricate the optimized aperture coupled patch antenna, designed for monitoring the contents of the petroleum-carrying pipeline. The microwave plotter used for this purpose is LPKF ProtoMat S62 and is shown

in Figure 5-1. This compact high-speed plotter provides a very high precision and performance for quickly and easily milling and drilling microwave circuit board prototypes. It has an automatic tool change in three-dimensional operation supported by a laser guided camera for extra precision. The software interface between the PC and the plotter is called “Board Master”, which allows the user to control the device in a reasonable easy manner. Software called “Circuit Cam,” is also needed as an interface between the microwave simulators (Ansoft HFSS and Designer) and the “Board Master”. This software accepts the simulated model in gerber format and then transforms it into ‘LMD’ format, compatible to ‘Board Master’. Detail operating process of this class of dry PCB prototyping tool is available in reference [74].



Figure 5-1: The LPKF ProtoMat® S62 [74]

The fabricated two layers aperture coupled antenna is shown in Figure 5-2. Note that the two layers are clear in figure (a), whereas the patch and microstrip feed line is shown in (b) and (c), respectively. The feed line is based on a roger substrate with $\epsilon_r=6$ and $t=1.27$ mm and the optimized width of the 50Ω feed line is 1.9 mm. The antenna substrate is selected to be Plexiglass substrate with $\epsilon_r=2.6$ to 3.5 and $t=3$ mm. Plexiglass is selected due to its importance in the petroleum industry as a material, proposed for next generation of petroleum carrying pipelines. Note that the feed line is connected with a SMA coaxial cable for connecting it to a signal sources. This antenna will be used to determine the correct relative permittivity of the Plexiglass substrate using experimental technique, as explained in the next section.

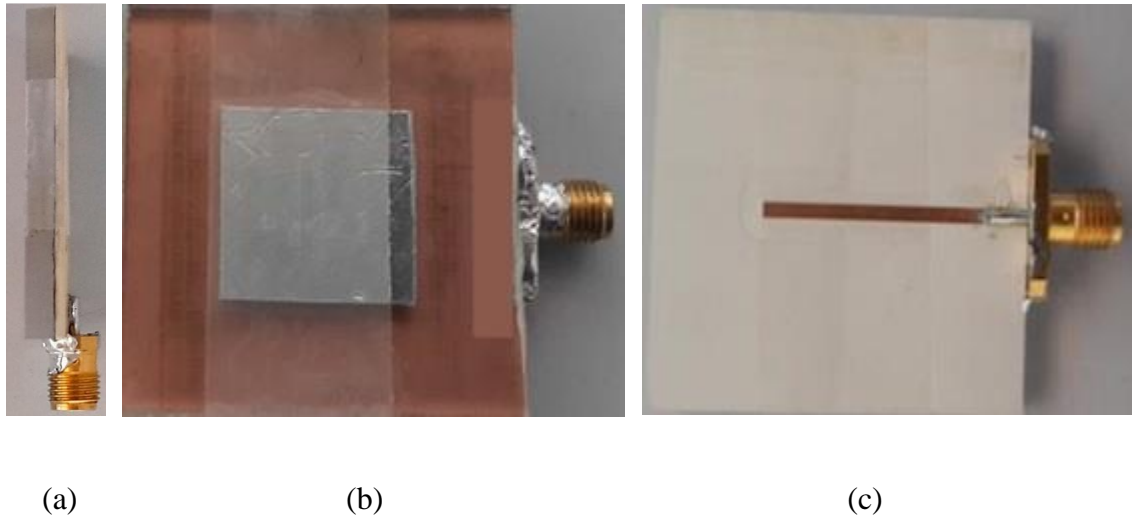


Figure 5-2: The Fabricated Sample, (a) Side View (b) Front View (c) Back View

The fabrication or plotting process of this antenna involved the following steps:

- (i) Export the optimized two-layer design of the antenna from Ansoft-HFSS to Ansoft-Designer.
- (ii) Using Ansoft-Designer, create a two-layer model in Gerber format.
- (iii) Import the Gerber file using Circuit-Cam software and introduce the necessary insulation to preserve the copper part from the milling tool. Save the model in “LMD” format.
- (iv) Import the “LMD” file using “Board Master” and plot the circuit on copper double sided printed circuit board (PCB)

Using “Board Master” software, the position of the antenna on the PCB board can be controlled. Also the depth of the milling tool needs to be carefully adjusted not to remove any substrate material. This is particularly important for microwave antenna design, as the height of the substrate can change the frequency response of the antenna or the feed line. Board Master software also allowed us to accurately position the aperture and the feed location on the copper board as per simulated design.

However, circular waveguide wall made of Plexiglass can change the frequency response of the antenna due to its curved shape. Therefore, an aperture coupled microstrip antenna based on a curved Plexiglass substrate is designed. The front and back view of the antenna is shown in Figure 5-3. Figure 5-3(a) shows the curvature of the substrate, which conforms to the curvature of a 2 inch pipeline. Figure 5-3(b) and 5-3(c) shows the patch and coupling aperture of the antenna. Note that the aperture on the ground needs to be correctly aligned to optimally excite the patch antenna using the feed line of Figure 5-2(c).

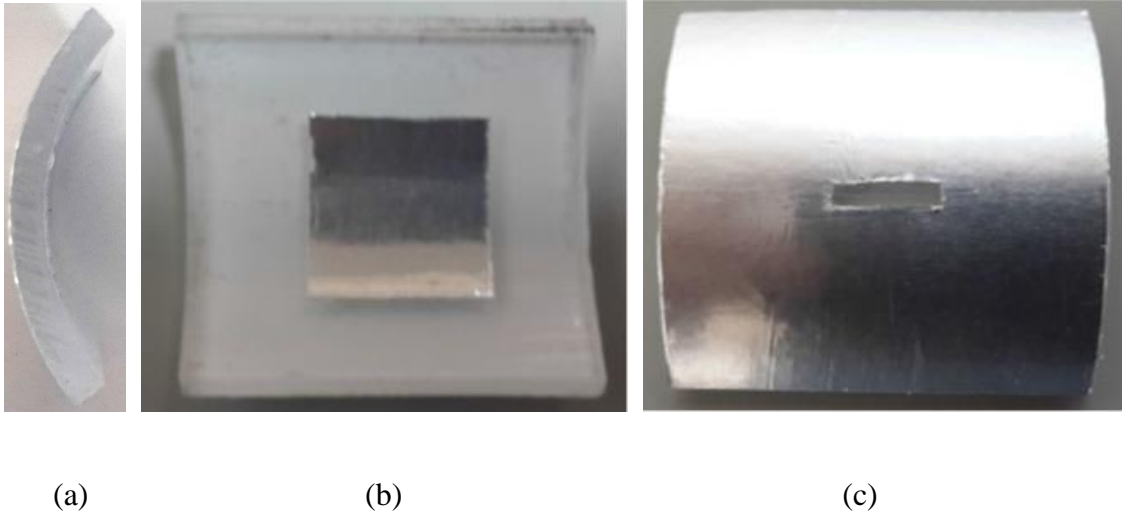


Figure 5-3: The Antenna Fabricated on a Curved Plexiglass Sample, (a) Side View (b) Front View (c) Back View

5.2.2 Assembly of the Pipeline Measurement Setup

A sample of steady-state petroleum carrying pipeline with three-phase mixture is shown in Figure 5-4. Note that the terminations in both end is sealed to avoid leakage. Since crude oil is sticky and thick liquid, it is difficult to setup any experiment involving crude oil, where this is chance of leakage. It is clear from this figure that the order of the phase contents are: top layer is filled with air, middle layer is occupied by oil and bottom layer is filled with water. This also corresponds to their relative permittivity, as air, oil and water have relative permittivity of 1, 2.15 and 81, respectively.

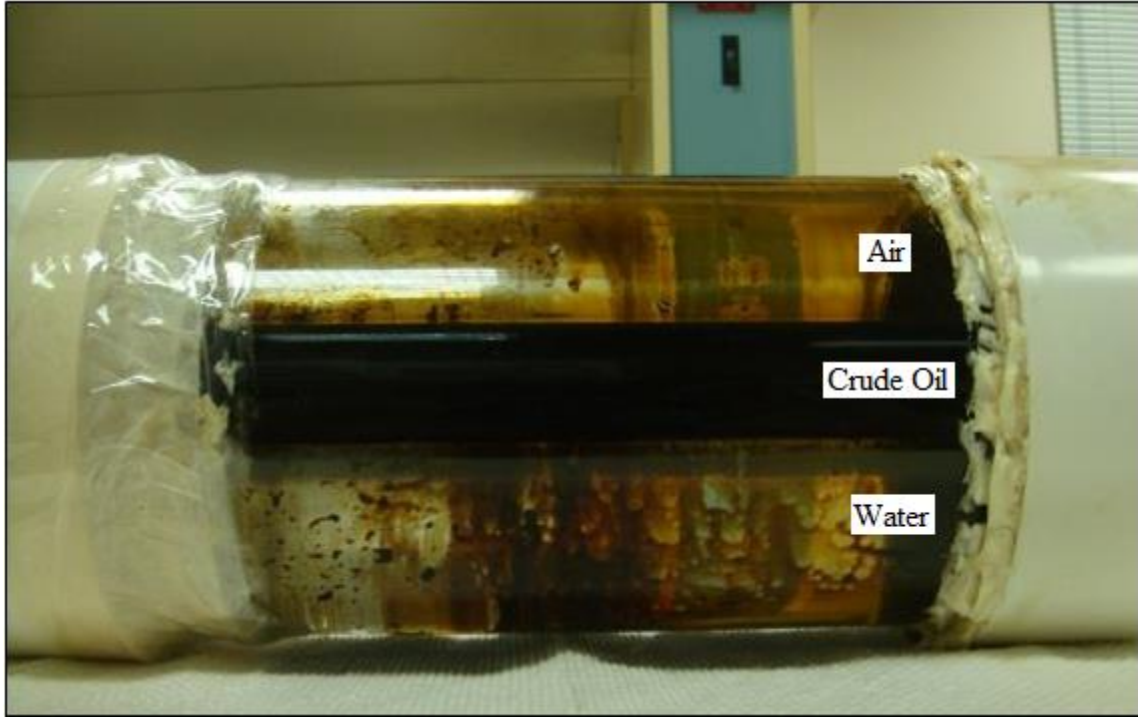


Figure 5-4: Pipeline Filled with 3-Phase Mixture of Air, Oil and Water

The copper coated or shielded Plexiglass pipe with integrated aperture coupled patch antenna is shown in Figure 5-5. It is clear from this figure that the feed line of Figure 5-2(c) is used to excite the microstrip patch, carefully positioned within the Plexiglass pipeline. The copper shielding and the pipeline wall acts as the ground plane and the antenna substrate, respectively. Since the thickness of the patch is very small, it has minimal affect the flow of the 3-phase mixture and the periodical cleaning mechanism of the pipeline.



Figure 5-5: Shielded Plexiglass Pipeline with Integrated Aperture Coupled Antenna

5.3 Experimental Setup

5.3.1 Antenna Scattering Parameter Measurements

The Vector Network Analyzer (VNA) is a very popular tool in measuring active and passive microwave devices [75]. This is a state of art equipment, which allows the measurements of the magnitudes and phases related to the reflection and transmission responses of a single or multi-port device [76]. In this research work, the reflection responses (S_{11} -parameter) of the aperture coupled antenna are measured using this device

as shown in Figure 5-6. An ENA series network analyzer of type Agilent-E5071C [75] is used in this study to measure the scattering parameters of the patch antenna loaded with the 3-phase mixture as a superstrate. The 300 KHz – 20 GHz network analyzer offered highest RF performance and fastest speed in its class, with a wide frequency range and versatile functions [75].



Figure 5-6: S_{11} Measurement of the Patch Antenna Using Vector Network Analyzer

At the initial stage of the design process, it was essential to determine the correct relative permittivity (ϵ_r) of the Plexiglass material that will be used as a substrate of the designed aperture coupled microstrip antenna. Since the typical range of the relative permittivity of Plexiglass is between 2.6 to 3.5, the simulator software (HFSS) is used to observe the resonance behavior of the designed 4 GHz patch antenna for this range. The resulted frequency response is plotted in Figure 5-7. Note that the resonant frequency of

the aperture coupled patch antenna varies between 3.65 GHz to 4.06 GHz for changing ϵ_r values. To determine the exact ϵ_r , the fabricated antenna of Figure 5-2 is connected to the network analyzer to observe the reflection response. This experimentally obtained resonant frequency is then compared with the simulated set of resonant frequencies to determine the correct ϵ_r , as shown in the next section.

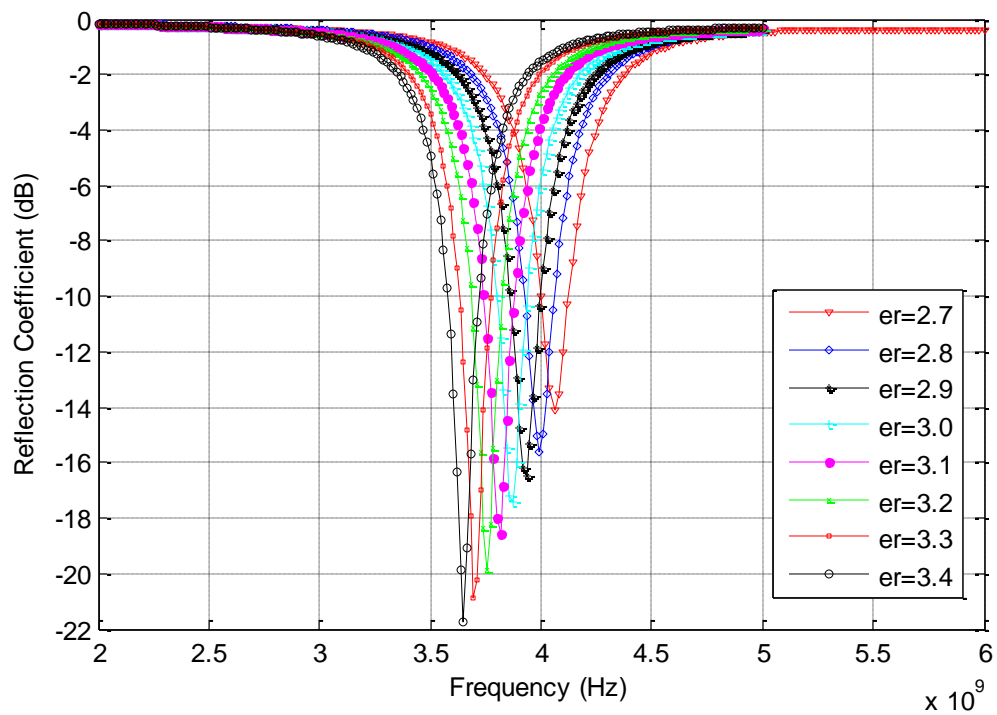


Figure 5-7: Reflection Coefficient for Different Plexiglass Dielectric Constant

According to this finding, the simulation models needed to be corrected before listing the S-parameter responses in the look-up table, which links S_{11} responses with content ratio within the multi-phase pipeline.

5.3.2 Antenna Radiation Pattern Measurements

To observe the radiation properties of this antenna, a radiation pattern measurement device with real-time scanning capabilities is used [77]. The operating principle of this device (called RFXpert) is based on the measurement of the near field response through a fast movement probe on a planar antennas consists of a 384 elements, positioned on its flatbed. The far field radiation patterns are then calculated and displayed through the interface software. The advantage of this process is the availability of the far-field data without requiring rotatable antenna radiation pattern measure setup within anechoic chambers. The RFXpert based radiation characteristics measurement setup is shown in Figure 5-8. Note that the antenna excitation signal is generated through the Agilent signal generator with the desired frequency and power level. Thus, when the excited antenna is placed on the flatbed of the device, the far field radiation pattern is displayed in the monitor. With proper setup, the RFXpert can also give the directivity of the antenna and the two dimensional cuts, as illustrated in the next section.

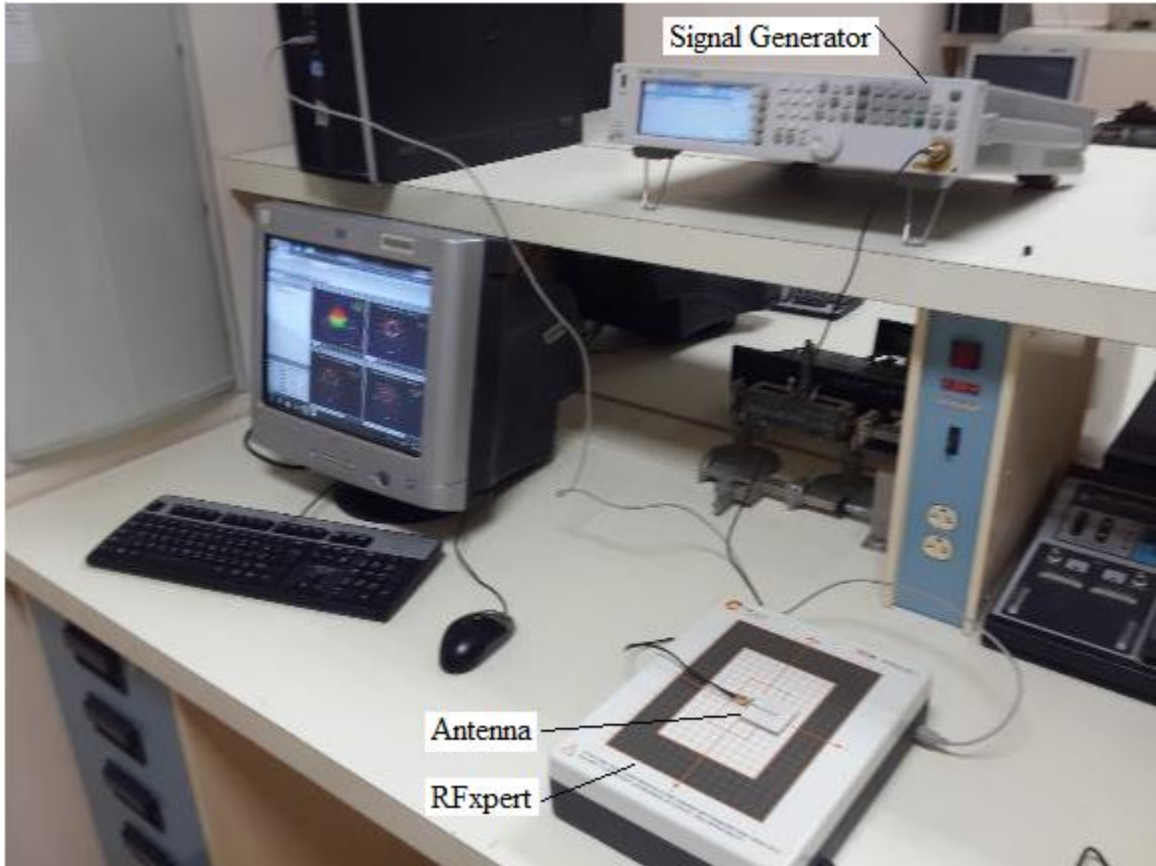


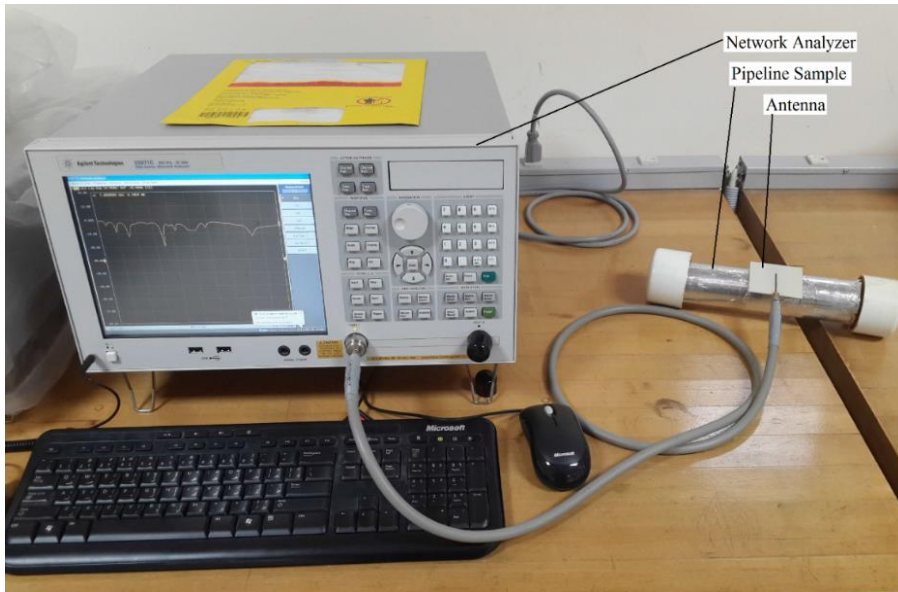
Figure 5-8: Aperture Coupled Microstrip Line Antenna Radiation Pattern Measurement

5.3.3 S_{11} Measurements Technique for the 3-Phase Contents of the Pipeline

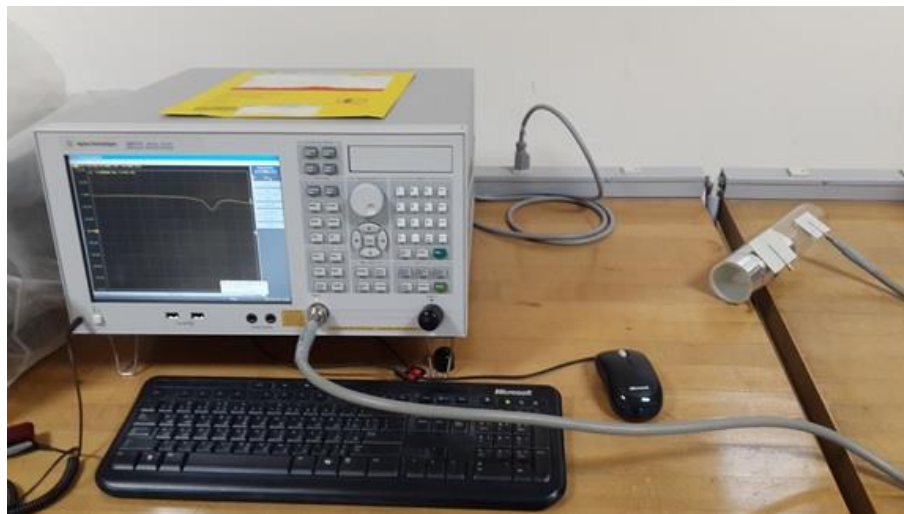
The 1st part of this measurement process; VNA was used to measure the reflection response (S_{11}) of the antenna, integrated within the 2-inch pipeline with multi-phase contents. This setup is shown in Figure 5-9(a) for a shielded Plexiglass pipeline for measuring two-phase content ratio for oil-air mixture. Similar setup but with different measurement technique for water-oil mixture uses an un-shielded pipeline or pipeline without silver shielding. In Figure 5-9(b), the pipeline has two antennas, one integrated in

the shielded part of the pipeline and the other in the non-shielded part. These antennas are used to measure the three-phase contents of the pipeline.

The aim of the 2nd part of this measurement is to develop a prototype of a standalone unit that can measure the pipeline content ratio without using network analyzer. Standard S-band components are used for this setup to redirect the reflected signal voltage from the antenna to an Arduino microprocessor unit [78] that compares the voltage level with the pre-stored look-up table to provide output.



(a)



(b)

Figure 5-9: S_{11} Measurement of the Aperture Coupled Antenna within the Pipeline Using Network Analyzer
(a) Two-phase Measurement and (b) Three-Phase Measurement

The setup for measuring the reflected signal using a microwave circuitry is shown in Figure 5-10. The 2-inch diameter pipeline used in this experiment is made of Plexiglass with permittivity of 2.7, wall thickness of 3 mm and length of 230 mm. The radiating patch

is carefully placed in the designated place within the pipeline; so that the aperture and the microstrip feed line can be properly aligned. The aperture is cut from the silver foil wrapped around the inner surface of the pipeline. The antenna assembly is very similar to the antenna fabricated and shown in Figure 5-3. The S-band (2-4 GHz) microwave components shown in Figure 5-10 are: voltage Control Oscillator (VCO), Circulator (CIR), Directional Coupler (DC) and a Crystal detector. In this experiment, the microwave signal is generated through the VCO, which need a 15 V for biasing and a tunable voltage is used to generate the required frequency. The signal is then fed to input port (port 1) of the circulator that output the power from port 2, where port 3 of the circulator is terminated with a 50 ohm matching impedance to protect the VCO from any unwanted reflected signals. The output signal from the circulator is connected to the input of the directional coupler. The output of the coupler is used to excite the aperture coupled antenna within the pipeline. The reflected signal (S_{11}) from the antenna is output from the coupled port of the directional coupler to an S-band crystal detector. Note that in this figure the signal voltage of the detector is input into a voltmeter to get the voltage or power level of the reflected signal. This allows the verification/fine-tuning of the look-up table, formulated using the software model in chapter 4, to relate the reflected signal level with the content ratio of multi-phase contents of the pipeline.

The setup with Arduino microprocessor is shown in Figure 5-11. The purpose of this proof of concept setup is to demonstrate that a self-sufficient measurement system can be developed with all the look-up tables stored in the memory of the microprocessor. Although the resolution of this basic setup is not very good, this setup proofs that a portable

device can be formulated from this concept to detect the content ratio of the petroleum-carrying pipeline.

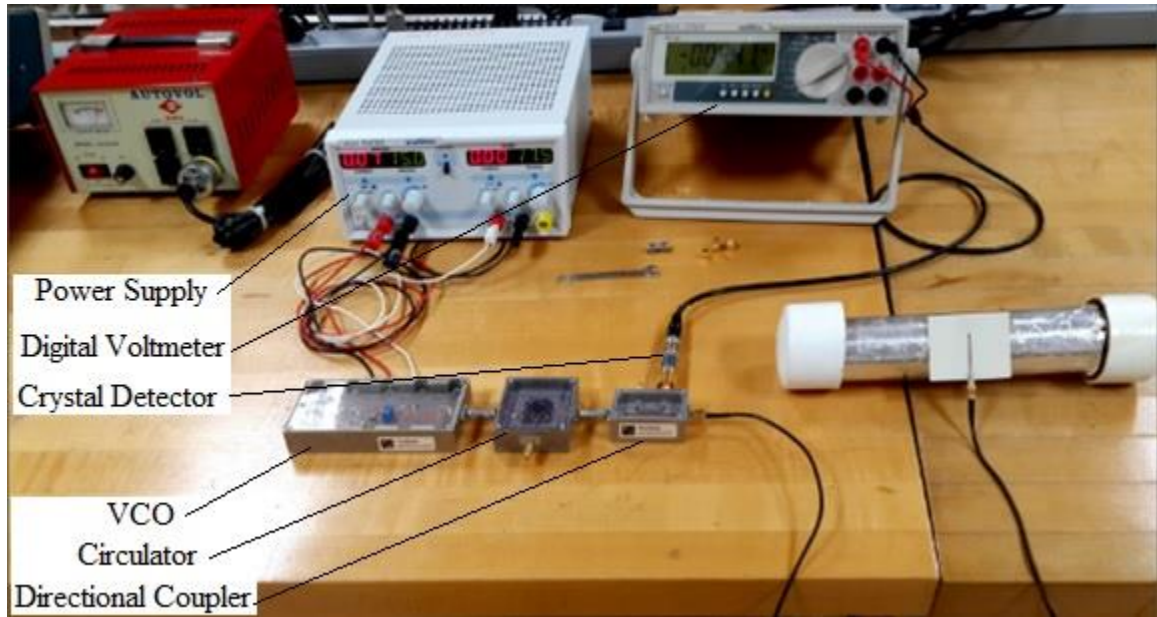


Figure 5-10: Microwave Circuitry for Detecting the Reflected Signal from the Pipeline

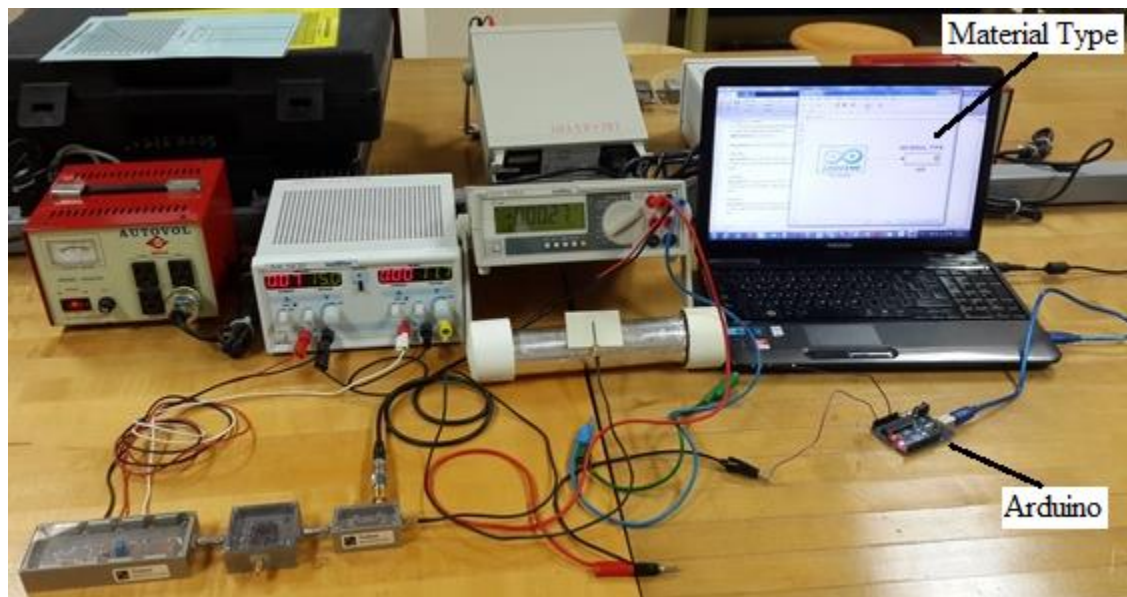


Figure 5-11: Microwave Circuitry with Arduino for Detecting, Analyzing and Displaying the Pipeline Contents

5.4 Experimental Results and Comparison

The experimental setups used in this research work are described in the previous section. The experimentally measured results are presented in this section. The experimental results are also compared with the related simulated responses presented in chapter 4.

5.4.1 Antenna Results

The measurements started with the determination of the correct relative permittivity of the Plexiglass material used for antenna substrate. This required the reflection response of the fabricated aperture coupled patch antenna on a flat Plexiglass substrate (of Figure 5-2) to be measured. Using the experimental setup of Figure 5-4, this measurement resulted in the antenna resonating at 4.0 GHz. Now superimposing this experimental response on the simulated chart of Figure 5-12, it can be concluded that the dielectric constant of the Plexiglass used in this research work is $\epsilon_r=2.7$. This finding is used in the simulated antenna models in chapter 4 to list the S-parameter responses in the look-up table. This look-up table links the antenna resonance with the content ratio of the pipeline.

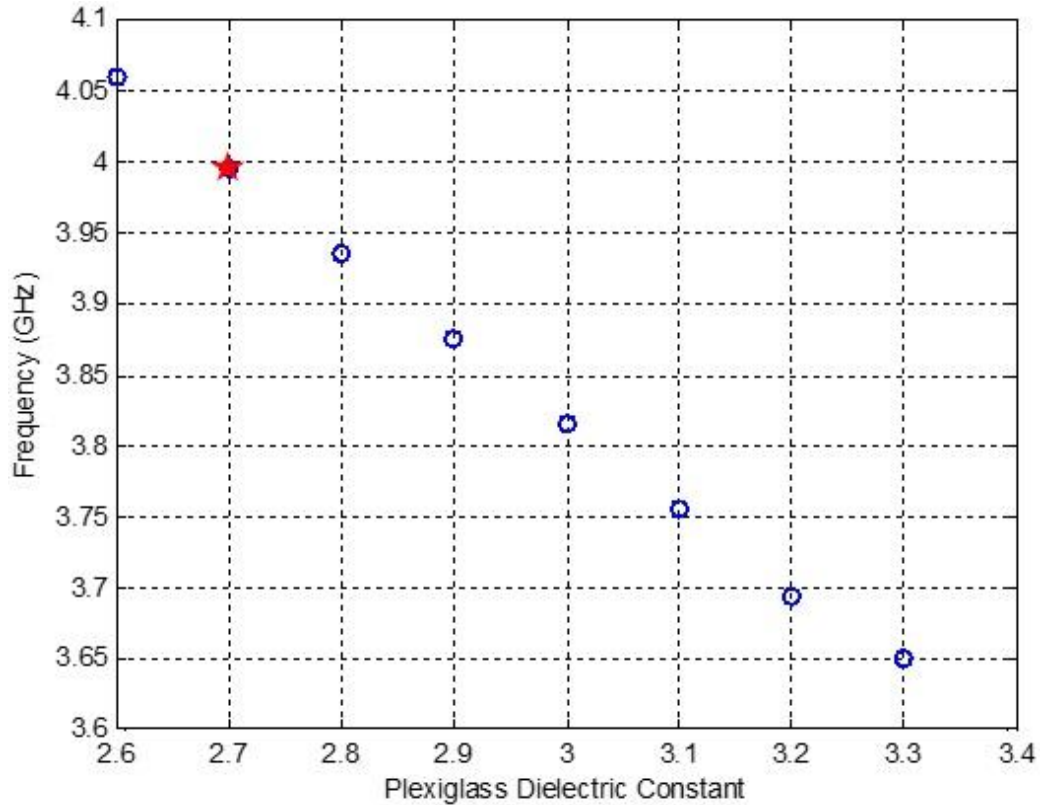


Figure 5-12: Antenna Resonant Frequency for Different Dielectric Constant of Plexiglass

Now using the correct relative permittivity of the Plexiglass substrate, the aperture coupled patch antenna was re-simulated (as presented in chapter 4). The simulated and experimental S_{11} responses of the antenna are superimposed in Figure 5-13. Note that the experimented 10 dB impedance bandwidth of the antenna is 4.6%. To experimentally verify the simulated radiation properties of this antenna, measurement setup shown in Figure 5-6 is used. The simulated and measured 3D radiation pattern is plotted in Figure 5-14. The $\phi=90^\circ$ cut of the pattern is shown in Figure 5-15. Although the experimental and simulated results are almost agreed, it is clear from these figures that the experimental setup is unable to measure the back lobe of the patch antenna.

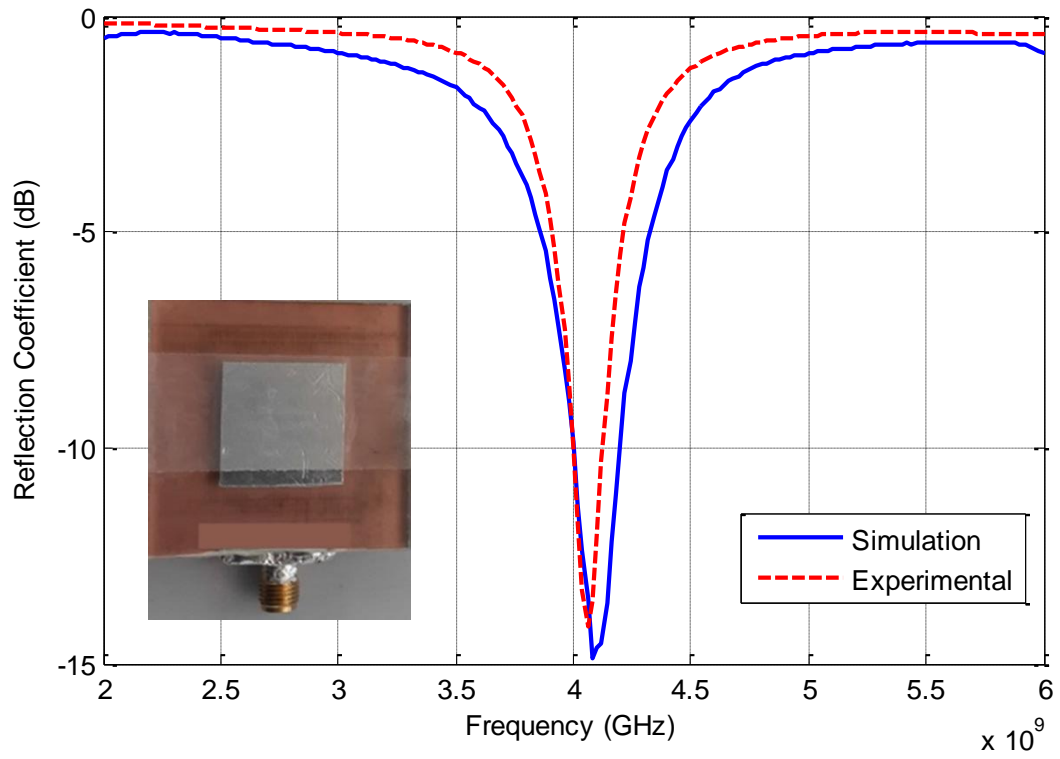
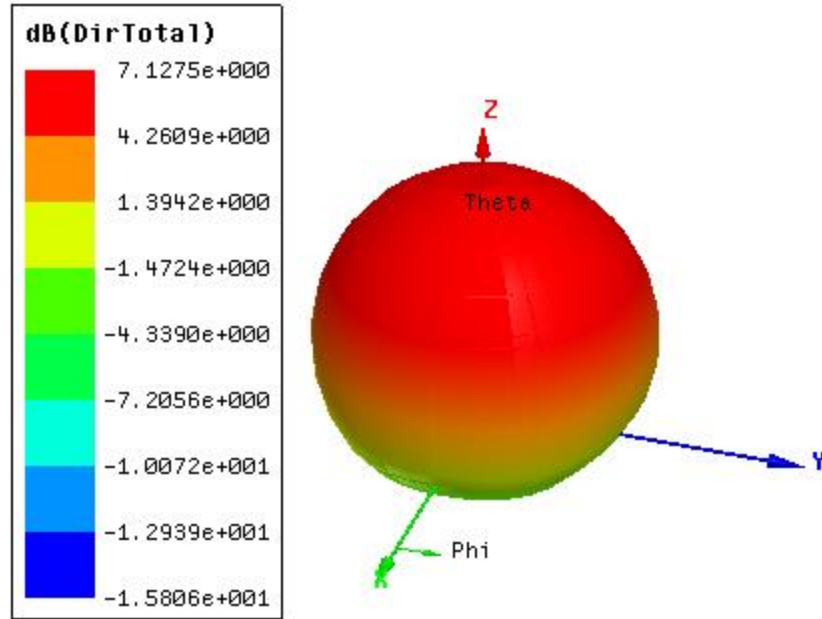
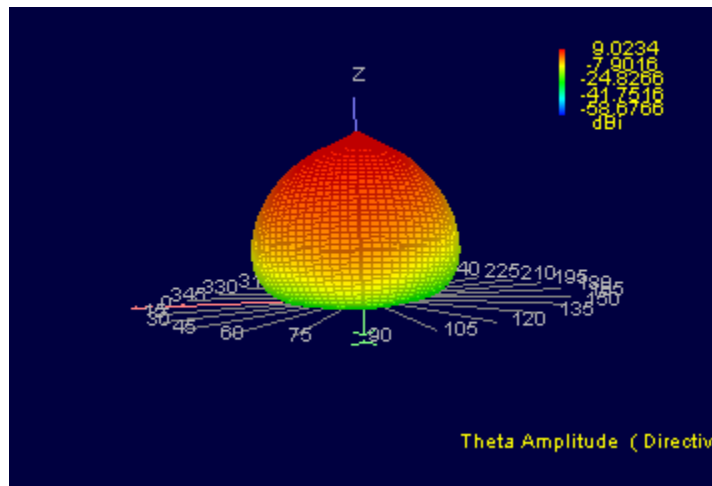


Figure 5-13: Simulated and Measured S_{11} for the Aperture Coupled Patch Antenna



(a)



(b)

Figure 5-14: 3D Polar Plot of the Designed Antenna Directivity, (a) Simulation Using HFSS (b) Measured Using RFXpert

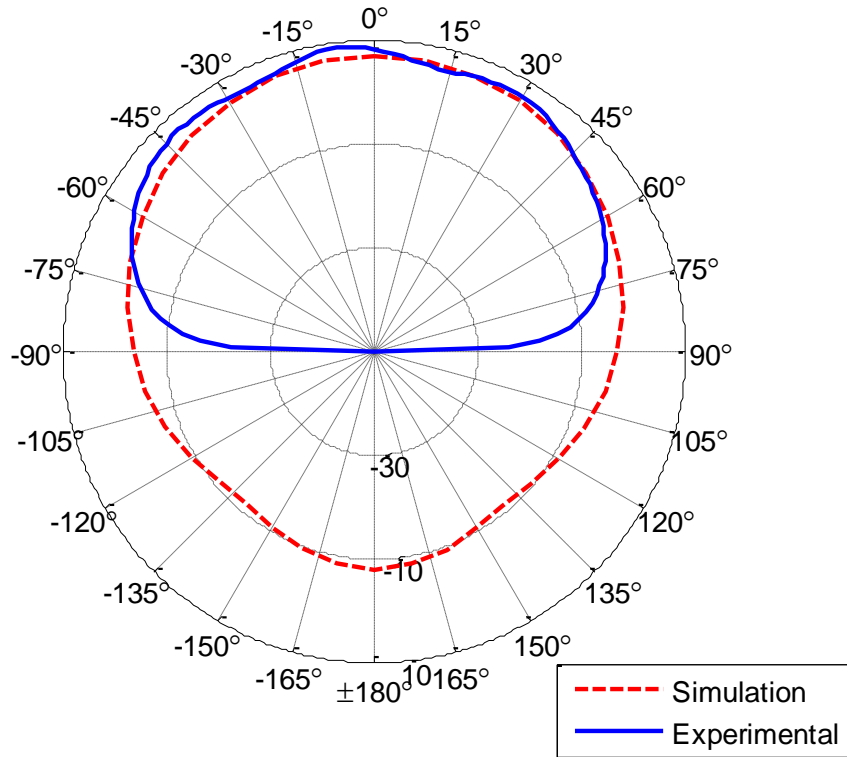


Figure 5-15: Simulated & Measured 2D Radiation Pattern at PHI=90°

To check the changes in resonance characteristics due to curved Plexiglass substrate, the S_{11} response of the antenna (shown in Figure 5-3) is also experimentally observed and plotted in Figure 5-16. Note that a slight reduction in the impedance bandwidth and a 9% shift in the resonant frequency are observed. This is important to fine-tune the look-up table used to link the content ratio of the pipeline with the resonant behavior of the antenna.

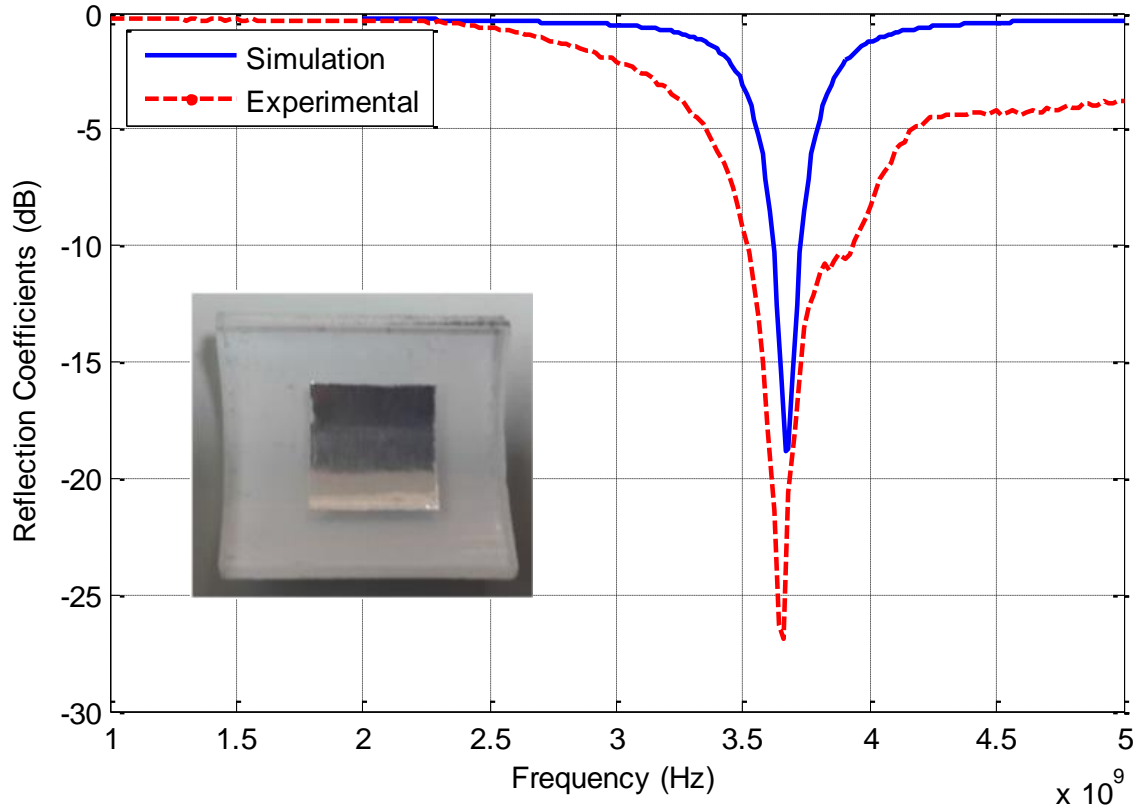


Figure 5-16: Simulated and Measured S_{11} for the Antenna Designed on a Curved Plexiglass

5.4.2 Antenna S_{11} Measurements for Two-Phase Contents of the Pipeline

The pipeline sample used in the measurements is provided from the Petroleum center of the Research Institute, KFUPM. The 2-inch pipeline is made from Plexiglass with $\epsilon_r=2.7$, wall thickness of 3 mm and length of 230 mm. The optimum designs of the Plexiglass pipeline with integrated antenna, discussed in the previous chapter, are for: (a) pipeline covered with silver shielding or conducting-layer and (b) pipeline without the silver shielding. Both cases are investigated here due to experimentally verifying their individual advantages in measuring the content ratio of the pipeline. Note that the design of patch antenna for monitoring the mixture is modified to resonate at 3 GHz. Since the

investigation started by monitoring two phase mixture (air and oil only), 3 GHz patch optimally worked with a two-phase mixture with 50% oil and 50% air. This is because (as explained in chapter 4) the antenna within the 2-inch shielded pipeline resonated at 2.4 GHz for oil-filled and at 3.5 GHz for air-filled cases. Another reason for selecting this frequency is to eliminate the higher order modes, which interfered with the measurement process as oil or water contents of the mixture are increased. The measurement results of a 2-inch pipeline, excited with a 3 GHz patch for both shielded and unshielded cases are presented in the following subsections:

(a) Measurement of the Shielded Pipeline with Two Phase (Oil-Air) Mixture:

The designed patch antenna is carefully placed within the 2-inch shielded pipeline sample in order to monitor the levels of its two-phase contents. As pointed out in chapter 4 that the antenna positioned on the side of the pipeline exhibited better measurement resolution compared to the antenna placed at the top/bottom of the pipeline. Using the network analyzer, the S_{11} responses of the measurement setup (shown in Figure 5-9) is plotted in Figure 5-17. Note that for the shielded pipeline, the figure displays distinct antenna resonances at 3.24 GHz, 3.19 GHz and 2.71 GHz for 0 % (all air), 10 % and 50 % oil within the oil-air mixture, respectively. In chapter 4, the simulated results of equivalent two-phase mixture with 10% increment of oil is shown in Figure 4-12. The simulated and measured reflection responses of the air filled (0% oil) shielded 2-inch pipeline is plotted in Figure 5-18. The oil-air mixture with 10% oil and 50% oil cases are validated with measured results as shown in Figure 5-19 and Figure 5-20, respectively. Excellent agreement between the simulated and experimental resonant frequencies validates the idea of look-up table in determining the contents of multi-phase pipeline. Additional reflection

losses (lower $|S_{11}|$) are due assumed loss-tangents of oil within the simulated model and inaccuracies during assembling the aperture coupled antenna within the pipeline.

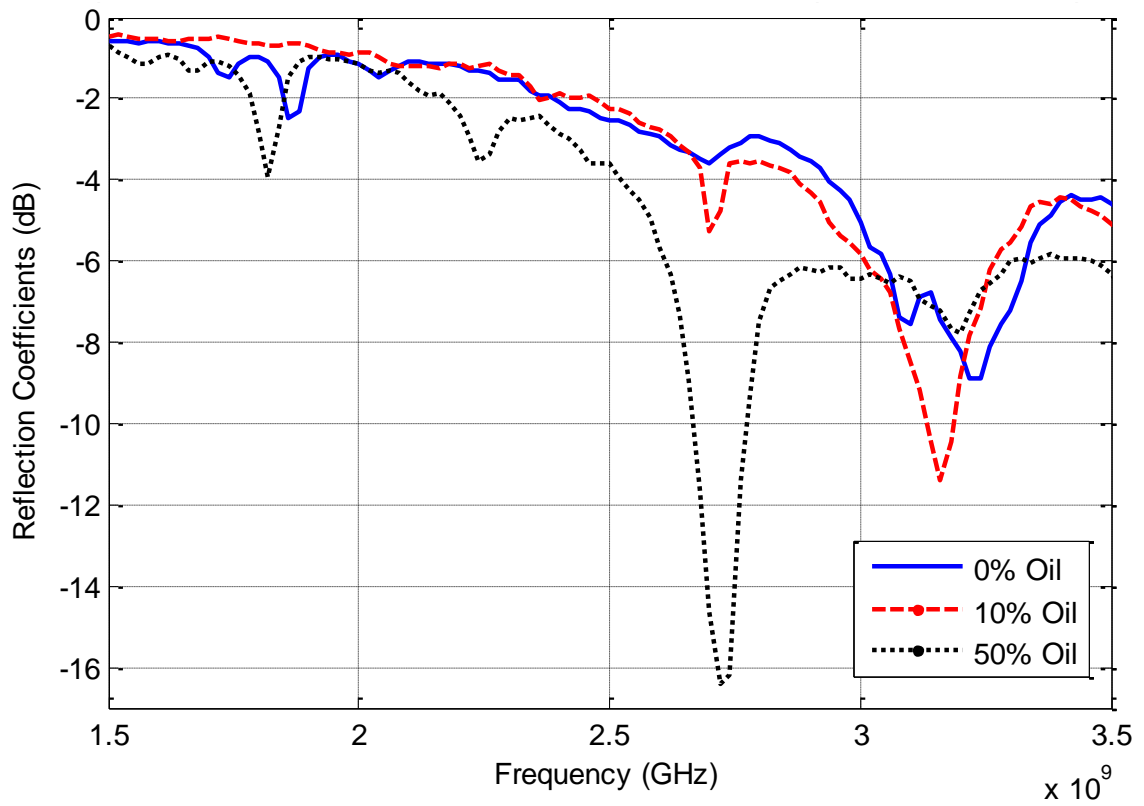


Figure 5-17: Measured S_{11} for a Pipeline Filled with Air, 10 % & 50 % of Crude Oil

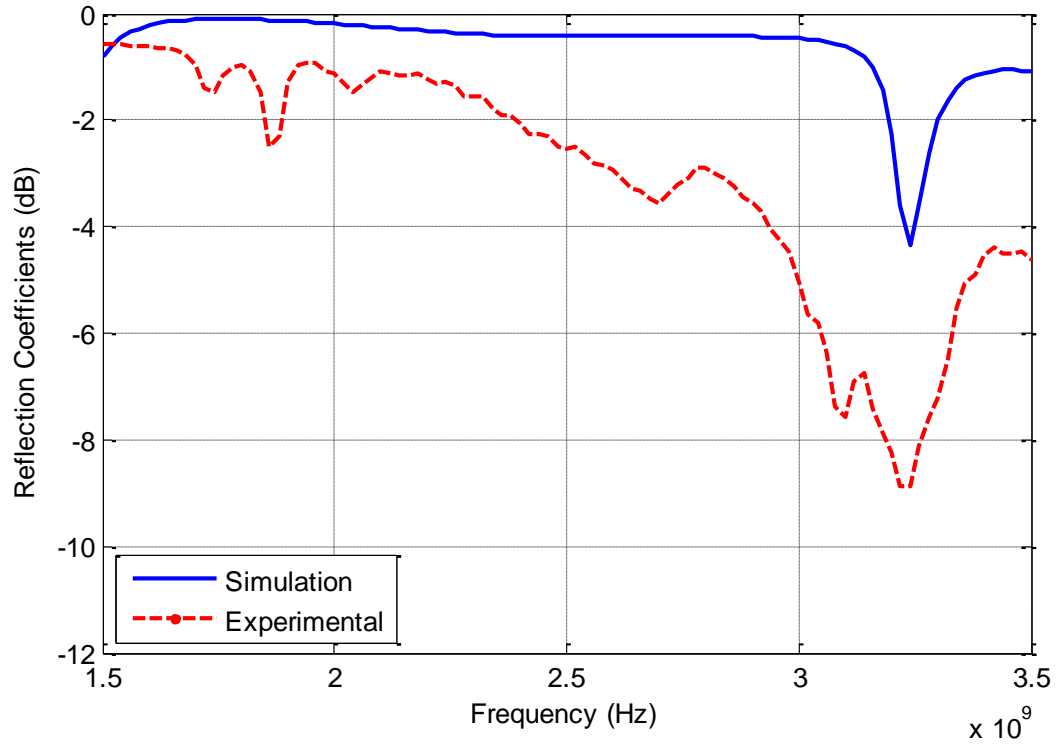


Figure 5-18: Simulated and Measured S_{11} for a Pipeline Filled with Air

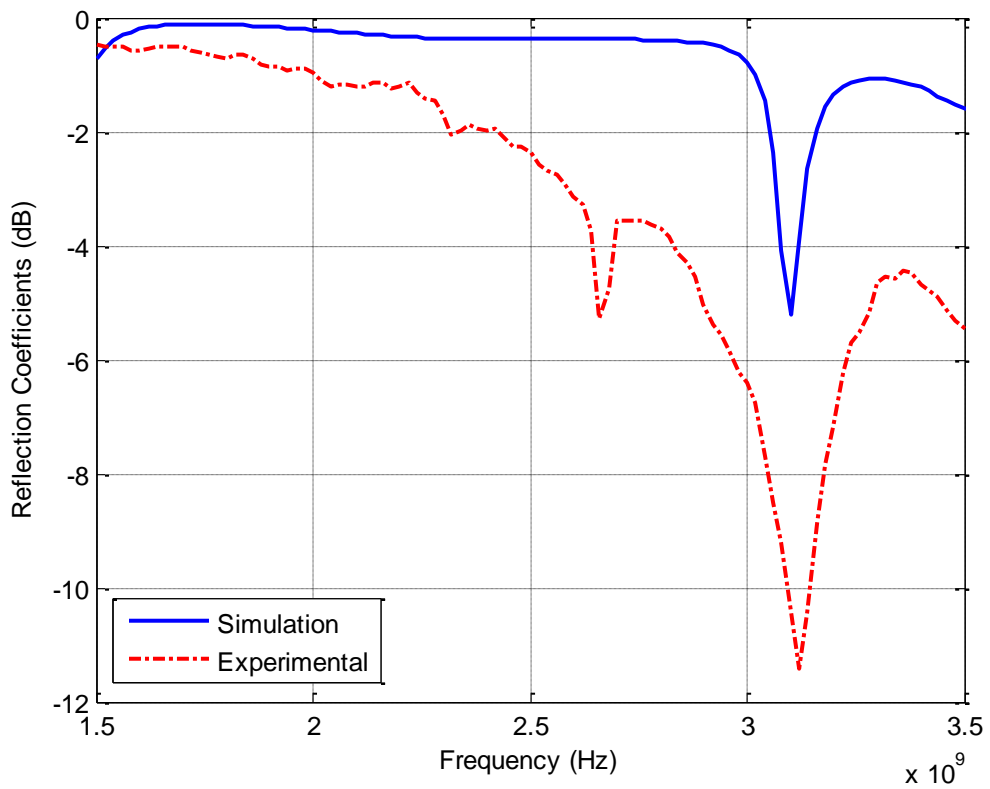


Figure 5-19: Simulated and Measured S_{11} for a Pipeline Filled with 10 % of Crude Oil

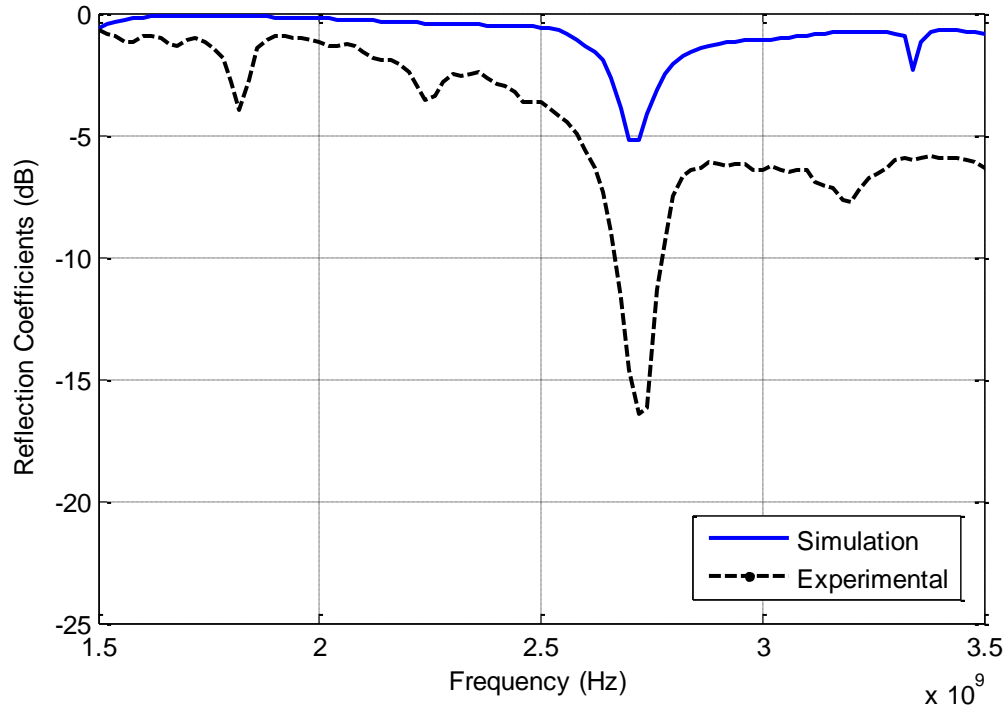


Figure 5-20: Simulated and Measured S_{11} for a Pipeline Filled with 50 % of Crude Oil

(b) Measurement of the non-Shielded Pipeline with Two Phase (Water-Air) Mixture:

To monitor the content ratio of the two-phase mixture of water-air, the 3 GHz antenna used earlier needs to be modified. This is because the resonant frequency of a water filled 2-inch pipeline is 0.44 GHz and the presence of higher order modes cause detection problem when using a 3 GHz aperture coupled antenna (as also explained in chapter 4). To remedy this situation, two methods can be adopted: (1) Redesign the antenna to resonate at a lower frequency or (2) excite an un-shielded portion of the pipeline with the same 3 GHz antenna. The 2nd method is used in this research work. The experimental setup used is similar to the one shown in Figure 5-9(a), but with non-shielded pipeline (pipeline not covered by silver sticker). The removal of the silver shielding from the outer edge of the

Plexiglass pipeline minimized the generation and support of the surface waves which probably reduced the number of unwanted reflected modes. This allowed the power level of the reflected waves due to change of water-air contents of the pipeline more distinctive and easy to monitor. The simulated reflection coefficient for different water-air contents of the two-phase mixture is re-produced in Figure 5-21, where the reflected power level of the 3.5 GHz signal changed with changing water level from 4% to 40% in steps of 4%. Note that the monitoring of water-air mixture is different from the one presented earlier for oil-air mixture. The earlier method depended on the shift of the resonant frequency with the changing contents of oil-air portion within the mixture. However, this measurement depends on the change in power level of the reflected wave (S_{11}) depending on the contents of water-air portion within the mixture. Therefore, for a 2-inch unshielded pipeline with integrated aperture coupled antenna, the experimentally observed power level of the S_{11} response is plotted in Figure 5-22, for four different levels of water within the water-air mixture. Compared to the simulated results, although the resonant frequency slightly shifts for different level of water, the power of the reflected signal demonstrates similar pattern. Figure 5-23 shows the superimposed plot of the simulated and measured S_{11} responses of the antenna, for the case of a pipeline filled with 8%. Thus, by measuring the lowest power level of the S_{11} signal, and using the look-up table created by the simulated responses, one should be able to determine the ratio of the water-air contents within the pipeline.

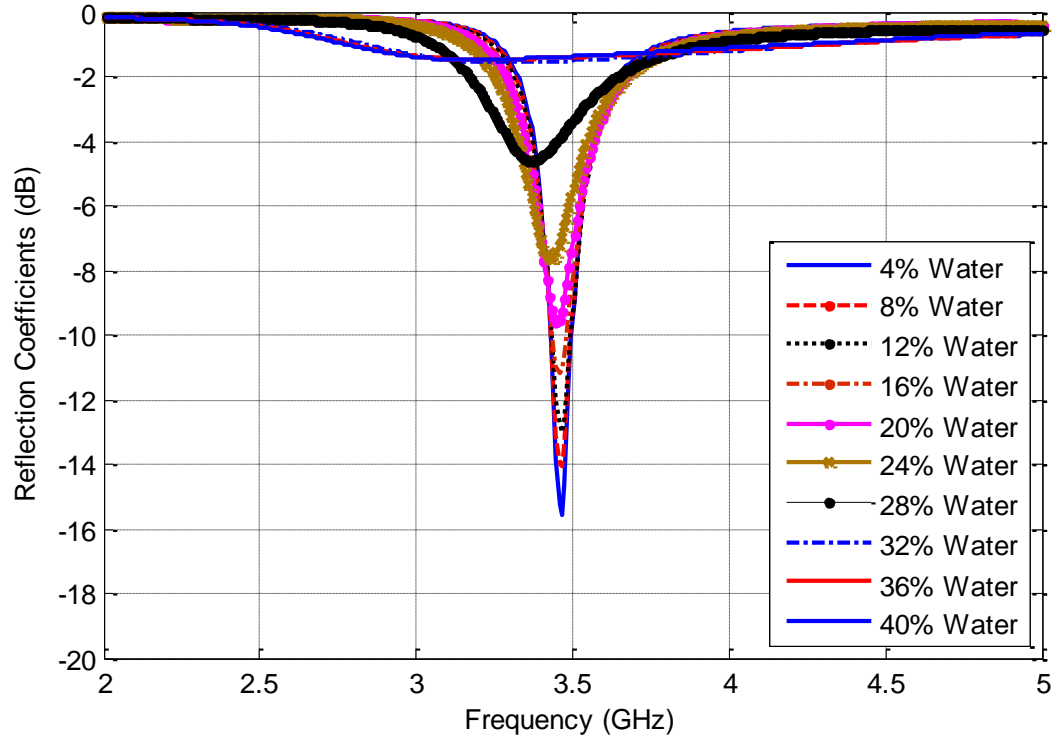


Figure 5-21: Simulated Reflection Coefficient of the 2-inch Pipeline for Different Water-Air Proportions

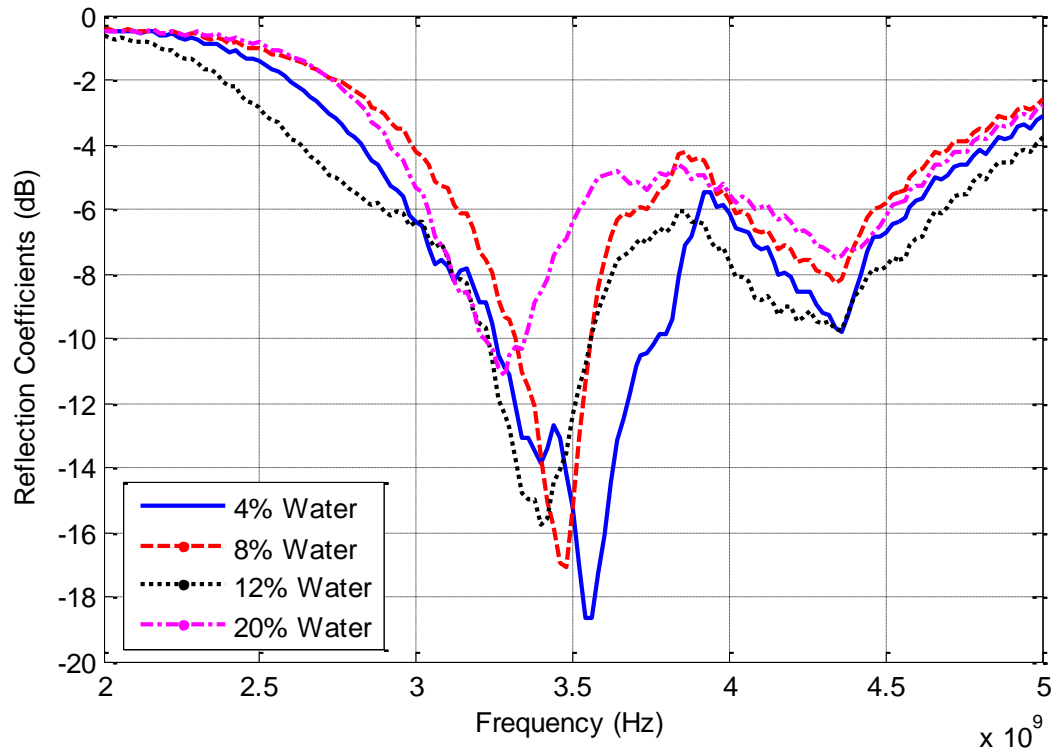


Figure 5-22: Measured Reflection Coefficient of the 2-inch Pipeline for Different Water-Air Proportions

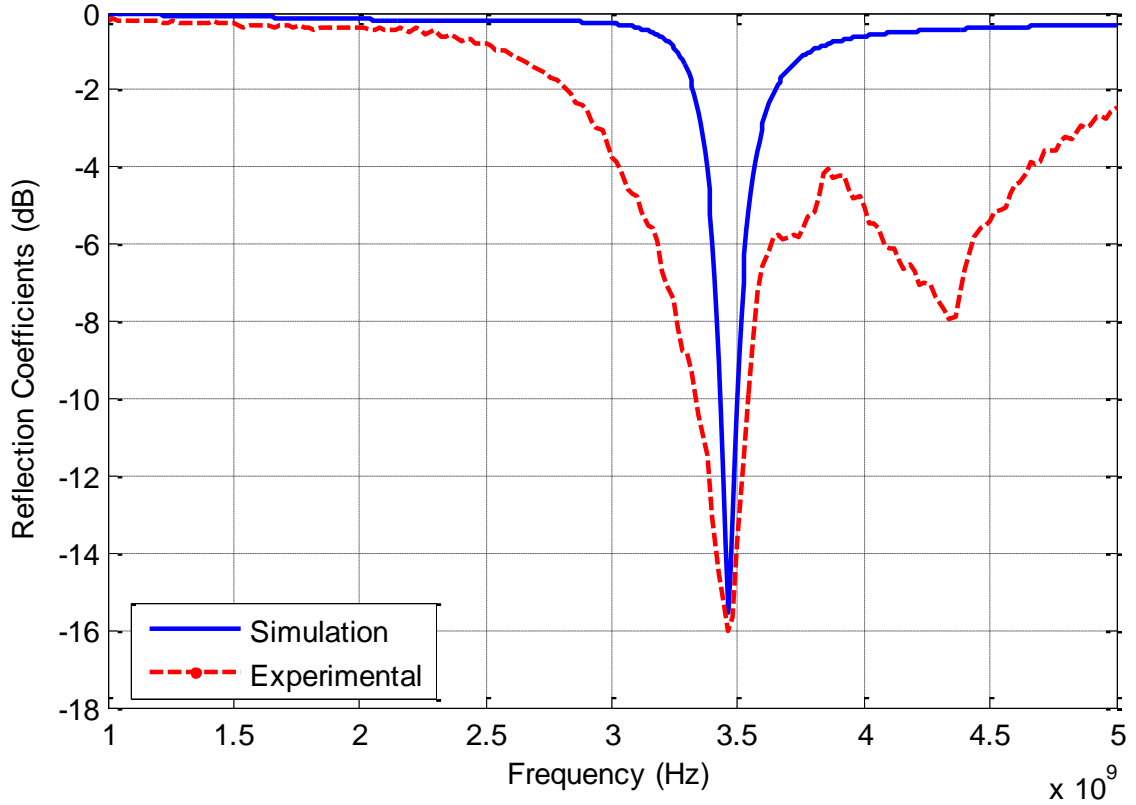


Figure 5-23: Simulated and Measured Reflection Coefficient of the 2-inch Pipeline filled with 8% of Water

The S_{11} responses of pipeline with water-oil (two-phase) mixture are not measured since the existence of the air cannot be completely avoided. Similar cases of measurements involving the three phase (air-oil-water) mixture within the pipeline are discussed in the next section.

5.4.3 Antenna S_{11} Measurements for Three-Phase Contents of the Pipeline

The experimental setup used for this case is shown in Figure 5-9(b). Note that two embedded aperture coupled antenna is used as follow; one integrated within the shielded section of the pipeline and the other integrated in the non-shielded part of the pipeline. They will be used to separately measure the oil-air and water-oil contents of the mixture, as explained in the previous section. The mutual coupling between the antennas is very low due to adequate separation between them. At the beginning of this experiment, the antenna in the non-shielded pipeline is excited to measure the power level of the reflected (S_{11}) signal. With the help of the look-up table, this value will help in determining the water level. For a three-phase mixture with 10% water, the antenna in the shielded pipeline is excited to measure the changing S_{11} resonant frequencies for different level of oil-air mixture. The experimental results for this case are plotted in Figure 5-24 for oil levels of 10% to 80% with steps of 10%. The related simulated S_{11} response of a 2-inch pipeline with three-phase mixture (10% water and changing oil level) is reproduced (from chapter 4) in Figure 5-25. Comparing the simulated and experimental responses, it is noted that the same trend is achieved, where it starts at a resonant frequency of 3.42 GHz and as the amount of oil increased the resonant frequency is shifted to the left in a distinct manner.

The following experiment uses the shielded antenna to determine the oil level within the three-phase pipeline. This is done by monitoring the resonant frequency of the antenna in the shielded region of the pipeline and comparing it with the look-up table of chapter 4. The result revealed that the oil content of the mixture is approximately 60% level of the pipeline. Now the antenna in the non-shielded part of the pipeline is energized to

determine the portion of the water within the pipeline. The related experimentally observed S_{11} response for the pipeline three-phase mixture (with 60% oil and changing water level) is plotted in Figure 5-26. Note that the power (voltage) level of the 3.3 GHz reflected signal decreases with increasing water level. This is accepted due to the high relative permittivity and conductivity of the sea water. The related simulated response for a 2-inch pipe with 60% oil and changing water level from 4% to 20% is re-plotted in Figure 5-27. Note that the experimental data validates the simulated results, which is used to create the look-up table of chapter 4.

The difference between the measured and the simulated reflection coefficients power level in the two-phase and three-phase cases are due to the difficulty in the alignment of the aperture location on the substrate to that located on the pipeline outer surface and this because of the curvature of the pipeline. This difference in the power level is not exists when the flat Plexiglass is placed on the fabricated antenna as shown in Figure 5-13.

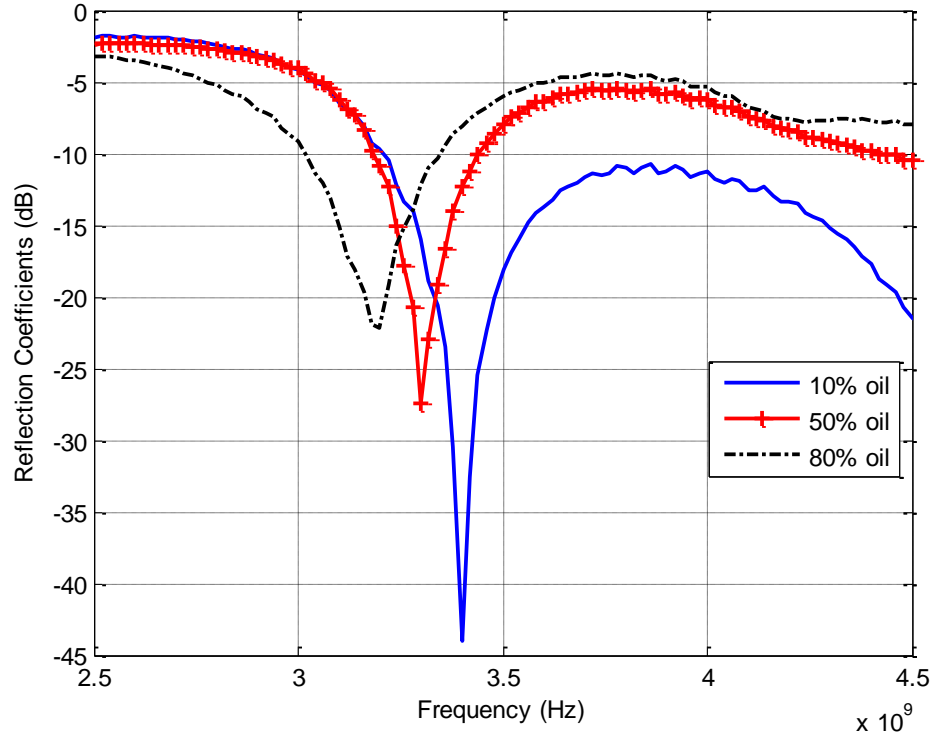


Figure 5-24: Measured S_{11} for a Pipeline for Different Air-Oil Proportions at a 10% of Water

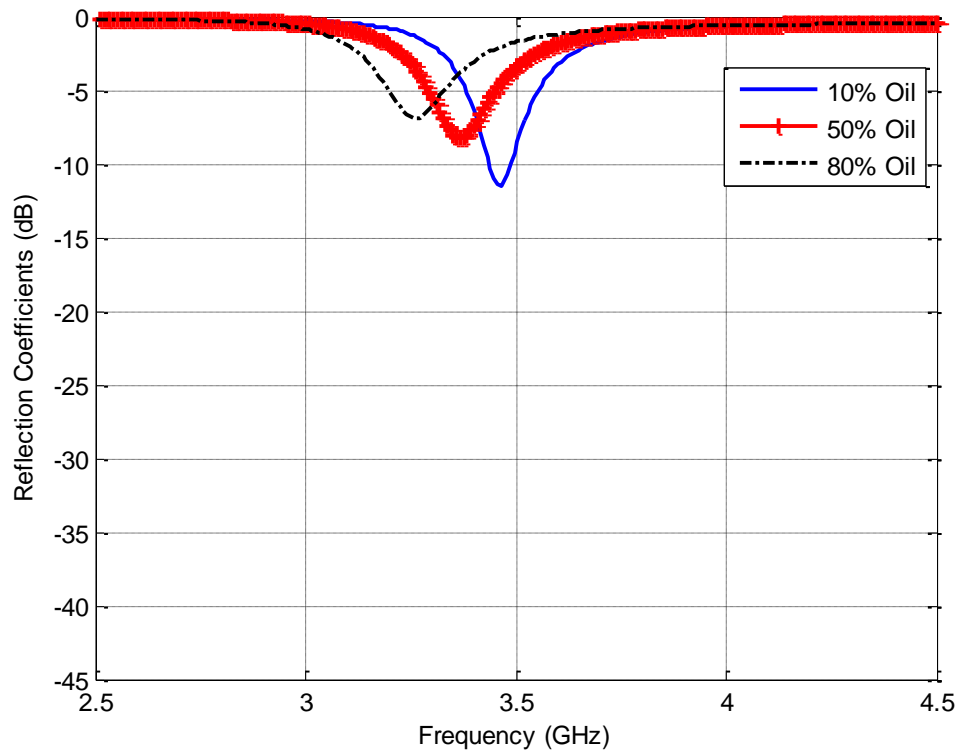


Figure 5-25: Simulated Reflection Coefficient of the 2-inch Pipeline for Different Air-Oil Proportions at a 10% of Water

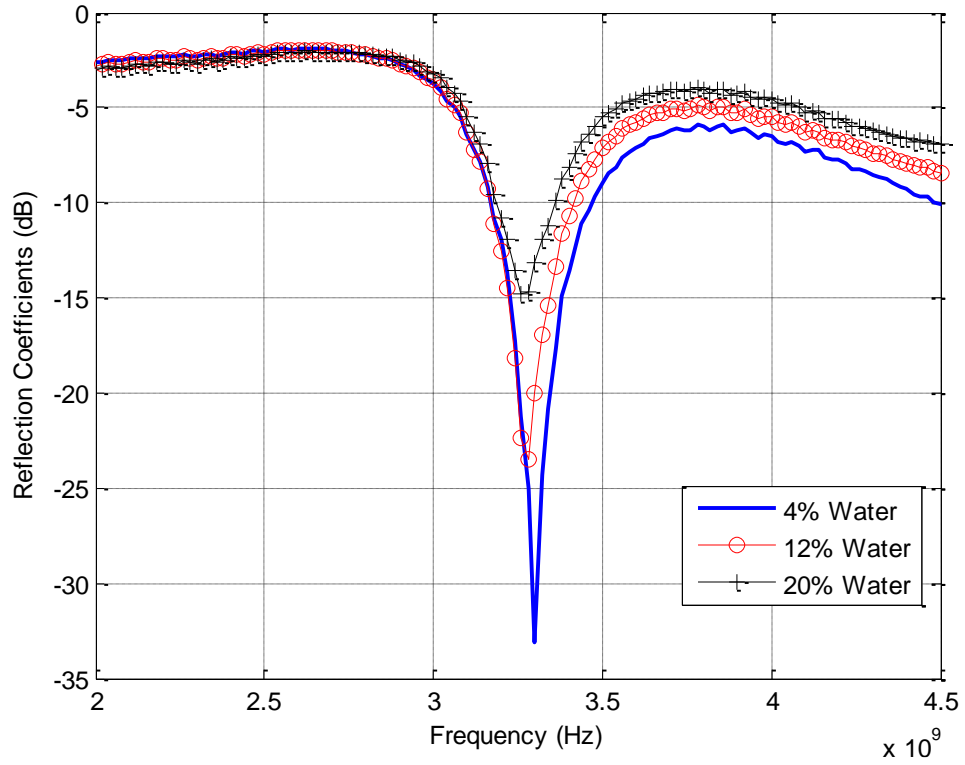


Figure 5-26: Measured S_{11} for a Pipeline for Different Water Proportions at 60% of Oil

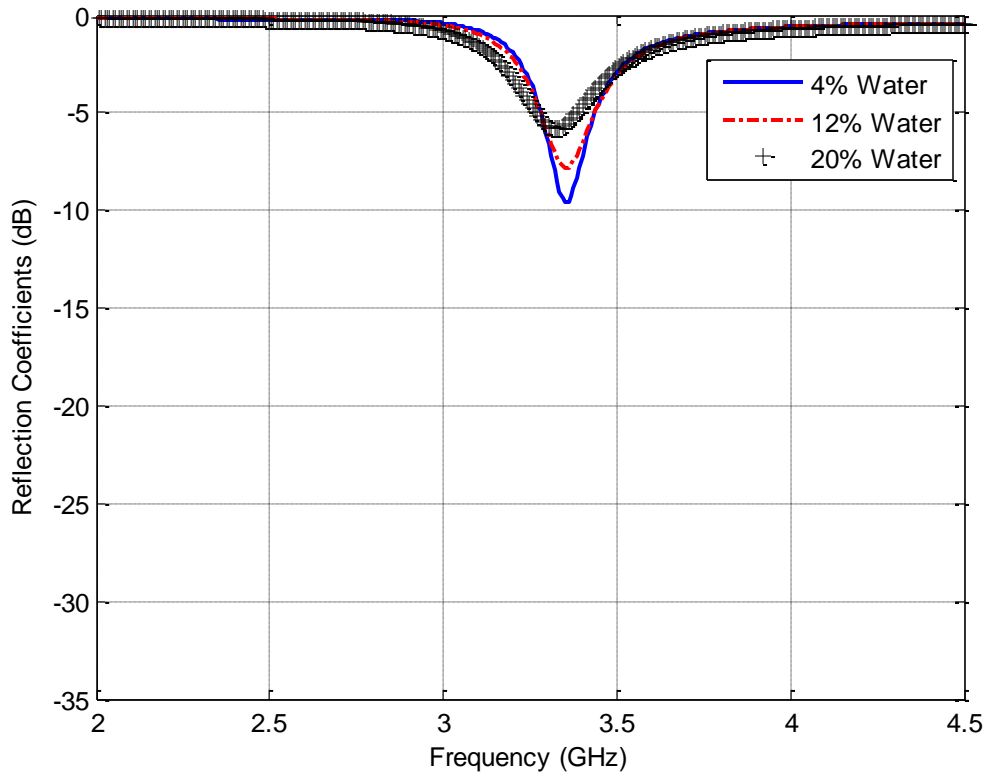


Figure 5-27: Reflection Coefficient of the 2-inch Pipeline for Different Water Proportions at 60% of Oil

5.4.4 Measurements of S_{11} Response without Using Network Analyzer

Now using the setup without involving the network analyzer, shown in Figure 5-10, the VCO is tuned to generate 3.3 GHz signal, which is used to excite the antenna located in the non-shielded part of the pipeline. Since the pipeline is filled with a three-phase mixture of which 60% oil is present, the range of voltage values measured using the voltmeter for different level of water are tabulated in Table 5-1.

Table 5-1: Detected Voltages Responses for Different Materials

	Air (mV)	Oil (mV)	Water (mV)
Min.	81	456	737
Max.	112	510	779

To make a simple prototype of the measurement device, the voltmeter is replaced with an Arduino microcontroller as shown in experimental setup of Figure 5-11. Since all the look-up tables can be stored in the Arduino microcontroller memory and it allows analogue input signals, simple program can display the contents of the three-phase mixture on an interfaced laptop. In this setup, the voltmeter that provides the 15-volt power supply to the VCO can be replaced with a battery. Similarly, an electronic circuit connected to a battery can also generate the variable voltages needed to be supplied to the VCO for tuning the frequency of the generated microwave signal. The power supply of the Arduino board can be provided from the laptop through a USB connection, used for displaying the content

ratio. However, when testing this setup a voltage drop after connecting the Arduino is occurred, which mean a block should be inserted before the Arduino either to amplify the signal or to match the input impedance of the Arduino with the one received from the crystal detector.

For hardware implementation of the Arduino board; the transmit and receive system has been designed and programmed. Figure 5-28 represent the MATLAB Simulink's blocks used to program the Arduino. It starts by selecting one of the analog input of the Arduino to receive the voltage level from the crystal detector that represent a certain pipeline contents level, the selected input was pin 4. The received data is directly converted to a digital value through an Analog to Digital Convertor (ADC) that is associated with the input pin. After that, a gain block is added to convert the 10-bit digital number to something we can interpret, by multiplying the digital number by the value of the Arduino maximum voltage, which is 5 and divide by the resolution of the Arduino, which is 1023. Then a MATLAB function that contain the tabulated look-up table is stored in the Arduino memory. Finally, the data containing the proper material type is sent through a serial transmit block, which represent a virtual serial connection to a computer for receiving and displaying the type of the material.

Figure 5-29 represent the program designed on the computer for receiving the data from Arduino, where Figure 5-29(a) represent the sub model inside the Arduino block shown in Figure 5-29(b). The program starts by Serial Configuration block to check the accuracy of the received data through a parity check, stop bit, hand shaking in addition to a baud rate that is used in the transmitter side, which is 9600 and the serial port used, which is COM8. After checking the received data, which is received by COM8 on the computer;

it is then entered to another MATLAB function that associate the received material type decision from Arduino and convert it to a string of characters to be displayed on the computer through a display block.

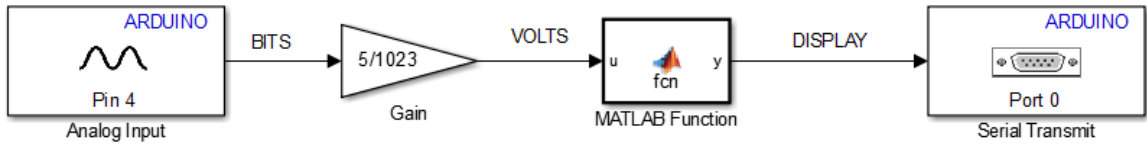
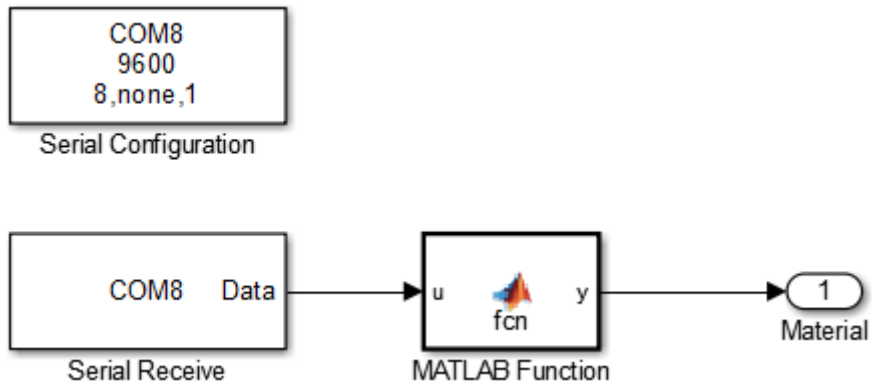
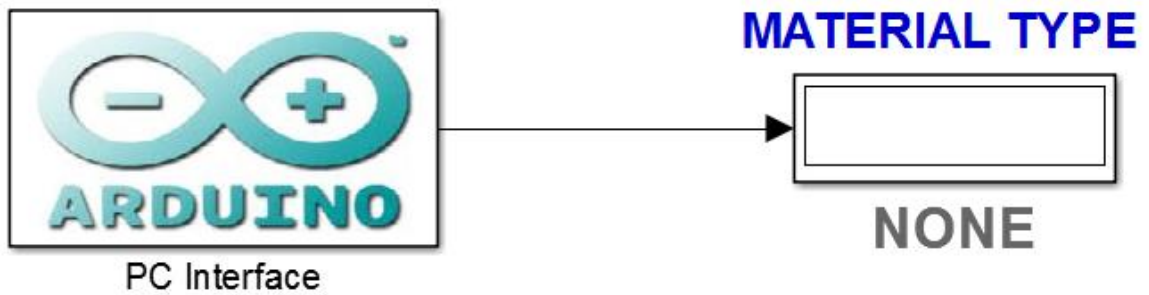


Figure 5-28: Arduino Program



(a)



(b)

Figure 5-29: Computer Side Program, (a) Sub Model for Receiving the Material Decision from Arduino (b)

Displaying the Pipeline Contents

5.5 Conclusion

Monitoring the content ratio of two-phase and three-phase petroleum carrying pipeline is presented. Different techniques are proposed to monitor water and oil contents of the pipeline. To determine the oil contents, the shift in the resonant (S_{11}) frequencies of the antenna, integrated in a shielded portion of the pipeline is used. To determine the water contents, a 2nd antenna, integrated in the non-shielded region of the pipeline is used to monitor the power/voltage level of the reflected signal (S_{11}). These measured values are compared with the look-up tables presented in chapter 4 to determine the oil and water contents of the pipeline. Once the two contents are known, the level of the 3rd content (air) can be calculated. Experimental results are used to verify the simulated results used to create the look-up tables.

CHAPTER 6

CONCLUSION and FUTURE WORK

6.1 Conclusion

In this research, a novel analytical solution for a circular waveguide loaded with two dielectric cylinders is presented to predict the modal behaviors of an ideal petroleum-carrying pipeline with partially loaded oil samples. The resulted mode charts are used to validate a similar HFSS (professional simulator) model of the pipeline in terms of selecting of proper meshing and ideal excitation methods. Once validated, this software model is used to produce simulated mode charts of the pipeline with multi-phase (air-oil-water) contents, which is too complicated to solve analytically.

To introduce practical excitation to the pipeline, two patch antennas are designed and optimally integrated within the pipeline. To monitor the oil and water levels, two different types of measurements are realized by integrating patch antennas in the shielded and non-shielded parts of the pipeline. For air-oil measurements, a 3-GHz antenna is used to avoid higher order modes and generate a distinctive resonance response (S_{11}) with changing oil level of the pipeline. For oil-water measurements, a 3.3 GHz patch antenna is integrated in the non-shielded part to relate the change in water level with the changes in the power level of the reflected signal (S_{11}). Look-up table is formulated for both cases for different level of oil and water contents of the pipeline.

To experimentally verify the simulated results, the measurement setups are fabricated. The experimental S_{11} responses verified the changes in resonant frequencies with changing level of oil within the pipeline. In the 2nd set of experiments, the monitored power level of the reflected signals (S_{11}) corroborated the simulated curves that link the change in water level with change in reflected power. Minor disagreements between the simulated and experimental results are due to the inaccuracy of the in house fabrication process. The drawback of this design that it cannot detect water level more than 30 %, so other antenna could be used to enhance the resolution of our results.

Finally, the standalone setup with microwave components and Arduino microcontroller is designed. This setup is individually tested for demonstration and encouragement of future work.

6.2 Future Work

The research work conducted here can be extended and enhanced in many ways. The enhancement can be on the analytical, design and simulation and experimental parts. Some of these enhancements are:

6.2.1 Analytical Solution

- Since water used in the extraction process of the oil from petroleum well is salty, which mean it has conductivity in addition to the permittivity, so it is imperfect dielectric. Therefore, in order to study this problem, water can be represented using

imperfect dielectric cylinders; accordingly, metallic waveguide loaded with imperfect dielectric cylinders has to be investigated.

- Since the Plexiglass pipeline sample has been used in this research, which represent a waveguide with a dielectric shell, an analytical solution for this case can be derived by considering the fields inside the Plexiglass cylinder to be outward travelling wave instead of a standing wave. To do this Hankel functions of first and second kind should be used.

6.2.2 Antenna Design

- Using a helical antenna around the Plexiglass pipeline as a microwave sensor instead of the aperture coupled antenna used in which more power can be radiated depending on the number of the loops used.

6.2.3 Circuit Design

- Enhance the sensing and programming to take care of different flow types, such as non-steady state flow etc. and display the content level of the multi-phase liquid together with the flow types.

Appendix A

Procedure Followed in Achieving the Optimum Design

The investigated characteristics are pipeline radius, antenna resonant frequency, antenna feeding type, antenna orientation, antenna placement and a conducting coating on the outer surface of the pipeline.

The procedure starts by considering a 4-inch pipeline sample provided from the Research Institute (RI) at KFUPM. The petroleum-carrying pipeline, which made from Plexiglass material, has a thickness of 5 mm, which should be considered in designing the superstrate layer of the antenna. So a superstrate layer should be added on the top surface of the patch in order to simulate this thickness of the pipeline.

The antenna was fed using coaxial feeding, where the inner conductor of the coax is attached to the radiating patch and the outer conductor is connected to the ground plane. This type of feeding is easy to fabricate and has a low spurious radiation.

A.1 Microstrip Patch Antenna without a Superstrate Layer

A coaxial fed microstrip patch antenna is illustrated in Figure A-1. This antenna substrate are made from Duroid, which has a relative permittivity of 2.2 and a thickness of 1.6 mm, the bottom surface of this substrate is defined as a ground plane, which is a perfect conductor plane. The patch is placed on the top surface of the substrate. The dimensions of the patch and the substrate in addition to its radiation behavior are summarized in

Table A-1. The patch is fed through a coaxial cable, which consists of two conductors and a polyethylene material with a dielectric constant of 2.25 to isolate the two conductors. An Air Box is included in the design which has a distance of 0.25λ from the edges of the substrate to enclose the space around the antenna.

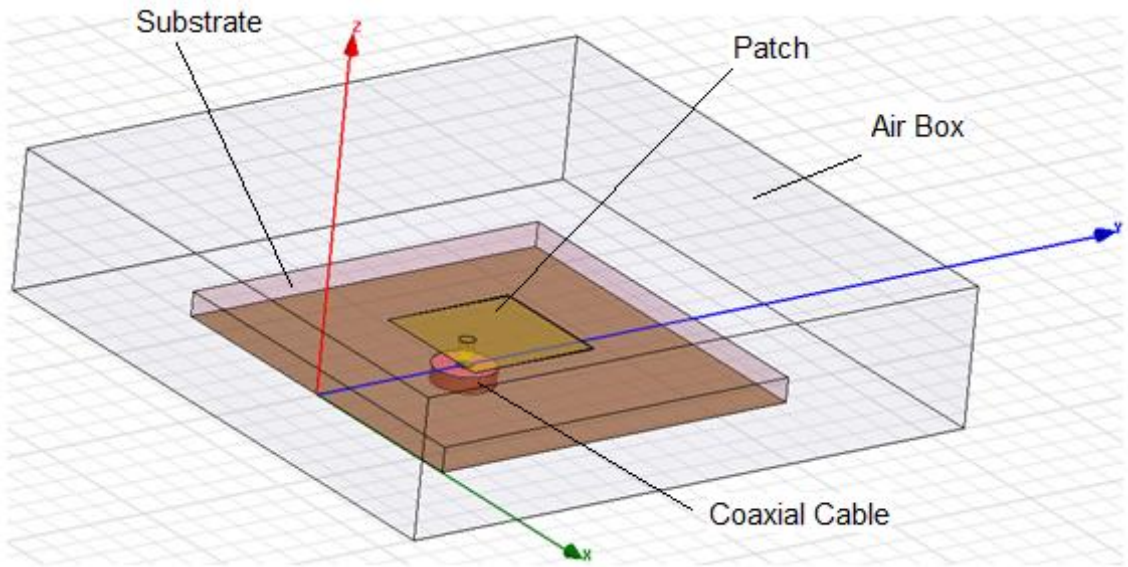


Figure A-1: A Coaxially Fed 10 GHz Microstrip Patch Antenna

Table A-1: Microstrip Antenna Specifications without the Superstrate layer

Patch Width (mm)	8.5
Patch Length (mm)	8.72
Substrate Width (mm)	25
Substrate Length (mm)	25
Substrate Height (mm)	1.6
Substrate Permittivity	2.2
Resonant Frequency (GHz)	10.02
Reflection Coefficient (dB)	-22.03
BW (GHz)	0.6
Gain (dB)	7.9387

The reflection coefficient of this antenna is shown in Figure A-2, which clearly that the antenna is radiating at 10GHz with a reflection coefficient of -22.03 dB and has a 10 dB bandwidth of 600 MHz. The 3D radiation pattern is also shown in the figure, which has a nice radiation on the top surface of the antenna and nothing radiating in the bottom side since there exists a ground plane as expected.

The 2D radiation pattern can be represented through two angular measurements in spherical coordinate system, which are Azimuth and Elevation, the azimuth cut is shown in Figure A-3. Where in part (a) of the figure represent the azimuth cut at $\phi=0^\circ$ and in part (b) represent the azimuth cut at $\phi=90^\circ$. Figure A-4 represent the elevation cut at $\theta=90^\circ$.

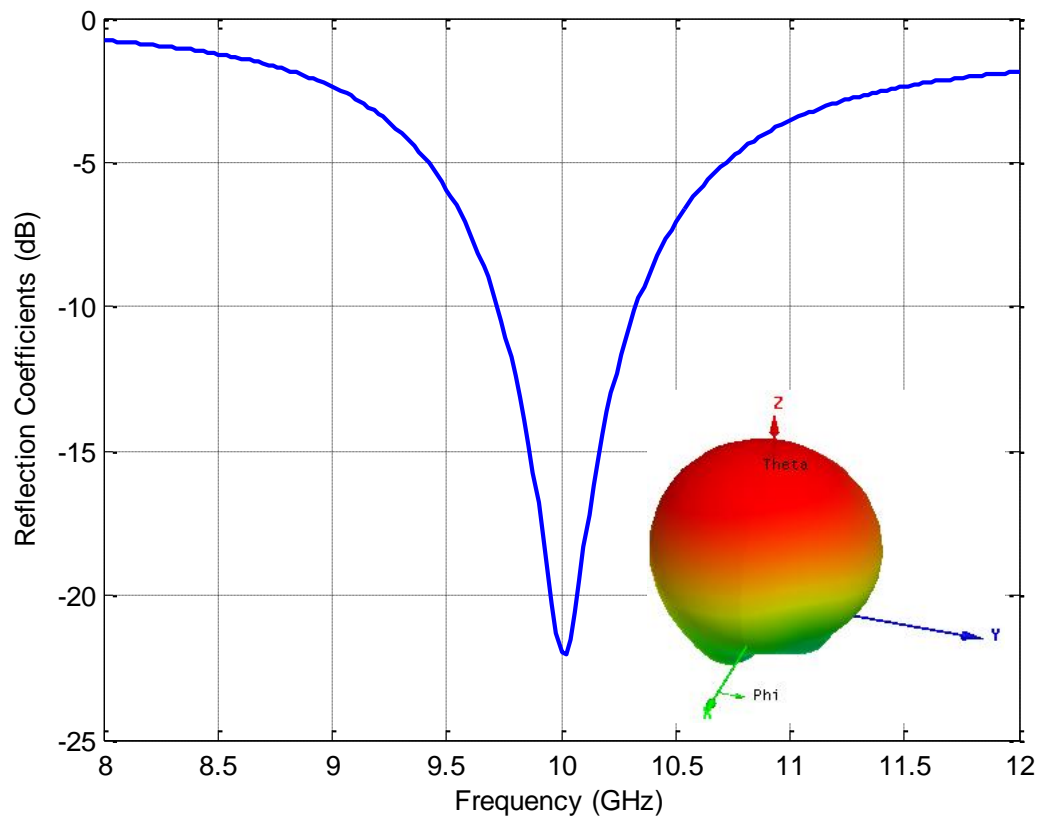


Figure A-2: Reflection Coefficient for the Patch without Superstrate Layer

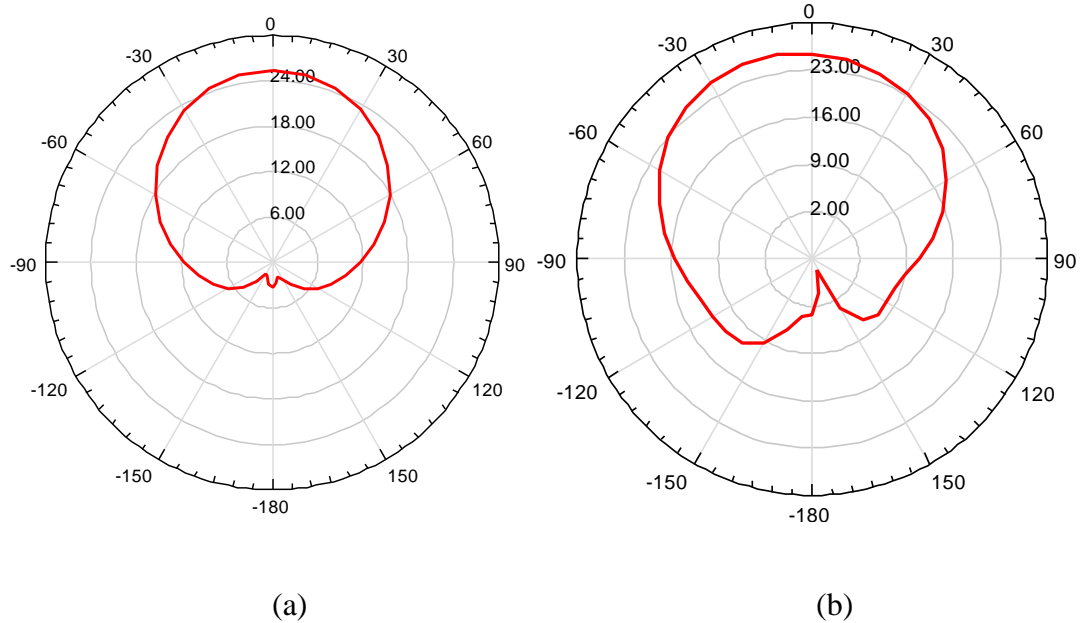


Figure A-3: 2D Radiation Pattern (a) Azimuth Cut ($\phi=0^\circ$), (b) Azimuth Cut ($\phi=90^\circ$)

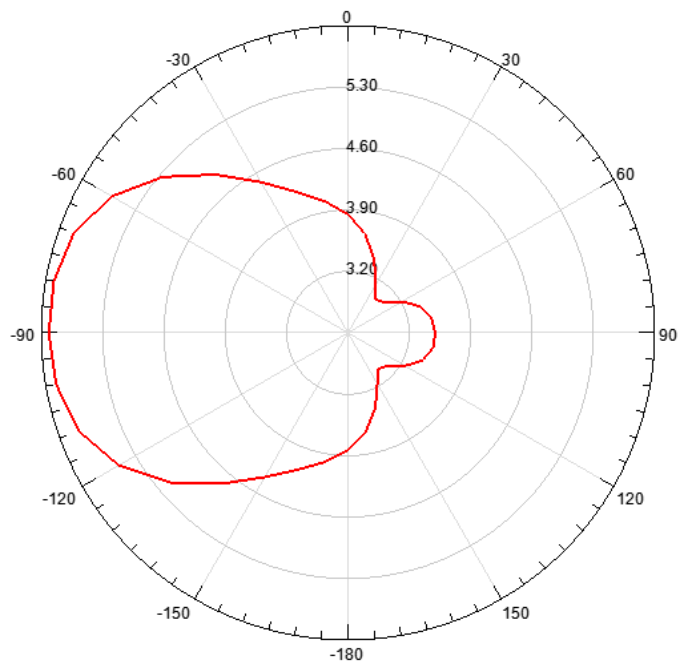


Figure A-4: Elevation Cut of a Radiation Pattern at ($\Theta=90^\circ$)

A.2 Microstrip Patch Antenna with a Superstrate Layer

If the patch is placed on the outer perimeter of the pipeline, then the antenna should be designed by placing a superstrate layer of 5 mm of thickness made from a Plexiglass as shown in Figure A-5; the dimensions of the patch, substrate and superstrate are tabulated in Table A-2. Figure A-6 shows the reflection coefficient for this patch and it has a value of -17.96 dB with a bandwidth of 1.3 GHz and the azimuth cut at $\phi=0^\circ$ and at $\phi=90^\circ$ of the radiation pattern is shown in Figure A-7.

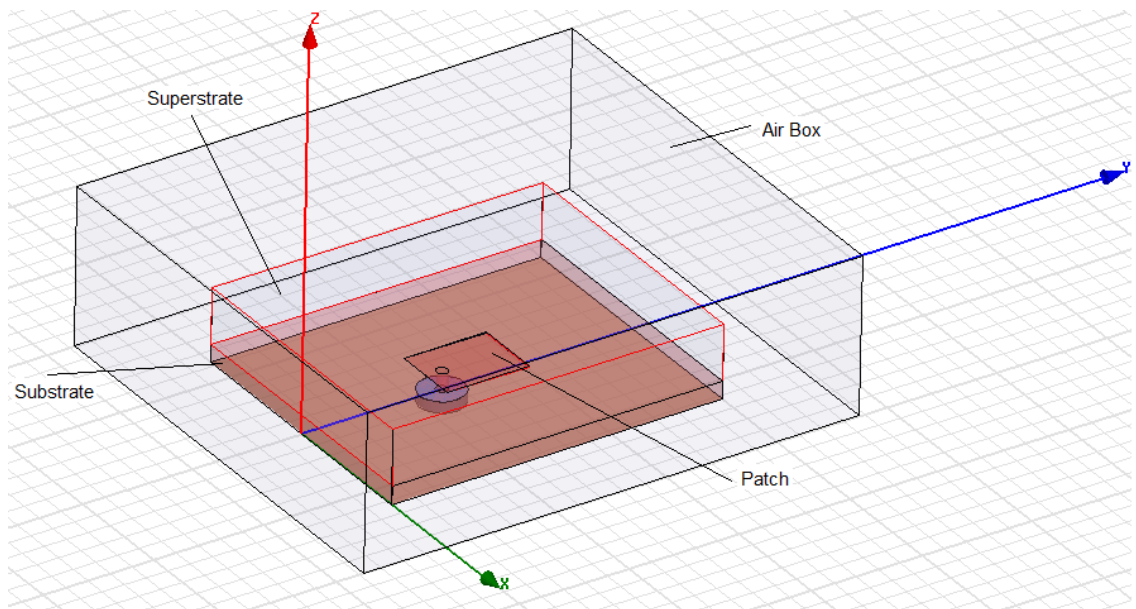


Figure A-5: Microstrip Antenna with Superstrate Fed with a Coaxial Input

Table A-2: Microstrip Antenna Specifications with the Superstrate layer

Patch Width (mm)	6
Patch Length (mm)	7.5
Substrate Width (mm)	25
Substrate Length (mm)	25
Substrate Height (mm)	1.6
Superstrate Height (mm)	5
Substrate Permittivity	2.2
Superstrate Permittivity	3.4
Resonant Frequency (GHz)	10
Reflection Coefficient (dB)	-17.96
BW (GHz)	1.3
Gain (dB)	9.33

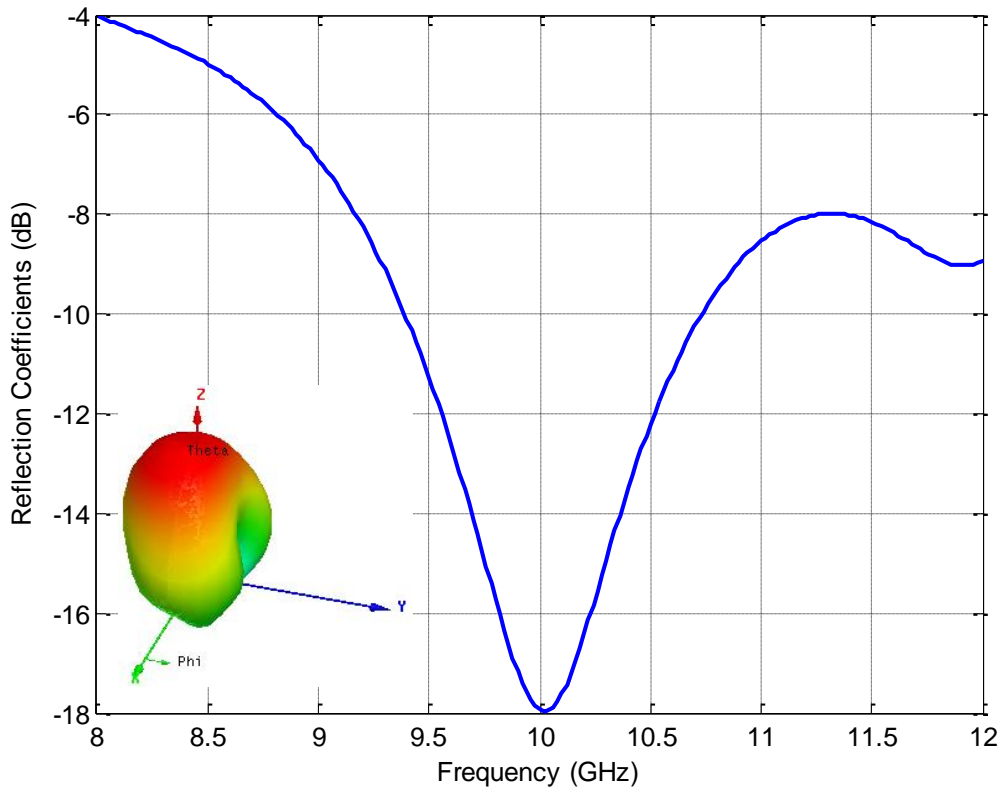


Figure A-6: Reflection Coefficient for the Patch with Superstrate

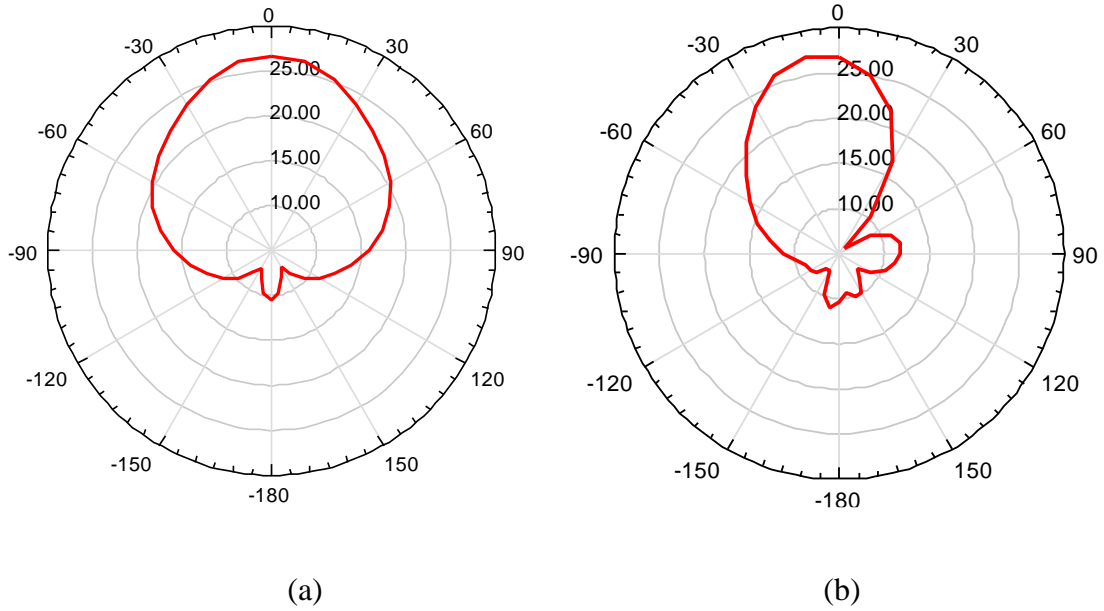


Figure A-7: 2D Radiation Pattern (a) Azimuth Cut ($\phi=0^\circ$), (b) Azimuth Cut ($\phi=90^\circ$)

A.3 Excitation of Two-Phase Petroleum Carrying Pipeline

A.3.1 Coaxial Fed of a 4-inch Pipe Sample

A.3.1.1 Single Microstrip Antenna on a Pipeline

The designed microstrip antenna should now be attached to the pipeline sample as shown in Figure A-8, which represents a section of a pipe with the designed antenna on its side. The superstrate layer here are encountered in the pipeline wall that is made from a Plexiglass material with a permittivity of 3.4. When the pipeline sample is filled with air, the antenna radiates at a resonant frequency of 9.92 GHz with a reflection coefficient of -

20.6704 dB, the 10 dB bandwidth equal to 1.53 GHz as shown in Figure A-9. Figure A-10 shows the two dimensional azimuth cuts at $\phi=0^\circ$ and $\phi=90^\circ$ of the radiation pattern.

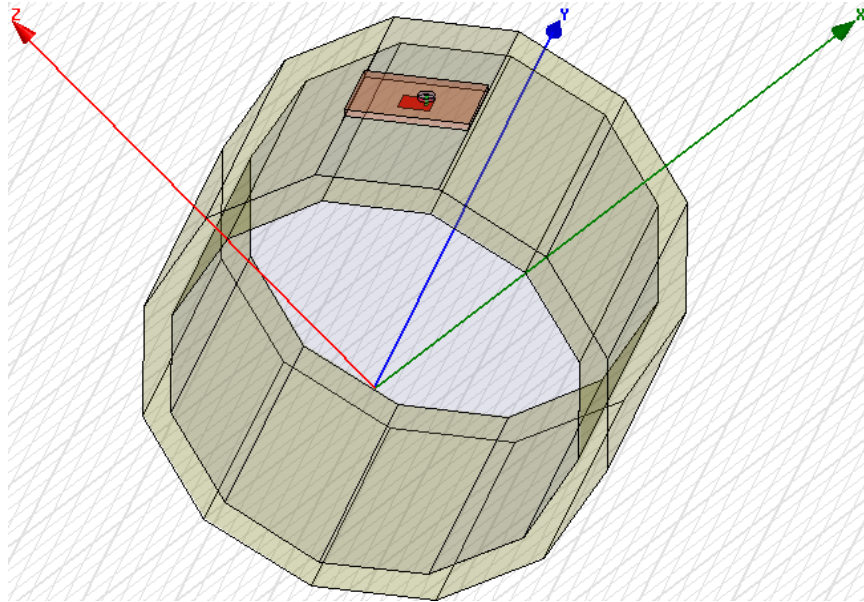


Figure A-8: Model of a Pipeline with the Designed Antenna on its Side

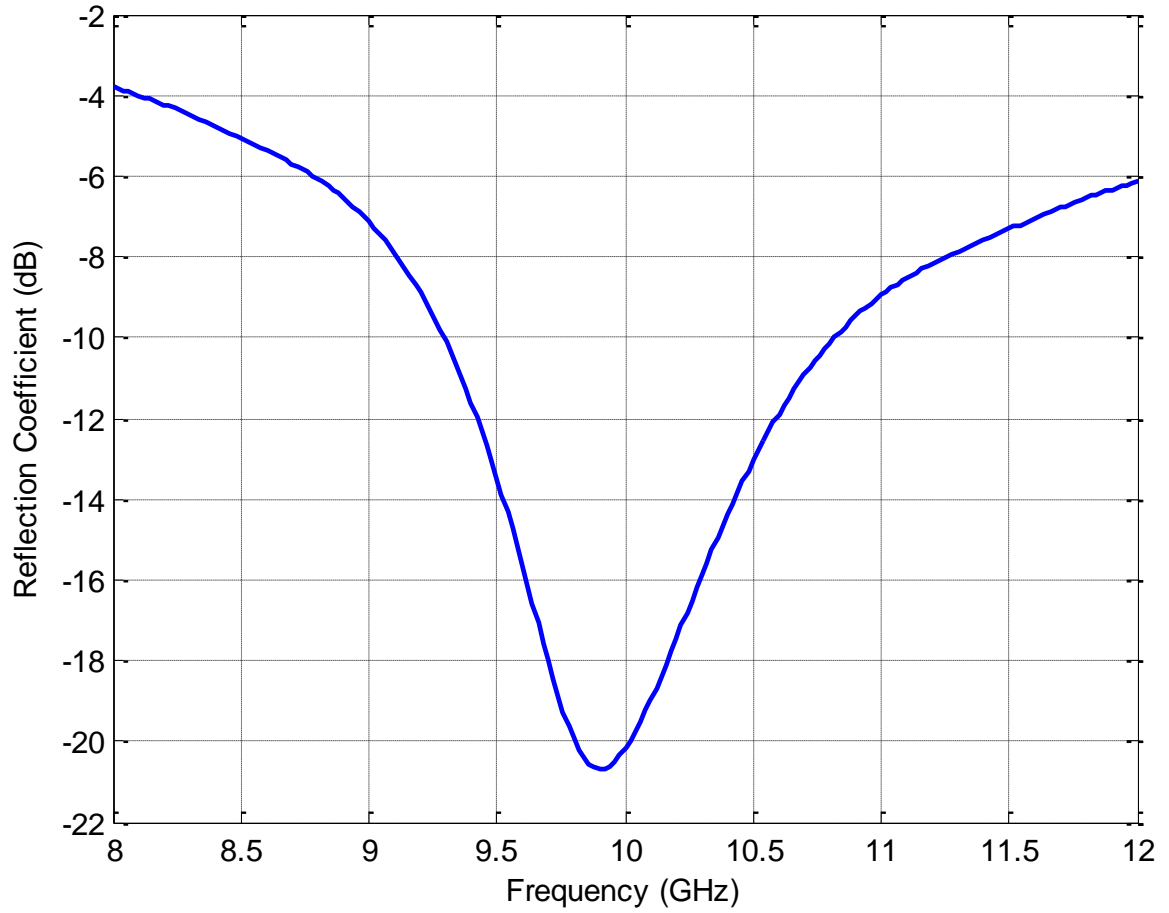


Figure A-9: The Reflection Coefficient of the Model

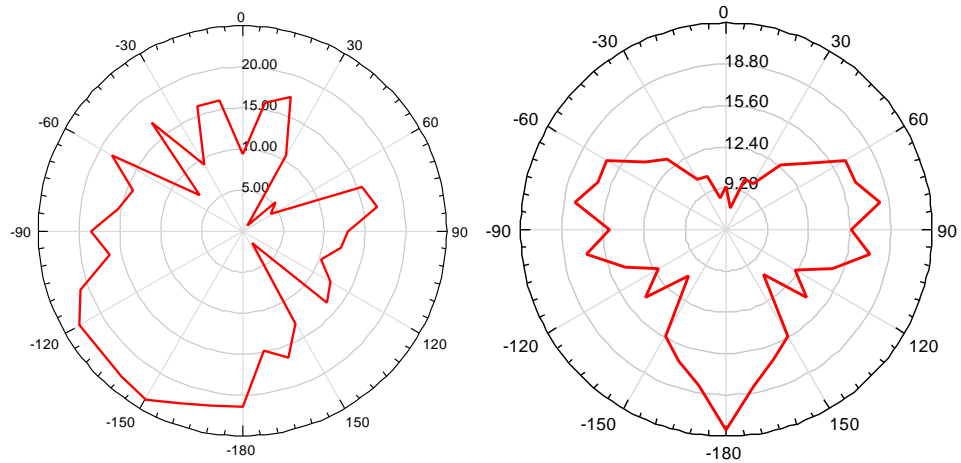


Figure A-10: Radiation Pattern (a) Azimuth Cut ($\phi=0^\circ$), (b) Azimuth Cut ($\phi=90^\circ$)

Three different materials are considered as a content of the pipeline shown above. These materials with the corresponding relative permittivity and operating frequency are summarized in Table A-3. The reflection coefficients of these scenarios is shown in Figure A-11. It is noticed that as the material dielectric constant increases the resonant frequency will reduce.

Table A-3: Center Frequency for the Three Medium under Investigation

Medium	Permittivity	Frequency (GHz)
Air	1	10
Oil	2.15	9.96
Sea Water	81	9.1

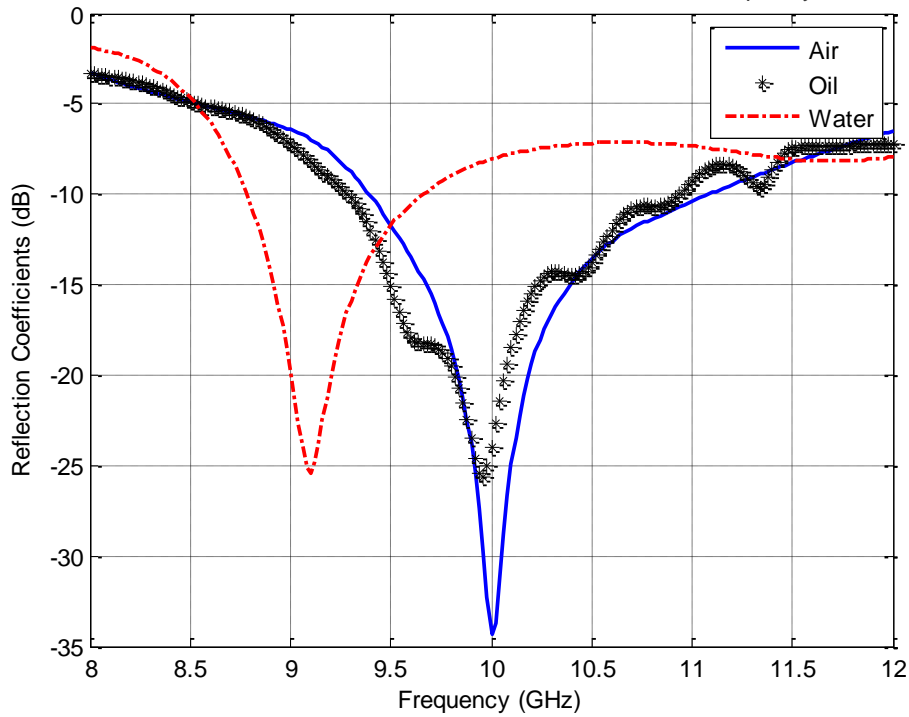


Figure A-11: Reflection Coefficient for Air, Oil and Water versus Frequency for a 4-inch Pipeline

A.3.1.2 Microstrip Antenna Transceiver Attached to the Pipeline

Microstrip antenna transceiver is designed to operate at a center frequency of 10 GHz and it is attached to the pipeline model as shown in Figure A-12. The purpose from this transceiver is to assign one antenna to send a signal and obtain the received signal in order to test if the transmission coefficient will have information about detecting level of the materials inside the pipeline. The reflection coefficient from the transmitted antenna and the transmission coefficient at the received antenna are plotted in Figure A-13. The antenna still resonates around 10 GHz with a -20 dB reflection coefficient. The transmission coefficient has a very low value of -27 dB; the low transmission is because the microstrip antenna is a low profile antenna, which does not radiate high power, especially at this frequency range, which has a wavelength of 30 mm. So, the pipeline radius considered somehow too big to be analyzed by this small antenna.

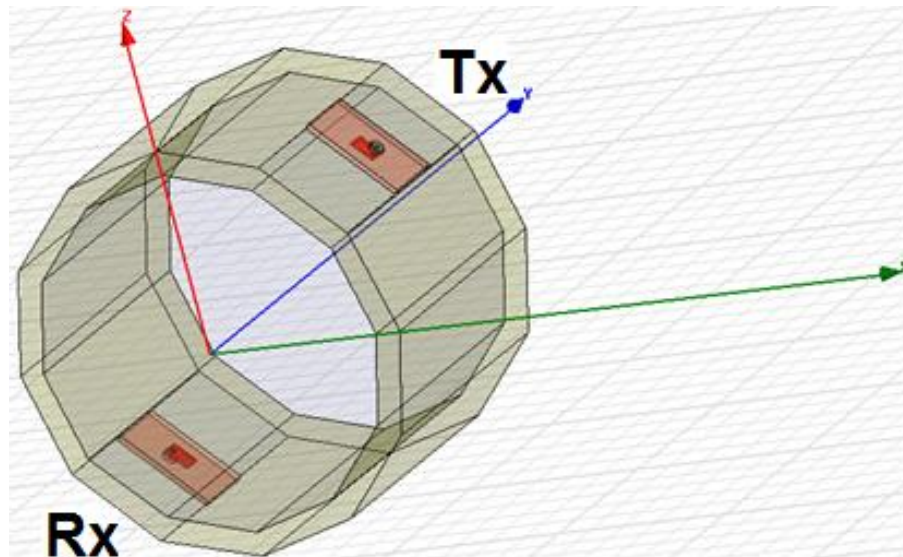


Figure A-12: Microstrip Antenna Transceiver Attached to the Pipeline Model

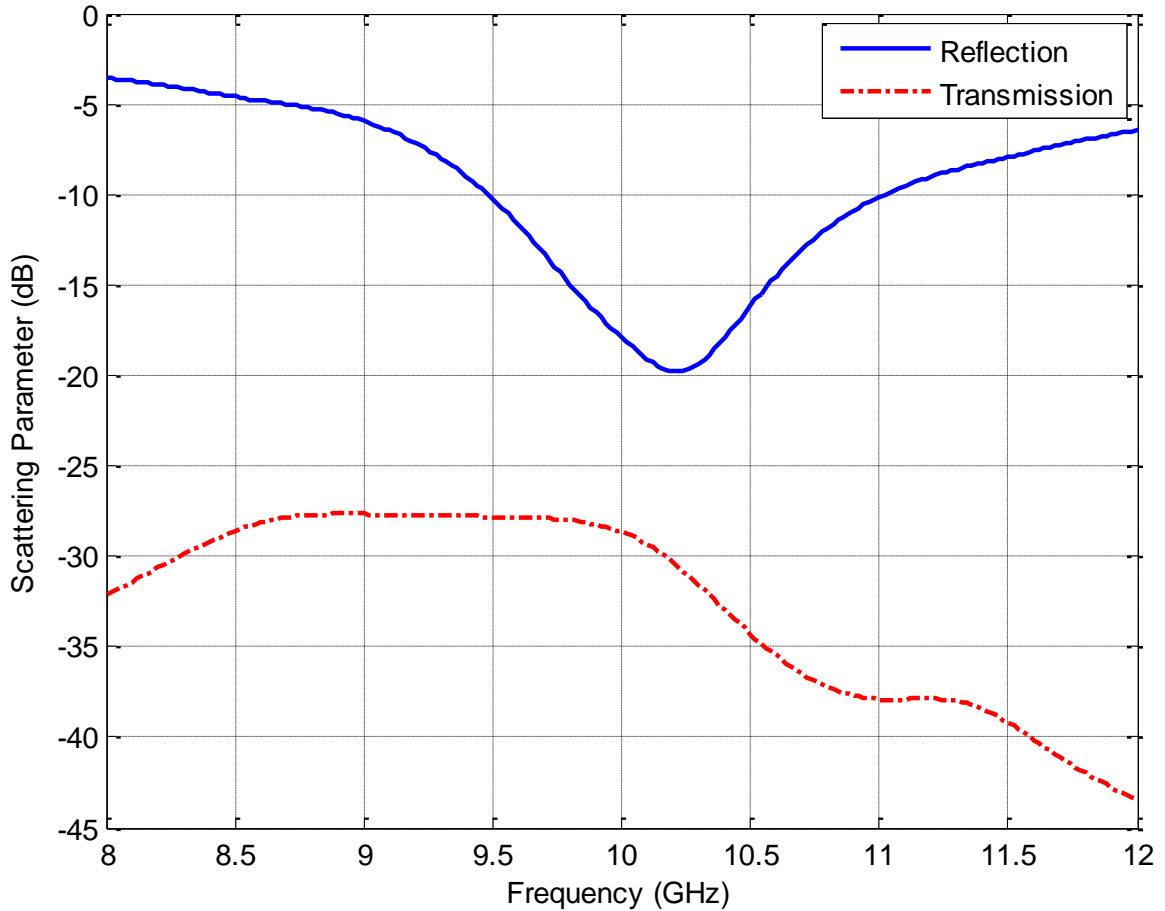


Figure A-13: Reflection and Transmission Coefficients for the Pipeline Transceiver

A.3.1.3 Pipeline with Multiple receivers

The purpose from attaching many receivers around the pipeline is to collect most of the signal transmitted from the transmitter to have better information about the materials inside the pipeline. Figure A-14 shows a section of the pipeline with six antennas attached to it and for the material inside the pipeline assumed to be air, the reflection coefficient for the six antennas is shown in Figure A-15. It can be noticed that all the antennas are resonating at a frequency of 10GHz. The transmission coefficient for the six antennas is

shown in Figure A-16, where in this figure the antennas have different transmission coefficient depending on its location with respect to the transmitter. The maximum transmission will be for the antenna in the directly opposite location to the transmitter. Therefore, if antenna 1 is assumed to be the transmitter, then the opposite one will be antenna 4 has maximum reception. Figure A-17 shows the radiation behavior from the transmit antenna.

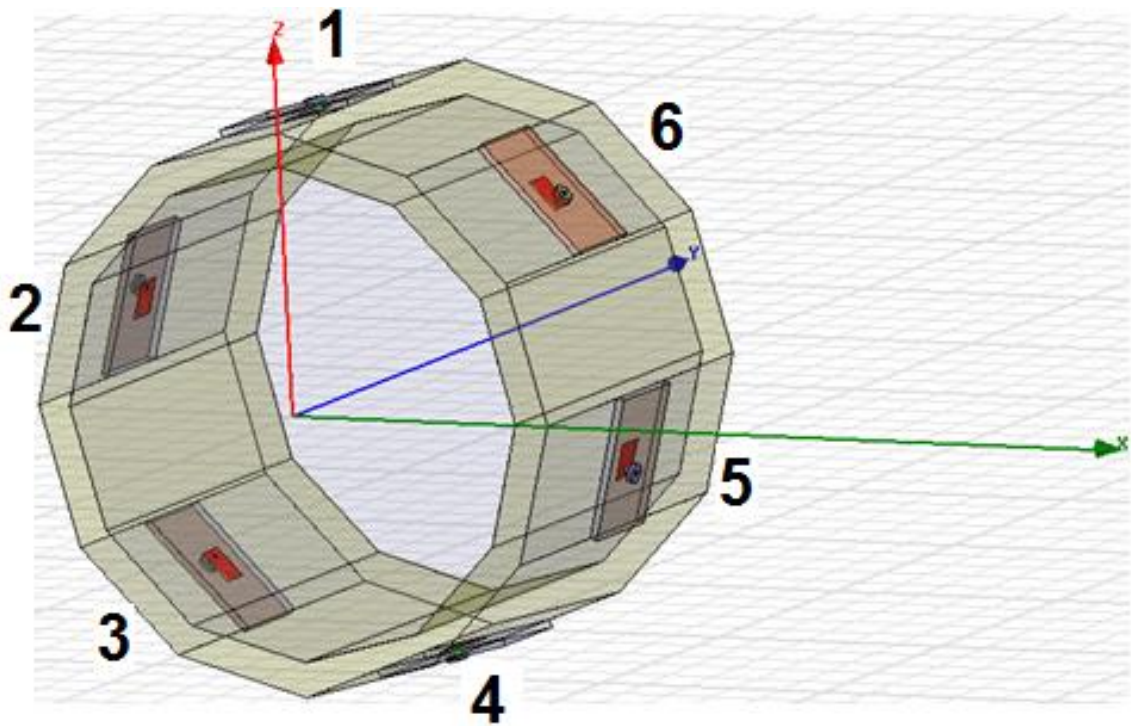


Figure A-14: Pipeline with Multiple Receivers

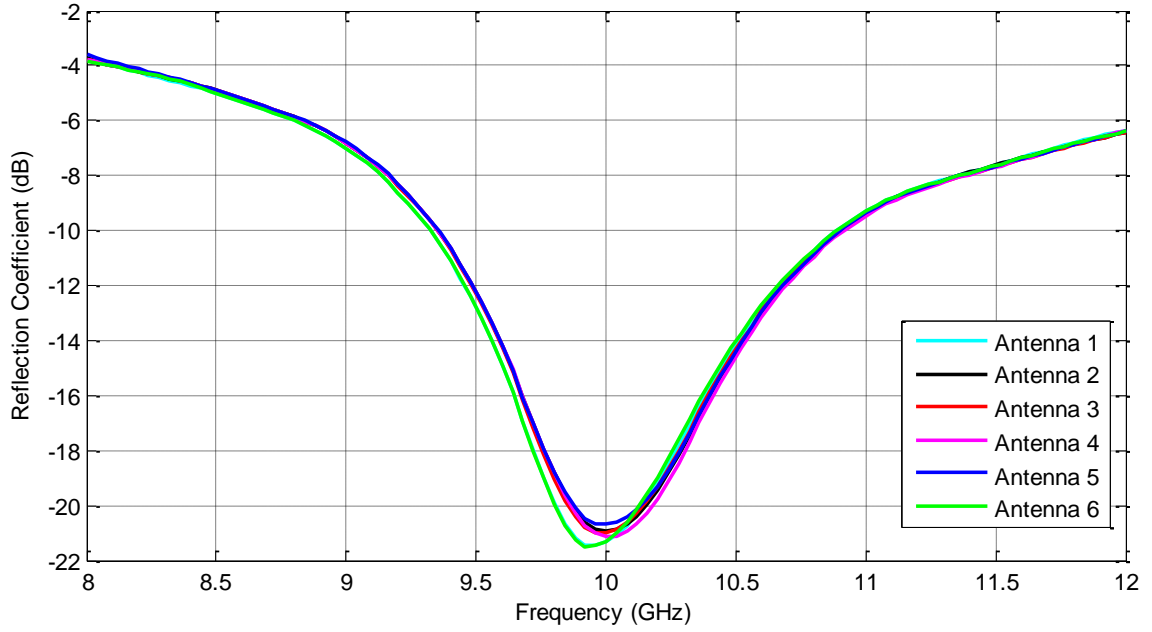


Figure A-15: Reflection Coefficient for Air Filled Pipeline

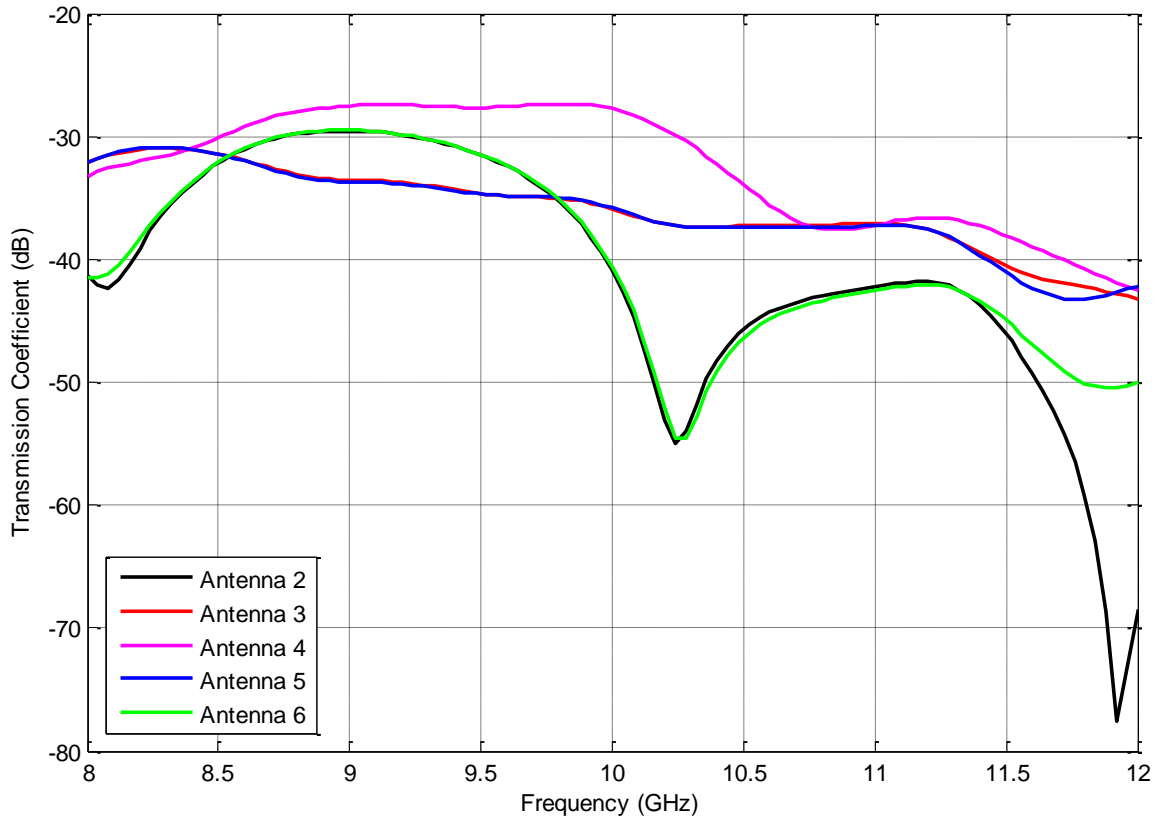


Figure A-16: Transmission Coefficient for Air Filled Pipeline

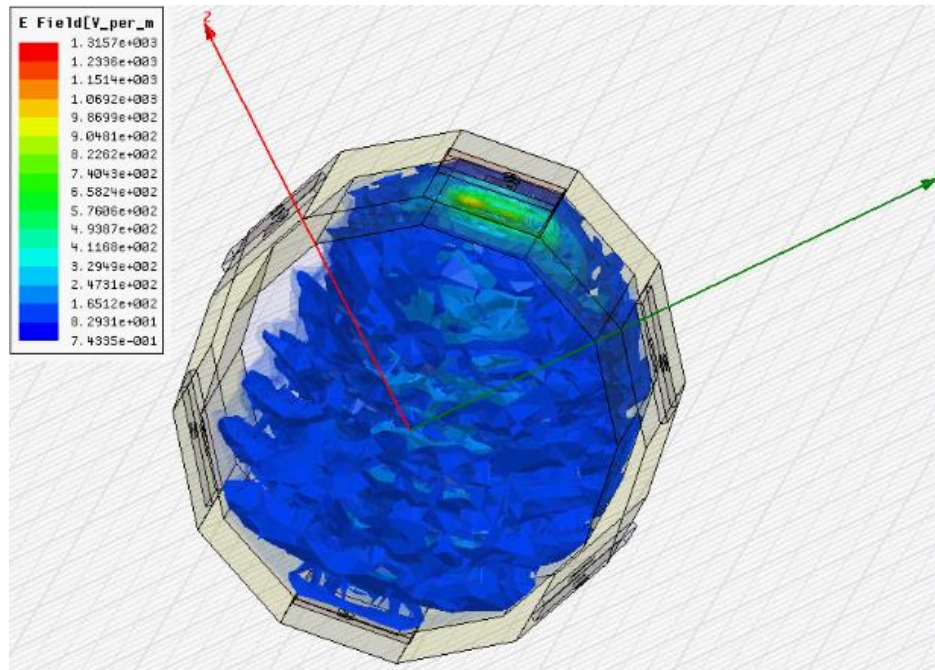


Figure A-17: Shape of the Radiation from the Transmitter

Figure A-18 and Figure A-19 shows the reflection and transmission coefficients in the case where the pipeline is totally filled with oil. It is noticed from the figure that all the antennas are resonating at the same frequency, which is a little less than the case of air since the dielectric constant is a little bigger. For the transmission coefficient, it behave similar to the air case, such that the opposite antenna to the transmitter has the maximum reception, but the received power is too small. One idea to solve the power problem is to use a 2-inch pipeline and placing the patch antenna on the inner perimeter of the pipeline as will be explained in the next sub section.

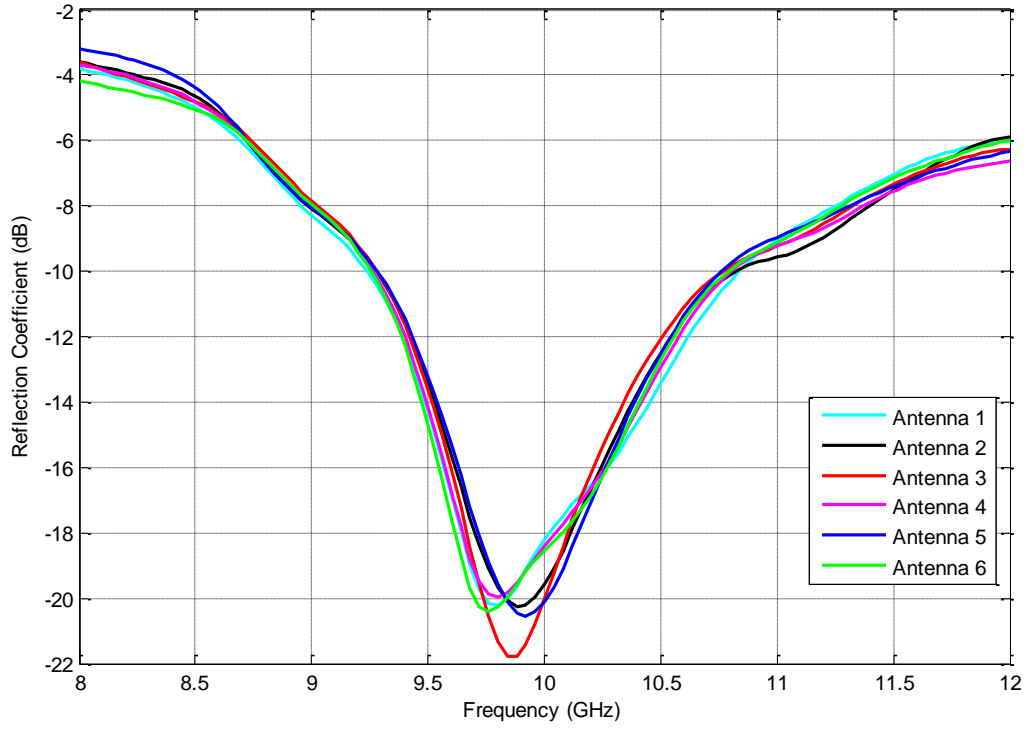


Figure A-18: Reflection Coefficient for Oil Filled Pipeline

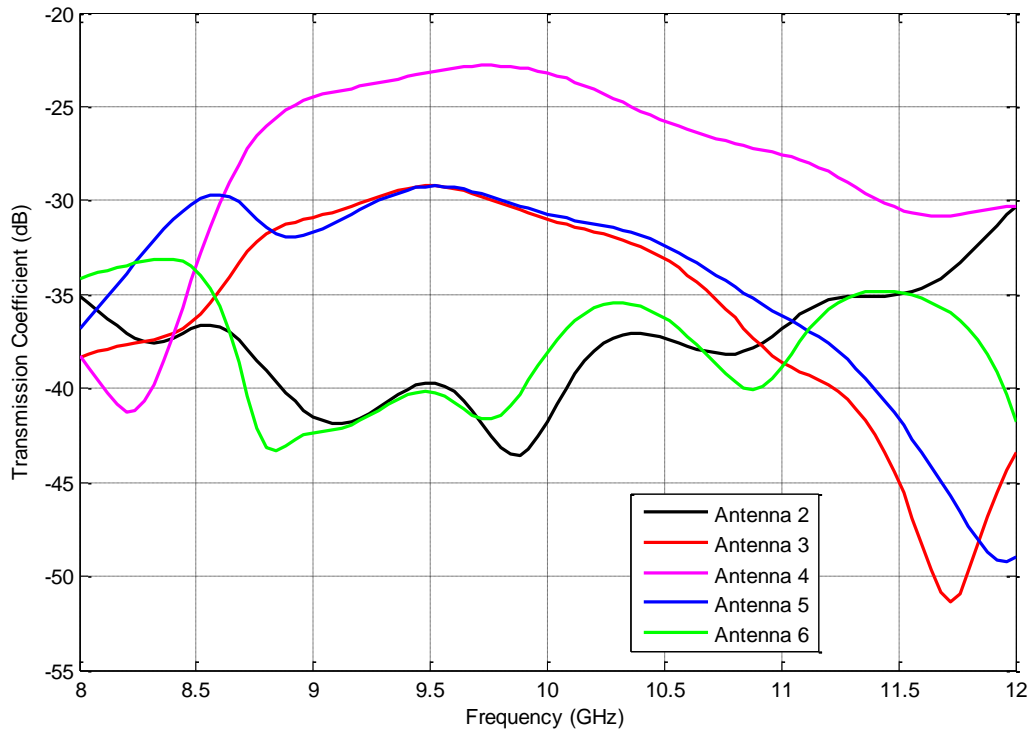


Figure A-19: Transmission Coefficient for an Oil Filled Pipeline

A.3.2 Coaxial Fed of a 2-inch Pipeline Sample

In order to have better results, a 2-inch pipeline sample is adopted. This sample has the same property of the previous 4-inch one. In addition to pipeline dimension change, the microstrip patch antenna and its substrate now is attached to the inner perimeter of the pipeline in order to focus the signal towards the interior region of the pipeline and reduce the amount of surface wave through the pipeline wall. This antenna was fed by a coaxial cable through a hole in the Plexiglass pipeline wall as shown in Figure A-20. The antenna is retuned to operate at 10 GHz, the modified antenna specifications is summarized in Table A-4. The reflection coefficient of this model is plotted in Figure A-21. This model has a resonant frequency for the air filled case of 10.08 GHz and for oil filled is 9.1 GHz while for the pipeline filled with seawater, which has a conductivity of 4 siemens/m has a resonant frequency of 8.28 GHz with a reflection coefficient of -10.1426 dB.

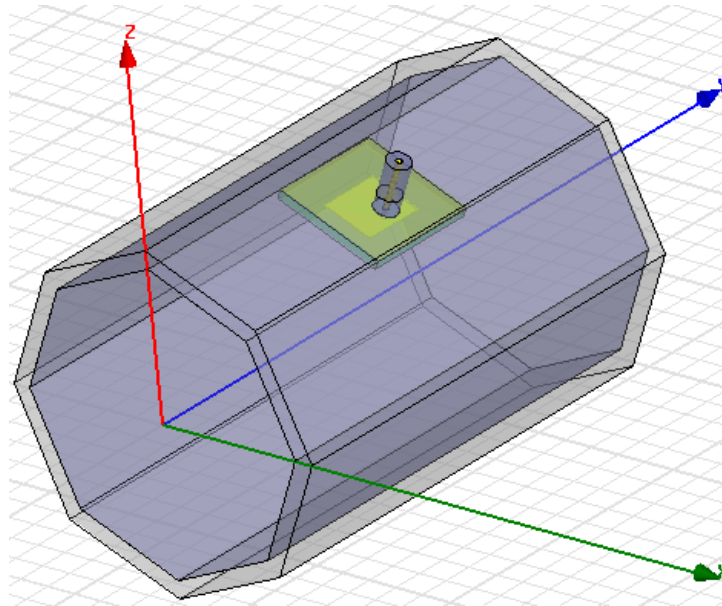


Figure A-20: MPA Located on the Inner Perimeter of a 2-inch Pipeline Sample

Table A-4: Microstrip Antenna Specifications that Located inside a 2-inch Pipeline

Patch Width (mm)	11
Patch Length (mm)	8.8
Substrate Width (mm)	20
Substrate Length (mm)	20
Substrate Height (mm)	1.6
Superstrate Height (mm)	3
Substrate Permittivity	2.2
Superstrate Permittivity	3.4
Resonant Frequency (GHz)	10
Reflection Coefficient (dB)	-17.96
BW (GHz)	1.3
Gain (dB)	9.33

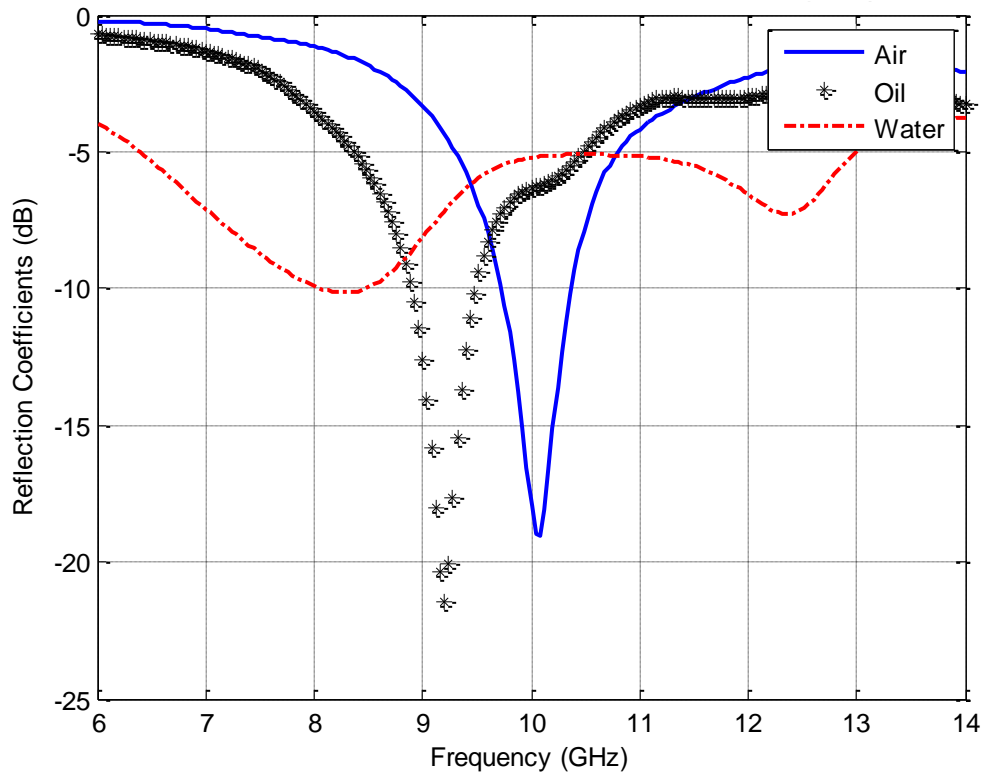


Figure A-21: Reflection Coefficient for Air, Oil and Water versus Frequency for a 2-inch Pipeline

When the previous design is tested in the laboratory a leakage problem is faced even with many tries to seal the hole, it keep leaks. To solve this problem an aperture coupling of the antenna is used. Moreover, to reduce the number of modes detected in the case of 10 GHz operating frequency; the resonant frequency is reduced to 3.6 GHz, where at this frequency only the dominant mode in the case of air will propagate (see 2nd table in chapter 4) and two modes in the case of oil.

Therefore, this frequency is selected and the patch antenna with aperture fed model on a part of a pipeline is shown in Figure A-22. In this model since at this frequency, the size of the patch is increased so it is wrapped on the inner surface of the pipeline sample and the outer surface is grounded except the location of aperture. In addition, the substrate, which located on the outer surface of the pipeline, is wrapped around that surface. This antenna is resonating at 3.665 GHz with a reflection coefficient of -18.8 dB as shown in the reflection coefficient plot in Figure A-23. The new patch antenna dimensions are listed in Table A-5.

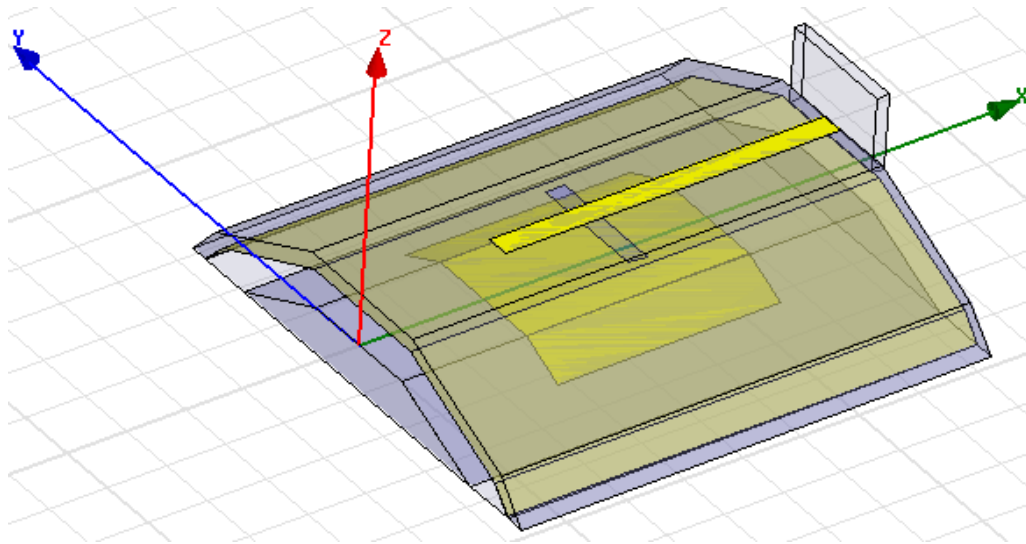


Figure A-22: 3.6 GHz Aperture Antenna on a Curve Plexiglass Section

Table A-5: 3.6 GHz Aperture Coupled Microstrip Antenna Specifications

Patch Width (mm)	19
Patch Length (mm)	19
Aperture Width (mm)	1.55
Aperture Length (mm)	10
Feed Width (mm)	2
Feed Length (mm)	28.5
Substrate Width (mm)	40
Substrate Length (mm)	44.5
Substrate Height (mm)	1.27
Superstrate Height (mm)	3
Substrate Permittivity	6
Superstrate Permittivity	3.4
Resonant Frequency (GHz)	3.665
Reflection Coefficient (dB)	-18.8078
BW (MHz)	100
Gain (dB)	5.9743

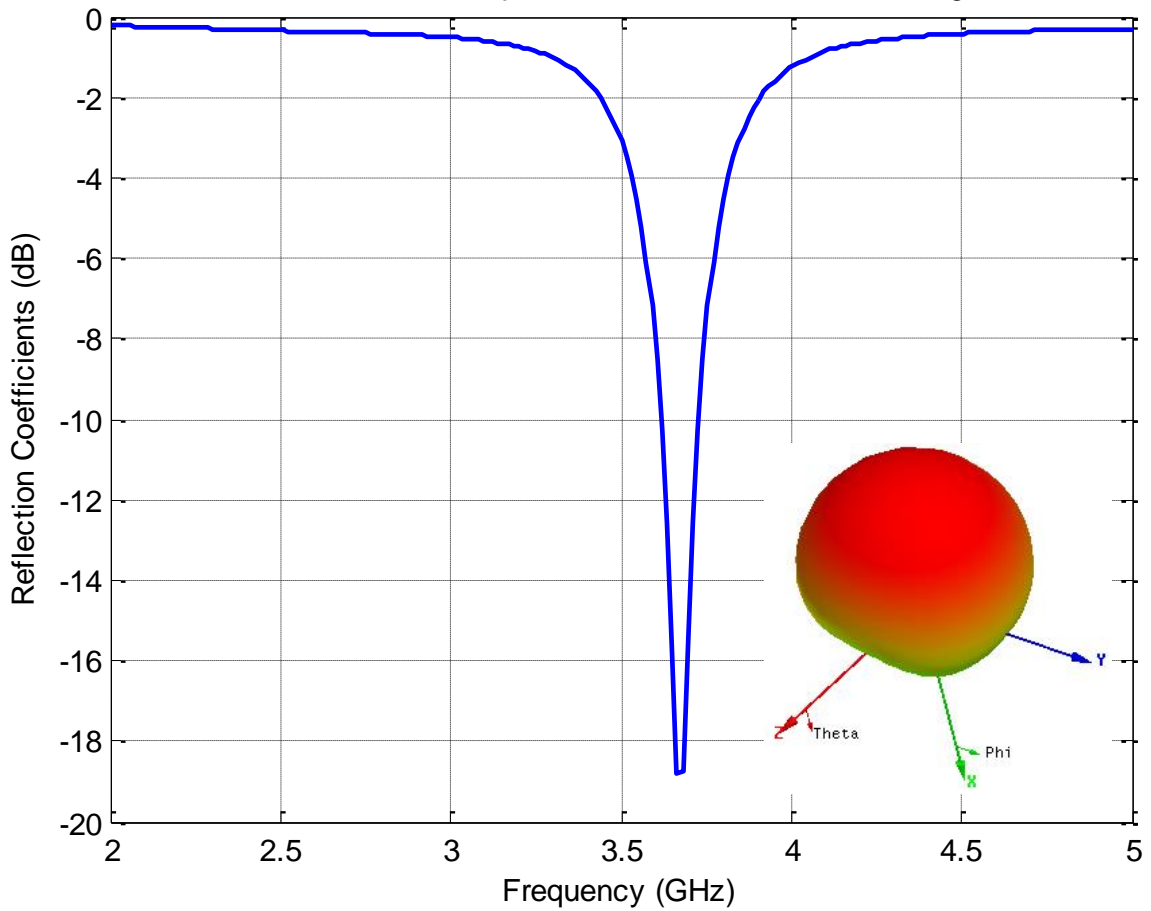


Figure A-23: Reflection Coefficient of the Aperture Antenna on a Curve Plexiglass Section

The patch now is attached to the 2-inch pipeline sample and its reflection coefficient are plotted for different oil and air combinations. The model is shown in Figure A-24 and the resulted reflection coefficient in Figure A-25. The levels here are corresponds to how much is covering the patch surface. For example, 0% patch means that the patch is in the air side and 100% patch means it is completely in the oil side and for 50% patch; the pipeline is half filled with oil.

It is noticed from Figure A-25 that this operating frequency are successfully reduced the number of modes compared to Figure 4-6 shown in chapter 4, to two modes and this is expected because of the existence of oil as the calculation in Table A-6 proofed. It is also noticed that as the percentage of oil increased the resonant frequency and the power will both be reduced. However, this figure cannot be used to determine the oil level since the other mode is interfering with the first mode of other proportions. For example, at frequency of 3.5 GHz the second mode of 75% and 100% levels are coincide with the first mode level of 0% patch. The Operating frequency and the reflection coefficient are tabulated in Table A-6 along with their oil percentage. In addition, it can be seen from the figure that starting of 58% of oil, the third mode appears around 4.75 GHz. Therefore, as the pipe completely filled with oil, this mode will be around what is calculated in Table 4-2.

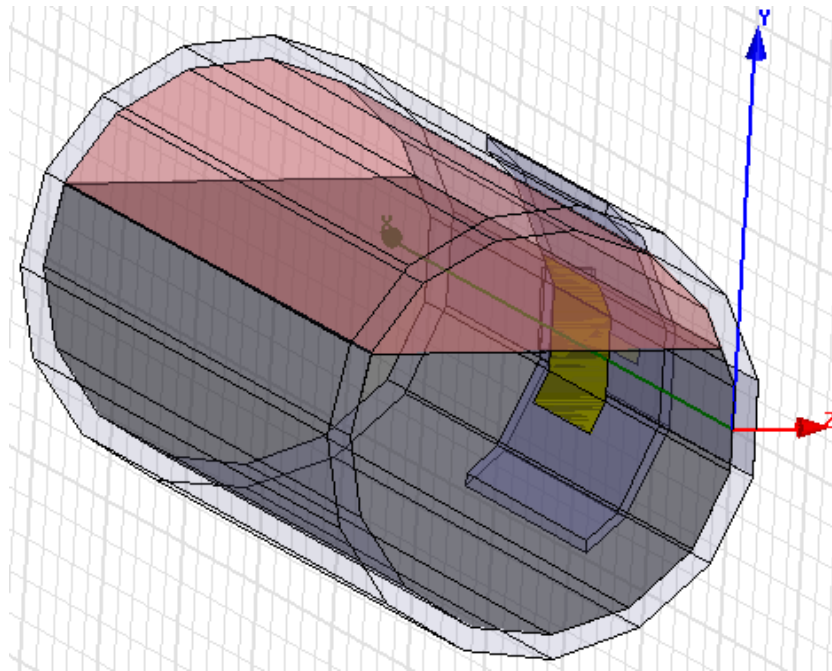


Figure A-24: 3.6 GHz Patch Antenna Attached to a 2-inch Pipeline Sample

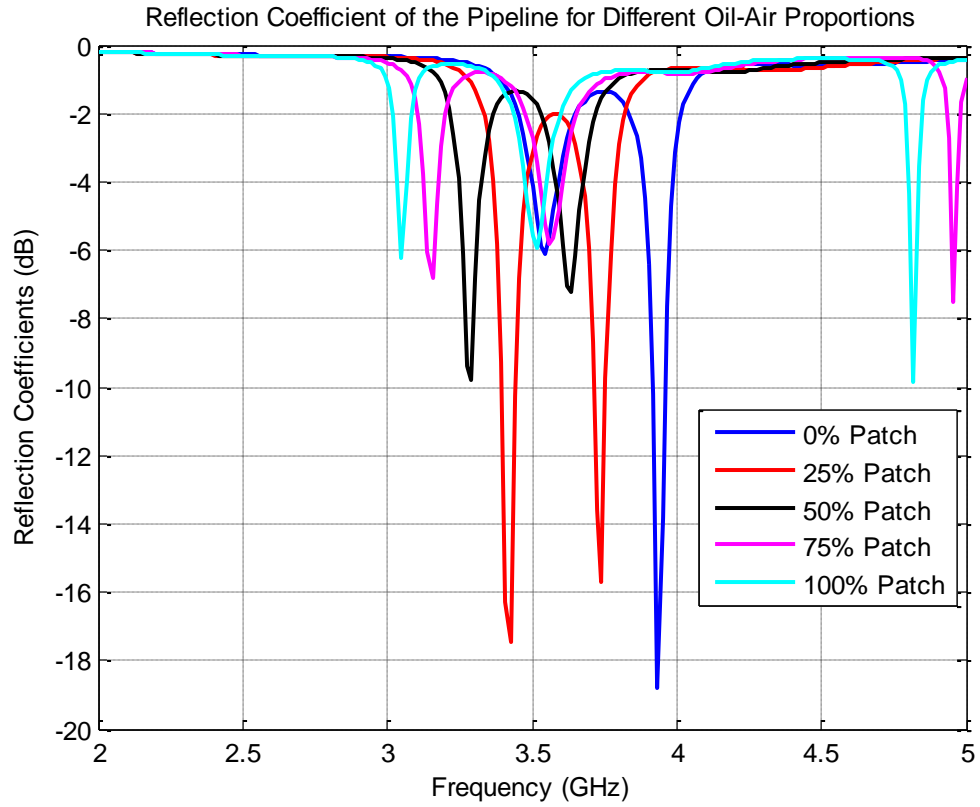


Figure A-25: Reflection Coefficient for Different Oil-Air Proportions

Table A-6: Antenna Behavior for Different Oil Percentages

Patch Percentage (%)	Resonant Frequency (GHz)	Reflection Coefficient (dB)	Oil Percentage (%)
0	3.545	-6.0854	31.75
25	3.425	-17.4712	40.875
50	3.29	-9.8151	50
75	3.155	-6.7937	59.125
100	3.05	-6.2016	68.25

From the last design, the existence of the second mode of some proportions cause a problem in detecting the oil level accurately since it is coincide with the first mode of other proportions. Therefore, the antenna need to be tuned to operate at a little bit smaller frequency. Therefore, the operating frequency reduced to 3 GHz to insure only the dominant mode in the case of oil will propagate. Moreover, the 3.0 GHz frequency is between the dominant modes of air and oil and it will be suitable to detect the different oil-air levels. The rest of the optimization procedure is shown in details in chapter 4.

References

- [1] Ibrahim Babelli and Michel Bérard , "System and Method for Measuring Flow in a Pipeline," in *WO 2006/072274*, 13 July 2006..
- [2] Hoi Yeung, Abba Ibrahim, "Multiphase Flows Sensor Response Database," *Flow Measurement and Instrumentation*, vol. 14, pp. 219-223, 2003.
- [3] Thorn R., Johansen G.A. and Hammer E.A., "Recent Developments in three-phase flow measurement," *Meas, Sci. Technology*, vol. 8, pp. 691-701, 1997.
- [4] T. M. H. M. Reza Taherian, "Microwave Devise And Method For Measuring Multiphase Flow". Patent 5485743, 23 Sep. 1994.
- [5] Z Wu, H McCann, L E Davis, J Hu, A Fontes and C G Xie, "Microwave-tomographic system for oil- and gas-multiphase-flow imaging," *Measurement Science and Technology*, vol. 20, no. 10, 2009.
- [6] Andreas Penirschke and Rolf Jakoby, "Microwave Mass Flow Detector for Particulate Solids Based on Spatial Filtering Velocimetry," *IEEE TRANSACTIONS ON MICROWAVE THEORY AND TECHNIQUES*, vol. 56, no. 12, DECEMBER 2008.
- [7] F. W. Fabian Wenger, "FLOW MEASUREMENT USING NEAR FIELD MICROWAVES". Patent 20110072909, 31 3 2011.
- [8] Andreas Penirschke, Aleksandar Angelovski, Rolf Jakoby, "Helix-shaped CRLH-Mass Flow Detector for the Cross-sectional Detection of Inhomogeneous Distributed Pneumatic Conveyed Pulverized Solids," in *Instrumentation and Measurement Technology Conference, IEEE*, Darmstadt, Germany , 2011.
- [9] Baoliang Wang, Yongfeng Fu, Zhiyao Huang, Haiqing Li, "IEEE Instrumentation&Measurement Technology Conference Proceedings," 2010.
- [10] R Krafft, J Hemp & M L Sanderson, "Investigation into the use of the electromagnetic flowmeter for two-phase flow measurements," in *Advances in Sensors for Fluid Flow Measurement, IEE Colloquium on*, 18 Apr 1996.
- [11] R. Harrington, Time harmonic electromagnetic fields, IEEE Press Classic Reissue, 1961.

- [12] H. A. Ragheb, A. Sebak, L. Safai, "Cut-off frequencies of circular waveguide loaded with eccentric dielectric cylinder," *IEE Proc. Microw. Antennas Propag.*, vol. 144, no. 1, pp. 7-12, February 1997.
- [13] H. Y. YEE and N. F. AUDEH, "Cutoff Frequencies of Eccentric Wweguides," *IEEE TRANSACTIONS ON MICROWAVE THEORY AND TECHNIQUES*, Vols. MTT-14, no. 10, pp. 487-493, October 1966.
- [14] J. B. Davies and P. Nagenthiram, "Irregular fields, non-convex shapes and the point-matching method for hollow waveguides," *Electron. Lett.*, vol. 7, pp. 401-404, July 1971.
- [15] EDWARD J. ROTHWELL and LYDELL L. FRASCH, "Propagation Characteristics of Dielectric Rod Loaded Waveguides," *IEEE TRANSACTIONS ON MICROWAVE THEORY AND TECHNIQUES*, vol. 36, no. 3, pp. 594-600, MARCH 1988.
- [16] S. P. Yeo, "Application of least-squares boundary residual method to the analysis of a circular waveguide loaded with nonconcentric dielectric rod," *IEEE Trans. Microwave Theory Tech.*, vol. 38, p. 1092-1095, Aug. 1990.
- [17] R. H. T. Bates, V. R. Varadan and V. V. Varadan, "General Introduction to the Extended Boundary Condition", Acoustic, Electromagnetic and Elastic Wave Scattering: Focus on the T-Matrix Approach, Pergamon Press, 1980.
- [18] T. S. Yeo, "Cutoff Frequencies of an Asymmetrically Loaded Cylindrical Waveguide," *IEEE Transactions on Microwave Theory Techniques*, vol. 46, no. 9, September 1998.
- [19] Ranajit Dey, Ila Agnihotri, Soumybrata Chakrabarty, Shashi Bhusan Sharma, "Cut-off Wave Number and Dispersion Characteristics of Eccentric Annular Guide with Dielectric Support," in *Applied Electromagnetics Conference IEEE*, 2007.
- [20] Barry E. Spielman and Roger F. Harrington, "WAVEGUIDES OF ARBITRARY CROSS SECTION BY SOLUTION OF A NONLINEAR INTEGRAL EIGENVALUE EQUATION," *IEEE TRANSACTIONS ON MICROWAVE THEORY AND TECHNIQUES*, Vols. MTT-20, pp. 578-585, Sept. 1972.
- [21] M. Swaminathan, E. Arvas, T. K. Sarkar, A. R. Djordjevic, "Computation of cutoff wavenumbers of TE and TM modes in waveguides of arbitrary cross sections using a surface integral formulation," *IEEE Transactions on Microwave Theory and Techniques*, vol. 38, no. 2, 1990.

- [22] MICHAL MROZOWSKI AND MICHAL OKONIEWSKI, "Comments on "Computation of Cutoff Wavenumbers of TE and TM Modes in Waveguides of Arbitrary Cross Sections Using a Surface Integral Formulation"," *IEEE TRANSACTIONS ON MICROWAVE THEORY AND TECHNIQUES*, vol. 38, no. 11, NOVEMBER 1990.
- [23] E. A. Navarro and V. Such, "Study of TE and TM modes in waveguides of arbitrary cross-section using an FD-TD formulation," *IEE PROCEEDINGS-H*, vol. 139, no. 6, pp. 491-494, DECEMBER 1992.
- [24] Hassan A. Rugheb, A. Sebak and L. Shafai, "CUTOFF WAVENUMBERS OF AN ECCENTRIC DIELECTRIC CYLINDER LOADING A CIRCULAR WAVEGUIDE," *Antennas and Propagation Society International Symposium*, vol. 1, pp. 302-305, 21-26 July 1996.
- [25] ANITA VISHEN, G. P. SRIVASTAVA, G. S. SINGH AND F. GARDIOL, "Calculation of Cutoff Wavenumbers for TE and TM Modes in Tubular Lbes with Offset Center Conductor," *IEEE TRANSACTIONS ON MICROWAVE THEORY AND TECHNIQUES*, Vols. MTT-34, no. 2, pp. 292-294, FEBRUARY 1986.
- [26] Liyang Zhang, Jingjun Zhang and Wenbing Wang, "Correct Determination of TE and TM Cutoff Wavenumbers in Transmission Lines with Circular Outer Conductors and Eccentric Circular Inner Conductors," *IEEE TRANSACTIONS ON MICROWAVE THEORY AND TECHNIQUES*, vol. 39, no. 8, pp. 1416-1420, AUGUST 1991.
- [27] w. H. LIN, "FREE TRANSVERSE VIBRATIONS OF UNIFORM CIRCULAR PLATES AND MEMBRANES WITH ECCENTRIC HOLES," *Journal of Sound and Vibration*, vol. 81, no. 3, pp. 425-435, 1982.
- [28] M. Chi and P. A. Laura, "Approximate method of determining the cutoff frequencies of waveguides of arbitrary cross section," *IEEE Transaction on Microwave Theory and Techniques (Correspondence)*, Vols. MTT-12, pp. 248-249, March 1964.
- [29] Aristides D. Kotsis and John A. Roumeliotis, "Cutoff Wavenumbers of Circular Metallic Waveguides with Eccentricity," in *In proceeding of: 19th Conference on the Computation of Electromagnetic Fields* , Budapest, 13 October 2013.
- [30] J. R. KUTTLER, "A New Method for Calculating TE and TM Cutoff Frequencies of Uniform Waveguides with Lunar or Eccentric Annular Cross Section," *IEEE*

TRANSACTIONS ON MICROWAVE THEORY AND TECHNIQUES, vol. 32, no. 4, pp. 348-354, 1984.

- [31] H. H. Meinke, "A survey on the use of conformal mapping for solving wave-field problems," in *Symposium on Electromagnetic Theory and Antennas*, Copenhagen, New York: Pergamon, 1963.
- [32] F. J. Tischer and H. Y. Yee, "Waveguides with arbitrary cross section considered by conformal mapping," in *Research Institute, University of Alabama, University UARI Rept.*, 12 January 1965.
- [33] J. B. Davies and C. A. Muilwyk, "Numerical solution of uniform hollow wave guides with boundaries of arbitrary shape," *Proceedings IEE (London)*, vol. 113, pp. 277-284, February 1966.
- [34] P. A. Laura, "A simple method for the determination of cutoff frequencies of waveguides with arbitrary cross sections," *Proceedings of the IEEE*, vol. 54, pp. 1495-1497, October 1966.
- [35] P. A. Laura, E. Romanelli and M. H. Maurizi, "On the analysis of waveguides of doubly-connected cross-section by the method of conformal mapping," *Journal of sound and vibration*, vol. 20, pp. 27-38, 1972.
- [36] E. Abaka and W. Baier, "TE and TM modes in transmission lines with circular outer conductor and eccentric inner conductor," *Electron. Lett.*, vol. 5, pp. 251-252, May 1969.
- [37] TAKEO ABE and YOSHIO YAMAGUCHI, "Propagation Constant Below Cutoff Frequency in a Circular Waveguide with Conducting Medium," *IEEE TRANSACTIONS ON MICROWAVE THEORY AND TECHNIQUES*, Vols. MTT-29, no. 7, July 1981.
- [38] C. E. Brennen, "FLOW PATTERNS," in *Fundamentals of Multiphase Flow*, Cambridge University Press, 2005, pp. 163-195.
- [39] S. Z. Rouhani and M. S. Sohal, "Two-phase flow patterns: a review of research results," *Progress in Nuclear Energy 11*, p. 219-259, 1983.
- [40] D. Barnea, "A unified model for predicting flow-pattern transitions for the whole range of pipe inclinations," *International Journal of Multiphase Flow*, vol. 13, pp. 1-12, 1987.

- [41] E Bondet de la Bernardie, O Dubrunfaut, J C Badot, A Fourier-Lamer, E Villard, P Y David, B Jannier, N Grosjean and M Lance, "Low (10–800 MHz) and high (40 GHz) frequency probes applied to petroleum multiphase flow characterization," *Meas. Sci. Technol.*, vol. 19, 2008.
- [42] M J Da Silva, E Schleicher and U Hampel, "Capacitance wire-mesh sensor for fast measurement of phase fraction distributions," *Meas. Sci. Technol.*, vol. 18, p. 2245–2251, 2007.
- [43] S R Wylie, A Shaw and A I Al-Shamma'a, "RF sensor for multiphase flow measurement through an oil pipeline," *Meas. Sci. Technol.*, pp. 2141-2149, 2006.
- [44] Sheikh S. I., Alqurashi K., Ragheb H., Babelli I., "SIMPLE MICROWAVE METHOD FOR DETECTING WATER HOLDUP," *Microwave and Optical Technology Letters (MOTL)*, vol. 50, no. 2, February 2008.
- [45] Andreas Penirschke, Aleksandar Angelovski and Rolf Jakoby, "Moisture Insensitive Microwave Mass Flow Detector for Particulate Solids," in *Instrumentation and Measurement Technology Conference (I2MTC), IEEE*, Austin, TX., 2010.
- [46] Andreas Penirschke and Rolf Jakoby, "Microwave Mass Flow Detector for Particulate Solids Based on Spatial Filtering Velocimetry," *IEEE TRANSACTIONS ON MICROWAVE THEORY AND TECHNIQUES*, vol. 56, no. 12, pp. 3193-3199, DECEMBER 2008.
- [47] Andreas Penirschke, Aleksandar Angelovski and Rolf Jakoby, "Helix-shaped CRLH-mass flow detector for the cross-sectional detection of inhomogeneous distributed pneumatic conveyed pulverized solids," in *Instrumentation and Measurement Technology Conference (I2MTC)*, Graz, Austria, 10-12 May 2011.
- [48] Aleksandar Angelovski, Andreas Penirschke and Rolf Jakoby, "Helix-shaped CRLH-TL sensor for inhomogeneties detection for pneumatic conveyed pulverized solids," in *Proceedings of the 6th German Microwave Conference*, Darmstadt, Germany, 14–16 March 2011.
- [49] S. L. Ceccio and D. L. George , "A review of electrical impedance techniques for the measurement of multiphase flows.," *Journal Fluids Engineering*, vol. 118, pp. 391-399., 1996.

- [50] E. A. Hammer, G. A. Johansen, T. Dyakowski, E. P. L. Roberts, J. C. Cullivans, R. A. Williams, Y. A. Hassan, and C. S. Claiborn, "Advanced experimental techniques.," 2006.
- [51] A. C. Kak and M. Slaney, *Principles of Computerized Tomographic Imaging*, New York: IEEE Press., 1988.
- [52] T. Dyakowski, "Process tomography applied to multi-phase flow measurement," *Measurement Science and Technology*, vol. 7, p. 343–353, 1996.
- [53] J. Chaouki, F. Larachi and M. P. Dudukovic, "Noninvasive tomographic and velocimetric monitoring of multiphase flows," *Industrial and Engineering Chemistry Research*, vol. 36, pp. 4476-4503, 1997 .
- [54] R. A. Williams and X. Jia, "Tomographic imaging of particulate systems," *Advanced Powder Technology*, vol. 14, pp. 1-16, 2003 .
- [55] H. M. Prasser, "Novel experimental measuring techniques required to provide data for CFD validation," *Nuclear Engineering and Design*, vol. 238, pp. 744-770, 2008.
- [56] R. A. Williams and M. S. Beck (eds.), *Process Tomography: Principles, Techniques and Applications*, Oxford, UK: Butterworth-Heinemann, 1995.
- [57] H. McCann, D. M. Scott (eds.), *Process Imaging For Automatic Control*, Boca Raton, FL: CRC Press, 2005.
- [58] D. M. Scott and R. A. Williams (Eds), *Frontiers in Industrial Process Tomography*, New York: AIChE & Engineering Foundation, 1995.
- [59] Kwun Ho Ngan, Karolina Ioannou, Lee D. Rhyne, Panagiota Angeli, "Effect of glycerol addition on phase inversion in horizontal dispersed oil–water pipe flows," *Experimental Thermal and Fluid Science*, 2011.
- [60] H. Yeung, "Multiphase flow measurement - the holy grail.," in *SENSOR Conference 2007 Proceedings I*, Nurnberg, Germany, May 2007.
- [61] C. A. Balanis, *Antenna theory-Analysis and Design*, John Wiley & Sons Ltd, 1997.
- [62] R. B. P. B. I. Garg, *Microstrip Antenna Design Handbook*, Artech House, Inc, 2001.
- [63] G. a. R. K. Kumar, *Broadband Microstrip Antennas*, Artech House, Inc, 2003.

- [64] B. R. Waterhouse, *Microstrip Patch Antennas: A Designer's Guide*, Kluwer Academic Publishers, 2003.
- [65] P. S. Nakar, *Design of a compact Microstrip Patch Antenna for use in Wireless/Cellular Devices*, Masters Thesis report, 2004.
- [66] C. A. Balanis, *Advanced Engineering Electromagnetics*, John Wiley & Sons, Inc., May 9, 1989.
- [67] J.-M. Jin, *Theory and Computation of Electromagnetic Fields*, John Wiley & Sons, Inc., 2010.
- [68] V. Finazzi, *A theoretical study into the fundamental design limits of devices based on one-and two-dimensional structured fibres*, Southampton: Optoelectronics Research Centre, September 2003.
- [69] P. Winternitz, K. B. Wolf, G. S. Pogosyan and A. N. Sissakian, "GRAF'S ADDITION THEOREM OBTAINED FROM $SO(3)$ CONTRACTION," *Theoretical and Mathematical Physics*, vol. 129, no. 2, pp. 1501-1503, 2001.
- [70] T. P. White, B. T. Kuhlmeier, R. C. McPhedran, D. Maystre, G. Renversez, C. Martijn de Sterke and L. C. Botten, "Multipole method for microstructured optical fibers. I. Formulation," *Journal of the Optical Society of America*, vol. 19, no. 10, pp. 2322-2330, October 2008.
- [71] Milton Abramowitz and Irene A. Stegun, *Handbook of Mathematical Functions: with Formulas, Graphs, and Mathematical Tables*, Dover Publications, 1965.
- [72] C. S. G. I. a. C. CSG, "Dielectric Constants Of Various Materials Table," CSGNetwork, [Online]. Available: <http://www.csgnetwork.com/dieconstantstable.html>.
- [73] Ansoft, "Ansoft HFSS Training Example: Aperture-Coupled Patch Antenna," 2012.
- [74] "LPKF Laser & Electronics," [Online]. Available: <http://www.lpkfusa.com/RapidPCB/CircuitboardPlotters/s62.htm>.
- [75] "Agilent Technologies," [Online]. Available: <http://www.home.agilent.com/agilent/home.jsp?cc=SA&lc=eng>.
- [76] N. Hercovici, "CAD of aperture coupled microstrip transmission lines and antennas: software and user's manual," 1996.

- [77] "EM Scan Real-Time Results," [Online]. Available: <http://www.emscan.com/>.
- [78] "Arduino Uno," ARDUINO, [Online]. Available: www.arduino.cc.
- [79] *Q&A With Zoltan Cendes, Founder, Chairman, And CTO Of Ansoft Corporation, By Jim Pomager, Editor in Chief, RF Global Net.*
- [80] D. A. P. M. A. I. By Larry Williams, 2009. [Online]. Available: <http://www.ansys.com/magazine/issues/vol4-iss1-2010/hfss.pdf>.
- [81] [Online]. Available: http://www.emtalk.com/mwt_mpa.htm.
- [82] D. R. S. Adams, "Ansoft HFSS Tutorial: Dipole Antenna," September 8 2009. [Online].
- [83] A. TECHNOLOGIES, "AGILENT E5071C ENA NETWORK ANALYZER," [Online]. Available: <http://www.fke.utm.my/lab2/radar/file/SOP%20-%20VNA.pdf>.

Vitae

Name : Yanal Shaher A. AlFaouri

Nationality : Jordanian

Date of Birth : 7/13/1985

Email : y_faouri@yahoo.com, yfaouri@kfupm.edu.sa

Address : Salt Street, P.O. Box. 333, Ain ElBasha 19374, Jordan

Academic Background :

June 2014 King Fahd University of Petroleum & Minerals
Ph.D. in Electrical Engineering
Graduating with GPA is “3.469” out of “4.00” (rated Very Good)

June 2010 King Fahd University of Petroleum & Minerals
Master Degree in Electrical Engineering
Graduating with GPA is “3.90” out of “4.00” (rated Excellent)

June 2007 University of Jordan, Amman, Jordan
B.Sc. Degree in Electrical Engineering
Graduating with GPA of “3.17” out of “4.00” (rated Very Good)
I ranked the 4th place in the Faculty of Engineering and Technology in that semester

July 2003 High school (Tawjihi) with an average of “89.3” out of “100”

Awards and Honors :

- Exceptional Teaching Award for the year 2012/2013
- Full MS and PhD scholarships from KFUPM

Research Experience :

Lecturer at King Fahd University of Petroleum and Minerals (KFUPM)

Sept. 2010 - Present

DISSERTATION: “**Microwave Technique for Monitoring Fluid Level in the Petroleum Carrying Pipeline**”

Advisor: Dr. Sheikh S. Iqbal

Co-advisor: Professor Hassan A. Ragheb

(Part of the dissertation has been published and the remaining parts will follow in the coming few months)

Research Assistant at King Fahd University of Petroleum and Minerals (KFUPM)

Feb. 2009 – Aug. 2010

THESIS: “**Design of an LTE Antenna for Mobile Communication**”

Advisor: Dr. Sheikh S. Iqbal

Co-advisor: Dr. Mohammad S. Sharawi

(Most of the thesis has been published as IEEE papers (see publication list))

Design Engineer at King Abdullah II Design and Development Bureau (KADDB)

March 2008 – Jan. 2009

(Design and Fabricate several PCBs for many electrical and electronics devices)

Teaching Experience :

During my graduate studies in KFUPM, I have taught several laboratories in the electrical engineering department

- Electromagnetics
- Microwave Engineering
- Advanced Electrical Circuits
- Electrical Circuits
- Fundamentals of Electrical Circuits (Non EE Students)

Skills :

- Use a wide range of tools, techniques, and equipment (including software) appropriate to their specific discipline
- Use laboratory and workshop equipment to generate valuable data
- Develop, promote and apply safe systems of work
- Communicate effectively, using both written and oral methods
- Use Information Technology effectively
- Manage resources and time
- Work in a multi-disciplinary team
- Undertake lifelong learning for continuing professional development

Publications :

- [1] Faouri, Y.S.; Ragheb H.A.; Iqbal, S.S., "Cutoff Properties of a Circular Waveguide Loaded with Two Eccentric Dielectric Cylinders," (Submitted) Microwave Antenna & Propagation, IET
- [2] Faouri, Y.S.; Iqbal, S.S., "Microwave Measurement of the Dielectric Properties of Sands," Loughborough Antennas & Propagation Conference (LAPC 2014), 10-11 Nov. 2014
- [3] Faouri, Y.S.; Ragheb H.A.; Iqbal, S.S., "Cutoff Wavenumbers of a Two Eccentric Dielectric Cylinders Loading a Circular Waveguide," The 30th International Review of Progress in Applied Computational Electromagnetics (ACES), 23-27 March 2014
- [4] Sharawi, M.S.; Iqbal, S.S.; Faouri, Y.S., "An 800 MHz 2 × 1 Compact MIMO Antenna System for LTE Handsets," IEEE Transactions on Antennas and Propagation, vol.59, no.8, pp.3128,3131, Aug. 2011
- [5] Faouri, Y.S.; Sharawi, M.S.; Iqbal, S.S., "Design of an LTE Antenna for Mobile Communication," The 2nd Scientific Conference for Higher Education Students, 28-31 March 2011
- [6] Sharawi, M.S.; Faouri, Y.S.; Iqbal, S.S., "Design and fabrication of a dual electrically small MIMO antenna system for 4G terminals," Microwave Conference (GeMIC), 2011 German , vol., no., pp.1,4, 14-16 March 2011

- [7] Sharawi, M.S.; Faouri, Y.S.; Iqbal, S.S., "Design of an electrically small meander antenna for LTE mobile terminals in the 800 MHz band," GCC Conference and Exhibition (GCC), 2011 IEEE , vol., no., pp.213,216, 19-22 Feb. 2011
- [8] Yanal Faouri, "Design of an LTE Antenna for Mobile Communications: Fourth Generation", VDM Verlag, 2010